Franz Tschuchnigg

3D Finite Element Modelling of Deep Foundations Employing an Embedded Pile Formulation

Dissertation

Eingereicht an der Fakultät für Bauingenieurwissenschaften

Technische Universität Graz

Begutachter:

Ao.Univ.-Prof. Dipl.-Ing. Dr.-techn. Helmut F. Schweiger, M.Sc

Institute for Soil Mechanics and Foundation Engineering
Graz University of Technology, Austria

Dr.-Ing. habil. Peter-Andreas von Wolffersdorff

Baugrund DRESDEN Ingenieurgesellschaft mbH
Germany

Graz, November 2012

Acknowledgements

This thesis was made possible by the great support of Ao.Univ.-Prof. Dipl.-Ing. Dr.techn. Helmut F. Schweiger. I greatly enjoyed working with him in the Computational Geotechnics Group at Graz University of Technology. Thank you very much, Helmut.

I am grateful to Dr.-Ing. habil. Peter-Andreas von Wolffersdorff for reviewing this thesis.

I am grateful to Em.Univ.-Prof. Dipl.-Ing. Dr.techn. Stephan Semprich as former Head of the Institute for Soil Mechanics and Foundation Engineering at Graz University of Technology, for making the research facilities available to me.

I thank all my colleagues at the Institute for Soil Mechanics and Foundation Engineering for the pleasant working atmosphere. In particular, I would like to thank Václav Račanský, Bert Schädlich, Christian Lackner, Ali Nasekhian, Vahid Galavi and Gregor Supp.

Graz, November 2012 Franz Tschuchnigg

Kurzfassung

Hochhäuser und setzungsempfindliche Gebäude können im Allgemeinen nicht auf Flachgründungen fundiert werden, sodass es einer Tiefgründung bedarf. Abhängig vom Bodenaufbau und den dazugehörigen Bodenparametern stellt in den meisten Fällen eine Pfahl-, Pfahl-Platten- oder Schlitzwandgründung die Lösung dar. Für diese Gründungssysteme ist die Einschätzung der Setzungen und differenziellen Verformungen üblicherweise das Kernthema. Um jedoch alle gegenseiteigen Beeinflussungen, welche innerhalb einer Tiefgründung auftreten, berücksichtigen zu können, ist der Einsatz von numerischen Methoden unverzichtbar. Die Finite Elemente Methode, neben anderen numerischen Verfahren, ist ein sehr leistungsfähiges Instrument für diese Art der Anwendungen. Da eine zweidimensionale Abbildung, der in dieser Arbeit untersuchten Problemstellungen, in der Regel nicht möglich ist, liegt das Hauptaugenmerk auf dreidimensionale Berechnungen.

Neben dem Standard-Finite Elemente Verfahren, indem Pfähle mit Volumenelementen diskretisiert werden und die Pfahl-Boden Interaktion mit Interfaceelementen abgebildet wird, wird eine alternative Modellierungsvariante für Tiefgründungen - die "Embedded Pile" Option - diskutiert. Der größte Vorteil dieses Ansatzes liegt darin, dass der Pfahl in beliebiger Richtung angeordnet werden kann und das Finite Elemente Netz nicht beeinflusst, wodurch es ermöglicht wird, große Pfahlgruppen zu modellieren. In dieser Arbeit wird eine verbesserte Formulierung dieser Modellierungstechnik präsentiert. Die wesentlichsten Optimierungen des Ansatzes liegen in der Definition der Interfacesteifigkeiten und der Modifikation des sogenannten elastischen Bereiches. Eine Vielzahl von Validierungsbeispielen, unter Verwendung verschiedener Stoffgesetze, demonstrieren die Einsatzmöglichkeiten und Vorteile dieser fortgeschrittenen Modellierungstechnik.

Letztendlich wird die Anwendung des optimierten "Embedded Pile" Konzeptes auf Randwertprobleme präsentiert. Unterschiedliche Tiefgründungssysteme werden hinsichtlich der maximalen Setzung, differenziellen Verformung und Wirtschaftlichkeit verglichen. Weitere Gegenüberstellungen unterschiedlicher Modellierungsansätze bekräftigen, dass die "Embedded Pile" Formulierung eine leistungsfähige Alternative zur Standard-FE Methode darstellt. Außerdem wird der Einfluss der Anfangssteifigkeit im Bereich kleiner Dehnungen auf das Setzungsverhalten von Tiefgründungen evaluiert. Die Ergebnisse zeigen, dass, sobald die hohe Anfangssteifigkeit bei kleinen Dehnungen berücksichtigt wird, der Einfluss der Randbedingungen auf die errechneten Setzungen deutlich abnimmt und man ein realistischeres Verformungsverhalten erhält.

Abstract

In general, high-rise buildings and building susceptible to settlements cannot be supported by shallow foundations and a deep foundation system is required. Depending on the soil profile and the corresponding soil properties, a pile, piled raft or diaphragm wall foundation is the solution for most cases. For these types of foundation systems assessment of settlements and differential settlements is generally the key issue, but to account for all interactions within a group of deep foundation elements, advanced numerical modelling is essential. The finite element method, amongst other numerical techniques, provides a very powerful tool for these applications. But since a 2D representation of the problem is generally not possible, the main focus of this thesis is on 3D analyses.

Besides the widely used standard finite element approch, where piles are discretized by means of volume elements and the pile-soil interaction is modelled with interface elements, an attractive alternative to model deep foundations is discussed, namely the embedded pile concept. The substantial benefit of this approach is that piles can cross solid finite elements in an arbitrary direction and do not influence the finite element mesh, thus it is possible to model large pile groups. In this thesis, an improved formulation of this modelling technique is presented. The main enhancements are related to changed interface stiffnesses of the embedded pile and a modification of the so-called elastic region approach. A number of validation examples, using different types of constitutive models, demonstrate the capabilities and advantages of this advanced modelling technique.

Finally, the application of the improved embedded pile concept to boundary value problems is presented. Different foundation concepts are compared concerning maximum settlements, differential settlements and economic efficiency. Further comparisons of the different modelling approaches clearly indicate that the embedded pile formulation is a conceivable alternative to volume piles. Additionally, the influence of small strain stiffness on the obtained settlement behaviour of deep foundations is studied extensively. The results demonstrate that once a model including small strain stiffness is used, the effect of the model boundary conditions on the computed displacement is diminished and a more realistic settlement behaviour can be obtained.

Table of contents

List of symbols

The symbols used in this thesis are listed in alphabetical order. Additional explanation is provided in the text at first appearance. Units and abbreviations are not included in this list.

Small letters

b	width of structure
c	cohesion
c'	effective cohesion
c_u	undrained shear strength
c'_i	effective cohesion of an interface
d	diameter of the embedded pile
dco	dilatancy cut-off
d_{GB}	diameter of the grout body
d_q	depth factor according to Hanson (1970)
d_v	virtual diameter of the grout body
d_{50}	average grain size
e	void ratio
e_{init}	initial void ratio
e_{max}	maximum void ratio
e_{min}	minimum void ratio
e_P	spacing between piles
f	yield function
f^c	volumetric part of yield function
f_{GB}	enlargement factor for ground anchor facility
f_{su}	ultimate shaft resistance
$\bar{h}$	slenderness ratio of a pile
$h_{O\text{-}Cell}$	height of O-Cell jacking device
l	length of structure
l_{pl}	length of plasticity along the pile shaft
m	power index, controlling stress dependency of stiffness
p'	mean effective stress
p'_{eq}	equivalent stress on isotropic normal compression line
p'_{hist}	highest mean effective stress
$p'_{initial}$	initial mean effective stress
p'_p	effective pre-consolidation stress
p_{bu}	ultimate stress at the pile base

$p_{lim.}$	limiting stress at the pile base
p_{ref}	reference stress
p_w	pore water pressure
q	Roscoe deviatoric stress invariant
q'	surcharge pressure
$\tilde{q}$	measure for deviatoric stress
q_a	asymptotic value of shear strength
q_f	ultimate deviatoric stress
q_r	constant distributed load
$s;\ t$	axis of MIT representations of stress paths
s_E	settlement of a single pile
s_G	settlement of a pile group
s_q	shape factor according to Hanson (1970)
t	thickness
t_i	virtual interface thickness
$\mathbf{t}^{skin}$	skin traction
t_r	raft thickness
t_s	embedded pile shear stress in axial direction
$t_{s,max}$	maximum shear stress in axial direction
$t_n,\ t_t$	normal stresses at an embedded pile
tan α	inclination of settlement trough
$\boldsymbol{u}$	displacements within a solid soil element
$\mathbf{u}^n$	vector of nodal displacements
u_p	pile displacements
$\mathbf{u}_{rel}$	relative displacement vector
u_{rel}	relative displacement of the embedded beam and the virtual soil node
u_s	soil displacements
$\mathbf{u}_p^{\ n}$	nodal displacement vectors of the embedded beam element
$\mathbf{u}_s^{\ n}$	nodal displacement vector of the soil
$\mathbf{u}_p$	embedded beam node displacement vector
u^p	displacement of embedded beam element node
$\mathbf{u}_s$	virtual soil node displacement vector
u^s	displacement of virtual soil node
u_y	vertical displacements
$u_{p,el}$	elastic pile deflection
$v_{g,}\ u_g$	global coordinates
$v_{loc},\ u_{loc}$	local coordinates
x, y, z	Cartesian coordinates

Capital letters

A	embedded pile cross section area
A_k, B_k	bearing capacity factors according to Berezantzev (1961)
A_m	model dimensions
A_p	cross sectional area of a pile
$A_{p,B}$	cross sectional area at pile base
B	strain-displacement matrix
BEM	boundary element method
B_m	model width
B_r	raft width
CSP	measure for amount of plasticity
D	pile diameter
D	elastic constitutive matrix
$\mathbf{D}_i$	constitutive matrix of an interface
D_m	model depth
DoF	degrees of freedom
E	Young's modulus
$\overline{E}$	stiffness ratio between pile and surrounding soil according to Rajapakse (1990)
E_{50}	deviatoric hardening modulus in Hardening Soil model at actual stress
$E_{50,ref}$	deviatoric hardening modulus in Hardening Soil model at reference pressure
E_0	isotropic Young's modulus at very small strains
EA	axial stiffness
$E_{el.R}$	stiffness inside the elastic region
E_i	initial stiffness in a drained triaxial test
EI	flexural rigidity
E_{oed}	actual stiffness for primary oedometer loading
$E_{oed,i}$	actual stiffness for primary oedometer loading of an interface
$E_{oed,ref}$	reference stiffness for primary oedometer loading
E_p	Young's modulus of the pile
E_r	Young's modulus of the raft
E_{soil}	Young's modulus of the soil
E_u	undrained stiffness modulus
E_{ur}	stiffness for un- and reloading at actual stress
$E_{ur,ref}$	stiffness for un- and reloading at reference stress
EA	axial stiffness
EI	bending stiffness

EP	embedded pile
ES_{avg}	average element size
F_{foot}	base resistance of an embedded pile
F_{max}	maximum base resistance of an embedded pile
$F_{max,GA}$	maximum force of the anchor rod
FE	finite element
FEA	finite element analysis
FEM	finite element method
G	shear modulus
G_s	group efficiency factor
G_{el}^{av}	the average shear stiffness of soil element
$G_{el.R,B}$	stiffness inside the elastic region above and below an embedded pile
$G_{el.R,S}$	stiffness inside the elastic region above along an embedded pile
G_i	shear modulus of an interface
G_L	shear modulus of the soil at the level of the pile base
G_0	initial isotropic shear modulus at small strains
$G_{0,ref}$	initial isotropic shear modulus at small strains at reference pressure
G_s	secant shear modulus
G_t	tangent shear modulus
G_{ur}	un- and reloading shear modulus
$G_{ur,ref}$	un- and reloading shear modulus at reference pressure
HS	Hardening Soil model
HSS	Hardening Soil Small model
I_2, I_3	moments of inertia
I_D	relative density
I_{rr}	reduced rigidity Index according to Vesic (1972)
$\mathbf{J}$	Jacobean matrix
K	coefficient of lateral earth pressure
$\overline{K}$	relative stiffness between pile and soil
K'	drained elastic bulk modulus
K_0	lateral earth pressure coefficient at rest
K_0^{nc}	lateral earth pressure coefficient at rest for normally consolidated conditions
K_{ep}	global stiffness response of an axially loaded embedded pile
$\mathbf{K}_e$	element stiffness matrix
K_{foot}	embedded pile spring stiffness at the pile base
K_s	elastic shear interface stiffness
K_n, K_t	elastic normal interface stiffnesses
K_v	axial stiffness

L	pile length
L_{tot}	total anchor length
L_{GB}	grout body length
L_m	model length
L_r	raft length
$\mathbf{M}$	matrix according to van Langen (1991(
M	bending moment
MC	Mohr-Coulomb model
LSC	load-settlement curve
Nel_{fixed}	fixed number of elements related to global mesh coarseness settings
N_c, N_q, N_γ	bearing capacity factors
N_c^*, N_q^*	bearing capacity factors according to Vesic (1975)
$\mathbf{N}$	matrix of interpolation functions
$\mathbf{N}_p$	matrix of interpolation functions of the embedded beam element
$\mathbf{N}_s$	matrix of interpolation functions of the soil
OCR	over-consolidation ratio
P_0	applied load
POP	pre-overburden pressure
PRF	piled raft foundation
$\overline{P}_{(z)}$	resultant axial load in pile cross-section
R	pile resistance
R_A	ratio A_p to area bounded by outer circumference of a pile
R_b	base resistance of a single pile
R_{bu}	ultimate base resistance of a single pile
R_{eq}	equivalent embedded pile radius
R_{inter}	interface reduction factor
R_{Pile}	load carried by piles
R_s	shaft resistance of a single pile
R_{su}	ultimate shaft resistance of a single pile
R_{tot}	total load
R_{ult}	ultimate load capacity of a single pile
$\mathbf{T}$	transfer matrix
$\mathbf{T}^{skin}$	material stiffness matrix of the embedded interface elements
$T_{top,max}$	maximum skin friction at the top of the embedded pile
$T_{bot,max}$	maximum skin friction at the bottom of the embedded pile
$\overline{T}(z)$	contact traction in vertical direction
U_x, U_y, U_z	translational degrees of freedom
VP	volume pile
W	pile weight

Small Greek letters

α	adhesion factor
α_{PR}	piled raft coefficient
α_b	depth ratio according to Berezantzev (1961)
α_c	model parameter defining the shape of the cap yield function
β	quantity K·tanδ' in the β-method
χ	rotation angle
δ'	effective soil-structure friction angle
$\boldsymbol{\delta}$	nodal displacement vector
δh	radial displacement due to dilation
δ_v	Virtual interface thickness factor
γ	bulk unit weight
$\gamma_{0.7}$	reference shear strain in Hardening Soil Small model
γ^p	plastic shear strain
γ_s	shear strain
$\gamma_{cut\text{-}off}$	cut-off shear strains
γ_{sat}	bulk unit weight of soil below ground water table
γ_{unsat}	bulk unit weight of soil above ground water table
ε_1, ε_2, ε_3	major, intermediate and minor principal strain
ε_v	volumetric strain
ε_v^{init}	initial volumetric strain
ε_v^p	plastic volumetric strain
$\Delta\varepsilon$	incremental strain
θ	Lode's angle
λ	nondimensional coefficient for the λ-method
ν	Poisson's ratio
ν'	drained Poisson's ratio at large strains
ν_t	Poisson's ratio of an interface
ν'_{ur}	Poisson's ration for un- and reloading
ξ, η, ζ	intrinsic coordinates
ρ	degree of non-homogeneity of the soil
σ'_1, σ'_2, σ'_3	major, intermediate and minor effective principal stress
σ'_m	centre of Mohr circle
σ'_n	effective normal stress
σ_n	normal stress
σ_n^{avg}	average normal stress
σ'_p	highest vertical stress reached
σ'_{r0}	initial effective radial stress
$\Delta\sigma'_r$	increase of effective radial stress

$\Delta\sigma'_{rp}$	increase of effective radial stress due to principal stress rotation
$\Delta\sigma'_{rd}$	increase of effective radial stress due to interface slip dilation
σ'_t	effective stress of the surrounding soil perpendicular to an EP
σ'_v	vertical effective stress
σ'_{yy}, σ'_{xx}	Cartesian effective stresses
σ'_{zz}, σ'_{xy}	Cartesian effective stresses
σ'^{0}_{yy}	in-situ effective vertical stress
$\Delta\sigma$	incremental stress
τ	shear stress
τ_f	shear stress at failure
τ_{xy}, τ_{yz}, τ_{xz}	global shear stresses
φ	friction angle
φ'	effective friction angle
φ'_{cs}	effective friction angle at critical state
φ'_i	effective friction angle of an interface
φ'_m	mobilized friction angle
ψ	ultimate dilatancy angle
ψ_t	ultimate dilatancy angle of an interface
ψ_m	mobilized dilatancy angle
ϖ	angle of plastification according to Janbu (1976)

Capital Greek letters

$\Gamma_{el.R}$	correction factor for stiffness inside the elastic region
Γ_{foot}	multiplier for the foot embedded interface stiffness
$\Gamma_{G,B}$	multiplier for the elastic region approach above and below an EP
$\Gamma_{G,S}$	multiplier for the elastic region approach along an embedded pile
Γ_n	multiplier for the normal and tangential embedded interface stiffness
Γ_s	multiplier for the axial embedded interface stiffness
Δ	difference
Δ_s	direct input value for axial embedded interface stiffness
Δ_n	direct input value for normal and tangential embedded interface stiffness
Λ	compensation factor for cap-plasticity
$\sum R_{pile}$	sum of loads carried by piles
ϕ_x, ϕ_y, ϕ_z	translational degrees of freedom

1 Introduction

1.1 Motivation

The development of numerical methods and the increase of their application to a wide range of geotechnical boundary value problems led to the reality that nowadays, numerical geotechnics take an important position within the daily geotechnical business. But the potential of these methods is closely linked to the modelling technique - which generally involves a number of assumptions - and the constitutive models applied. Both require a profound knowledge of soil mechanics, awareness of limitations of the constitutive models and last but not least experience. The latter comprises on the one hand in-depth understanding of numerical modelling, and on the other, know-how from a practical point of view. A number of different numerical techniques have been developed in the last 30 years, however the finite element method plays an important role in computational geotechnics these days.

In this thesis the behaviour of deep foundations is studied by means of the finite element method. The influence of constitutive models on the behaviour of single piles, pile groups and piled raft foundations is investigated.

It is well known that almost all boundary value problems in geotechnical engineering are of three-dimensional nature. Nevertheless, when using analytical methods, the problems are generally reduced to two-dimensional geometries. Also, when utilizing numerical methods it is common practise to define either plane strain or axisymmetric 2D models instead of full three-dimensional analysis. When dealing with deep foundations, such a simplification is due to geometrical restrictions usually not possible; therefore a full three-dimensional representation of the entire geometry is required. Hence, this thesis focuses mainly on 3D finite element analyses.

In the standard finite element approach, deep foundation elements are discretized by means of volume elements and the pile-soil interaction is modelled with interface elements. But if a large number of piles, columns or barrettes have to be constructed the computational models, using the standard FE approach, get very expensive, leading to very large models and thus long calculation times. Additionally, the number of piles is limited because of soft- and hardware restrictions. As a consequence this approach is not very popular in practical engineering.

An attractive method to reduce the complexity of such models is the utilization of a so-called embedded pile formulation (Sadek & Shahrour 2004) where piles are not explicitly modelled with continuum finite elements but replaced by a special "formulation" which can take into account the behaviour of a pile penetrating a finite element in any orientation. The main part of this work deals with this alternative method of modelling deep foundation elements, which also enables the study of large pile groups or piled raft foundations, since a discretization of piles is not necessary.

1.2 Scope and outline of thesis

The thesis starts with a brief overview of single pile behaviour, where the main focus is related to the estimation of the ultimate base and ultimate shaft resistance of an axially-loaded pile. Additionally, different methods of calculating single pile settlements are discussed. In the following, the influence of the pile group effect is discussed and some special constraints related to piled raft foundations are presented.

Chapter 3 gives a short introduction to numerical modelling of deep foundations by means of FEM, followed by an extensive literature review. It must be pointed out that the literature review only contains numerical studies of deep foundations performed with the finite element method. The author is aware that other powerful numerical methods also exist, however related references are given in the particular chapters. Chapter 3 also includes an overview of some basic terms and aspects of FEM for deep foundation analysis. The behaviour of interface elements and some special issues linked to deep foundations are emphasised. Then, the standard finite element approach is discussed in detail. The effect of mesh discretization and the influence of dilatancy are highlighted.

The embedded pile concept is described in full detail in chapter 4. The geometrical definition of such an element is discussed first followed by the constitutive relations of an embedded pile. Special attention is addressed to the definition of the embedded pile interface stiffnesses and the so-called elastic region approach.

Chapter 5 demonstrates at the beginning some deficiencies of the original embedded pile concept as currently implemented in PLAXIS 3DF. The influence of the embedded foot interface stiffness on the settlement behaviour is presented, followed by similar studies concerning the skin interface stiffness. The necessity of stress dependent interface stiffness is illustrated in detail as well. Next, the explanation for the influence of the vertical mesh coarseness is given. After that the elastic region approach is studied in detail investigating the stress flow inside

the created virtual volume and then a new definition of the stiffness inside the elastic region is proposed. Finally, the effect of the ultimate skin friction distribution on the behaviour of embedded piles is discussed and an improved embedded pile formulation is presented.

Chapter 6 contains the validation of the improved embedded pile concept. First, axially-loaded single piles embedded in linear elastic soil are analysed and compared with results presented in the literature. Then elasto-plastic soil behaviour is used and the behaviour of the embedded piles is compared with measurements and results obtained with other modelling techniques. Horizontally loaded piles are then investigated. Subsequently the performance of vertically loaded pile groups and piled raft foundations is studied, again first assuming linear elastic soil conditions and finally using more advanced constitutive models. At the end of chapter 6, the behaviour of horizontally-loaded pile groups computed with the embedded pile formulation is compared with the pile group response obtained with other programs.

The application to boundary value problems is provided in chapter 7. The first project discussed is the DC Towers in Vienna. Due to the small distance between the two towers, it is necessary to model both towers. A comparison of the executed foundation concept with an alternative foundation system, namely a piled raft foundation is discussed. The second boundary value problem is the Sky Tower in Bucharest, the most impressive part of the Floreasca City Centre. The optimisation of the deep foundation concept concerning a reduction of differential settlements in combination with an economical design will be presented. Also given are a parametric study and a validation of the numerical model, namely a back-analysis of a barrette load test. Then, another application of the embedded pile concept is highlighted: the ground anchor facility, where the grout body of an anchor is modelled by means of embedded piles. Obtained axial forces are compared with results published in the literature. Finally, the project "Wien Mitte", a large and - concerning the constructional constraints - complex railway station is discussed. The building is founded on jet grouted columns, which are modelled with embedded piles. To show the capability of the concept, preliminary studies are presented first. After that the settlement prediction of the entire construction is shown.

Conclusions and some recommendations for further research are given in chapter 8. References are provided in chapter 9.

Details related to the constitutive models used are presented in Appendix A. In Appendix B the basic theory of an isoparametric interface element is illustrated and in Appendix C the displacement approximation within a solid 15 noded wedge element is discussed.

2 Deep foundations - An overview

2.1 Introduction

In this chapter an overview of the behaviour of single piles, pile groups and piled raft foundations is presented. For these types of deep foundation systems, assessment of settlements and in particular differential settlements are, most of the time, key issues. However, usual "static" approaches to calculate the ultimate capacity of piles are also discussed, where the behaviour of a pile is related to measured soil properties. This aims to show firstly that a number of different empirical and theoretical approaches exist, but secondly, and mainly, that these correlations can be used to define the input values for the embedded pile concept discussed below. "Dynamic" approaches, which use pile-driving data to estimate the load capacity of driven piles, are not presented. Also, the use of in-situ tests (e.g. CPT or SPT test) to predict the ultimate resistance of piles is not discussed in the following chapters.

2.2 Behaviour of vertically-loaded single piles

2.2.1 Ultimate load capacity

The ultimate load capacity R_{ult} of a single pile consists of two components, the ultimate shaft resistance R_{su} and the ultimate base resistance R_{bu}. The sum of these two components less the weight of the pile (W) results in the ultimate load capacity R_{ult}.

$$R_{ult} = R_{su} + R_{bu} - W \tag{1}$$

R_{su} and R_{bu} are strictly speaking interdependent, but for all approaches presented in this chapter they are considered independent of each other. E.g. Yang (2006) showed that the influence zone above the pile tip has, depending on the soil type, a length up to 2.5 times the pile diameter D. Of course when dealing with finite element analyses the interaction of tip and shaft resistance is automatically taken into account.

For drained conditions, R_{su} can be calculated by integrating the pile-soil shear strength over the pile shaft surface.

$$R_{su} = \int_0^L D \cdot \pi \cdot \left(c' + K \cdot \sigma'_v \cdot \tan \delta'\right) dz \tag{2}$$

L is the pile length, c' the effective cohesion, K the coefficient of lateral earth pressure, σ'_v the effective vertical stress and δ' the effective soil-structure friction angle. According to Poulos & Davis (1980), it is usually accepted that the ultimate base resistance for drained conditions can be evaluated using the classical bearing-capacity theory (Terzaghi 1943).

$$R_{bu} = A_{p,B} \cdot (c' \cdot N_c + q' \cdot N_q + 0.5 \cdot \gamma \cdot D \cdot N_\gamma) \tag{3}$$

$A_{p,B}$ is the pile cross sectional area at the base, q' is the magnitude of surcharge pressure at the surface, γ is the bulk unit weight of the soil and N_c, N_q, N_γ are bearing capacity factors. Prandtl (1920) derived with analytical stress field solutions expressions for N_c and N_q. N_γ is found from an approximate calculation. Fig. 1 shows a schematic overview of the loads and resistances acting on a pile, where R_b and R_s represent the actual base and actual shaft resistance respectively. Both the base resistance and the shaft resistance of a single pile develop as a function of pile displacements, but in general R_{su} and R_{bu} are not mobilized at the same displacement. Fig. 1 also represents the distribution of normal force along a pile.

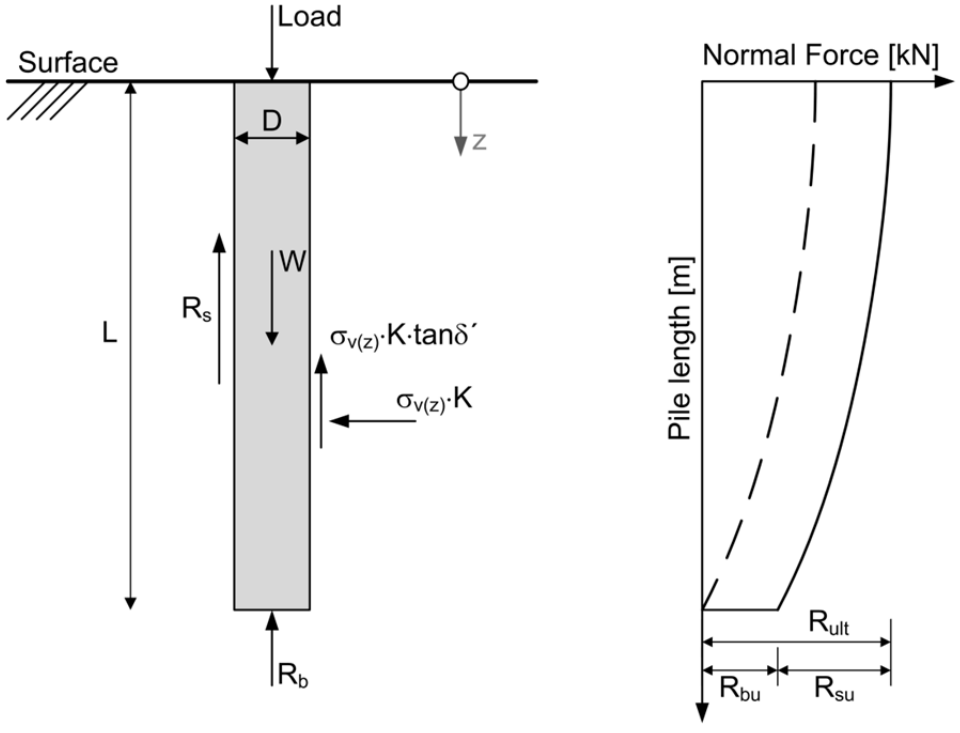

Fig. 1 Schematic overview of loads and resistances acting on a single pile (left), normal force distribution along a single pile (right)

Small loads result in small relative displacements between pile and soil and most of the load is supported by shaft resistance R_s. Once the ultimate shaft resistance is mobilized further, load is transferred to the pile base and the base resistance gets mobilized. In general, R_{su} is mobilized at relatively small vertical pile displacements, while large settlements are necessary to mobilize R_{bu}. Kulhawy (1984) states that about 5-10 mm of vertical pile displacements are enough to reach the full shaft resistance and settlements of about 10% of the pile diameter are required to mobilize most of the base resistance. Körber (2009) showed that the application of lift cells enables a higher mobilization of base resistance at small vertical pile displacements.

Depending on the behaviour of the pile two different cases can be distinguished: an end-bearing pile, where most of the load is carried by the base resistance R_b, and a skin friction pile, where the majority of the load is transferred via the pile shaft to the soil. If the sum of the pile resistances are plotted over the vertical displacements of the pile one obtains the load-settlement curve (LSC). Fig. 2 shows the load-settlement curves for a skin friction and an end-bearing pile. With these curves it is possible to work out the actual resistances R_b, R_s and total pile resistance R for a certain amount of vertical pile displacements.

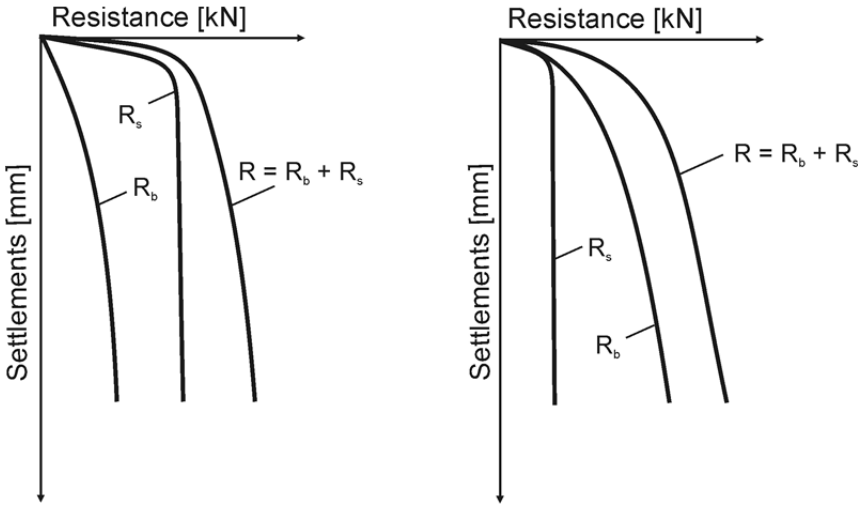

Fig. 2 Load-settlement curve for skin friction pile (left) and end-bearing pile (right), (after Kempfert et al. 2003)

The shape of the LSC depends on the pile installation, soil stiffness, soil strength and pile type. Rollberg (1978) presented different load-settlement curves found in the literature (Fig. 3).

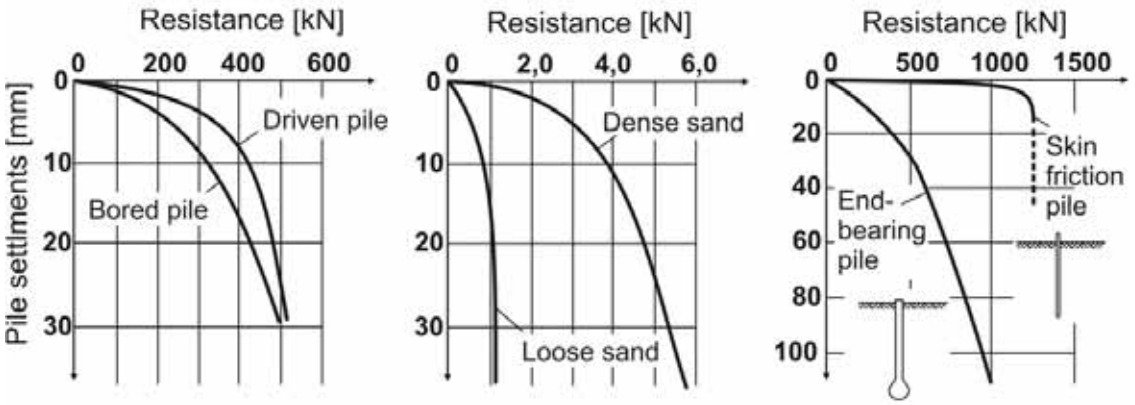

Fig. 3 Influence of installation method (left), soil strength (middle) and load transfer (right) on load-settlement curves (after Rollberg 1978)

2.2.1.1 Estimation of ultimate base resistance

A brief summary of different methods for determining the ultimate base resistance available in the literature is given in the following.

Meyerhof (1976) suggested that the maximum stress at the pile base p_{bu} can be estimated as:

$$p_{bu} = c' \cdot N_c + \sigma'_v \cdot N_q \leq p_{\lim.} \tag{4}$$

$p_{lim.}$ is a limiting value of p_{bu} related to a critical depth of pile penetration into the bearing layer. Meyerhof (1976) provided a diagram with graphs for the bearing capacity factors N_c and N_q.

Vesic (1975) defined the bearing capacity of deep foundations based on the cavity expansion theory.

$$p_{bu} = c' \cdot N_c^{\,*} + \eta \cdot \sigma'_v \cdot N_q^{\,*} \tag{5}$$

$$\eta = \frac{1 + 2 \cdot K}{3} \tag{6}$$

$$N_q^{\,*} = \frac{3}{3 - \sin\varphi'} \cdot e^{\left(\frac{\pi}{2} - \varphi'\right) \cdot \tan\varphi} \cdot \tan^2\left(\frac{\pi}{4} + \frac{\varphi'}{2}\right) \cdot I_{rr}^{\frac{4 \cdot \sin\varphi}{3 \cdot (1 + \sin\varphi)}} \tag{7}$$

$$N_c^* = (N_q^* - 1) \cdot \cot \varphi' \tag{8}$$

N_c^* and N_q^* are the bearing capacity factors, which are related to the reduced rigidity index I_{rr} as presented by Vesic (1972). Vesic (1975) provided tables for N_c^* and N_q^*.

Hansen (1970) modified the classical approach of Prandtl (1920) and introduced a depth factor d_q and a shape factor s_q.

$$p_{bu} = \sigma'_v \cdot N_q \cdot d_q \cdot s_q \tag{9}$$

$$d_q = 1 + 2 \cdot \tan \varphi' \cdot (1 - \sin \varphi')^2 \cdot k \tag{10}$$

$$k = \frac{L}{D} \qquad \text{for L/D} \leq 1 \tag{11}$$

$$k = \arctan\left(\frac{L}{D}\right) \qquad \text{for L/D} \geq 1 \tag{12}$$

$$s_q = 1 + \sin \varphi' \cdot \frac{b}{l} \tag{13}$$

b and l are the width and the length of the deep foundation element; when dealing with piles, the ratio of b/l reduces to 1. For deep foundations, the L/D ratio is always bigger than 1; therefore Equation 12 in combination with Equation 10 is used for the calculation of d_q.

Janbu (1976) presented a theoretical approach where the bearing capacity factor N_q is related to an angle of plastification ϖ. Janbu (1976) states that ϖ is in the range of about 60° for compressible to 105° for very dense soil types.

$$N_q = \left(\tan \varphi' + \sqrt{1 + \tan^2 \varphi'}\right)^2 \cdot e^{2 \cdot \varpi \cdot \tan \varphi'} \tag{14}$$

Berezantzev et al. (1961) presented results of theoretical and experimental investigations on the ultimate load capacity of vertically-loaded single piles in dense sand and reduced the bearing capacity factor N_q with increasing penetration depth L.

$$p_{bu} = A_k \cdot \gamma \cdot D + B_k \cdot \alpha_B \cdot \gamma \cdot L \tag{15}$$

α_B is a function of the depth ratio L/B and the effective soil friction angle, A_k and B_k are the bearing capacity factors. Berezantzev et al. (1961) provided tables for the factors α_B, A_k and B_k. Cheng (2004) presented slightly corrected values of N_q. Fleming et al. (2009) suggested that Berenzantev's approach should be used following Bolton (1986), where φ' is related to the relative density of the soil and corrected with the mean soil stress p' and the critical state friction angle φ'_{cs}.

2.2.1.2 Estimation of ultimate shaft resistance

A number of different approaches also exist concerning the ultimate skin resistance of axially-loaded piles. This chapter provides an overview of frequently used methods.

The so-called α-method introduced by Tomlinson (1957) relates the ultimate shaft resistance f_{su} of piles in clay to the undrained shear strength c_u, where α is the so-called adhesion factor.

$$f_{su} = \alpha \cdot c_u \tag{16}$$

It was found that α is not constant but reduces with increasing undrained shear strength. A comparison of values for the adhesion factors recommended by various workers can be found in Sladen (1992). Sladen (1992) showed that α can be expected to be a function of the effective stress level and the undrained shear strength (Equation 17).

$$\alpha = 0.5 \cdot \left(\frac{\sigma_v'}{c_u} \right)^{0.45} \tag{17}$$

Burland (1973) suggested that the ultimate shaft resistance should be estimated in terms of effective stresses. This approach is well-known in the literature as β-method, due to the fact that the quantity $\tan \delta' \cdot K$ is denoted as β, a similar factor to α except that β is related to effective stress parameters δ' and K.

$$f_{su} = K \cdot \sigma'_v \cdot \tan\delta' = \beta \cdot \sigma'_v \tag{18}$$

The stress state in the soil is of course influenced by the pile installation, hence the horizontal earth pressure coefficient K is different for different installation methods. Ratios between K and K_0^{nc} (normally consolidated earth pressure coefficient) are summarized in Kulhawy (1984). They range from 0.5 for jetted piles to 2.0 for driven piles with large displacements. From Equation 18 it follows that, with the assumption that the ratio $K/K_0^{nc} = 1$, the final distribution of shear stress at failure is very similar for a soil with high and a soil with low frictional strength. However, not only does the pile type (and thus the installation method) influence the bearing capacity, but also the construction technique of a drilled shaft, as reported e.g. by Brown (2002).

Based on a large number of pile load tests, Vijayvergiya & Focht (1972) presented a semi-empirical approach for the prediction of the skin friction capacity of piles in clayey soils. This approach is mostly denoted as λ-method, the non-dimensional factor λ being obtained from back-analysis of observed capacities of pile load tests. The value of λ strongly depends on the pile length.

$$f_{su} = \lambda \cdot (\sigma'_v + 2 \cdot c_u) \tag{19}$$

Lehane et al. (1993) proposed an approach based on instrumented pile tests to estimate the ultimate skin resistance of sands that takes into account the increase of radial effective stress due to loading. Starting from an effective radial stress σ'_{r0} (related to the installation process and the soil type), the radial stress increases because of principal stress rotation and interface slip dilation by the quantity $\Delta\sigma'_r$ until the ultimate shear stress is mobilized. According to Lehane et al. (1993), $\Delta\sigma'_r$ related to the rotation of principal stresses ($\Delta\sigma'_{rp}$) is relatively small for compression loading, and the increase due to dilation ($\Delta\sigma'_{rd}$) can be assessed from a boundary displacement δh applied to an elastic soil mass (with a shear modulus G).

$$f_{su} = (\sigma'_{r0} + \Delta\sigma'_r) \cdot \tan\delta' \tag{20}$$

$$\Delta\sigma'_{rd} = 4 \cdot \delta h \frac{G}{D} \tag{21}$$

When estimating the skin friction for piles loaded in tension, the change of radial effective stresses should also be taken into account. Fleming et al. (2009) stated

that the change in skin friction due to loading in tension instead of compression is in the order of 15 - 30%.

A comparison of a wide range of approaches to estimate the point and skin resistance of a single pile is given in Burgstaller (2010), including a number of correlations of CPT and SPT results with pile bearing capacities.

For both point bearing capacity and skin resistance, some approaches use a so-called critical depth, at which the resistance stays practically constant. Many authors argued that this limiting end-bearing stress and limiting side resistance is not a real phenomenon, but can be explained by a combination of other effects. Bolton (1986) showed that the dilatancy is suppressed under high confining stresses. Kulhawy (1984) demonstrated that tip and side resistance of deep foundations do not reach a limiting value. He outlined a rational explanation that the rate of increase for the tip resistance decreases with depth due to a reduction of the rigidity index. And the decrease of the shaft resistance with depth is related to the decreasing friction angle with overburden, and the variation of the coefficient of horizontal soil stress with depth. Fellenius & Altae (1995), Altae et al. (1993) and Fellenius (2001) argued that neglecting the presence of residual stresses is one reason for the fallacy of a critical depth. Also, Kraft (1991) gave several reasons for the misleading assumption of limiting values for unit shaft and toe resistance. Randolph (2003) showed that strain softening behaviour of the soil could also lead to a significant reduction of shear capacity, due to the reduction of the soil-structure friction angle δ' to its residual value.

2.2.2 Pile settlements

In general, settlements of a single pile are a combination of displacements due to the tip load and deformations caused by skin friction plus the elastic shortening of the pile. Of course, if soil conditions are undrained, pile deformations are furthermore a combination of immediate and consolidation settlements. Poulos & Davis (1980) classified the calculation methods to predict pile displacements into three categories: "load-transfer" methods, methods based on the theory of elasticity and numerical methods. Group 1 uses measured relationships between pile resistance and pile settlements, while group 2 obtains the soil displacements using Mindlin's equations in most cases. In the following an overview of customarily-used methods is given.

A widely-used approach is the one by Poulos & Davis (1980) or Poulos (2001a). They provided charts based on numerical analyses that take a number of parameters into account like pile and soil stiffness. A rather simple method of predicting settlements of single vertically-loaded piles was presented by Cassan

(1966), who used hyperbolic functions to describe the skin friction, the vertical stress in the pile and the resulting settlements. Vesic (1977) proposed a semi-empirical method for calculating the settlements of a single pile, whereas Randolph & Wroth (1978) presented an approximate closed form solution for the settlement prediction of single piles. The method developed by Randolph & Wroth (1978) can deal with pile compressibility and soil inhomogeneity as well. The analysis is based on the idea that the load transferred from the pile shaft to the soil and the pile tip load are initially examined separately, and for the settlements of the entire pile, both effects are combined. A detailed description of the approach including some further developments is given in Fleming et al. (2009). In the literature one can find a number of other approximate methods for settlement predications based on the approach of Randolph & Wroth (1978). Most of the time, they differ in the assumptions concerning the distribution of stiffness with depth. Fleming (1992) presented another method to predict the settlements of axially-loaded piles where he proposed to use hyperbolic functions to describe the base and shaft resistance individually.

In the author's opinion, all methods mentioned above are limited to the conditions assumed in their derivation. Thus, they are to be handled with care if they are applied to different circumstances. The finite element method provides a general tool that can be used with different constitutive models to account for varying boundary conditions, however it has to be clear that the behaviour of a pile is primarily dominated by the strength and the stiffness of the surrounding soil. And as stated by Poulos (1989), another advantage is that FEM offers the possibility to model the history of the pile, like installation processes or loading sequences, which, in combination with non-linear soil behaviour, results in a better understanding of pile behaviour.

2.3 Behaviour of vertically-loaded pile groups

Rarely do pile foundations consist of one single pile, but of a group of piles, therefore the behaviour of pile groups is briefly outlined in this chapter. Both the bearing capacity and the global stiffness response of a pile group differ in general from the behaviour of single piles. The main effects which influence the behaviour of pile groups are, according to Rudolf (2005): the stiffness of the raft and/or the superstructure, the pile type, the installation procedure, the size of the pile group, the ratio of pile spacing to pile length and the soil type. The settlements of a pile group in working load conditions are in general bigger than the vertical displacements of a single pile with equivalent load (Fig. 4). The group effect is related to increased settlements of a pile, if this pile is affected by the displacement field of a neighbouring pile (Randolph & Wroth 1979). At high load levels, pile groups show in general a stiffer response than single piles, which

comes from the fact that the stress state in the soil increases. But as stated by Kempfert et al. (2003), pile groups in the allowable load range experience generally higher displacements than single piles. Within a pile group, the behaviours of the individual piles also differ significantly. Fig. 4 illustrates the load-settlement behaviour of the centre, edge and corner pile of a 9-pile group. The load carried by the piles varies depending on the stiffness of the superstructure. If the raft and/or the superstructure is relatively stiff, more load is initially transferred to the corner piles. If the stiffness of the raft is low, the load distribution within a pile group strongly depends on the pattern of the applied load.

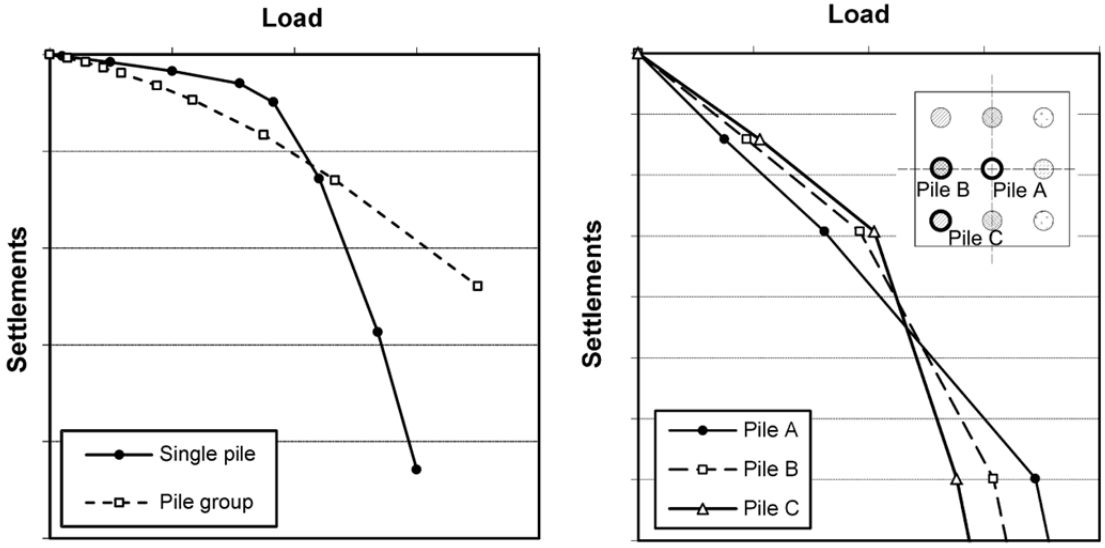

Fig. 4 Single pile vs pile group (left); load-settlement behaviour of individual piles within a pile group (right)

A typical quantity to describe the group effect is the group efficiency factor G_s, which is defined as the ratio of the average group settlement (s_G) divided by the settlement of a single pile (s_E) at the same load level.

$$G_s = \frac{s_G}{s_E} \tag{22}$$

To evaluate the load-settlement behaviour of pile groups, a number of approaches are available in the literature. There are empirical methods as presented by Skempton (1953) or Hettler (1986) and other approaches that use equivalent piers or equivalent rafts (e.g. Randolph 1994). The size and the position of the equivalent raft depend on the load transfer mechanism of the pile (end-bearing or friction pile), while the equivalent pier needs an equivalent diameter and homogenized stiffness. Analytical methods to calculate settlements

of pile groups can be divided into a group that does not take pile-pile interaction into account and another group that accounts for pile interactions by means of interaction factors. Detailed information related to the first group is given in Rudolf (2005) and an overview of the possibilities of the latter group is presented by Poulos (2006).

All approaches mentioned have deficiencies either to the geometrical definition of the pile group or to a realistic representation of the soil. In the author's opinion, pile groups are a typical example of boundary value problems where numerical analyses - and especially 3D modelling - are essential. Various authors showed the potential of different numerical methods; e.g. El-Mossallamy (1996), who used a coupled finite element and boundary element method; Comodromos & Bareka (2009), who conducted the finite difference method to analyse axially-loaded pile groups; or Chow (2007), who applied a combination of finite layer and FE technique to study pile group effects. Of course, the finite element technique is also increasingly utilised to calculate the performance of such foundations. A detailed literature review, indicating the capabilities of the finite element method, is given in chapter 3.2.

2.4 Behaviour of vertically-loaded piled raft foundations

In contrast to conventional pile foundations in which the piles are designed to carry the entire load, the design of piled raft foundations allows sharing of the load between the raft and the piles. This separation of the load has a significant effect on the load-settlement behaviour of such foundations, the mobilization of skin friction and also the distribution of the shaft resistance along a pile. Compared with a pile group where a pile-pile and pile-soil interaction exists, a piled raft foundation (PRF) involves two additional interactions, namely a raft-soil and raft-pile interaction. Fig. 5 shows schematically the concept of a piled raft foundation. The overall aim of a PRF is, in general, a reduction of vertical and differential settlements in combination with an economic design. Burland et al. (1977) coined in that context the term "settlement reducing piles".

The load carrying behaviour of a PRF is generally represented with the α_{PR} factor, which is the ratio of the sum of the load carried by the piles ($\sum R_{pile}$) and the applied total load (R_{tot}). Hanisch et al. (2002) reported that executed PRFs were generally designed with α_{PR} factors between 0.3 and 0.8. Of course α_{PR} is not a constant value, but depends strongly on the load level.

$$\alpha_{PR} = \frac{\Sigma R_{Pile}}{R_{tot}} \tag{23}$$

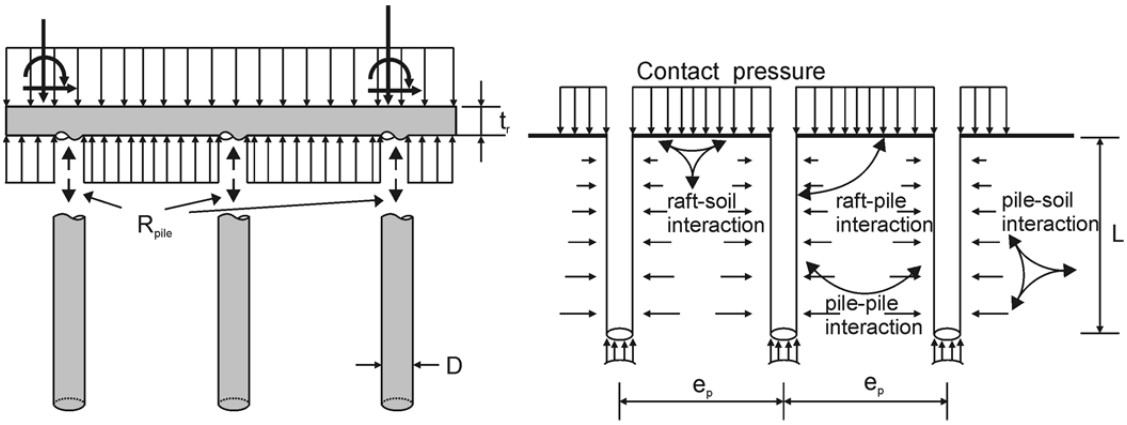

Fig. 5 Soil-structure interactions for piled raft foundations (after Hanisch et al. 2002)

Due to the raft soil interaction, the global stiffness response of a piled raft foundation is in general stiffer than a pile group with the same number of piles. Fig. 7 compares the load-settlement behaviour of a single pile with an equivalent load with LSCs of two piled raft foundations with different pile spacings (e_p). Additionally, the load distribution between the individual piles and the raft is illustrated. This shows clearly the complex interactions of a piled raft foundation. Both the load distribution between the piles and the load carried by the raft vary significantly with increasing settlements.

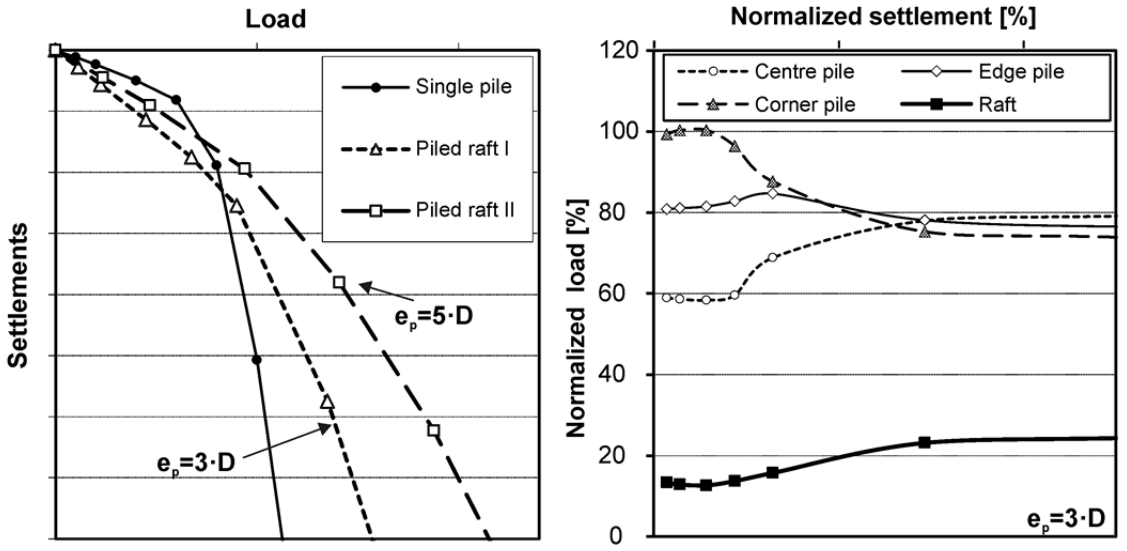

Fig. 6 Single pile vs PRF (left); variation of normalized load with normalized settlement (right)

To assess the behaviour of piled raft foundations various methods ranging from empirical and analytical to numerical are available. An overview of different approaches is given in Rudolf (2005), Hanisch et al. (2002) and Poulos (2001b).

But because the relative proportion of load carried by piles and raft is the key point of interest regarding an economic design, it is necessary to take all the above-mentioned interactions into account. Additionally, the soil behaviour must be represented as realistically as possible to ensure that the different load carrying mechanisms, which depend on both strength and stiffness of the surrounding soil, can be represented by the calculation model. Thus, simplified or analytical methods are perhaps useful for preliminary design and rough settlement predictions, but for the design and frequently required optimisation of the final foundation concept (for example Reul 2010 or Schreib et al. 2010), numerical methods are, in the author's opinion, absolutely essential.

3 Numerical modelling of deep foundations by means of FEM

3.1 Introduction

Within the last decades, numerical modelling has been established as a widely used tool for deep foundation analyses. The finite element method, amongst other numerical methods, is a very powerful tool that takes into account all different interactions of complex structures existing within deep foundations. In today's engineering praxis, no high-rise buildings founded on piles or barrettes are designed without, at least, the support of numerical analysis. One reason is that in the last three decades the rapid development of computer technologies enabled the switch from rather simple 2D computational models to complex 3D analyses.

However, numerical modelling needs a profound knowledge of soil mechanics, the behaviour of constitutive models and the numerical method used. This requirement of background knowledge in combination with practical experience is essential for complex numerical modelling. An overview of numerical modelling in geomechanics is given in Schweiger (1994). As mentioned in chapter 1, this thesis deals only with the finite element method, but naturally other numerical methods are also used in the field of deep foundation analysis. The theory of the finite element method (FEM) has been presented in a number of textbooks; detailed descriptions are given for example in Beer & Watson (1992), Zienkiewicz & Taylor (1991) or Bathe (1982).

The first part of this chapter gives a general literature review of numerical modelling of deep foundations by means of FEM. Some basic aspects of the finite element method as used in this thesis for modelling deep foundations are discussed. Interface elements, which are important to model soil-structure interactions, are also presented, as well as the standard finite element approach. The influence of mesh discretization is studied and the effect of soil dilatancy is investigated. Finally, the current limitations of this widely used approach are stressed.

All results discussed in this work are related to finite element codes of PLAXIS. The 2D studies were performed with the versions PLAXIS 2D Version 8 (Brinkgreve et al. 2006), PLAXIS 2D Version 9 (Brinkgreve & Broere 2008), PLAXIS 2D 2010 (Brinkgreve et al. 2010) and PLAXIS 2D 2011 (Brinkgreve et al. 2011). For most of the three dimensional studies, PLAXIS 3D Foundation (3DF) Version 2 (Brinkgreve & Swolfs 2007) was used. However some analyses were also performed with PLAXIS 3D 2011 (Brinkgreve et al. 2011).

The constitutive models used are either the linear elastic-perfectly plastic Mohr-Coulomb model (MC) or the Hardening Soil model (HS), which is a hardening plasticity model. In the last chapters of this thesis, the Hardening Soil Small model (HSS) is also used. A short summary of these constitutive models is given in Appendix A. A detailed description of the Hardening Soil model can be found in Schanz (1998) and Schanz et al. (1999). The HSS model is described in Benz (2007). In general, the results refer to drained conditions; if undrained conditions are considered, this is mentioned explicitly.

3.2 Literature review

Several methods to analyse the behaviour of single piles, pile groups and piled raft foundations exist. Poulos et al. (1997) divided them into three groups. Group one relates to simplified calculation methods, which involve a number of simplifications regarding the soil behaviour, the geometry and the loading condition. Group number two deals with approximate compute-based methods and group number three includes more rigorous computer-based methods. The latter group can be subdivided again into boundary element method (BEM), combined BEM and FEM analyses, finite difference method, finite layer technique (Small & Booker 1986) and FEM calculations. The lastly mentioned approach can be subdivided once more into simplified FEM calculations and full three dimensional finite element analyses (FEA). The literature review presented in the following is only related to the numerical modelling of deep foundations by means of the standard finite element approach.

A number of authors investigated the behaviour of single piles by means of FEM. Ellison et al. (1971) studied the load deformation mechanism of bored piles with 2D FE analyses, while Desai (1974) performed 2D FE calculations of axially-loaded piles in sandy soils and presented distributions of shear and normal stresses along the pile shaft. Wittke et al. (1974) presented FE back analyses of a horizontal pile load test, which showed a good agreement with measurements. Baguelin & Frank (1980) conducted studies of vertically- and horizontally-loaded piles and stated that FEM can be used to improve the theoretical knowledge of pile behaviour, and to evaluate existing design methods. Meissner (1983) used an elasto-plastic constitutive model to investigate the behaviour of vertically- and horizontally-loaded single piles. Jardine et al. (1986) investigated the influence of non-linear stress-strain behaviour in soil-structure interaction. Trochanis et al. (1991) performed 3D finite element analyses to evaluate the behaviour of axially- and laterally-loaded piles. They modelled the soil as Drucker-Prager material and defined interface elements, which enable pile-soil slippage and pile-soil separation. Lee & Salgado (1999) used a non-linear elasto-plastic constitutive model to investigate the development of base resistance. El-

Mossallamy (1999) presented comparisons of measurements, FEM and boundary element analyses of large diameter bored piles in overconsolidated clay. For the behaviour of the soil, he used a double hardening elasto-plastic constitutive model. More recently, Wehnert (2006) studied the influence of mesh dependency and presented results of different constitutive models. He stated that the most important thing for modelling a realistic base resistance is the right choice of soil stiffness, especially if a disturbance of the soil at the pile tip (due to installation) is expected. Lee & Long (2008) investigated the skin friction behaviour of drilled cast-in-place piles in sand. They included thin elements next to the pile shaft to model effects of localized shear during installation. Loukidis & Salgado (2008) conducted FE analysis to study the development of ultimate shaft resistance and the change in stress during axial loading of a vertical pile. Said et al. (2009) used an advanced interface model proposed by De Gennaro & Frank (2002) to back-analyse full scale pile load tests. Also, Lashkari (2011) proposed a critical state compatible elasto-plastic model for the description of sand-structure interaction and validated his approach with experimental data of centrifuge tests. Mroueh & Shahrour (2009) presented 3D FEA of battered piles under combined (lateral and vertical) load. Basu et al. (2011) performed 1D FE analyses of jacked piles in sand. They showed that the number of jacking strokes plays an important role when determining the shaft resistance. Henke (2008) and Dijkstra (2009) modelled pile installation effects by means of finite elements and Engin & Andresen (2011) compared zipper type techniques for FEA to model pile penetration problems. Recently König (2008) and Giannnopoulos et al. (2010) studied the effects of time on the capacity of piles. They evaluated effects related to both consolidation and creep processes. Giannnopoulos et al. (2010) demonstrated that creep in piled foundations in soft clay can yield a significant increase of pile capacity.

In order to reduce the computational effort, the first pile groups analysed were simplified to axisymmetric (Hooper 1973) or plane strain problems (Desai et al. 1974) with the approximation of an equivalent stiffness for the pile group. Pressley & Poulos (1986) examined the mechanism of group effects among piles using 2D axisymmetric finite element models. They demonstrated that at close spacings a block failure mechanism develops and with increasing pile spacing the failure mechanism tends toward the behaviour of a single pile. Ottaviani (1975) presented 3D FEA to study the settlement behaviour and the load transfer mechanism of single piles and pile groups embedded in linear elastic homogeneous soil. Chow & Teh (1991) studied the behaviour of vertically-loaded pile groups in nonhomogeneous soil. Liu & Novak (1991) investigated the pile-soil interaction of a raft supported by a single pile by means of finite and infinite elements. Katzenbach et al. (1994) and Arslan et al. (1994) conducted 3D finite element analysis of piled raft foundations using an elasto-plastic constitutive model. Katzenbach et al. (1998) studied the effects of interaction between raft and piles within a piled raft foundation employing 3D FEA. They

investigated different pile spacings and pile lengths. A parametric study on the behaviour of piled raft foundations was presented by Prakoso & Kulhawy (2001). They modelled a number of plane strain models to investigate the influence of system geometries on differential displacements, raft bending moments and load ratios. Reul (2000) and Reul & Randolph (2003) performed detailed back-analysis of piled raft foundations in overconsolidated clay and compared the results with in-situ measurements. Reul (2004) demonstrated with numerical studies the influence of pile-pile and pile-raft interaction within a piled raft foundation. Therefore, he conducted various 3D FE calculations and considered different system configurations. Reul & Randolph (2004) presented, based on 3D FEA, strategies for an optimised design of piled raft foundations subjected to nonuniform load conditions. Krajewski & Reul (2009) studied the influence of mesh discretization on the behaviour of piled raft foundations. They investigated both the h-refinement, where the number of elements is increased, and the p-refinement, where the interpolation function is increased, which means the characteristics of approximation of the element itself are better. Ittershagen (2009) conducted 3D FEA of a piled raft foundation and compared the measured and calculated load-settlement behaviour. Recently, Wehnert et al. (2010) presented back-analyses of three pile load tests by means of 2D and 3D calculations and finally a settlement analysis of a piled raft foundation supported by more than 500 large diameter bored piles. They stated that for the boundary value problem considered, neither a 2D cross section nor a simplified model of a specific part of the deep foundation would have been adequate to forecast the differential settlements.

3.3 Basic terms and aspects of FEM of deep foundation analysis

3.3.1 2D versus 3D modelling

In order to apply FEM for boundary value problems geometrical idealizations and assumptions have to be made. Current practise for analyses of geotechnical problems uses 2D plane strain models. In special cases, like slopes or strip footings, where one dimension is very large compared to the other two dimensions, the assumption of plane strain conditions is justifiable. For other detached geotechnical problems a simplification to axisymmetric boundary conditions is possible, e.g. circular footings. But most of the time, finite element analyses are performed for projects where the geometry, the soil layering or the load situation of the problem is rather complex. And then, the "standard" question arises: Is full 3D modelling required? Potts (2003) also states that 2D plane strain or axisymmetric assumptions are often questionable in real

applications. He showed exemplarily the influence of a non-isotropic retaining wall stiffness on wall deflections where 3D modelling is naturally required.

From the author's point of view, it is not necessary to go straight to full 3D modelling, because 2D modelling is very convenient for preliminary studies and a number of practical problems can also be analysed easily with 2D calculation, assuming plane strain conditions in certain regions. Therefore, it is very important to point out that 2D calculations are still up to date. Nevertheless, when dealing with deep foundations, the possibilities for two-dimensional models are very limited. Only the special case of an axially-loaded vertical single pile in horizontally layered soil can be modelled in axisymmetric conditions.

The problem when modelling deep foundations in 2D is that the geometry and the layout of the foundation elements do not allow a plane strain representation and one has to modify either the dimensions or the stiffness of the deep foundation elements, e.g. Desai et al. (1974) or Prakosa & Kulhawy (2001). In the author's opinion, a combination of both approaches is the best choice for normal circumstances. But once the spacing between the piles is large the equivalent stiffness method should be adopted, otherwise, relatively small pile dimensions have to be used, leading to a different behaviour of the piles.

In this thesis principle studies of axially-loaded single piles are modelled in axisymmetric conditions, but all other analyses are performed using 3D models. In chapter 7, comparisons of 2D plane strain cross sections with full 3D calculations, on the basis of a real boundary value problem, are presented.

3.3.2 Finite elements as used in this thesis

Two different element types are available in PLAXIS 2D, namely a six noded element with quadratic shape function or a fifteen noded element with a shape function of fourth order. In PLAXIS 3DF, 15 noded wedge elements (quadratic shape function) are used, and PLAXIS 3D uses 10 noded tetrahedral elements, also with an interpolation function of second order. Fig. 7 shows the different types of elements used in the PLAXIS codes. If inclined soil layers are defined in PLAXIS 3DF, the mesh generator automatically degenerates the 15 noded wedge elements to 13 noded pyramids or 10 noded tetrahedral elements. The stresses within the finite elements are worked out by means of numerical integration in stress points. The Gauss quadrature is used for the evaluation of stresses in standard finite elements, and the Newton-Cotes integration scheme is utilized at interfaces (see next chapter of this thesis).

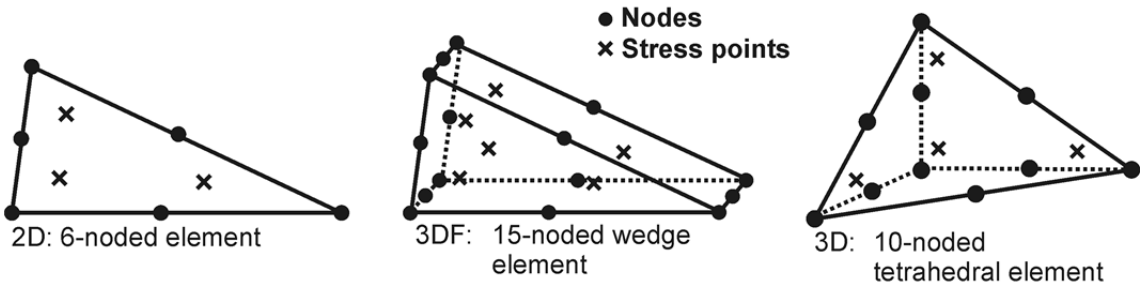

Fig. 7 Finite elements as used in PLAXIS 2D (left), PLAXIS 3DF (middle) and PLAXIS 3D (right)

3.4 Interface elements

The nodal conductivity of the FE method constrains the adjacent structural and soil elements to move together. To model relative displacements between the soil and structures, interface elements are used. Principally, different methods to model soil-structure interfaces exist. Potts & Zdravković (1999) give an overview of methods presented in the literature. The programs used for this work use an interface formulation with a virtual thickness; this approach is similar to the one presented by Goodman et al. (1968).

The shape functions of an interface have to be compatible with the soil elements, hence if a 15 noded soil element (Fig. 7) is used the interface consists of five pairs of nodes. When using 6 noded soil elements, it consists only of three pairs of nodes. The Newton Cotes integration scheme is used to evaluate the stresses at the interface elements, which means that the stress points coincide with the position of nodes and the number of stress points depends on the shape function used for the solid soil elements. Fig. 8 shows schematic representations of interface elements. The basic theory of an isoparametric interface element is given in Appendix B.

3.4.1 Definition of interfaces

An interface is defined geometrically with a virtual thickness (t_i). This imaginary thickness controls, together with the interface stiffnesses, the elastic deformations of an interface. These deformations should be as small as possible, but numerical ill conditioning must be avoided.

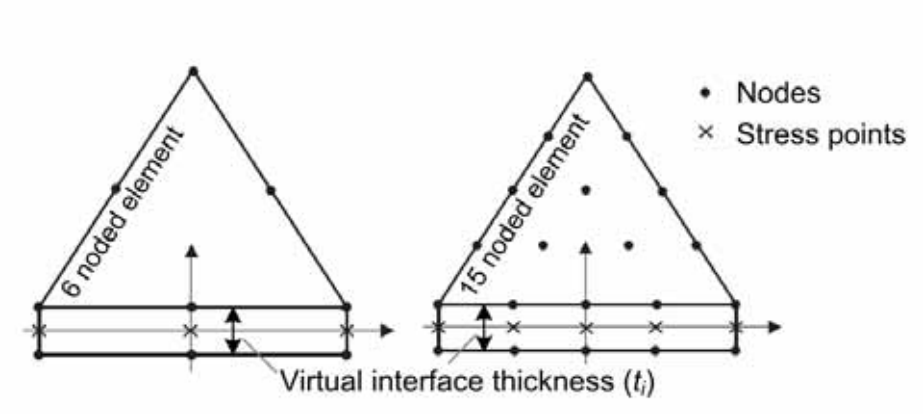

Fig. 8 Interfaces as used in PLAXIS 2D (after Brinkgreve et al. 2011)

In principle, it is possible to use different constitutive models for the surrounding soil and the interface elements, but a Mohr-Coulomb criterion is always used to define failure at the interface. The strength of an interface is defined with the interface reduction factor R_{inter}.

$$c'_i = R_{inter} \cdot c' \tag{24}$$

$$\tan\varphi'_i = R_{inter} \cdot \tan\varphi' \tag{25}$$

$$\psi_i = 0° \; for \; R_{inter} < 1.0, \; otherwise \; \psi_i = \psi \tag{26}$$

c'_i is the effective cohesion of an interface, φ'_i is the effective interface friction angle and ψ and ψ_i are the dilatancy angle and the dilatancy angle of an interface, respectively. Strength reduction factors for various soils and construction materials can be found e.g. in Potyondy (1961). As long as the interface is elastic only elastic slip and elastic gap displacements can occur. Gap displacements are related to effective normal stresses σ'_n on an interface and a normal interface stiffness K_n, whereas elastic slip displacements are governed by shear stresses τ and interface shear stiffness K_s.

$$Elastic\ gap = \frac{\sigma'_n}{K_n} \tag{27}$$

$$Elastic\ slip = \frac{\tau}{K_s} \tag{28}$$

$$K_n = \frac{E_{oed,i}}{t_i} \tag{29}$$

$$K_s = \frac{G_i}{t_i} \tag{30}$$

The oedometric interface stiffnesses $E_{oed,i}$ and the shear interface stiffness G_i are related to the defined soil stiffnesses E_{oed} and G respectively. The Poisson's ratio of an interface ν_i is defined as 0.45.

$$E_{oed,i} = 2 \cdot G_i \frac{1-\nu_i}{1-2\cdot\nu_i} \tag{31}$$

$$G_i = R_{inter}{}^2 \cdot G \tag{32}$$

$$K_n = \frac{E_{oed,i}}{t_i} = K_s \frac{2-2\cdot\nu_i}{1-2\cdot\nu_i} \tag{33}$$

$$K_s = \frac{G_i}{\delta_v \cdot ES_{avg}} = \frac{G_i}{t_i} \tag{34}$$

Equations 33 and 34 show that the elastic interface stiffness is controlled by R_{inter}, the virtual thickness factor of an interface δ_v and the average element size of solid elements in the finite element model (ES_{avg}). The first two values are an optional input to the analysis and the average element size is an internal defined value. The output program shows the internal calculated value of ES_{avg}. But the calculated elastic displacements (according to Equation 27 and 28) - with this value of average element size - do not fit with the results obtained with the finite element software. Fig. 9 shows the difference of the calculated elastic gap displacements for a simple finite element model with a constant distributed normal stress σ'_n on the interface. The example was analysed with five different mesh coarsnesses.

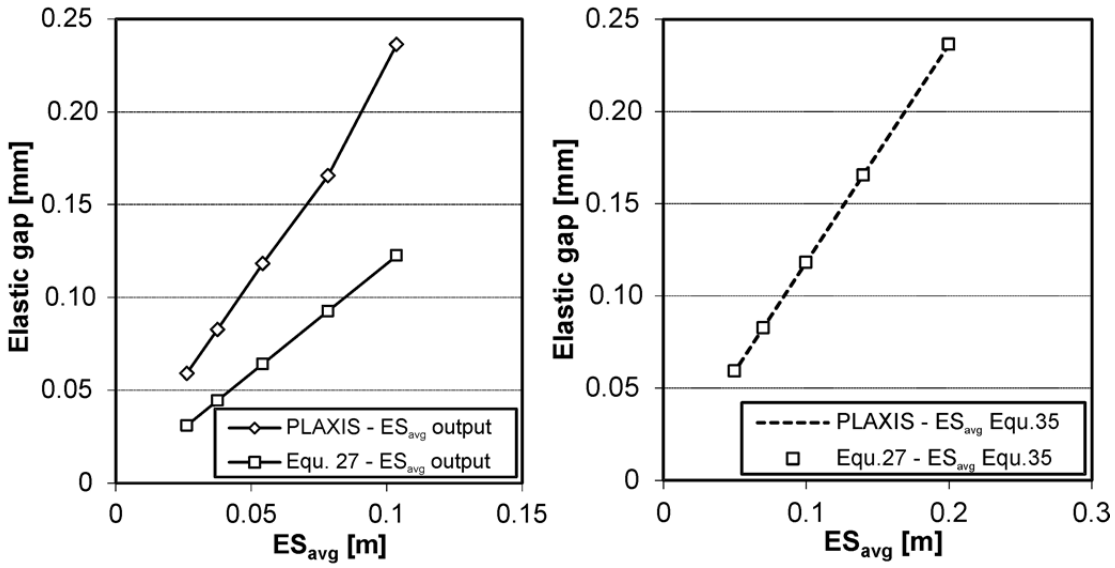

Fig. 9 Elastic gap of an interface

The value given in the output is related to the model dimensions and the total number of solid finite elements, whereas ES_{avg} used internally is related to the settings of the global mesh coarseness (Nel_{fixed}), meaning local mesh refinements do not have an effect on the average element size used for the definition of the virtual interface thickness.

$$ES_{avg} = \sqrt{\frac{A_m}{Nel_{fixed}}} \tag{35}$$

When using the HS model for the definition of the interface, the stress dependency of stiffness is also taken into account for K_s and $K_{n.}$ Equation 36 shows the definition of interface shear modulus G_i, where $G_{ur,ref}$ is the un- and reloading shear modulus of the soil at reference pressure, p_{ref} is the reference pressure and m is the power index, controlling the stress dependency of stiffness. The factor Λ increases the deviatoric hardening modulus at reference pressure ($E_{50,ref}$) to take additional cap-plasticity into account. This factor is defined internally and is related to a number of parameters as $E_{50,ref}$, $E_{oed,ref}$, φ' and others.

$$G_i = R_{inter}{}^2 \cdot G_{ur,ref} \cdot \left(\frac{\sigma'_n \cdot \sin\varphi' + c' \cos\varphi'}{p_{ref} \cdot \sin\varphi' + c' \cdot \cos\varphi'} \right)^m \cdot \Lambda \tag{36}$$

As long as the interfaces are not activated plastic behaviour is excluded, but elastic gapping and/or slipping can occur. For inactive interfaces, the stiffnesses K_s and K_n are increased by a factor of 10. As a consequence, both shear and normal stresses are potentially already present before the interface is activated.

3.4.2 Special issues related to deep foundations

3.4.2.1 Singular plasticity points

Van Langen & Vermeer (1991) presented a special use of interfaces to prevent singular plasticity points. Fig. 10 shows a singular plasticity point for a single pile problem. Standard finite elements cannot handle such singularities, because C^0 continuity is required. Due to the fact that large displacement discontinuities occur at the edge of piles, the finite element analysis tends to overestimate the bearing capacity of a pile.

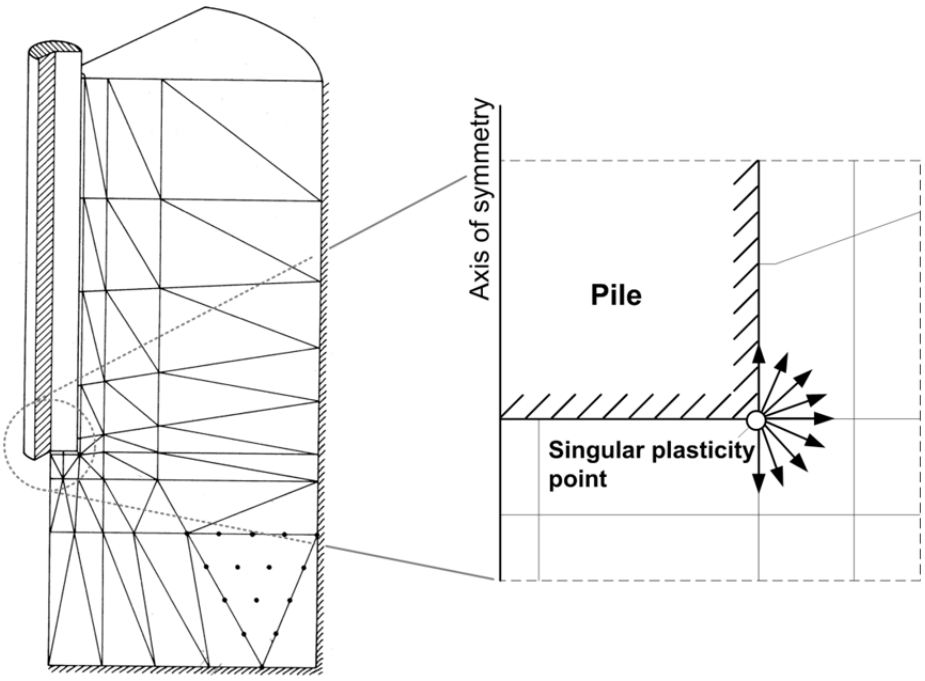

Fig. 10 Singular plasticity point at the pile base (after Van Langen & Vermeer 1991)

With interface elements potential slip planes can be introduced in the model (as shown in Fig. 11), and as a consequence, point C is split into four separate points and can move freely. Van Langen & Vermeer (1991) stated that the simple mesh computes high stress concentrations close to the edge of the pile that yield, compared to the improved mesh with introduced slip planes, to a 25% higher bearing capacity of the pile. The difference is of course also related to the discretization of the finite element mesh. It is important to point out that these potential slip planes are not zones of weakness, because the same strength as in the surrounding soil is defined along the interface extension.

When using PLAXIS 2D or 3DF the same tendencies are obtained, but with 15 noded elements and a reasonable fine mesh the influence on the load-settlement behaviour of a single pile is relatively small, due to the fact that the distance from the pile edge to the Gauss points in the soil is small. Nevertheless, standard finite elements without potential slip planes are getting highly distorted, and this lack of flexibility yields to a bad quality of both shear and normal stresses close to the edge of the pile base (stress oscillations).

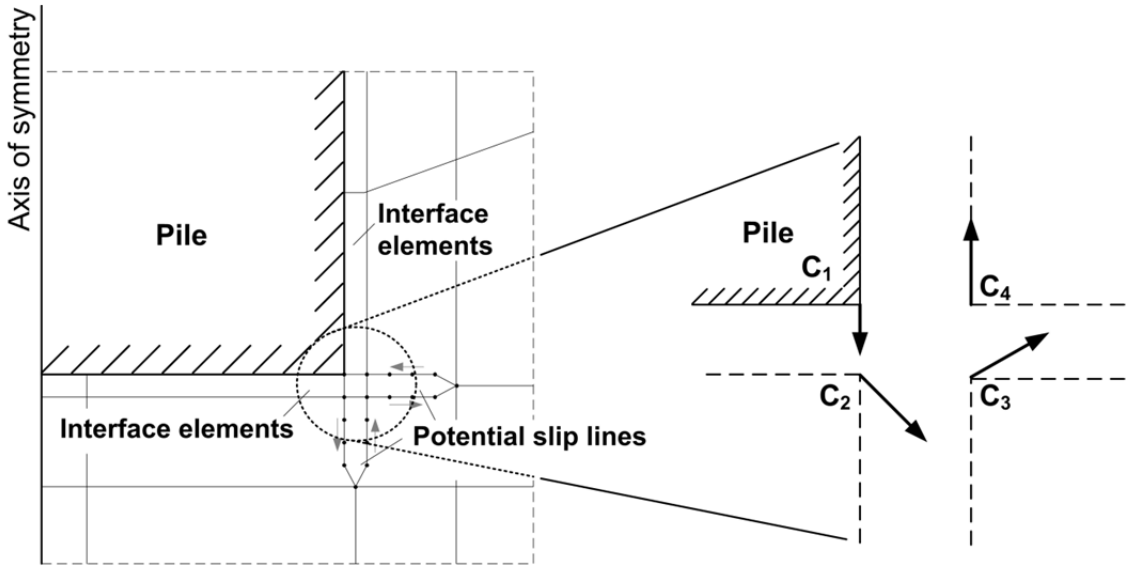

Fig. 11 Special use of interface elements (after Van Langen & Vermeer 1991)

3.4.2.2 Numerical problems

When dealing with interface elements, numerical ill-conditioning and problems related to unstable integration point stresses can occur. The problem of ill-conditioning is related to the interface stiffnesses K_s and K_n. As shown in chapter 3.4.1 of this thesis, interface stiffnesses have the dimension [kN/m^3]. Potts & Zdravković (2001) state that it is hard to select appropriate stiffnesses for interfaces, because it is difficult to perform laboratory test to define the "correct" interface stiffness. Van Langen & Vermeer (1991) recommended that K_s and K_n should be defined in a way that the initial response of the global load-settlement behaviour of a structure should be similar to the initial computed load-settlement curve without interface elements. This ensures that the influence of an interface is restricted to plastic slip along the soil-structure interaction.

Potts & Zdravković (2001) presented 2D axisymmetric calculations of a vertically-loaded single pile in homogenous undrained material. They studied the influence of the interface stiffness and performed two different calculations, with $K_s = K_n =$ 1e3 kN/m^3 and $K_s = K_n =$ 1e5 kN/m^3. Similar calculations were

performed with PLAXIS 2D. In general, the interface stiffnesses in PLAXIS are related to the global mesh coarseness settings, but because different mesh coarsnesses result in dissimilar behaviour of piles (see chapter 3.5.2), the interface thickness is changed directly in the "mesh file" of the project directory. Equation 33 indicates that the normal stiffness K_n is linked to the shear interface stiffness, hence it is not possible to define the same quantities. But for this type of problem, the normal stiffness of the interface is of minor importance. The PLAXIS calculations were performed with shear interface stiffnesses K_s of 4,57e4 kN/m^3, 3,36e9 kN/m^3 and 6,71e2 kN/m^3. Fig. 12 shows the difference in the pile behaviour when using different stiffnesses. When using low values for the interface stiffness, the behaviour of the pile is much softer. With the default value of 4,57e4 kN/m^3 for the shear interface stiffness, the calculation shows reasonable agreement with the results presented by Potts & Zdravković (2001).

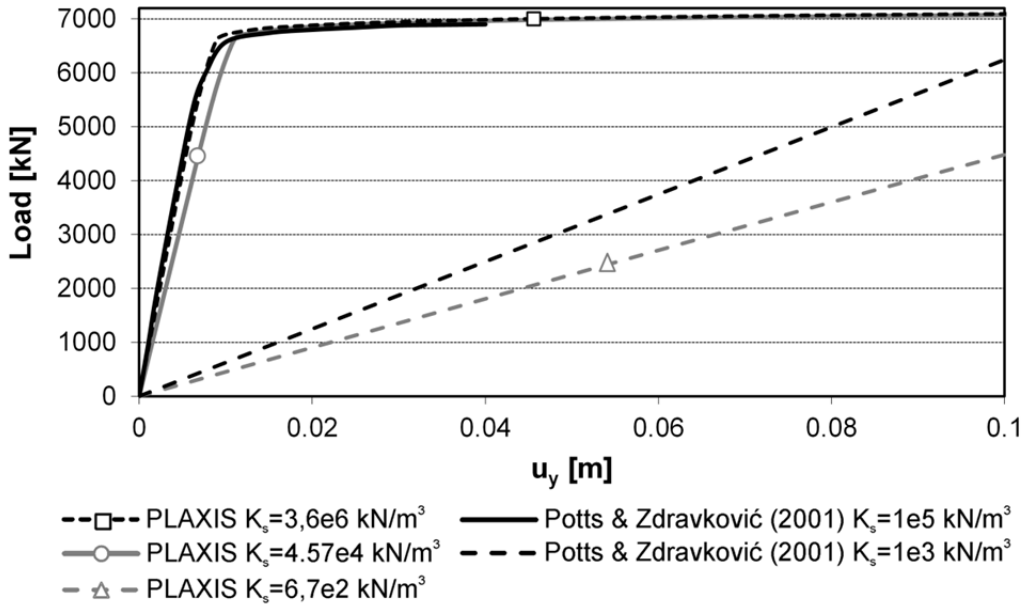

Fig. 12 Influence of interface stiffness on load-settlement curve of an axially-loaded single pile

The upper bounds of interface stiffness are limited by possible ill-conditioning, which takes place if element stiffness matrices of adjacent elements vary in magnitude by a significant amount. Potts & Zdravković (2001) showed that ill-conditioning of the global stiffness matrix could yield to stress fluctuations along the interface. They modified K_s and K_n independently und summarized that for the simple problem of an overturning elastic block stress oscillations occur once K_s or K_n are bigger than 100 times the surrounding soil stiffness. However, this ratio is most likely also problem dependent.

Tests with PLAXIS 2D showed that for the same problem of overturning of an elastic block, slight stress oscillations start to occur when K_n is bigger than 2000 times the Young's modulus of the surrounding soil. But the results demonstrated that stress oscillations related to ill conditioning is not a severe problem. One explanation therefore is that the element stiffness matrix $\mathbf{K}_e$ is related to the inverse of the determinant of the Jacobean matrix **J** (Potts & Zdravković 2001).

$$\mathbf{K}_e = \int_{-1}^{1}\int_{-1}^{1} t \cdot \mathbf{B}^T \cdot \mathbf{D} \cdot \mathbf{B} \cdot |\mathbf{J}| \cdot d\xi \cdot d\eta \tag{37}$$

where **B** is the element strain-displacement matrix, **D** is the elastic constitutive matrix, **J** is the Jacobean matrix, ξ and η are the intrinsic coordinates for numerical integration and t is the thickness, which is unity for plane strain problems. As |**J**| decreases when using finer solid elements close to the interface, the strain matrix **B** increases and the contribution of the surrounding solid elements to the global stiffness matrix increases. When using PLAXIS, the mesh is automatically refined in the region where interface elements are defined, hence less ill-conditioning occurs. Only when using really high values for the interface stiffnesses ($E_{interface} > E_{soil} \cdot e19$) does the global stiffness become nearly singular and unable to be solved, but for practical applications, such high ratios are in general not used. However, when using PLAXIS stress oscillations also occur sometimes at interfaces. For example Fig. 13 shows a calculation of a single vertically-loaded pile in homogeneous soil and the obtained shear stresses along the shaft interface. The initial conditions are calculated with the K_0-procedure. The soil parameters used for the calculation are given in Tab. 1.

Tab. 1: Input parameters for Mohr-Coulomb model

parameter		**value**	**unit**
Young's modulus	E	1e5	kPa
Poisson's ratio	ν'	0.30	--
effective friction angle	φ'	25.0	°
effective cohesion	c'	0	kPa
dilatancy angle	ψ	0	°
bulk unit weight of soil	γ	18.0	kN/m^3
lateral earth pressure coefficient at rest	K_0	1.0	--

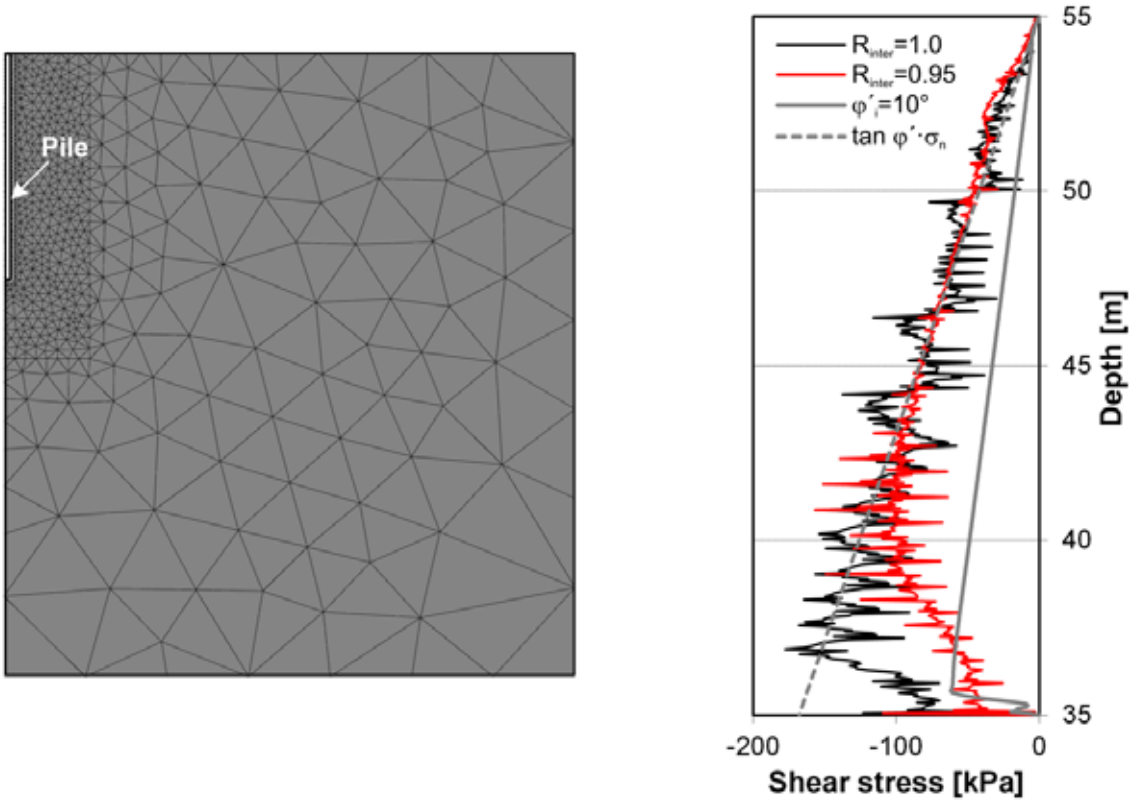

Fig. 13 Finite element model (left) and mobilized skin friction (right)

Three different interface strengths were defined. In the calculations with R_{inter} = 1.0 and 0.95, stress oscillations occur; in the third calculation - where a separate material set with a friction angle φ'_i of 10° is assigned to the interface - a smooth skin friction distribution is mobilized. This indicates that the quality of the shear stress distribution is actually related to the strength of the soil and the interface instead of to the interface stiffness, particularly the relative stiffness G_i/G. Fig. 14 shows the plastic points at failure for the calculation with R_{inter} = 1.0 and for the calculation with an interface friction angle φ'_i = 10°. In the calculation with reduced frictional behaviour in the interface, no plastic points are located in the soil body next to the pile and also no stress fluctuation occurs. This indicates that plasticity in the soil next to the pile is probably the reason for the stress oscillation.

The same model recalculated with undrained shear parameter (c_u = 50 kPa and φ' = 0) does not show any stress oscillations at the interface. Fig. 15 illustrates the stress paths of an integration point in the soil and the interface 15.7 m below the surface. The stress paths are plotted in the s-t representation, where s represents the centre and t the radius of the Mohr's circle. σ'_{yy} and σ'_{xx} are the vertical and the horizontal effective stress in the soil and σ'_1 and σ'_3 are the major and minor effective principal stresses. The subscript initial indicates the initial stress situation.

$$s = \frac{\sigma_1 + \sigma_3}{2} \tag{38}$$

$$t = \frac{\sigma_1 - \sigma_3}{2} \tag{39}$$

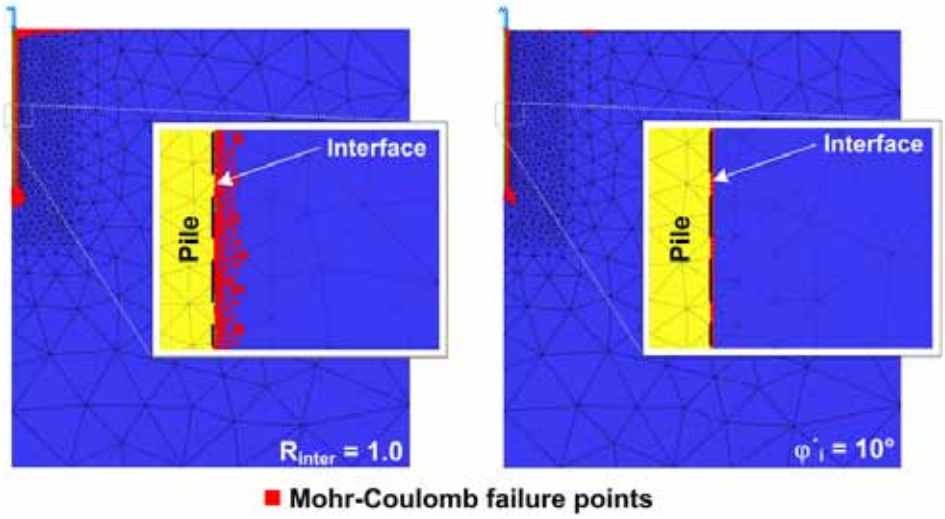

Fig. 14 Plastic points at failure – R_{inter} = 1.0 (left) and φ'_i (right)

The Mohr circle of the soil is a bit smaller than the maximum allowable deviatoric stress. This is because the integration point is not located at the soil-structure interaction plane, thus the stresses do not exceed the failure criterion.

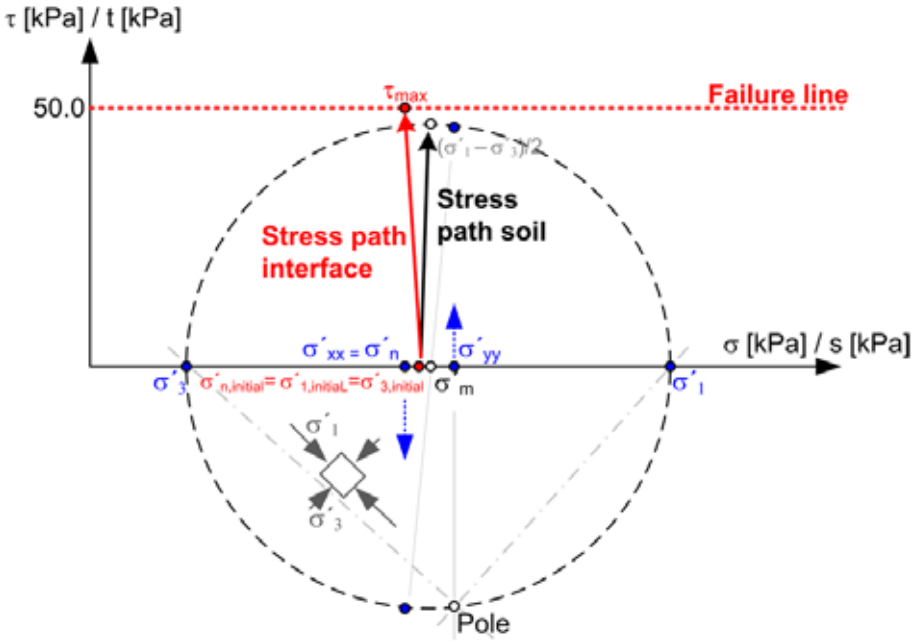

Fig. 15 Stress paths of the soil and the interface in a depth of -15.7 m (c_u = 50 kPa; φ' = 0)

In the calculation with effective strength parameters (Tab. 1) and a R_{inter} value of 1, the situation is similar and the deviatoric stresses in the soil are a bit smaller than the shear stresses in the interface, but in this calculation significant stress fluctuations occur. Fig. 16 illustrates again the stress paths of an integration point in the soil and the interface 15.7 m below the surface. The allowable shear stress at the interface is governed by the effective normal stress σ'_n at the interface and the friction angle φ_i.

$$\tau_{max} = \sigma'_n \cdot \tan\varphi_i' + c'_i \tag{40}$$

However in the soil, the maximum shear stress is related to the minor and major effective principle stress. Due to the different definitions of the failure criterion, the ultimate deviatoric stress in the soil and in the interface is not the same. This is the reason why the soil fails before the limiting interface strength is reached, even if the shear stress in the soil is smaller than at the interface.

Of course the stresses in the soil are related to the mesh coarseness of the finite element model. When using 15 noded elements, the position of the Gauss points is already very close to the interface, meaning relatively large elements are necessary to induce a decrease of stress in the soil so that no failure occurs. But when using relatively coarse meshes in combination with 6 noded elements, the stress points in the soil could possibly not exceed the failure line and stress oscillations at the interface might not occur.

If we assume for simplicity that the normal stress at the interface and the centre of the Mohr circle after loading are identical ($\sigma'_n = \sigma'_m$) and the cohesion c'_i is 0, a simple relation between the maximum shear stress in the soil and in the interface can be deduced.

$$\left(\frac{\sigma'_1 - \sigma'_3}{2}\right) = \sigma'_m \cdot \sin\varphi' \tag{41}$$

$$\tau_{max} = \sigma'_m \cdot \tan\varphi' \tag{42}$$

$$\tau_{max} = \left(\frac{\sigma'_1 - \sigma'_3}{2}\right) \frac{\tan\varphi'}{\sin\varphi'} \tag{43}$$

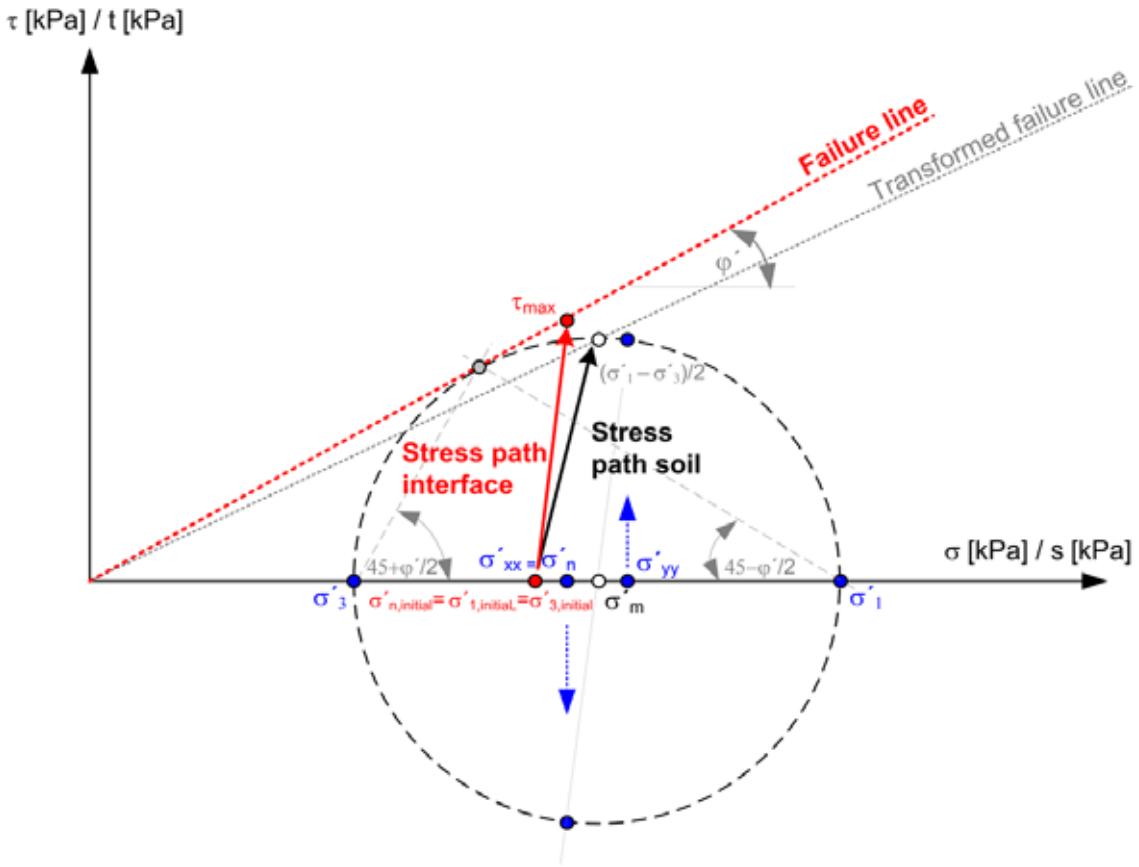

Fig. 16 Stress paths of the soil and the interface in a depth of -15.7 m ($c´ = 0$; $\varphi' = 25°$)

Equation 43 shows that the overestimation of the allowable shear stress in the interface, compared to the surrounding soil, increases with an increasing friction angle. Fig. 17 illustrates the influence of the friction angle on the difference of the ultimate shear stress in the interface versus maximum shear stress in the soil.

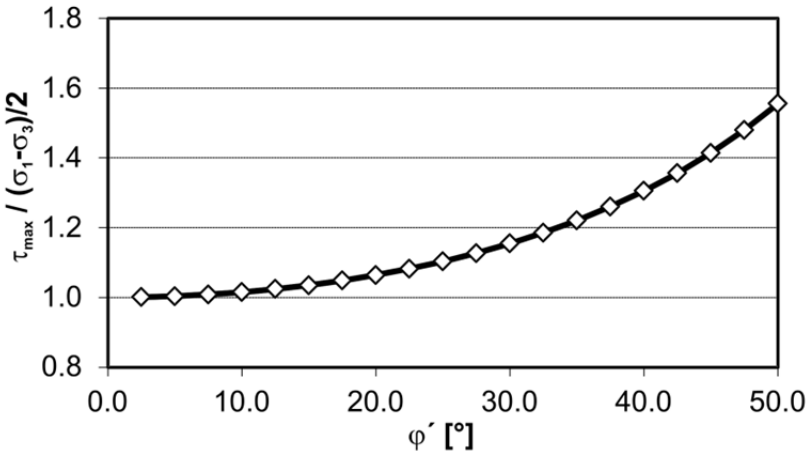

Fig. 17 Influence of friction angle on allowable deviatoric stress

Another reason for stress oscillations is related to the integration scheme used for the evaluation of the element stiffness matrix. PLAXIS uses the Newton-Cotes integration scheme, where, according to Van Langen (1991), the quality of calculated stresses in the interface is much better compared to the Gauss integration. Detailed information related to integration rule utilized for interfaces is given in Appendix B.

3.5 Modelling deep foundations employing the standard FE approach

3.5.1 Introduction

In the standard finite element approach, the piles are modelled with volume elements and the interaction of the pile with the surrounding soil is generally described with interface elements. The "roughness" of the soil-structure interaction is defined with a strength reduction factor R_{inter}, which determines the interface strength with respect to the soil strength. A detailed description of interface properties is given in chapter 3.4.1 of this thesis.

Two-dimensional analyses are used in the following for principle studies of axially-loaded single piles. PLAXIS 3DF has the disadvantage that piles modelled with the standard finite element approach have to be vertical. This is because the 3D mesh is based on a 2D mesh of a horizontal cross section. Therefore, it is not possible to model inclined structures. Fig. 18 shows a 3DF finite element model for a single pile.

The problem with this approach is that for a large number of piles, it leads to computationally demanding models that may be beyond the capabilities of the code or simply take too long to analyse from a practical point of view. Hence this modelling technique is not very popular in practical engineering. An alternative way to define piles in a 3D model is the embedded pile approach. This concept is explained in detail in chapter 4.

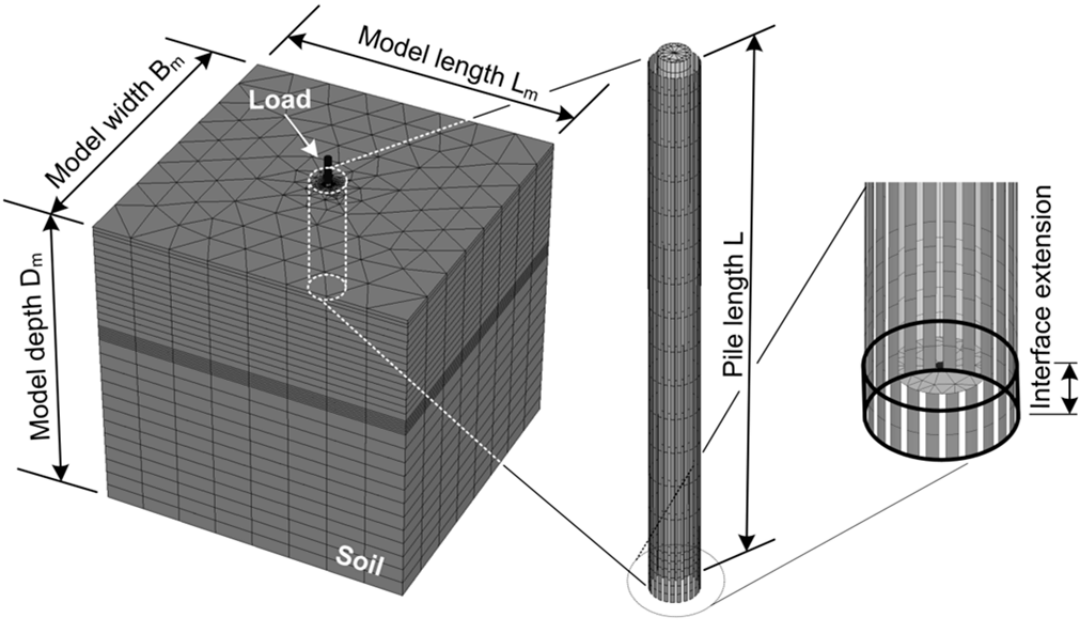

Fig. 18 Standard finite element approach in PLAXIS 3DF

3.5.2 The influence of the mesh coarseness

In this chapter, the influence of the mesh coarseness on the load-settlement behaviour of axially-loaded single piles is studied. The example chosen is similar to the one presented by Potts & Zdravković (2001). The model dimensions $L_m/B_m/D_m$ are 50/50/55 m. The pile length L is 20.0 m and the diameter is 1.0 m. The soil is modelled as Tresca material with a saturated bulk unit weight γ_{sat} of 18 kN/m^3, an undrained stiffness E_u of 1e5 kN/m^2, an undrained shear strength c_u of 100 kPa and a Poisson's ratio ν of 0.49. The pile is defined as linear elastic material with a Young's modulus E of 2e7 kN/m^2 and a Poisson's ratio of 0.15. The initial stresses are defined with a lateral earth pressure coefficient at rest K_0 of 1.0. Fig. 19 shows the different mesh coarsnesses studied, where model 1 and model 2 have globally the same mesh coarseness and model 3 and model 4 are discretized with local mesh refinements. In model 4, additional geometry lines are defined to force the program to generate very small elements next to the pile. It should be noted that models 2, 3 and 4 are discretized more or less with the same number of elements.

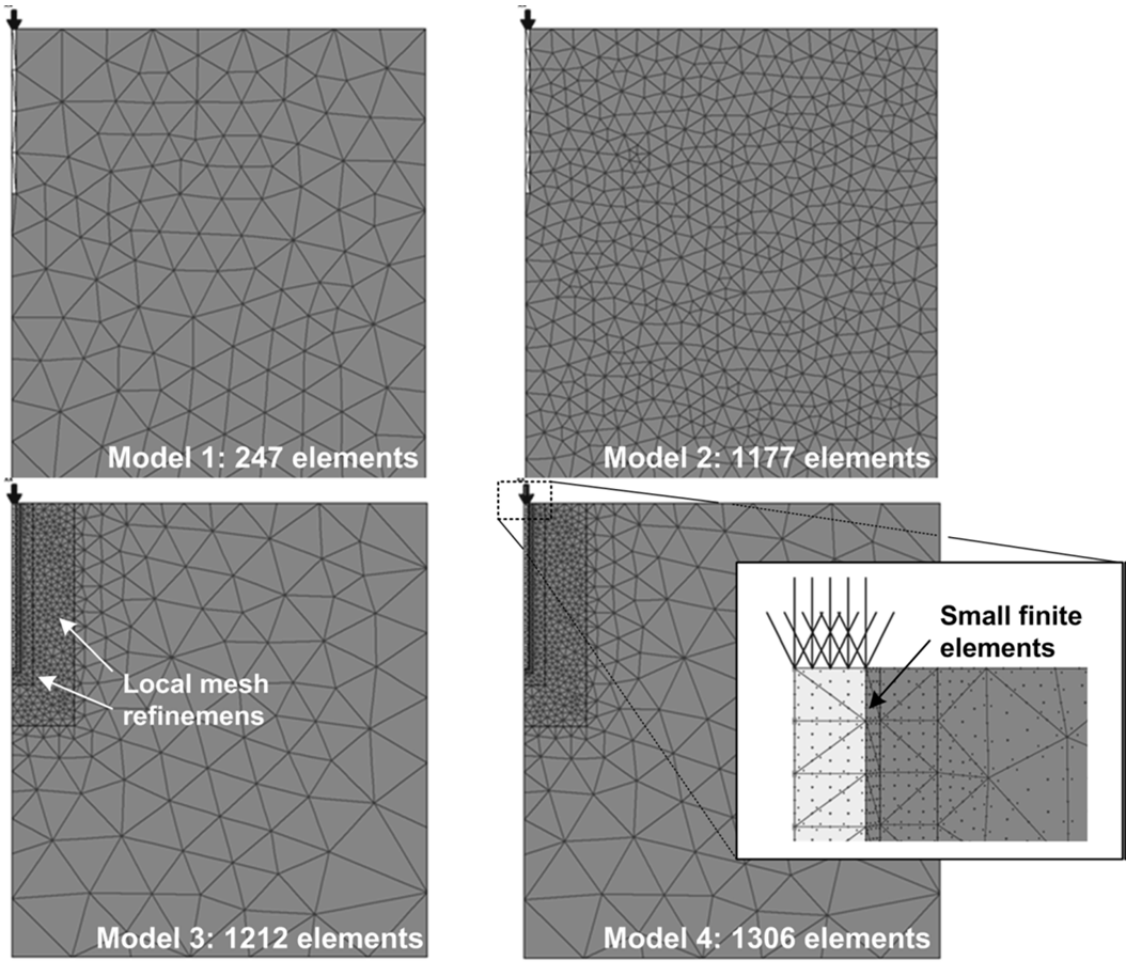

Fig. 19 Different mesh discretizations

When using the standard finite element approach, the soil-structure interaction is usually modelled by means of interface elements, but it is also possible to model this sensitive zone close to the pile shaft with very thin solid elements. Therefore model 1 to 4 is analysed with and without interface elements. In addition to the h-refinement, where the mesh is discretized with more elements, the influence of the shape function (p-refinement) is also shown in Fig. 20. The reference solution presented by Potts & Zdravković (2001) is defined with a 5 cm thin layer next to the pile shaft.

The theoretical ultimate shaft capacity, which is the undrained shear strength times the shaft area, is 6283 kN. The results show that for coarse meshes without interface elements the bearing capacity is highly overestimated. Even with model two and 15 noded elements the ultimate bearing capacity is about 60% higher than the reference solution.

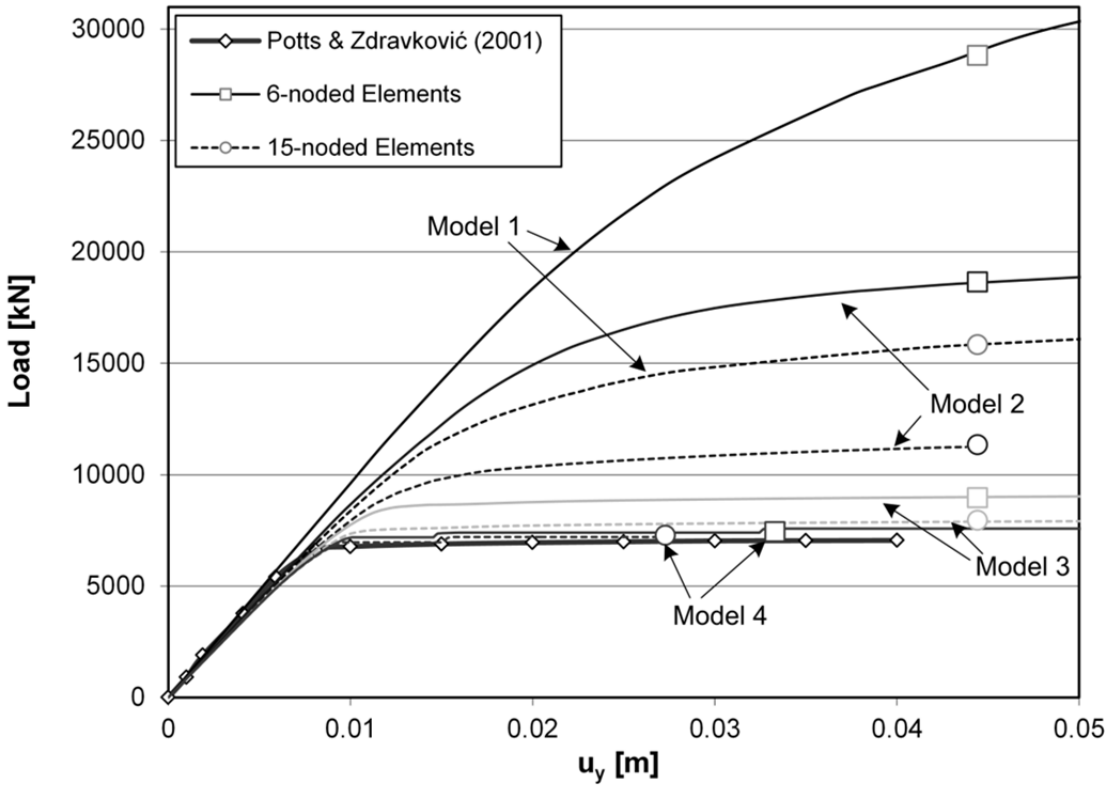

Fig. 20 Influence of mesh coarseness (without interface elements)

The reason is that the stresses are worked out in the Gauss points, which are not located in the soil-structure interaction plane, and that the used shape functions calculate a variation of stress over the finite element, which is not correct for these types of problems. Only with very fine meshes close to the pile shaft - hence a small distance between the integration points in the soil and the pile - is it possible to compute the shaft resistance R_s properly.

Fig. 21 shows the load-settlement curves for model 2 and model 3 with interface elements along the pile shaft. The mesh coarsenesses are very similar to the models 2 and 3 shown in Fig. 19 but are not identical, because of the fully automatic mesh generation of the program, which enforces a local mesh refinement along interfaces (see chapter 3.4.2). It shows clearly that interfaces improve the behaviour significantly, due to the fact that the integration points are located at the "real" position of the problem (soil-structure interaction). But the mesh coarseness still has an effect on the behaviour, especially when using low order elements (6 noded elements). The different inclinations of the first part of the load-settlement curves are governed by the elastic deformations of the interface.

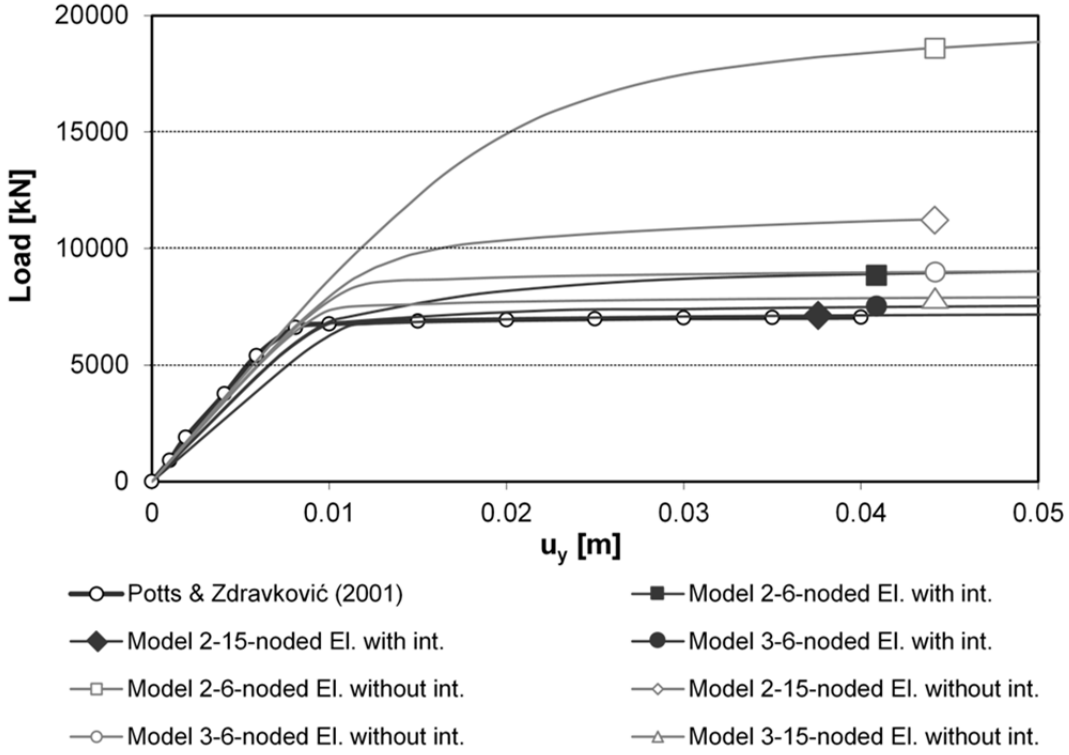

Fig. 21 Influence of mesh coarseness

Similar studies were also performed with PLAXIS 3DF. Fig. 22 shows two mesh discretizations studied and Fig. 23 the obtained load-settlement curves. To reduce the number of elements and to allow a finer mesh discretization, an axis of symmetry is taken into account. The behaviour is similar to the two-dimensional studies: without interface elements fine mesh discretizations are necessary, and when using interface elements, the mesh dependency is reduced significantly. The first part of the load-settlement curves shows almost the same inclination; this indicates that the interface stiffnesses used are stiff enough.

In general, the shape of a pile in PLAXIS 3DF is approximated, where only the corner nodes of the 15 noded wedge elements correspond with the circumference of the pile geometry. However, if the pile shape is optimised by means of "curved" elements, the middle nodes of the solid elements are also part of the pile boundary.

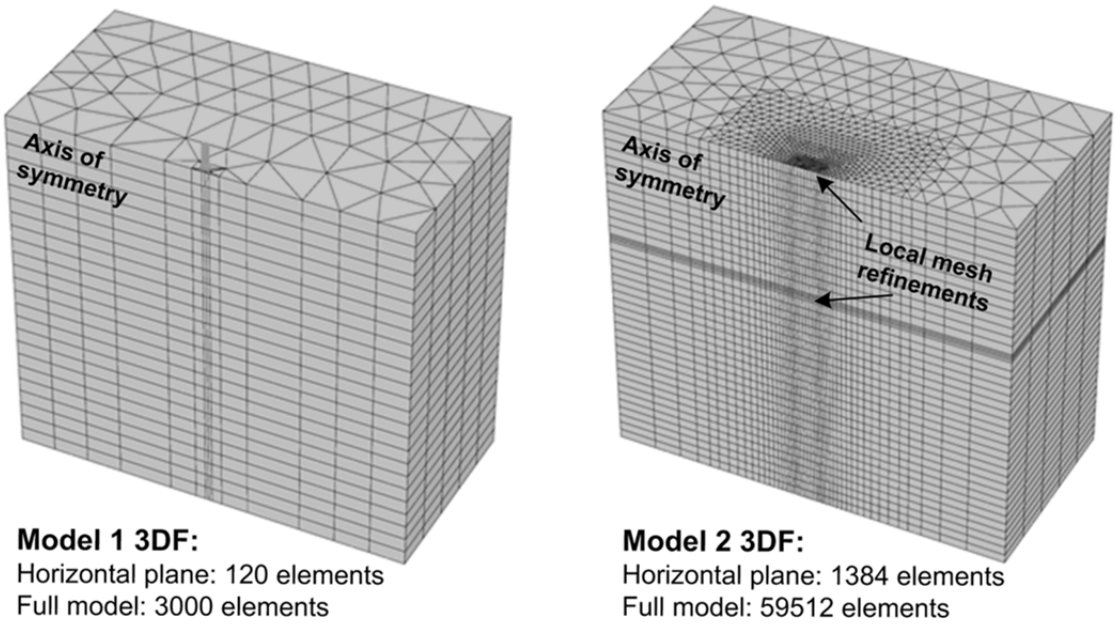

Fig. 22 Different mesh discretizations-PLAXIS 3DF

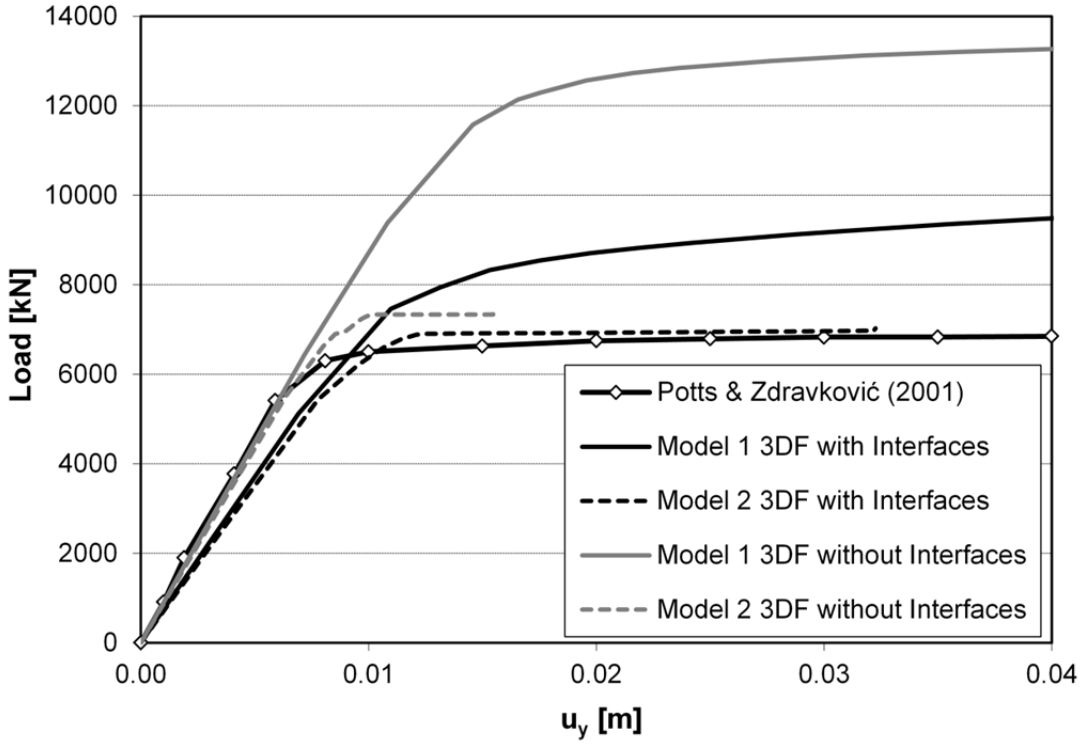

Fig. 23 Influence of mesh coarseness – PLAXIS 3DF

3.5.3 The Influence of dilatancy

When dealing with kinematically constrained problems in combination with dilatant soil behaviour, the shear dilatancy in granular materials has a significant effect on both the computed failure load and the global stiffness response of a structure. This effect was reported for example by Brinkgreve (1994) and Vermeer & De Borst (1970). An axially-loaded pile is a typical example where the change in volume associated with shear distortion yields to an increase of normal stress along the pile shaft, and as a consequence, to an increase of shaft resistance. Potts & Zdravković (2001) conducted numerical studies on axially-loaded piles using the MC model with associated ($\varphi' = \psi$) and non-associated flow rule ($\psi = 0$). They showed that calculations with associated plasticity lead neither to a limiting value of shaft nor base resistance, and that the behaviour of the interface elements dominates the behaviour of the pile.

A solution would be the use of $\psi = 0$, but most sands exhibit some dilation which would than lead to a conservative design as shown by Wehnert (2006). He presented a back-analysis of a pile load test in Berlin sand with $\psi = 0$, which results in a significant underestimation of the pile bearing capacities. To predict a realistic behaviour of an axially-loaded pile the plastic dilation has to be taken into account but bounded with a critical state condition. This can be done in the Hardening Soil model with a so-called dilatancy cut-off (see Appendix A). But, according to Equation 26, the problem arises that ψ_i is automatically set to zero for R_{inter} values smaller than 1. Thus a separate parameter set with reduced strength parameters must be assigned to the interface elements. But, it is important to generate the initial stresses with unreduced strength parameters, otherwise wrong normal stresses are present along the pile and as a consequence the ultimate shaft resistance is underestimated.

Numerical studies of a 15 m long axially-loaded bored pile situated in loose sand (Tab. 16) were conducted to show the influence of the dilatancy cut-off (*dco*). The dilatancy angle is defined with 4°, however to show the influence of plastic dilation on kinematically constraint problems, some calculations were also performed with $\psi = 0$. The void ratios e - necessary for the *dco* option - are defined as $e_{min} = 0.63$, $e_{max} = 1.0$ and $e_{init.} = 0.88$. Fig. 24 illustrates the load-settlement curves for R_{inter} values of 1.0 and 0.7. As expected, the calculation with $\psi = 0$ significantly underestimates the bearing behaviour of the pile. At 10 cm settlements, the difference in bearing capacity between the calculations with $\psi = 0$ and $\psi = 4$ is almost 150%. With a R_{inter} value of 1.0, the point where the critical state of density is reached can be evaluated. For these soil conditions, it happens at about 6 cm of vertical pile displacements. As a consequence the shaft resistance R_s remains almost constant for further loading. With a strength reduction factor of 0.7 the maximum void ratio is not reached, hence the

dilatancy cut-off is not active. Also interesting is that the influence on the base resistance is very small. Fig. 25 shows the base and shaft resistance normalized by the applied load. For this type of sand with a rather low dilatancy angle, the influence of *dco* on the load separation between pile shaft and pile base is relatively small. This is of course different for dense soils with high dilatancy angles.

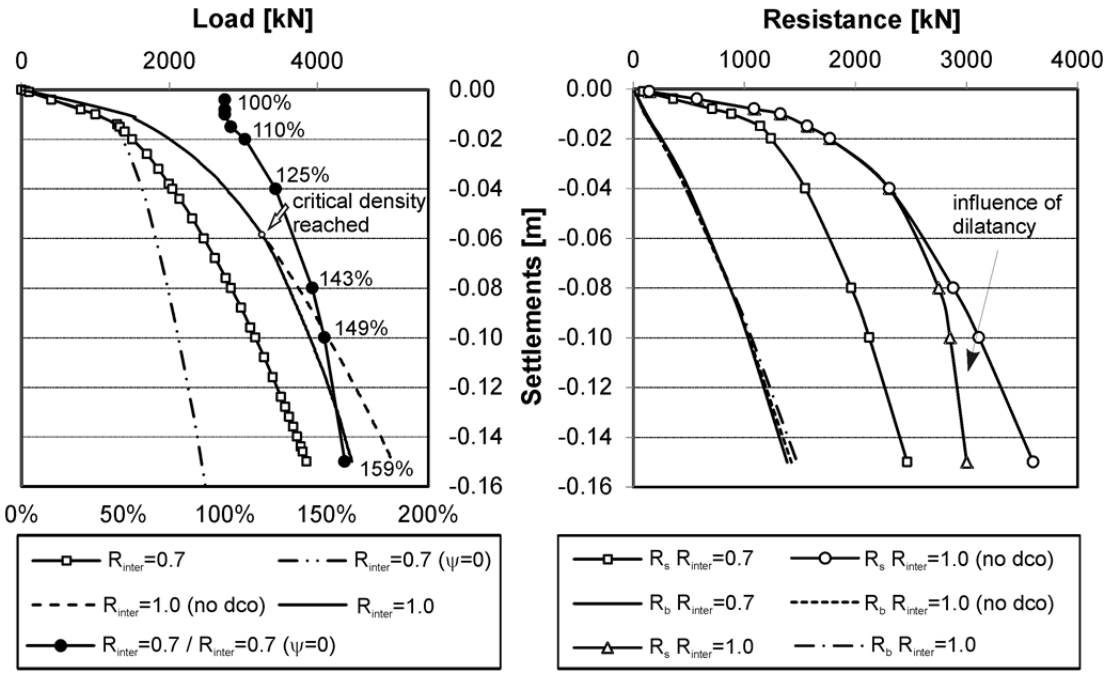

Fig. 24 Influence of dilatancy (after Kaineder 2009)

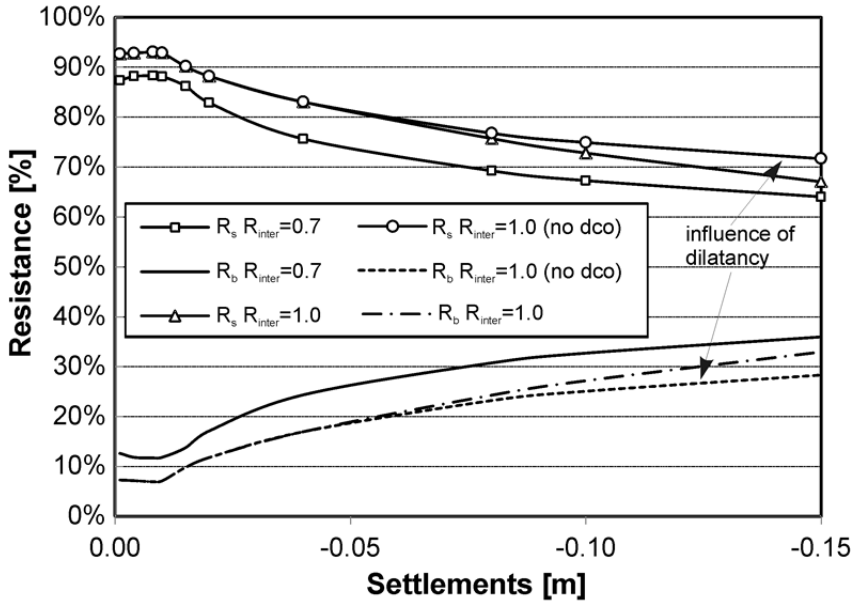

Fig. 25 Influence of dilatancy on the normalized shaft and base resistance (after Kaineder 2009)

To calculate the change of e in an interface, the thickness t_i is used. According to Equation 35, this interface thickness is related to the average element size ES_{avg}. But in reality the thickness of the shear zone is a few times larger than the average grain size d_{50}. Marcher (2003) recommended on the basis of a literature research a value of 10 times d_{50} for shear band thickness. When using the standard finite element approach in combination with the HS model, this real interface thickness δ_{real} can be assigned to an interface. This value modifies the interface stiffnesses, and as a consequence, the behaviour of the dilatancy cut-off.

To demonstrate the effect of the interface thickness on the computed load-settlement curves, the same example was recalculated with a very dense sand (ψ = 16°). Fig. 26 illustrates load-settlement curves with different interface thicknesses. When using the default interface thickness, which is related to ES_{avg}, the state of critical density is not reached (for R_{inter} = 0.7). With a realistic shear band thickness of 3.5 mm the load-settlement curve predicts a much lower bearing capacity of the pile. As a consequence, the mesh coarseness also has a significant influence on the dilatancy cut-off, because coarser meshes yield a bigger average element size, resulting in high t_i values. Thus it is important to use a realistic interface thickness for piles embedded in dilatant material.

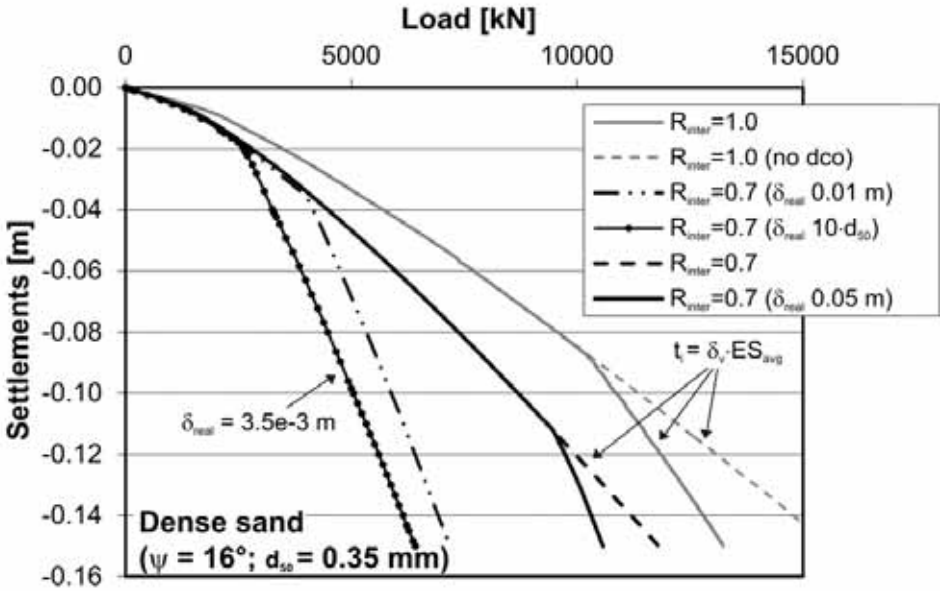

Fig. 26 Influence of interface thickness on the load-settlement behaviour

3.5.4 Limitations of the standard finite element approach

The limitations of the standard finite element approach as used in this thesis are mainly related to the maximum amount of degrees of freedom (DoF). The maximum number of DoF that can be solved by the software depends, of course, on the computer hardware, the constitutive model used and on the type of the analyses (e.g. drained or undrained). Numerical studies using PLAXIS 3DF and the HS model were conducted. With a standard Pentium (R) D 3GHz CPU, 3 GB RAM and a 32 bit operating system, it is possible to solved analyses with up to 67 520 15 noded wedge elements. For undrained material behaviour, where the excess pore pressure is also an unknown solved in the finite element nodes, the ultimate number of elements was 48 400 elements. If a special calculation kernel is used, which allows it to address 3 GB virtual memory, FE models with up to 104 640 elements in drained and 76 240 elements in undrained conditions can be analysed. With a 64-bit operating system and increased random access memory, the models able to be handled by the program increase significantly. Fig. 27 illustrates the structural elements of a PLAXIS 3DF finite element model with 137 volume piles.

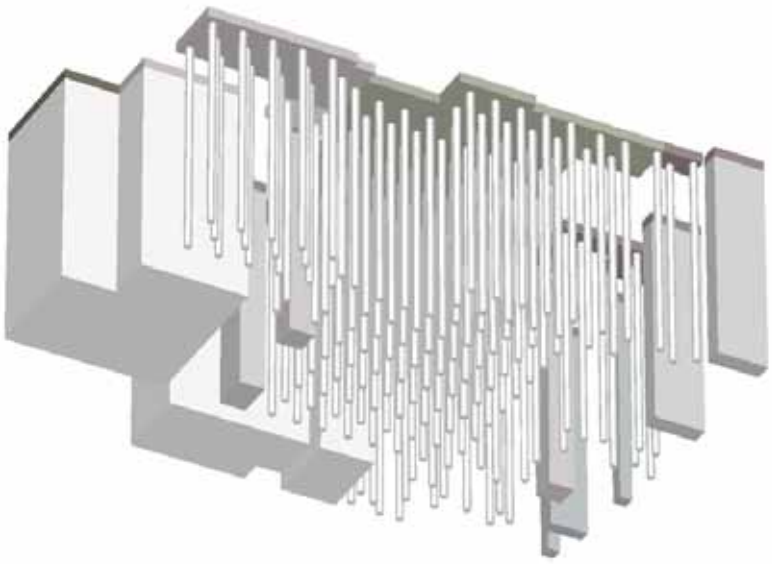

Fig. 27 Structural elements of a 3D FE model with 137 volume piles

However, when dealing with complex deep foundations a reasonable fine mesh, discretization is necessary to obtain reliable displacements and even finer meshes to evaluate stresses, hence the number of piles that can be modelled with the standard FE approach is limited. Therefore an alternative modelling technique is discussed in the next chapter: the embedded pile concept.

Another limitation is related to some deficiencies of the interface elements. For instance, the interface elements used are not able to describe effects like soil softening or creeping. Information related to more advanced interfaces are given in Gennaro & Frank (2002) or Karabatakis & Hatzigogos (2002).

4 The embedded pile concept

4.1 Introduction

Numerical methods are increasingly utilised to calculate the performance of deep foundations, but as explained in chapter 3.3.1 of this thesis, a two-dimensional representation of pile groups is usually not sufficient and 3D modelling is required. This naturally leads to very large models if a high number of piles are discretized with volume elements, thus problems that are difficult to analyse. An attractive method to reduce the complexity of such models is the use of a so-called embedded pile formulation, where piles are not explicitly modelled with continuum finite elements but replaced by a special “formulation” that can take into account the behaviour of a pile penetrating a finite element in any orientation. The benefit of this concept is that piles are not discretized by means of volume elements and thus do not affect the finite element mesh.

Embedded piles are available in both finite element codes PLAXIS 3DF and PLAXIS 3D. The studies presented in this thesis are mainly related to PLAXIS 3DF, nonetheless in chapter 6 some validations for PLAXIS 3D are also presented.

4.2 Definition of embedded piles

4.2.1 Geometrical and numerical definition of embedded piles

An embedded pile (EP) consists of a beam element that can be placed in an arbitrary direction in the subsoil, embedded interface elements to model the interaction of the structure and the surrounding soil, and embedded non-linear spring elements at the pile base to describe the base resistance. When assigning the embedded pile, additional nodes are automatically generated inside the existing finite elements and the pile-soil interaction behaviour is linked to the relative displacements between the pile nodes and the "virtual" nodes in the soil element (Sadek & Shahrour 2004). Fig. 28 shows schematically an embedded pile within a 15 noded soil element (PLAXIS 3DF) and a 10 noded tetrahedral element (PLAXIS 3D).

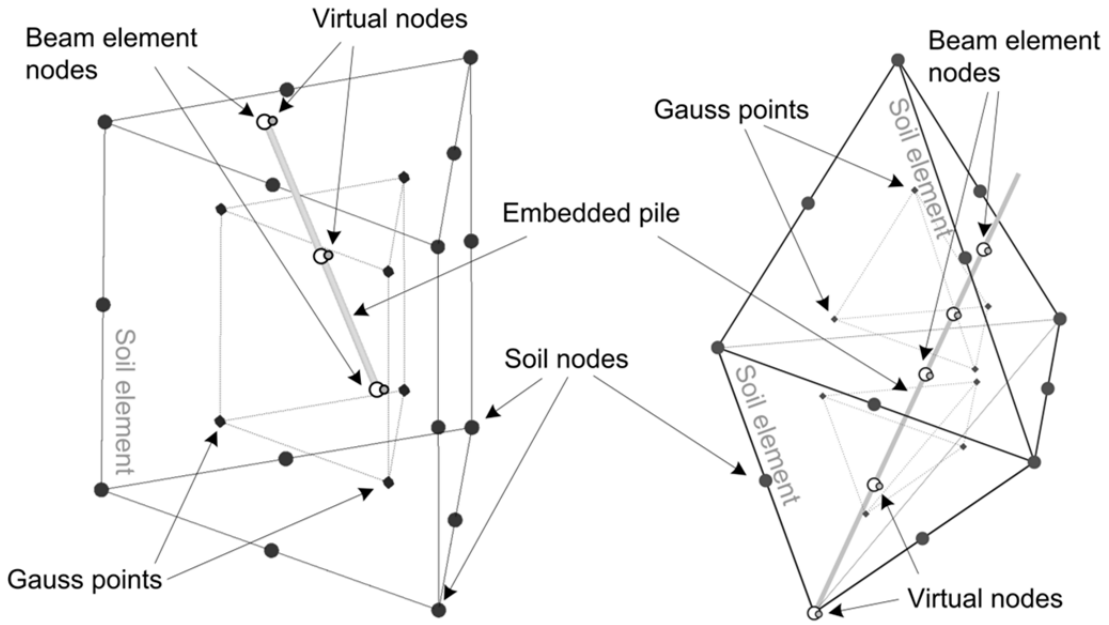

Fig. 28 Embedded pile with a 15 noded wedge element (left) and a 10 noded tetrahedral element (right)

Geometrically, an embedded pile remains a line element, although plasticity of the soil is disabled in a zone around the pile. Since the pile soil interaction is modelled along the beam element (line element), it was - until now - not possible to model complex installation effects.

Beam element nodes are always generated when the embedded pile crosses a solid finite element. In PLAXIS 3DF the final node of the embedded pile can be located somewhere within the 15 noded wedge element, and the program automatically adds a third beam element node between the last intersection with the solid element and the final beam element node. In PLAXIS 3D the final node of the embedded pile corresponds with a corner node of the solid element (see Fig. 28). The reason why is explained in detail in chapter 5.4.

If a single vertical embedded pile is modelled with a point load (P_0) at the pile head, a finite element node is of course automatically defined at the position of the embedded pile. That implies that the vertical pile is geometrically situated at the edge of several 15 noded elements. However, numerically the EP is only related to one solid element (Fig. 29).

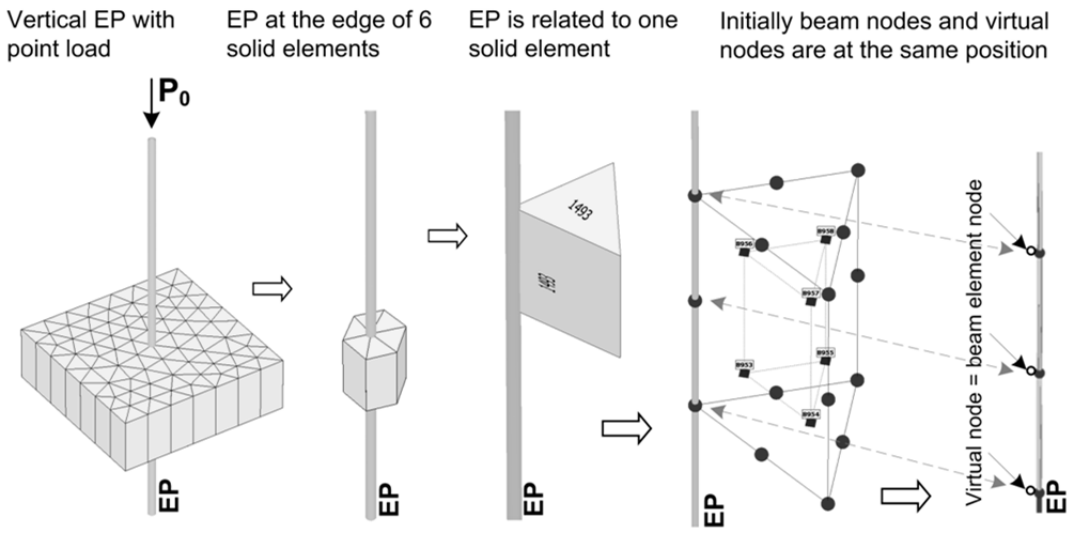

Fig. 29 Discretization of a single vertical-loaded EP

As shown in Fig. 29, an embedded pile consists of 3 noded line elements with quadratic shape function. One node has six degrees of freedom (U_x, U_y, U_z, ϕ_x, ϕ_y, ϕ_z). The embedded interface elements connect the virtual nodes inside the solid soil elements and the nodes of the embedded beam. The relative displacement vector $\boldsymbol{u}_{rel}$, between the virtual soil node displacements $\boldsymbol{u}_s$ and the embedded beam node displacements $\boldsymbol{u}_p$, describes the pile-soil interaction.

$$\mathbf{u}_s = \mathbf{N}_s \cdot \mathbf{u}_s^{\,n} \tag{44}$$

$$\mathbf{u}_p = \mathbf{N}_p \cdot \mathbf{u}_p^{\,n} \tag{45}$$

$$\mathbf{u}_{rel} = \mathbf{u}_p - \mathbf{u}_s \tag{46}$$

$\mathbf{N}_s$ and $\mathbf{N}_p$ are matrixes of interpolation functions of the soil and the pile respectively and $\mathbf{u}_s^{\,n}$ and $\mathbf{u}_p^{\,n}$ are the nodal displacement vectors of the soil and the embedded beam element. The element stiffness matrixes of embedded piles are numerically integrated with the Newton-Cotes integration scheme.

4.3 Input parameters of an embedded pile

4.3.1 Basic input

The input for an embedded pile consists basically of three groups. The first group, which is described in detail in the next chapter of this thesis, defines the special interface elements - in other words, the pile-soil interaction. The second group is related to the beam properties of the pile and the third group describes the connection of the pile head with the solid finite elements. Three options exist in the latter group: free, hinged and rigid. In the first option, the top beam node of the embedded pile can move relative to the connected finite element. The standard case for a single pile, because otherwise parts of the load (depending on the relative stiffness) are transferred directly to the soil, yielding a completely different load-settlement response. In the second option, no relative displacements between these two nodes are allowed, and in the third option, the rotation is also coupled to the element at the pile head. Of course, such a coupling is only possible if the solid element has rotational degrees of freedom (e.g. floor elements). The third option is important when dealing with horizontally-loaded pile groups, where the pile-raft connection is thought to be bending stiff.

The input for the beam consists of a diameter d, the cross section geometry (pile or tube), the unit weight γ and the stiffness E. The diameter d determines an elastic zone in the soil around the beam, i.e. plastic soil behaviour is excluded in the vicinity of the beam element (Engin 2006). The cross section geometry defines the pile cross section area A in combination with d, thus the moments of inertia I_2 and I_3. If the piles are not circular an equivalent radius R_{eq} is calculated.

$$R_{eq} = \max\left\{\sqrt{\frac{A}{\pi}},\ \sqrt{\frac{I_2 + I_3}{A}}\right\} \tag{47}$$

The unit weight γ represents a delta unit weight to the surrounding soil, due to the fact that the beam is a line element. This means that layered soil conditions with different bulk unit weights yield automatically to a varying unit weight of the embedded pile.

An alternative is the definition of a user-defined pile, where the cross section area and the moments of inertia are a direct input. Nevertheless, beam elements of embedded piles cannot have non-linear properties.

4.3.2 Pile resistance

With embedded interface elements, it is possible to account for relative displacements between the EP and the surrounding soil. The pile-soil interaction behaviour is linked to these relative displacements between the embedded beam nodes and the virtual soil nodes. For the embedded pile interface elements, an elastic-plastic model is used.

Equation 48 gives the constitutive equation, where $\mathbf{t}^{skin}$ is the skin traction along the embedded pile and the $\mathbf{T}^{skin}$ matrix contains the stiffnesses of the embedded interface elements.

$$\mathbf{t}^{skin} = \mathbf{T}^{skin} \cdot \mathbf{u}_{rel} \tag{48}$$

$$\mathbf{t}^{skin} = \begin{bmatrix} t_s \\ t_n \\ t_t \end{bmatrix} \tag{49}$$

$$\mathbf{T}^{skin} = \begin{bmatrix} K_s & 0 & 0 \\ 0 & K_n & 0 \\ 0 & 0 & K_t \end{bmatrix} \tag{50}$$

$$\mathbf{u}_{rel} = \begin{bmatrix} u_s^p - u_s^s \\ u_n^p - u_n^s \\ u_t^p - u_t^s \end{bmatrix} \tag{51}$$

t_s is the shear stress in axial direction, t_n and t_t are the normal stresses of the embedded pile, K_s is the axial interface stiffness, K_n and K_t are the normal interface stiffnesses and u^s and u^p are the displacements of the virtual soil node and the embedded beam element respectively. Fig. 30 illustrates schematically the embedded interface stiffnesses.

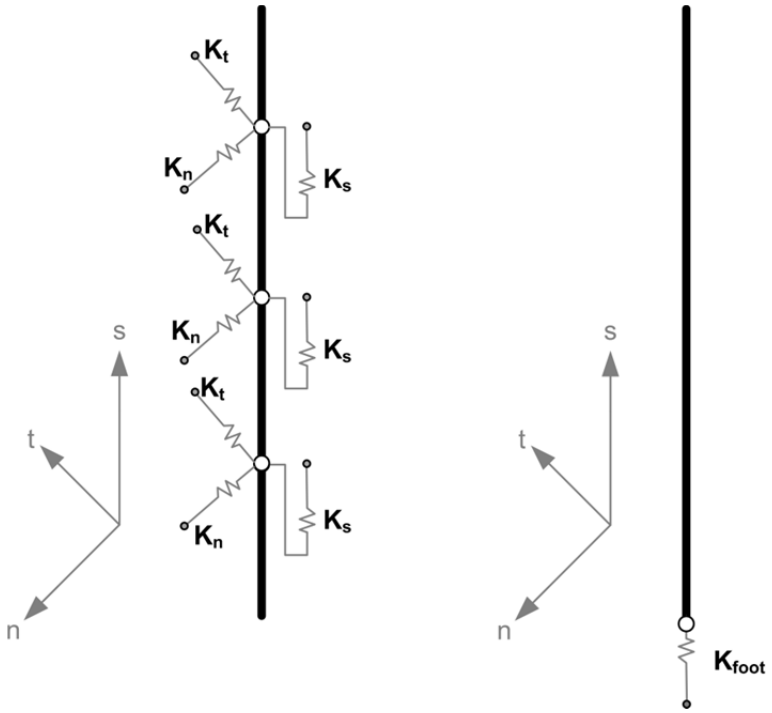

Fig. 30 Embedded interface stiffness at the pile shaft (left) and the pile base (right) (after Brinkgreve & Swolfs 2007)

The constitutive equation for the base resistance of an embedded pile is very similar, with F_{foot} denoting the base resistance of the embedded pile, K_{foot} the spring stiffness at the pile tip and u^{p}_{food} and u^{s}_{food} the displacements of the last embedded beam node and the connected virtual node in the soil.

$$F_{foot} = K_{foot} \cdot \left(u^{p}_{foot} - u^{s}_{foot} \right) \tag{52}$$

A maximum base resistance F_{max} must be assigned to the non-linear spring elements at the base of an embedded pile.

As long as the shear stress t_s is smaller than the maximum skin friction, only numerical relative displacements take place, depending on the interface stiffness K_s. Once the maximum skin resistance at an integration point is reached, relative displacements between the embedded pile and the surrounding soil occur. The same is true for the behaviour of the foot resistance.

For the definition of the ultimate skin resistance three different options are available. The first and simplest one is the linear distribution, where a constant or linear distribution for the ultimate skin resistance is defined with two input values ($T_{top,max}$, $T_{bot,max}$). The second option is the multi-linear distribution, with which it is possible to define values for the skin friction in certain depths. For example, this is necessary when layered soil conditions and therefore different

skin resistances, are present along the pile. In these two embedded interface definitions, the bearing capacity of the pile is therefore an input to the analysis and not a result, because the maximum skin friction is predefined and thus independent of the stress state in the surrounding soil. In the optimal case pile load test data is available to define the maximum bearing capacity of an embedded pile. If that is not the case, classical approaches as presented in chapter 2 of this thesis can be used.

Another option to work out the maximum skin friction and maximum base resistance of a single pile is to perform a 2D axisymmetric calculation. In the author's opinion, this procedure is preferable. But once dealing with pile groups or a piled raft foundations, the interaction between the piles has to be taken into account and, as a consequence, the influence on the bearing capacity. However, it is difficult to define prior ultimate skin friction profiles for piles within pile groups, because each pile mobilizes differently depending on raft stiffness, spacing, load level, etc. This deficiency is maybe not crucial for working load conditions, but once ultimate limit state considerations are an issue it may have a significant influence.

The third option to define the skin resistance is the layer dependent option. With this definition, the maximum shear stress $t_{s,max}$ of an embedded pile is related to the strength parameters of the soil and the normal stress $\sigma'_n{}^{avg}$ along the interface.

$$t_{s,max} = \left(\sigma'_n{}^{avg} \cdot \tan\varphi'_i + c_i\right) \cdot 2 \cdot \pi \cdot R_{eq} \tag{53}$$

$$\sigma'_n{}^{avg} = \frac{\sigma'_t + \sigma'_n}{2} \tag{54}$$

σ'_t and σ'_n are the effective stresses of the surrounding soil perpendicular to the pile. An embedded beam element is numerically always defined within one solid soil element (Fig. 29), hence the effective stresses of the six Gauss points of this element are extrapolated to the embedded beam nodes/stress points (Newton-Cotes integration scheme) and transformed to the local coordinate system (*s*, *t*, *n* direction). With all components of the effective stresses perpendicular to the pile, $\sigma'_n{}^{avg}$ is calculated in each stress point of an embedded pile.

When using the layer dependent option, the embedded interface elements behave similar to normal interface elements as used in the standard finite element approach (Equation 24 and 25), with the difference that the interaction is modelled along a line element. The input for the layer dependent option is a R_{inter} value for the strength reduction. In addition, a limiting value for the skin resistance has to be defined. With this definition of the skin resistance a potential

change of normal stress along the pile is automatically taken into account, for example due to the raft-soil interaction in piled raft foundations. Thus, the ultimate bearing capacity of the pile is a result of the analysis.

The normal stresses t_n and t_t, at the embedded interface elements, are not limited with a failure criterion. But of course plasticity in the surrounding soil, outside the elastic region, can take place. As shown in chapter 6.2 of this thesis, embedded piles are also suitable for horizontal loads. If EPs are defined at the axis of symmetry, the input of the base and shaft resistance must be defined according to the symmetry conditions.

4.4 Embedded pile interface stiffness

As shown in Equation 48, mobilization of stresses along an embedded pile is determined by the relative displacement vector $\mathbf{u}_{rel}$ and the interface stiffness matrix $\mathbf{T}^{skin}$. In principle, the embedded interface stiffnesses should be defined with the result that the initial slope of the global load-settlement behaviour of a single pile is similar to the first part of the computed load-settlement without using interface elements. This ensures that the pile displacements u_p are governed by the stiffness of the surrounding soil and that the influence of an interface is restricted to plastic slip along the soil-structure interaction. Fig. 31 shows schematically the global stiffness response of a vertically-loaded single pile.

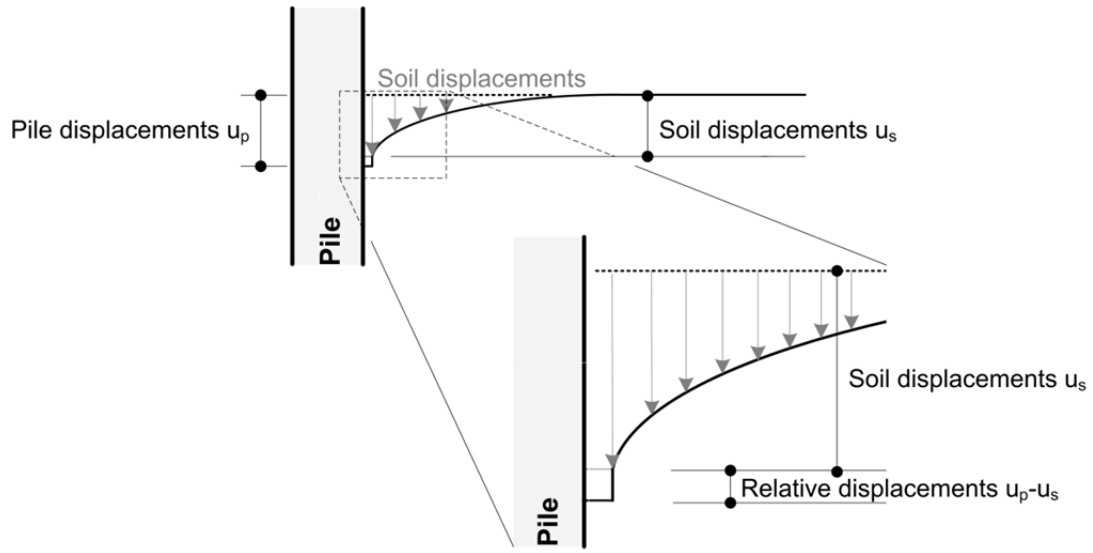

Fig. 31 Global stiffness response of an axially-loaded pile

As long as the maximum skin friction is not reached, the relative displacements u_{rel} are only related to the interface stiffness K_s. This indicates that the interface stiffness must be high compared to the shear modulus G of the soil. In general, the definition of the interface stiffness, as used in the standard FE approach, is related to the shear stiffness of the surrounding soil. Due to the fact that an embedded pile is a line element, the traction along the pile skin $\mathbf{t}^{skin}$ has the unit [kN/m], and as a consequence K_s has the same unit as the soil stiffness [kN/m^2]. The normal and tangential stiffnesses K_n and K_t are linked to the axial stiffness of the EP. ν_i is the interface Poisson's ratio, which has a default value of 0.45.

$$K_s = 50 \cdot G \tag{55}$$

$$G = \frac{E}{2(1+\upsilon)} \tag{56}$$

$$K_n = K_t = \frac{2(1-\upsilon_i)}{1-2\cdot\upsilon_i} K_s \tag{57}$$

When considering Equation 52, it is clear that the foot interface stiffness K_{foot} must have a different unit, namely [kN/m^3].

$$K_{foot} = 10 \cdot G \cdot R_{eq} \tag{58}$$

If a primary loading problem is considered and the stress dependent stiffness of high order constitutive models is not taken into account (m = 0), a difference in the calculated shear stiffness of the soil comes from the different definition of elastic parameters in the constitutive models. The linear elastic-perfectly plastic Mohr-Coulomb model uses a Poisson's ratio ν. High order constitutive models like the Hardening Soil model use the unloading/reloading Poisson's ratio ν_{ur}. Therefore, different embedded interface stiffnesses are defined when using different constitutive models for the adjacent soil. A simple example for typical input ratios shows the influence on the shear modulus G of the soil, and at the same time the influence on the embedded interface stiffnesses. The comparison indicates that when using a high order constitutive model, the embedded interface stiffnesses are much higher.

Simple Constitutive models (e.g. MC model):

$E = E_{primary\ loading}$
$\nu = 1/3$

$$G_{soil} = \frac{12 \cdot E}{24}$$

High order constitutive models (e.g. HS model):

$E_{ur} = E_{primary\ loading} \cdot 5$
$\nu_{ur} = 0.2$

$$G_{soil} = \frac{50 \cdot E}{24}$$

To study the influence of the embedded interface stiffnesses (see chapter 6) and to improve the global behaviour of the embedded pile approach, a modified calculation kernel was used, which allows the definition of the interface stiffnesses independently of the soil shear modulus. Additionally, the modified kernel allows the definition of independent embedded interface stiffnesses for the axial and the normal/tangential direction.

$$K_s = 50 \cdot G \cdot \Gamma_s + \Delta_s \tag{59}$$

$$K_n = K_t = 50 \cdot G \cdot \frac{2(1-\upsilon_i)}{1-2 \cdot \upsilon_i} \Gamma_n + \Delta_n \tag{60}$$

$$K_{foot} = 10 \cdot G \cdot R_{eq} \cdot \Gamma_{foot} \tag{61}$$

Γ_s is a multiplier on the shear modulus G for the axial interface stiffness, Γ_n for the normal and tangential interface stiffness, Γ_{foot} for the foot interface stiffness, and Δ_s and Δ_n are direct input values for K_s and K_n/K_t, respectively.

Due to the fact that an embedded pile has no volume and the interfaces are defined at the position of the embedded beam element, instead of G at the stress point next to the pile, the G_{el}^{av}, which is the average shear stiffness of the allocated soil element, is used to define the embedded interface stiffnesses. When using constitutive models, which take the stress dependent stiffness into account, the shear stiffness at different stress points within one element is not the same. Fig. 32 shows schematically the definition of G_{el}^{av}.

$$G_{el}^{av} = \frac{G_{stress\ P.1} + ... + G_{stress\ P.6}}{6} \tag{62}$$

Because of the non-linear behaviour of soils, the unbalanced force in a finite element calculation is applied in a number of load steps, and if the stress dependency of stiffness is taken into account the stiffness matrix is based on the stiffness at the beginning of each step. This means that the stiffness of the soil and, as a consequence, the embedded pile interface stiffness is updated at the beginning of each step on the basis of the stress state obtained at the end of the previous step. Thus the interface stiffnesses of an EP change during a calculation phase.

$$G_{el,step\,i}^{\ av} = \frac{\sum_{stress\ Points} G_{step\,i-1}}{Number\ of\ stress\ points} \tag{63}$$

Hence the embedded interfaces as used in this thesis are generally defined as follows:

$$K_s = 50 \cdot G_{el}^{\ av} \cdot \Gamma_s + \Delta_s \tag{64}$$

$$K_n = K_t = 50 \cdot G_{el}^{\ av} \cdot \frac{2(1-\upsilon_i)}{1-2\cdot\upsilon_i}\Gamma_n + \Delta_n \tag{65}$$

$$K_{foot} = 10 \cdot G_{el}^{\ av} \cdot R_{eq} \cdot \Gamma_{foot} \tag{66}$$

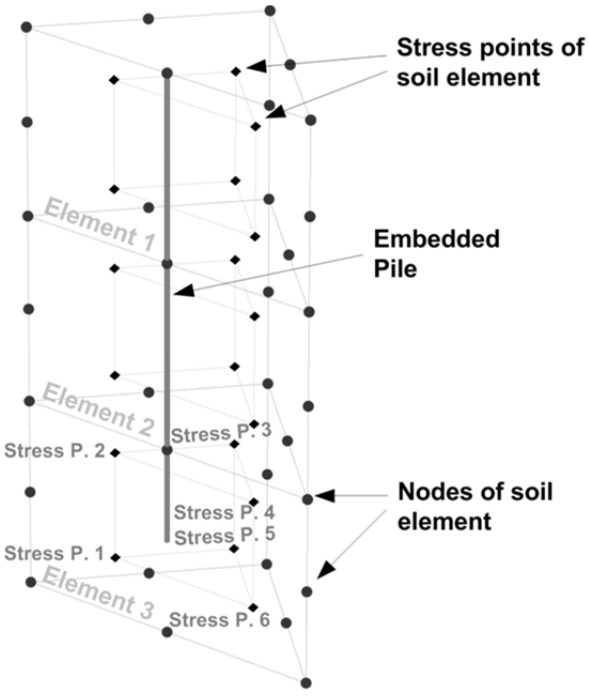

Fig. 32 Definition of the average shear stiffness of the allocated soil element

4.5 Elastic region approach

Engin et al. (2007) showed that the computed load-settlement curves of embedded piles are strongly affected by the mesh discretization of the boundary value problem. They also showed that when using fine meshes, premature failure occurs due to numerical instabilities. To get rid of the mesh dependency and the numerical problems, they introduced the so-called elastic region. Fig. 33 shows that this simple approach improves the behaviour of embedded piles significantly.

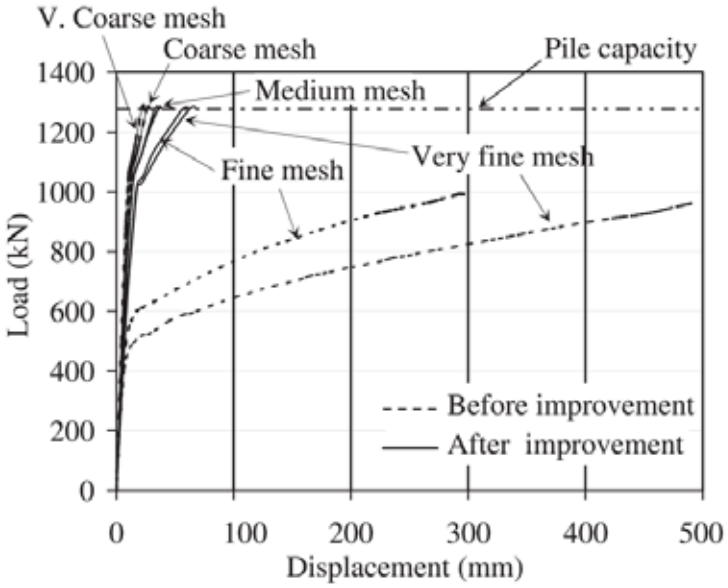

Fig. 33 Influence of elastic region approach on the load-settlement behaviour (Engin et al. 2007)

The stiffness within the elastic region is defined similarly to the stiffness of the soil, which means that for high-order constitutive models, the element stiffness matrix at a particular load increment depends on the stresses determined at the previous load step. Since the stiffness matrix is determined by numerical integration, this procedure is referred to the integration (Gauss) points.

$$\mathbf{K}_e = \int \mathbf{B}^T \cdot \mathbf{D} \cdot \mathbf{B} \cdot dVol \tag{67}$$

A summation over all stress points within the finite element is necessary for building up the element stiffness matrix. At the beginning of the calculation, there is a loop over all stress points to check whether they are inside the equivalent pile diameter R_{eq}. If that is the case, the stiffness is calculated for the surrounding soil but the Gauss points inside the elastic region are forced to remain elastic. Fig. 34 illustrates schematically the modified stress points inside a

15 noded wedge element. The elastic region consists of two sub-regions, namely the elastic region along the pile shaft and the elastic region above the pile and below the pile base. The latter regions are defined as half spheres with the diameter R_{eq}.

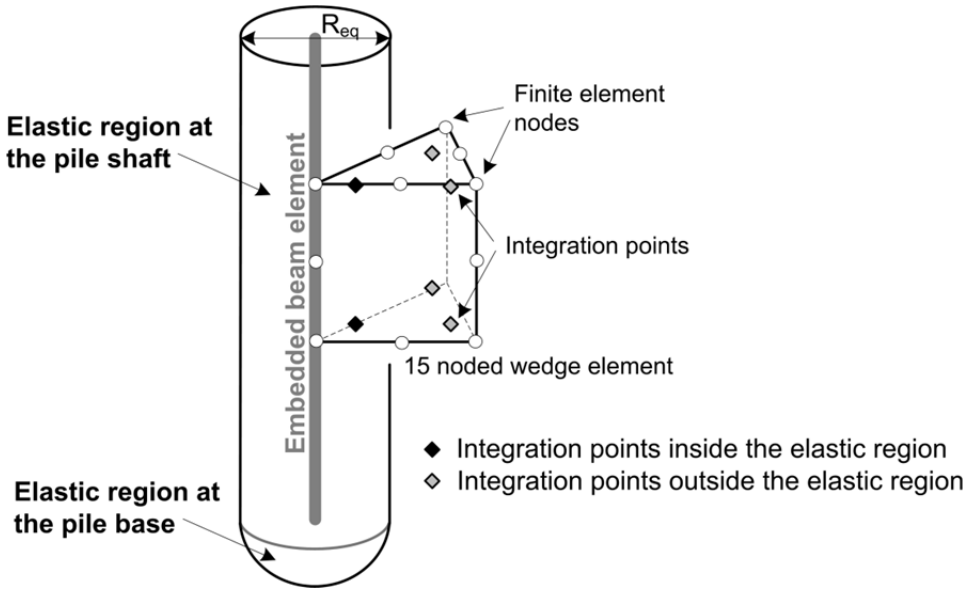

Fig. 34 Schematic representation of the elastic region approach

In the standard definition of the elastic region, the stiffness inside this region is not modified, thus the shear stiffness G is the same as in the surrounding soil. An adapted calculation kernel was used to study the influence of the stiffness inside the modified zone, which allows an increase of the stiffness inside the elastic region along the pile shaft $G_{el.R,S}$, by a factor $\Gamma_{G,S}$, and the elastic region above and below the EP $G_{el.R,B}$, by a factor $\Gamma_{G,B}$.

$$G_{el.R,S} = G_{el}^{av} \cdot \Gamma_{G,S} \tag{68}$$

$$G_{el.R,B} = G_{el}^{av} \cdot \Gamma_{G,B} \tag{69}$$

But a modification of the stiffness inside an elastic region creates a "virtual" volume with higher stiffness compared to the surrounding soil and the shape of this region is related to the mesh coarseness next to the embedded pile. Fig. 35 shows the virtual volumes for two different equivalent radii $R_{eq,1}$ and $R_{eq,2}$. The shape of the elastic region along the pile shaft is influenced by the horizontal (2D) mesh coarseness and, for the elastic region below the pile base, by the vertical mesh discretization.

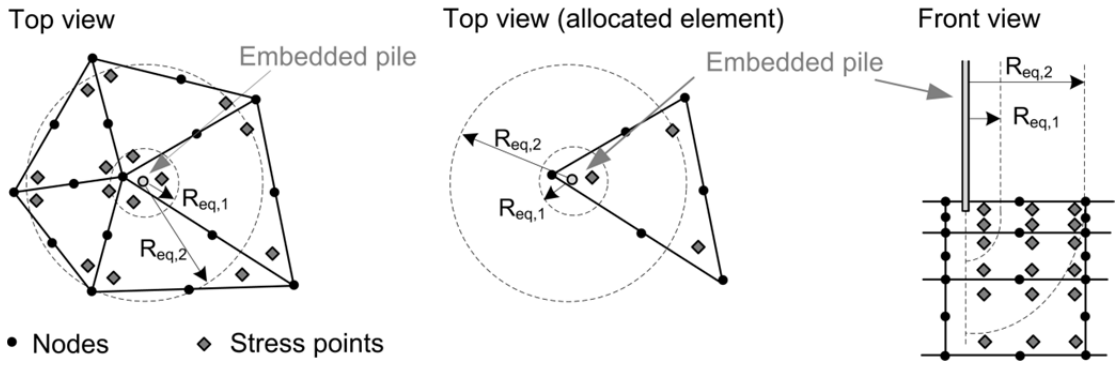

Fig. 35 Modified Gauss points inside the elastic region

The modification of the stiffness inside the elastic region also has an effect on embedded interface stiffnesses K_s, K_n and K_t (Equation 64 to 66). However, the influence on the interface stiffnesses is quantitatively different compared to the influence on the global load-settlement behaviour, because globally, all Gauss points inside the equivalent pile radius R_{eq} are modified, but for the embedded pile interface stiffnesses only the modification of the stiffnesses of the "allocated" element has an influence (Fig. 35). For example, if a very coarse mesh in combination with a slender pile is modelled, it is possible that no stress points are inside the elastic region, so the embedded interface stiffness is consequently calculated with the shear stiffness of the soil. On the other hand, if a fine mesh is used, it could be that all stress points of the allocated element are inside the elastic region and the stiffnesses K_s, K_n and K_t are increased by the factor $\Gamma_{G,S}$. Of course, the foot interface stiffness is also affected by the factor $\Gamma_{G,B}$.

$$G_{el}^{av} \leq G \text{ for embedded interface stiffnesses} \leq G_{el}^{av} \cdot \Gamma_{G,S} \tag{70}$$

The explanations indicate that the global stiffness response of an embedded pile is a result of a number of effects, such as pile length, pile stiffness, surrounding soil stiffness, pile diameter, bearing capacity of the embedded pile, interface stiffnesses, mesh coarseness and stiffness inside the elastic region. The influence of particular effects is shown in the next chapter of this thesis.

5 Numerical investigation of basic features of the EP concept

5.1 Introduction

For the embedded pile option it is necessary to fulfil the following four criteria:

1.) Correct load-settlement behaviour.
2.) Realistic distribution of the ultimate skin friction and realistic mobilization of the skin friction.
3.) Mobilization of the end-bearing capacity.
4.) Avoid numerical problems.

These 4 criteria are not entirely independent of each other but are related to some extent.

Some problems obtained with the standard definition of embedded piles, as implemented in the commercial calculation kernel of PLAXIS 3DF, are shown in the first part of this chapter. In the subsequent chapters, tests with different settings of the interface stiffnesses, the elastic region and the mesh coarseness are discussed. Finally an improved embedded pile concept is presented. The validation of the improved embedded pile option is presented in chapter 6 of this thesis and chapter 7 demonstrates the application of the improved approach to boundary value problems.

5.2 Deficiencies of the original embedded pile concept

Calculations of single, axially-loaded, embedded piles were performed, using three different mesh coarsenesses: fine, medium and coarse (Fig. 36). The finite element models have the dimension $B_m/L_m/D_m$ of 20/20/20 m. The parameters of the embedded pile with an effective length of 9.5 m are given in Tab. 2. From that follows a maximum skin resistance of ~1913 kN, a maximum base resistance of 1320 kN and a total bearing capacity of about 3233 KN. The pile is located in overconsolidated clay, described with the Hardening Soil model. The properties are shown in Tab. 3. The overconsolidation is taken into account with a pre-overburden pressure (*POP*) of 50 kN/m^2 and a lateral earth pressure coefficient K_0 of 0,8. The groundwater table is located 3.5 m below the surface. The point

load at the pile head is applied step-by-step. In total, 12 calculation phases were defined.

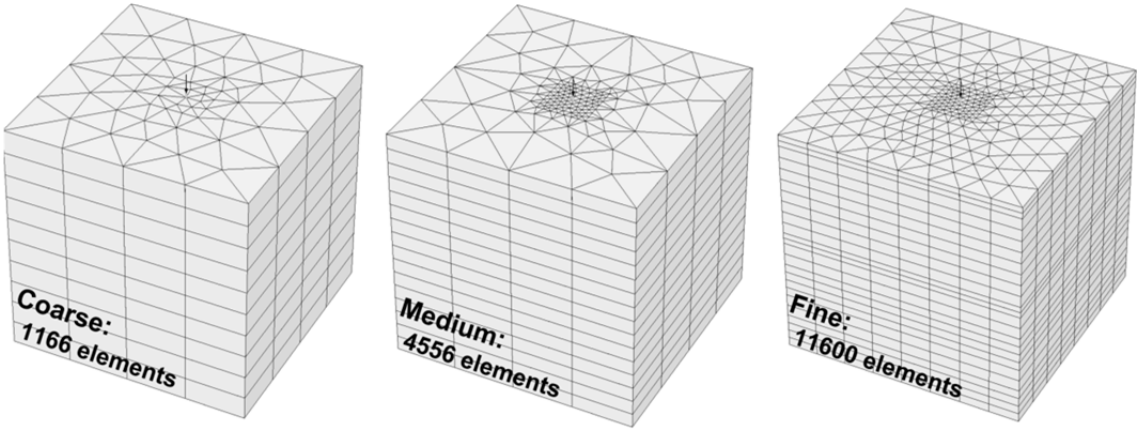

Fig. 36 Finite element models of a single pile with coarse (left), medium (middle) and fine (right) mesh discretization

Tab. 2: Input parameters for embedded pile

parameter		**value**	**unit**
Young's modulus	E	3e7	kPa
bulk unit weight	γ	5.0	kN/m^3
diameter	d	1.3	m
skin resistance at pile top	$T_{top,max}$	201.37	kN/m
skin resistance at pile bottom	$T_{bot,max}$	201.37	kN/m
base resistance	F_{foot}	1320	kN

Fig. 37 illustrates the computed load-settlement curves. Numerical failure occurs too early ("premature" failure). The predefined bearing capacity is roughly 3233 kN and the weight of the pile is ~63 kN, so the maximum point load to reach the predefined bearing capacity should be about 3169 kN. It turns out that the premature failure occurs once the skin resistance is fully or almost fully mobilized. When applying the theoretical failure load in one single calculation phase, it could be that no premature failure occurs. Other calculations with higher soil stiffnesses showed jumps and oscillations in the load-settlement behaviour. This behaviour indicated that some numerical problems occurred.

Fig. 37 also shows that the load-settlement behaviour of an embedded pile is strongly mesh-dependent. Fig. 38 illustrates that the mesh coarseness also has an influence on the mobilization of the base resistance, hence on the load separation between the pile skin and pile base.

Tab. 3: Properties of overconsolidated clay (HS)

parameter		**value**	**unit**
unit weight above groundwater table	γ_{unsat}	20.0	kN/m^3
unit weight below groundwater table	γ_{sat}	20.0	kN/m^3
reference secant stiffness in drained triaxial test	$E_{50,ref}$	45 000	kPa
reference oedometric stiffness	$E_{oed,ref}$	27 150	kPa
reference unloading/reloading stiffness	$E_{ur,ref}$	90 000	kPa
isotropic Poisson's ratio	ν'_{ur}	0.2	--
reference pressure	p_{ref}	100	kPa
power index for stress dependency of stiffness	m	1.0	--
effective friction angle	φ'	20	°
effective cohesion	c'	20	kPa
dilatancy angle	ψ	0	°
K_0 value for normal consolidated conditions	K_0^{nc}	0.658	--
pre-overburden pressure	POP	50	kPa

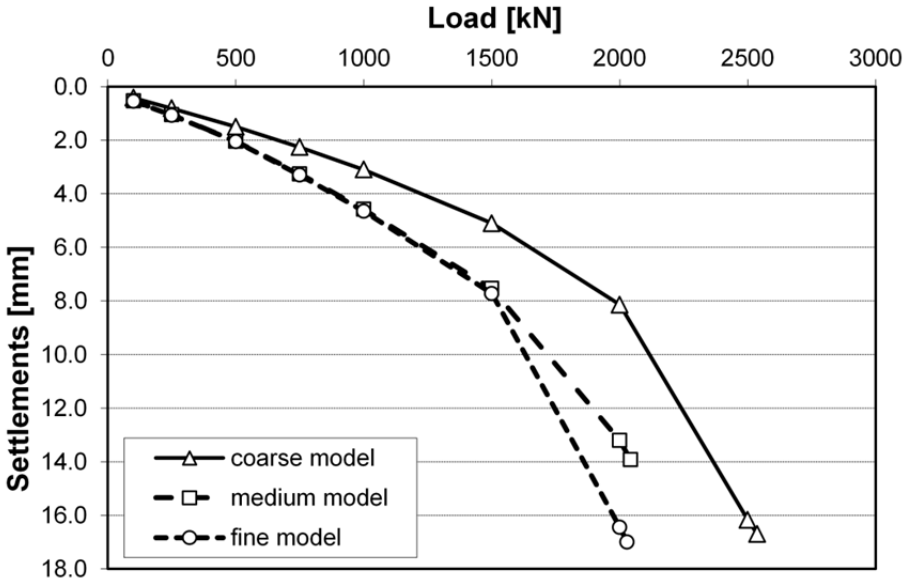

Fig. 37 Load-settlement curves for different mesh coarsenesses

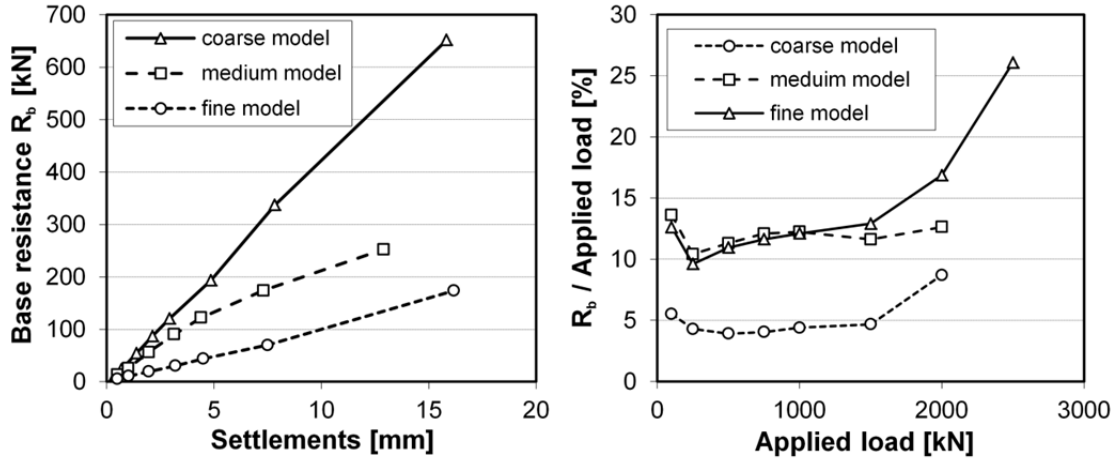

Fig. 38 Influence of mesh coarseness on mobilized base resistance R_s

Another deficiency found is related to the foot interface stiffness. To show the influence of K_{foot} the medium mesh discretization (Fig. 36) is used. To simplify the problem (to the essential), the linear elastic-perfectly plastic Mohr-Coulomb (MC) model was used for the soil (Tab. 4). The parameters for the MC model were adjusted, so that in the middle of the model both constitutive models yield the same initial stiffness. The pile properties are given in Tab. 2, with the difference that for this study no skin friction was allowed and the pile weight was set to 0. Three different definitions of the foot interface stiffness were considered, the default setting with Γ_{foot} of 1 and two increased foot interface stiffnesses with Γ_{foot} of 10 and 500.

Tab. 4: Input parameters for Mohr-Coulomb model

parameter		**value**	**unit**
unit weight above groundwater table	γ_{unsat}	20.0	kN/m^3
unit weight below groundwater table	γ_{sat}	20.0	kN/m^3
Young's modulus	E	33 185	kPa
Poisson's ratio	ν'	0.30	--
effective friction angle	φ'	20.0	°
effective cohesion	c'	20.0	kPa
dilatancy angle	ψ	0	°
lateral earth pressure coefficient at rest	K_0	0.8	--

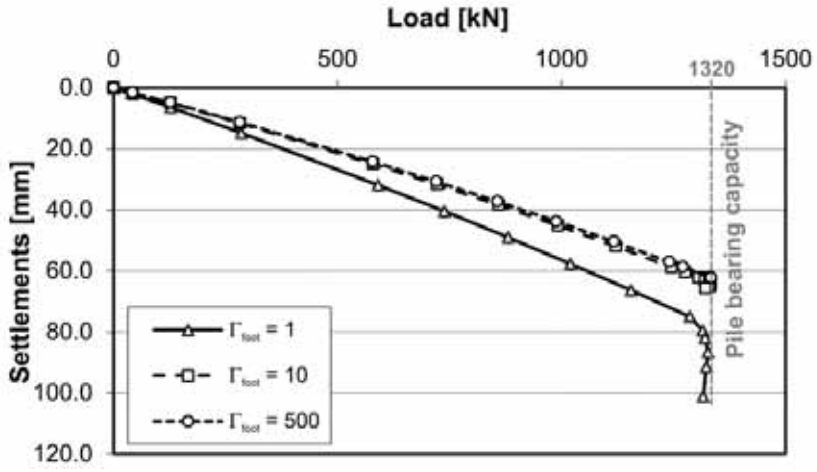

Fig. 39 Influence of K_{foot} on the load-settlement behaviour of a single pile

Fig. 39 illustrates the calculated load-settlement curves. All three models reach the predefined bearing capacity of the pile (F_{max} = 1320 kN). The difference between the default settings and an increase of the foot interface stiffness by a factor of 10 is significant. A further increase to a factor Γ_{foot} of 500 has a relatively small influence on the global stiffness response. This is because the relative displacements between the last embedded beam node and the connected virtual node in the soil, to mobilize the base resistance R_s, are linearly connected to K_{foot}. Fig. 40 shows the vertical displacements and the relative displacements along the embedded pile for a load level of 1000 kN. The vertical displacements u_y are almost constant because the relative stiffness between the pile and the soil is high. Fig. 40 shows that the difference of settlements is identical to the difference of the relative displacements (u_{rel}).

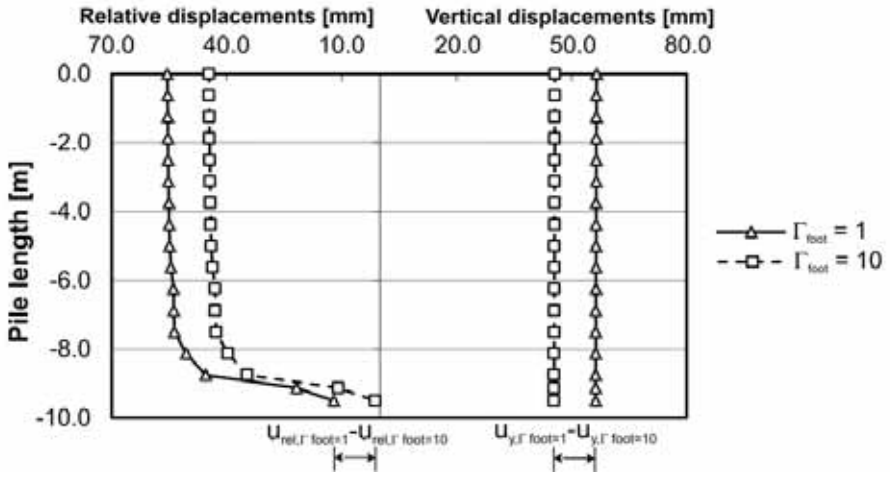

Fig. 40 Influence of K_{foot} on settlement behaviour (load level 1000 kN)

Another problem obtained with these calculations was that the vertical mesh dependency, or the position of the embedded pile tip node, has a significant effect on the computed settlements of an embedded pile. In principle, the settlements (u_p) are the sum of elastic pile deflection ($u_{p,el}$) plus soil displacements at the pile tip (u_s) plus the relative displacements (u_{rel}), to mobilize the base resistance. For floating piles, where the relative stiffness between the pile and surrounding soil is relatively large, the pile displacements u_p should be mainly governed by the soil displacements, thus the soil stiffness.

$$u_p = u_{p,el} + u_s + u_{rel} \tag{71}$$

Fig. 41 explains the location of the last embedded beam node within a solid wedge element. Twelve different positions for the last embedded pile node were studied and the maximum vertical pile displacements (u_p) were compared. Due to the fact that no skin friction is defined along the embedded pile and the weight of the pile is defined with zero, the vertical displacements should be almost the same in all calculations. But Fig. 42 shows that this is not the case; the maximum settlements of the pile are obtained once the end of the embedded pile corresponds with an edge-node of a solid soil element. Once the last node of the embedded pile is in the soil element, the vertical displacements decrease. The minimum is found if the node position is in the middle of the "second half" of the wedge element. In this particular example, the difference of vertical settlements of the pile, as a result of different positions of the pile tip node, is roughly 35%.

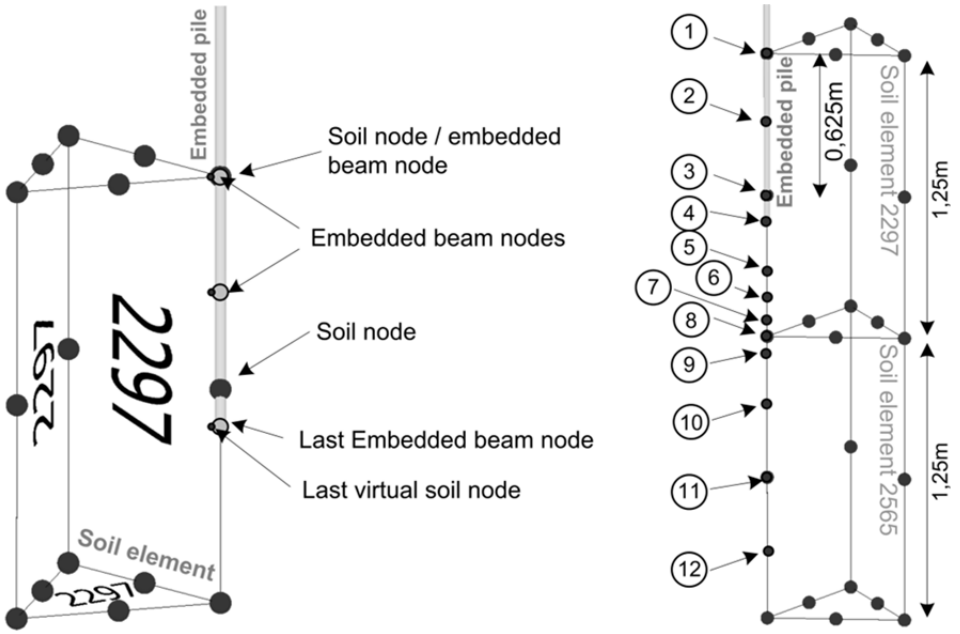

Fig. 41 Definition of nodes within a 15 noded wedge element (left) and positions of last embedded beam nodes (right)

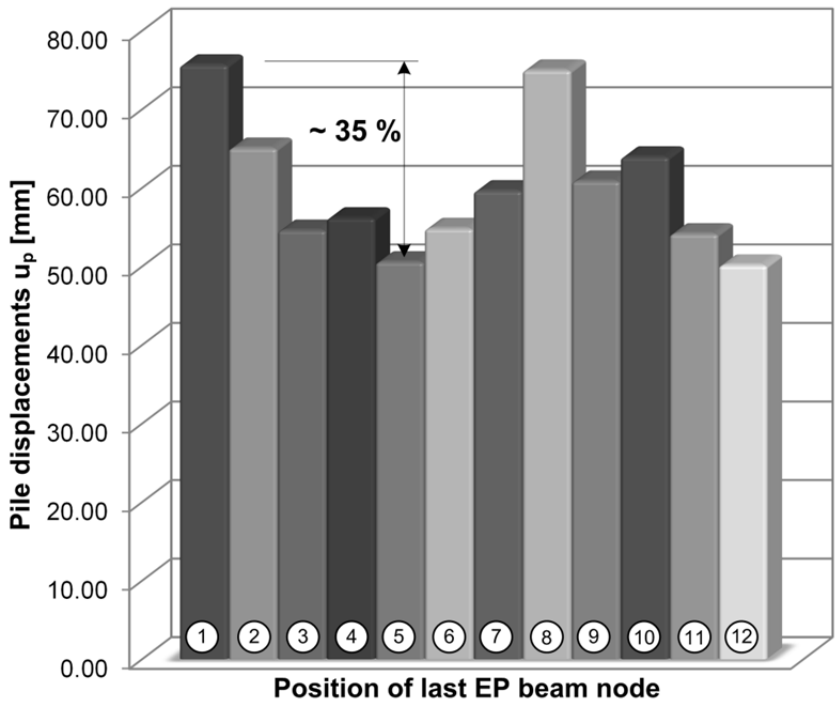

Fig. 42 Influence of last embedded beam node position on vertical pile displacements

If the skin resistance of an embedded pile is taken into account, the results show that the mobilized skin friction close to the pile base is largely affected by the foot interface stiffness K_{foot}. Fig. 43 shows, for the load levels 500 kN and 1500 kN, the mobilized skin friction t_s along an embedded pile and the corresponding relative displacements. With the default foot interface stiffness the mobilized skin friction at the pile base is unrealistically large, but on the other hand, when increasing K_{foot} by a factor of 100 small skin tractions, even negative values of t_s, are mobilized close to the pile tip.

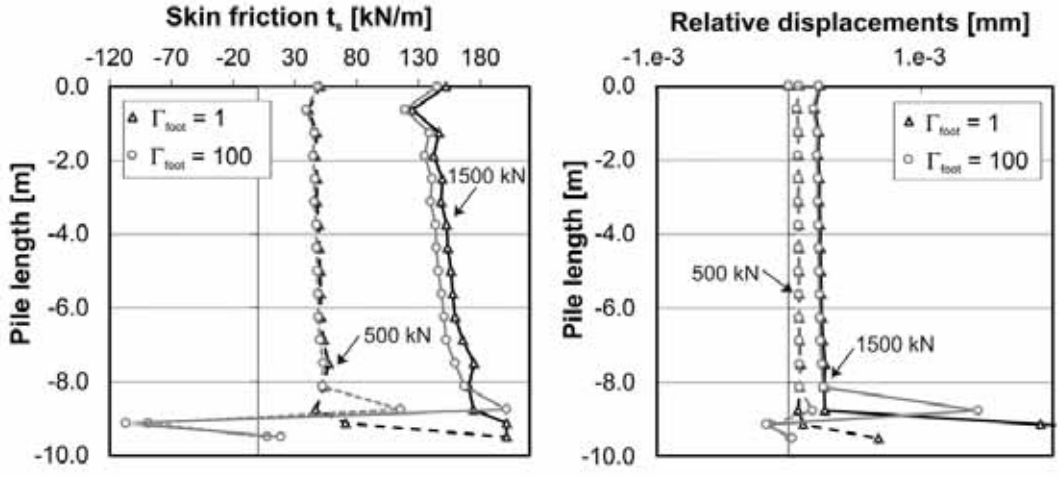

Fig. 43 Influence of K_{foot} on mobilized skin friction t_s

5.3 On the influence of the embedded pile interface stiffnesses

The global stiffness response K_{ep} of an axially-loaded single pile is defined as the sum of the skin resistance R_s plus the base resistance R_b divided by the pile displacements. Equation 72 demonstrates that for a floating pile, the soil displacements u_s should dominate the global stiffness response and the relative displacements u_{rel} are relevant to the mobilization of the pile resistances. As long as the predefined pile resistances are not reached, these relative displacements should not have a big influence on K_{ep}. Of course, the relative displacements are generally not constant along the pile length but depend on the pile stiffness, the load level, the soil stiffness and the pile bearing capacity. For an end-bearing pile, the pile stiffness should control mainly the load-settlement behaviour.

$$K_{ep} = \frac{\int 2 \cdot \pi \cdot t_{s(y)} \cdot dy + F_{foot}}{u_p} = \frac{\int 2 \cdot \pi \cdot t_{s(y)} \cdot dy + F_{foot}}{u_s + u_{p,el} + (u_p - u_s)} \tag{72}$$

$$u_{rel(y)} = u_{p(y)} - u_{s(y)} \tag{73}$$

$$t_{s(y)} = u_{rel(y)} \cdot K_s \tag{74}$$

$$F_{foot} = u_{rel(y=l)} \cdot K_{foot} \tag{75}$$

In principle, the soil stiffness, pile stiffness (relative stiffness), pile diameter and pile length have an effect on the mobilization of the shaft and base resistance. The influence of the pile length is taken into account automatically, because when using high order constitutive models the interface stiffnesses are related to the average stiffness of the allocated element. The diameter of the pile has a linear effect on the foot interface stiffness (Equation 66) but regulates the size of the elastic region.

The geometry of the FEM model studied is shown in Fig. 44. The embedded pile has a diameter of 0.8 m, an effective length of 10.0 m and a Young's modulus (E_p) of 3e7 kPa. No groundwater is modelled and two different homogeneous soil conditions are considered, very dense sand and soft Rotterdam clay. The soil is described with both, the HS and the MC model. The input parameters are given in Tab. 5 to Tab. 8.

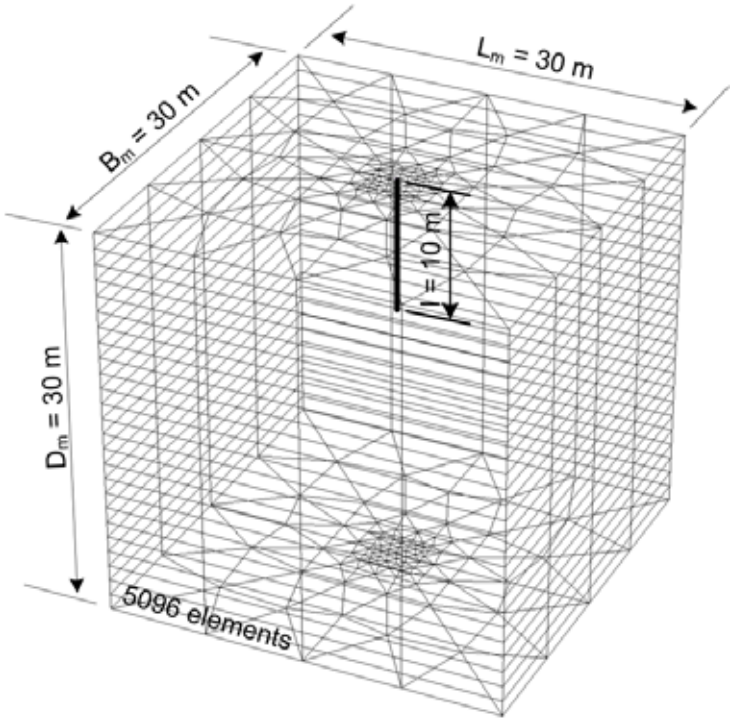

Fig. 44 Finite element model

Tab. 5: Hardening Soil properties of very dense sand

parameter		**value**	**unit**
unit weight above groundwater table	γ_{unsat}	18.0	kN/m^3
unit weight below groundwater table	γ_{sat}	20.0	kN/m^3
reference secant stiffness in drained triaxial test	$E_{50,ref}$	60 000	kPa
reference oedometric stiffness	$E_{oed,ref}$	60 000	kPa
reference unloading/reloading stiffness	$E_{ur,ref}$	180 000	kPa
isotropic Poisson's ratio	ν'_{ur}	0.2	--
reference pressure	p_{ref}	100	kPa
power index for stress dependency of stiffness	m	0.6	--
effective friction angle	φ'	42	°
effective cohesion	c'	0.1	kPa
dilatancy angle	ψ	16	°
K_0 value for normal consolidated conditions	K_0^{nc}	0.331	--

Tab. 6: Hardening Soil properties of soft Rotterdam clay

parameter		**value**	**unit**
unit weight above groundwater table	γ_{unsat}	16.0	kN/m^3
unit weight below groundwater table	γ_{sat}	18.0	kN/m^3
reference secant stiffness in drained triaxial test	$E_{50,ref}$	4 300	kPa
reference oedometric stiffness	$E_{oed,ref}$	1 800	kPa
reference unloading/reloading stiffness	$E_{ur,ref}$	14 400	kPa
isotropic Poisson's ratio	ν'_{ur}	0.2	--
reference pressure	p_{ref}	100	kPa
power index for stress dependency of stiffness	m	0.9	--
effective friction angle	φ'	27	°
effective cohesion	c'	15	kPa
dilatancy angle	ψ	0	°
K_0 value for normal consolidated conditions	K_0^{nc}	0.546	--

Tab. 7: Mohr-Coulomb properties of very dense sand

parameter		**value**	**unit**
unit weight above groundwater table	γ_{unsat}	18.0	kN/m^3
unit weight below groundwater table	γ_{sat}	20.0	kN/m^3
Young's modulus	E	44 600	kPa
Poisson's ratio	ν'	0.30	--
effective friction angle	φ'	42.0	°
effective cohesion	c'	0.1	kPa
dilatancy angle	ψ	0	°
lateral earth pressure coefficient at rest	K_0	0.331	--

Tab. 8: Mohr-Coulomb model properties of soft Rotterdam clay

parameter		**value**	**unit**
unit weight above groundwater table	γ_{unsat}	16.0	kN/m^3
unit weight below groundwater table	γ_{sat}	18.0	kN/m^3
Young's modulus	E	1 340	kPa
Poisson's ratio	ν'	0.30	--
effective friction angle	φ'	27.0	°
effective cohesion	c'	15.0	kPa
dilatancy angle	ψ	0	°
lateral earth pressure coefficient at rest	K_0	0.546	--

5.3.1 Foot interface stiffness

Fig. 40 illustrates that the relative displacements to mobilize the full foot resistance are in the range of 20% of the total pile displacements (for Γ_{foot} = 1), but this value should be much smaller because the displacements beneath the pile base should primarily depend on the compressibility of the soil. As a consequence, the foot interface stiffness defined in the embedded pile formulation is probably too small and should be increased. To find a suitable value for the foot interface stiffness to improve the load-settlement behaviour, some studies are presented in this chapter. The aim is to find a factor for the foot interface that reduces the "additional" settlements necessary to mobilize the base resistance, and on the other hand, to find a value that does not lead to numerical ill conditions (chapter 3.4.2).

Because of the difference of the soil conditions, different ultimate base resistances F_{max} were defined. For the dense sand, F_{max} is 2300 kN, and for the soft Rotterdam clay, F_{max} equals 500 kN. These values are a cautious estimate using Vesic's approach (see chapter 2.2.1). To study the influence of K_{foot} the load transfer via the pile shaft is set to zero.

Fig. 45 shows the influence of the foot interface stiffness on the load-settlement behaviour of the pile, for very dense sand. There is a big influence on the load-settlement behaviour between the standard definition of the base interface stiffness (Γ_{foot} = 1) and an increased spring interface stiffness. Until an increase by a factor of 5, the influence is significant. A further increase of Γ_{foot} from 5 to 500 has a rather small impact on the global stiffness response of the pile.

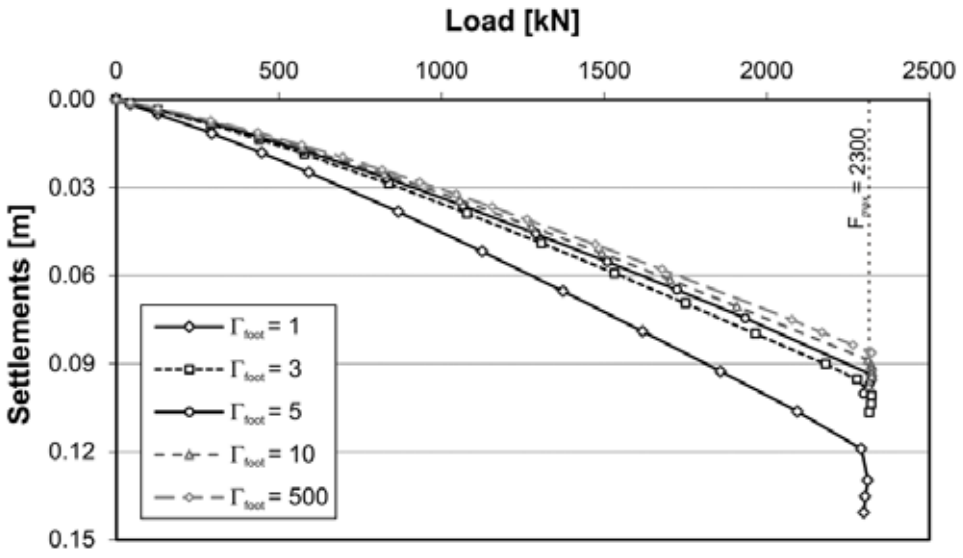

Fig. 45 Influence of Γ_{foot} on the load-settlement behaviour (dense sand; MC)

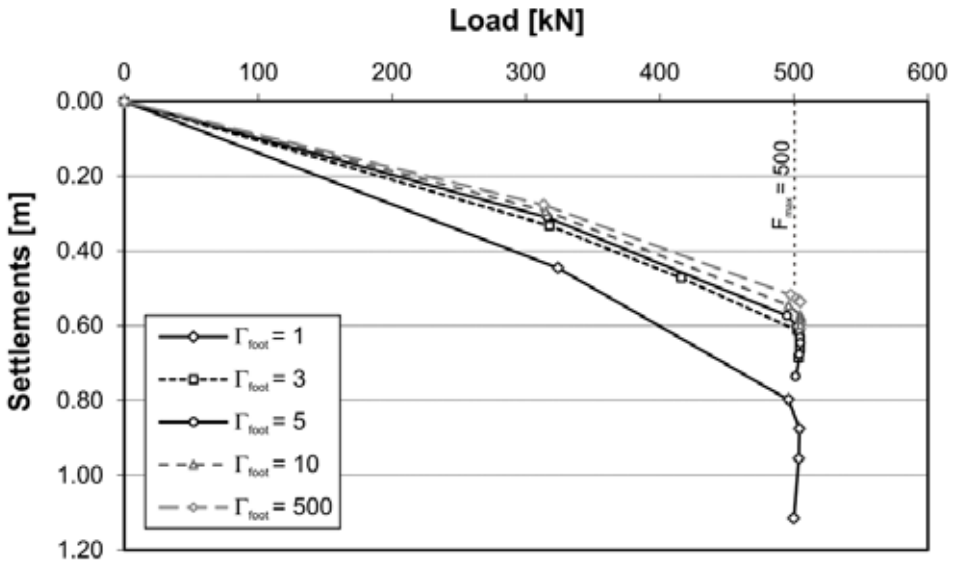

Fig. 46 Influence of Γ_{foot} on the load-settlement behaviour (soft Rotterdam clay; MC)

The unrealistically high value of Γ_{foot} = 500 was chosen to check if numerical instabilities occur once the base interface stiffness is very high. But with the Mohr-Coulomb model, no numerical problems arise. Fig. 46 represents the same results for the soft Rotterdam clay. The settlements are unrealistically high, but the aim of this study was to prove the performance for extreme values of both the strength and stiffness of the surrounding soil.

When using the Hardening Soil model for the surrounding soil, numerical problems were encountered. Fig. 47 shows the load-settlement curves when using the soft Rotterdam clay with a Γ_{foot} value of one for two different loading

procedures. In one analysis, the theoretical failure load is applied in one calculation phase, and in the other, the load is increased stepwise (10/100/300/500/525 kN). With higher values of Γ_{foot}, the numerical instabilities are even more pronounced.

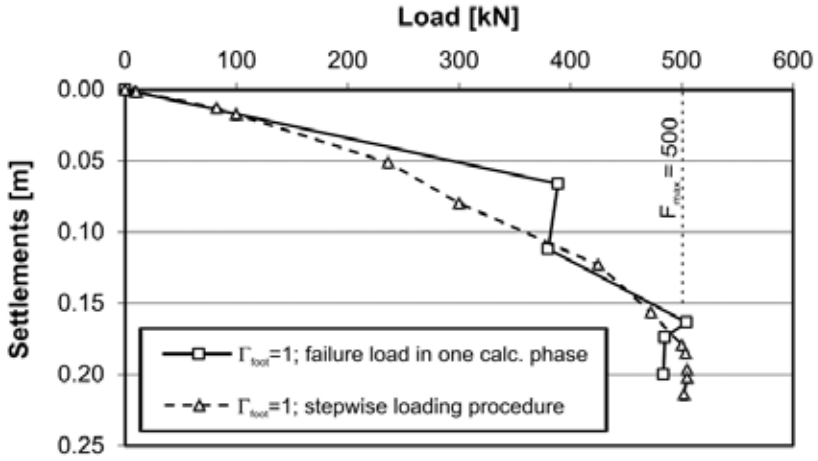

Fig. 47 Influence of loading procedure (soft Rotterdam clay; HS)

A number of calculations showed that a modification of the iterative settings of the FEM program yield much better results. With deactivated arc length control (Memon & Su 2004), less numerical instabilities are found, but the load steps are relatively large and the program is "satisfied" earlier. The reason is most probably related to the global error check, where the weight of the soil is also an inactive load (Equation 76).

$$Global\,error = \frac{\sum \left\| Out\,of\,balance\,nodal\;forces \right\|}{\sum \left\| active\,loads \right\| + CSP \cdot \left\| inactive\,loads \right\|} \tag{76}$$

$$CSP = \frac{total\;elastic\,work}{total\;work} = \int \frac{\Delta\varepsilon \cdot \Delta\sigma}{\Delta\varepsilon \cdot \mathbf{D} \cdot \Delta\varepsilon} \tag{77}$$

$\Delta\varepsilon$ and $\Delta\sigma$ are the incremental strains and the incremental stresses respectively, and *CSP* indicates the amount of plasticity. To force the program to apply the pile head load in more steps, the global tolerated error can be reduced. As a consequence the denominator of Equation 76 is smaller, thus making the result more accurate.

To evaluate the influence of the foot interface stiffness when using the HS model, the tolerated error was reduced to 0.5% and the iteration procedure of the automatic step size algorithm was modified so that the load steps would not increase within one calculation phase. Of course the numerical problems are less

pronounced if skin friction along an embedded pile is allowed, because more plasticity is involved in the calculation and therefore the load steps applied are automatically smaller.

Fig. 48 shows the influence of the foot factor on the load-settlement behaviour for the soft Rotterdam clay. When using the dense sand, the same impact of K_{foot} on K_{ep} was found.

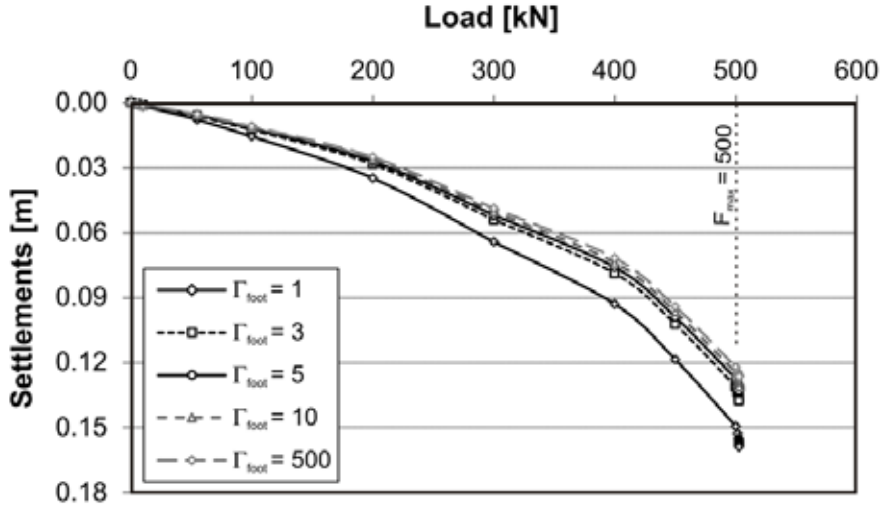

Fig. 48 Influence of Γ_{foot} on the load-settlement behaviour (soft Rotterdam clay; HS)

The results for both materials and both constitutive models show that the interface stiffness is not high enough and the influence on the load-settlement behaviour is intolerably high. When using high order constitutive models, the influence of Γ_{foot} is smaller because K_{foot} is controlled by the unloading/reloading stiffness E_{ur}.

Nonetheless, the foot interface stiffness should be increased by a factor of 5 to 10.

5.3.2 Skin interface stiffnesses

The interaction of an embedded pile along the pile shaft is modelled by means of embedded interfaces (Fig. 30). Three different interface stiffnesses are used, namely an elastic shear interface stiffness K_s, and a normal and tangential interface stiffness K_n and K_t. The definitions of the stiffnesses are given in Equation 64 and 65.

In the first part of this chapter, the influence of the constitutive model on the embedded pile interface stiffness, and as a consequence on the skin friction mobilization, is presented. In the following, the necessity of a stress-dependent interface stiffness will be discussed and the influence of Γ_s, Γ_n, Δ_s and Δ_n on the global load-settlement behaviour is shown. For all calculations in this chapter the base resistance is set to zero. The studies were performed with the medium fine model shown in Fig. 36. The parameters used for the soil and the embedded pile are given in the Tab. 2, Tab. 3 and Tab. 4, but no overconsolidation (*POP*) is taken into account. The ultimate skin traction profile is defined with a constant distribution of skin friction ($T_{top,max} = T_{bot,max} = 201.368$ kN/m); from that follows that the piles have a maximum shaft capacity of 1913 kN.

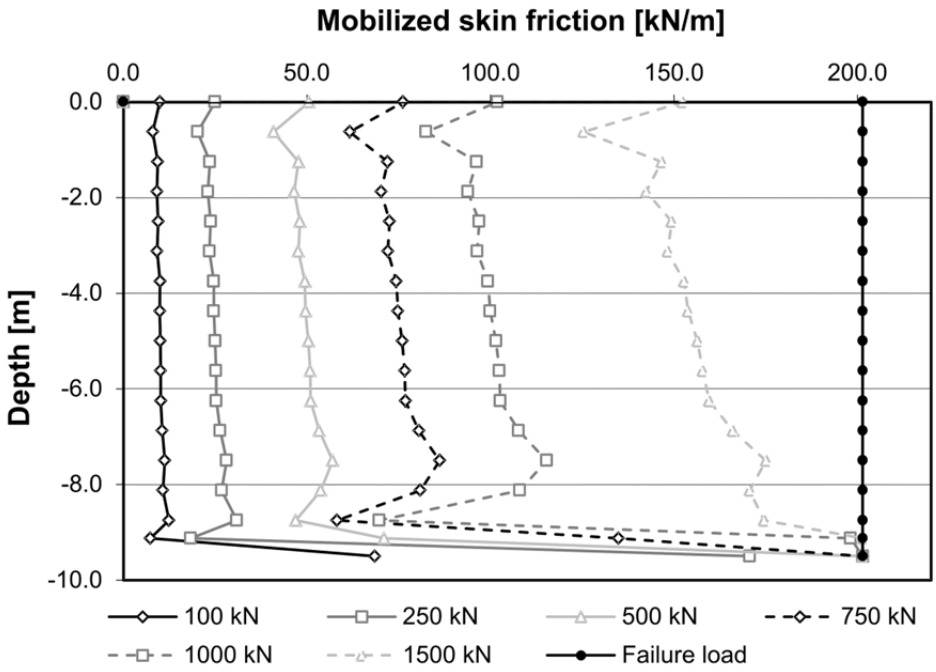

Fig. 49 Skin friction mobilization for different load levels (MC model)

The results for different load levels obtained with the Mohr-Coulomb model are illustrated in the Fig. 49 to Fig. 51. The mobilization of skin friction (Fig. 49) along the pile shaft is almost constant; a linear increase towards the pile base is notable only for load levels close to the failure load. The high skin friction mobilization close to the pile base comes from the influence of the missing foot resistance, which yields large values of relative displacements at the pile tip. The ultimate skin friction profile, or the ultimate bearing capacity, is reached (no premature failure). Due to the constant mobilization of skin friction, the normal force distribution is approximately linear (Fig. 50), and as a result of the high relative stiffness between the pile and surrounding soil the pile settlements are nearly constant (Fig. 51).

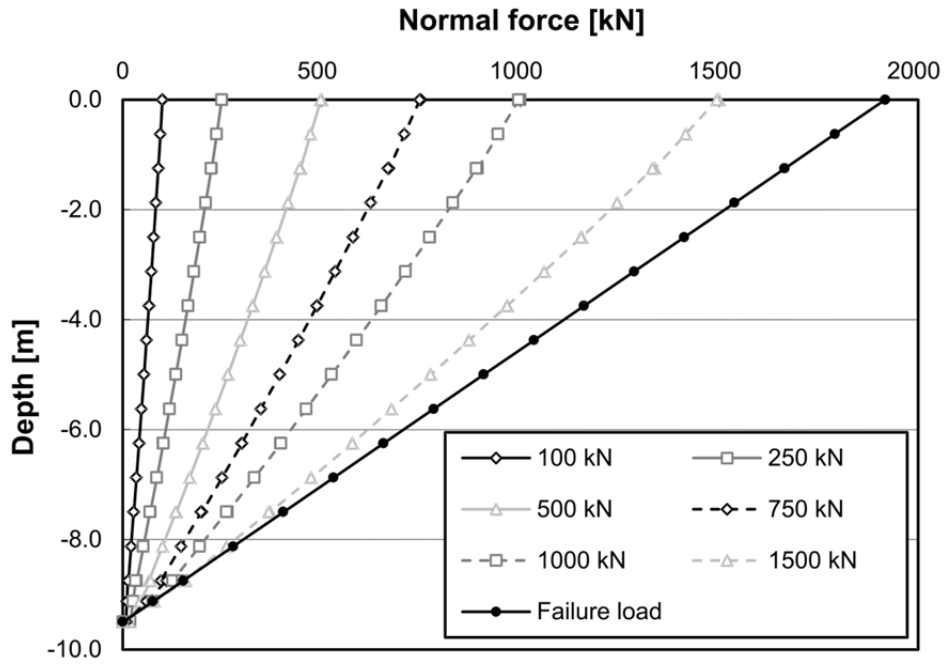

Fig. 50 Normal force distribution for different load levels (MC model)

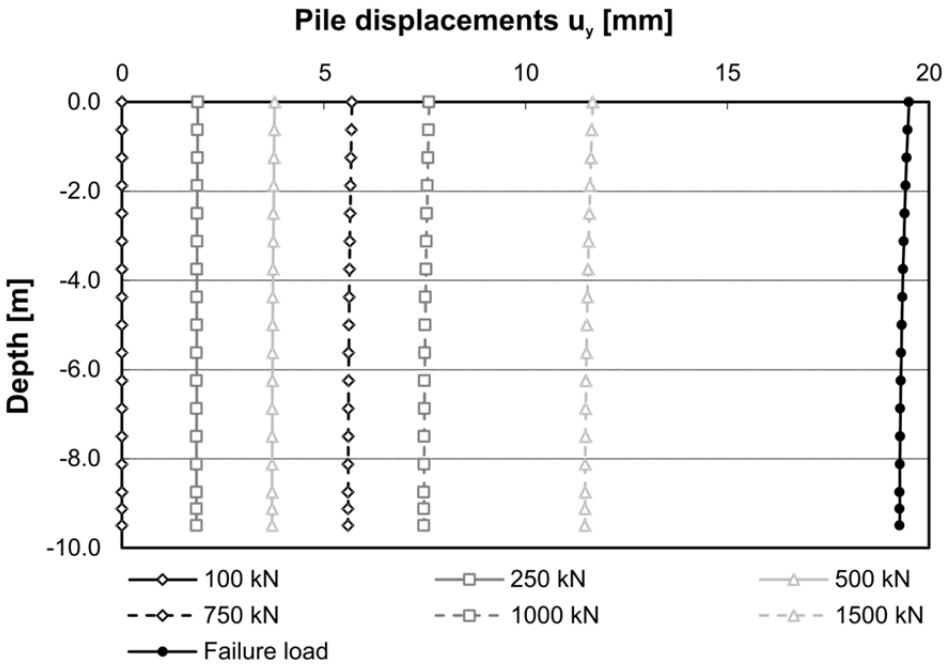

Fig. 51 Vertical pile displacements for different load levels (MC model)

When using the HS model, stress dependency of stiffness is generally taken into account. Equations 63 to 66 show that the stiffness of the surrounding soil affects the embedded interface stiffnesses.

$$E_{ur} = E_{ur,ref} \cdot \left(\frac{c' \cdot \cos\varphi' + \sigma'_3 \cdot \sin\varphi'}{c' \cdot \cos\varphi' + p^{ref} \cdot \sin\varphi'} \right)^m \tag{78}$$

Fig. 52 shows the mobilized skin friction along the pile shaft for the load levels 250 kN and 1000 kN. In one calculation the *m* value, which controls the change of stiffness related to the stress level, is set to zero, and in another calculation the standard *m* value of 0.9 is used.

The mobilization of t_s develops stepwise because K_s is related to the average value of *G* within the allocated soil element. Of course, this is true as long as the relative displacements are almost constant (high relative stiffness). From the inclined shear stress distribution along the pile shaft, it follows that the normal force in the pile has to decrease non-linearly over depth (Fig. 53).

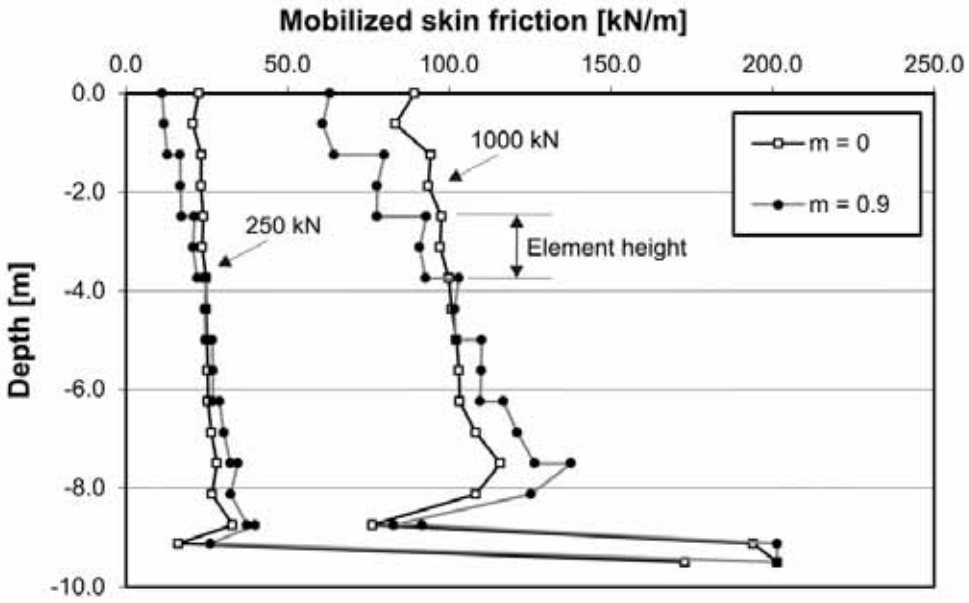

Fig. 52 Skin friction mobilization for different *m*-values (HS model)

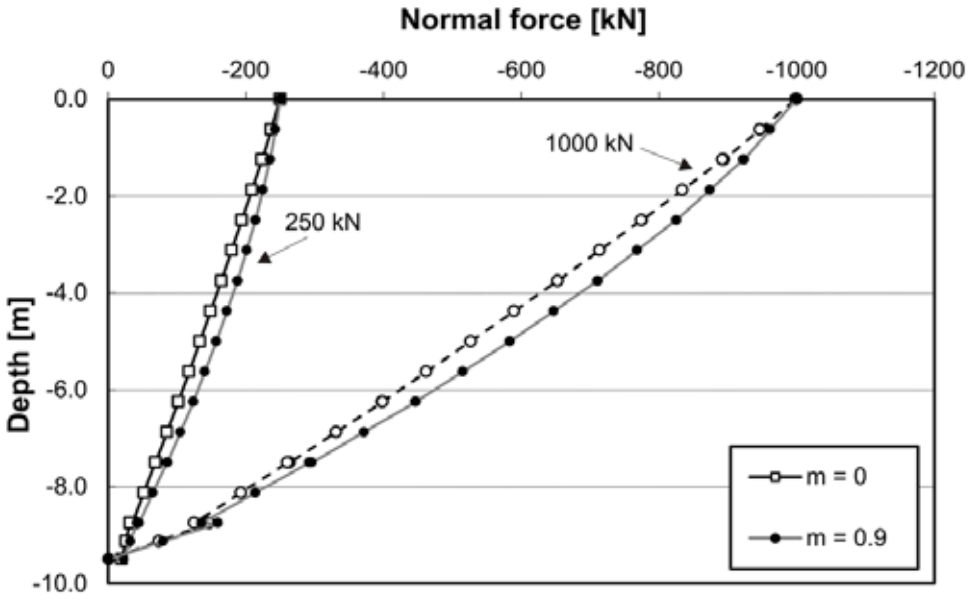

Fig. 53 Normal force in the pile for different *m*-values (HS model)

In the following, the embedded interface stiffnesses are defined independently from the soil stiffness ($\Gamma_s = \Gamma_n = 0$); instead, a constant value of $K_s = \Delta_s = 5e5$ kN/m^2 is used. Fig. 54 illustrates the mobilization of t_s for the load levels 100, 500 and 1000 kN for both the HS and the MC model. The MC model mobilizes the skin friction almost constantly. When using the HS model for the surrounding soil in combination with a constant interface stiffness, no "step-shaped" mobilization is obtained, but the skin friction is significantly inclined. The cause for this behaviour is the stress dependent stiffness of the surrounding soil, which yields a different relative displacement profile over depth (Fig. 55).

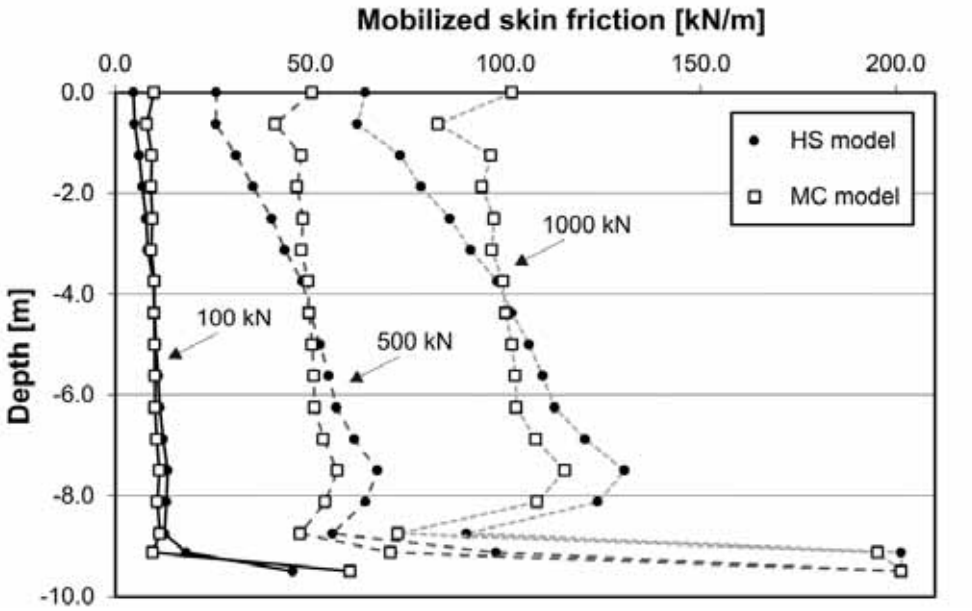

Fig. 54 Skin friction mobilization for different load levels (HS & MC model)

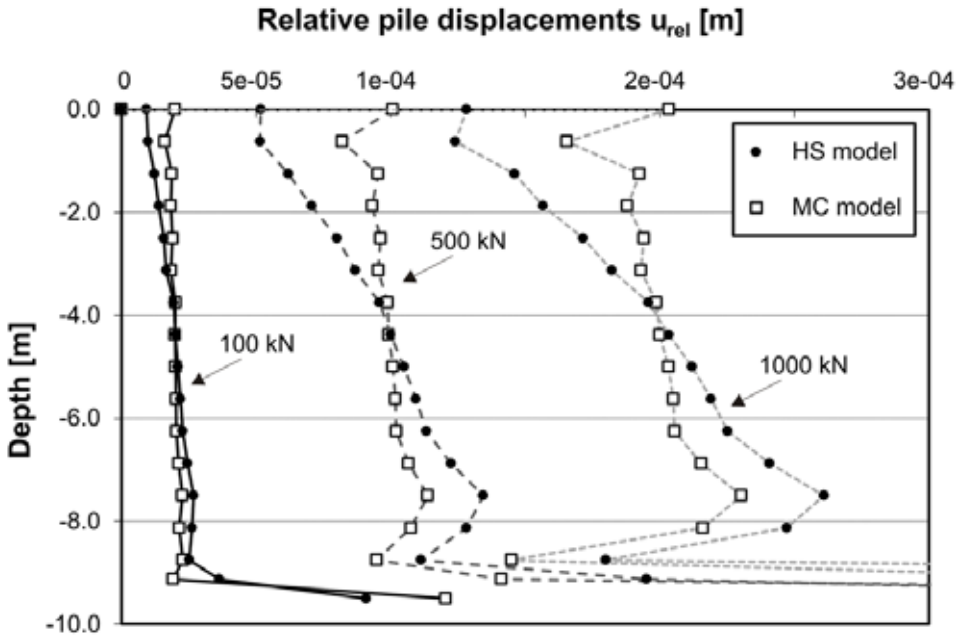

Fig. 55 Relative displacements for different load levels (HS & MC model)

The improved embedded pile concept should allow the calculation of both an accurate distribution of the skin friction and a realistic mobilization of the skin friction. As shown in Fig. 55, the constitutive model of the surrounding soil plays a significant role. Stewart & Kulhawy (1981) presented load transfer functions depending on the soil respectively pile stiffness. Rajapakse (1990) performed elastic analysis of axially-loaded piles in non-homogeneous incompressible elastic soil and presented the influence of relative stiffness, between pile and soil, and the impact of increasing soil stiffness over depth on the skin friction distribution (Fig. 56).

Rajapakse (1990) normalized all results, with $\overline{h}$ representing the slenderness ratio of the pile, $\overline{T}(z)$ the contact traction in vertical resp. z-direction, $\overline{E}$ the stiffness ratio and ρ the degree of non-homogeneity of the soil.

$$\overline{h} = \frac{L}{(D/2)} \tag{79}$$

$$\overline{T}(z) = \frac{T_{z(z)}\,(D/2)^2}{P_0} \tag{80}$$

$$\overline{E} = \frac{E_p}{G_{(z=L)}} \tag{81}$$

$$\rho = \frac{G_{(z=0)}}{G_{(z=L)}} \tag{82}$$

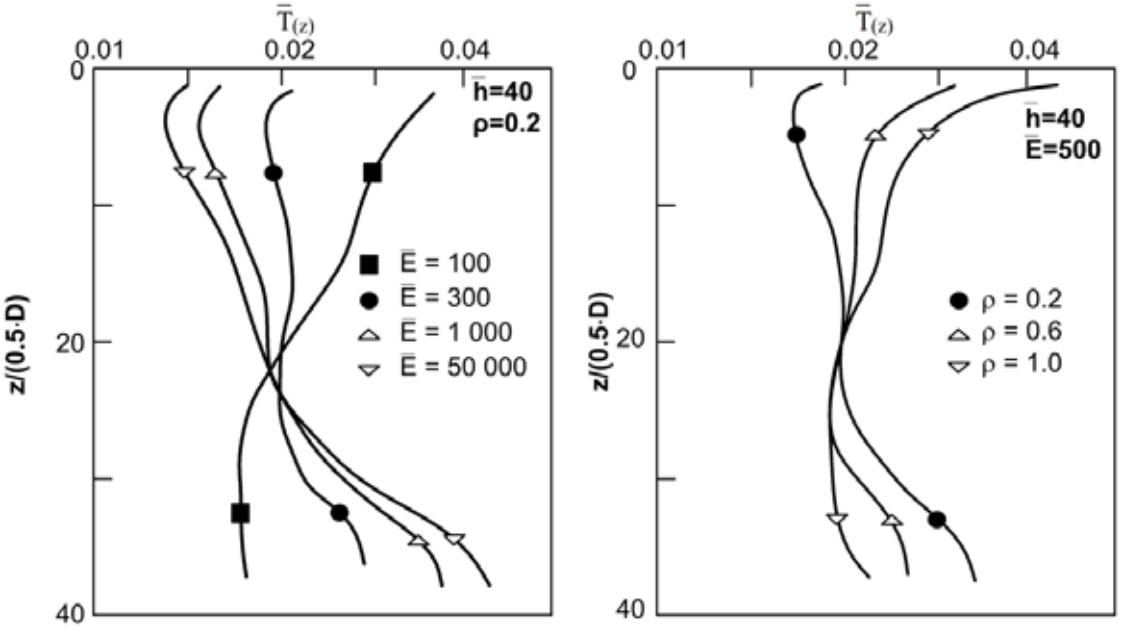

Fig. 56 Contact traction for different stiffness ratios (left) and different degrees of soil non-homogeneity (right) (after Rajapakse 1990)

Rajapakse (1990) concluded that the traction along the pile shaft depends considerably on the slenderness ratio and the degree of soil non-homogeneity. With decreasing stiffness ratios, more skin friction is mobilized at the upper parts of the pile, because the relative displacements along the pile shaft are significantly affected by the elastic deflection of the pile. The increase of stiffness with depth yields an inclined skin friction profile, which increases towards the pile tip.

The open question is if it is necessary to also use a stress dependent stiffness for the embedded pile interfaces. To study the effect of varying interface stiffnesses, a 2D axisymmetric model with the dimensions B_m = 50 m and D_m = 55 m was defined. The axially-loaded pile has a length of 20 m, a diameter of 0.8 m and a stiffness E_p of 3e7 kPa. To obtain reliable stress distributions close to the pile, a relatively fine mesh, consisting of nearly 1100 15 noded elements, is used, and interfaces with a R_{inter} value of 0.7 are defined. The four different scenarios investigated are given in Tab. 9, and Tab. 10 displays the HS parameters used.

Fig. 57 illustrates the skin friction mobilization for different load levels. Scenarios A and C, with stress dependent stiffnesses, behave differently compared to the calculation with a constant stiffness of the interface. A and C mobilize more skin friction at the lower part of the pile and B and D show a

constant mobilization of shear stresses. As a result, more plasticity is also present in the calculations with constant interface stiffness. This is indicated with the length l_{pl} in Fig. 57. The distribution of the ultimate skin friction is similar for all for cases (equation 40). The global load-settlement behaviour of a pile is governed by the stiffness of the soil, therefore case A and B, as well as C and D, yield similar load-settlement curves (Fig. 58). However, due to the different mobilizations, a difference in the first part of the load-settlement curve is obtained: the calculations with stress-dependent interface stiffnesses behave less stiff. Another important effect is that the maximum skin friction is mobilized at a different load level; this shift is related to a higher tip load when modelling the surrounding soil with stress dependent stiffness.

Tab. 9: Different scenarios analysed

	soil	**interface**
scenario A	stress dependent stiffness	stress dependent stiffness
scenario B	stress dependent stiffness	constant stiffness
scenario C	constant stiffness	stress dependent stiffness
scenario D	constant stiffness	constant stiffness

Tab. 10: Hardening Soil properties of dense sand

parameter		**value**	**unit**
unit weight above groundwater table	γ_{unsat}	18.0	kN/m^3
unit weight below groundwater table	γ_{sat}	20.0	kN/m^3
reference secant stiffness in drained triaxial test	$E_{50,ref}$	30 000	kPa
reference oedometric stiffness	$E_{oed,ref}$	30 000	kPa
reference unloading/reloading stiffness	$E_{ur,ref}$	90 000	kPa
isotropic Poisson's ratio	ν'_{ur}	0.2	--
reference pressure	p_{ref}	100	kPa
power index for stress dependency of stiffness	m	0.55/0	--
effective friction angle	φ'	41	°
effective cohesion	c'	0.1	kPa
dilatancy angle	ψ	15	°

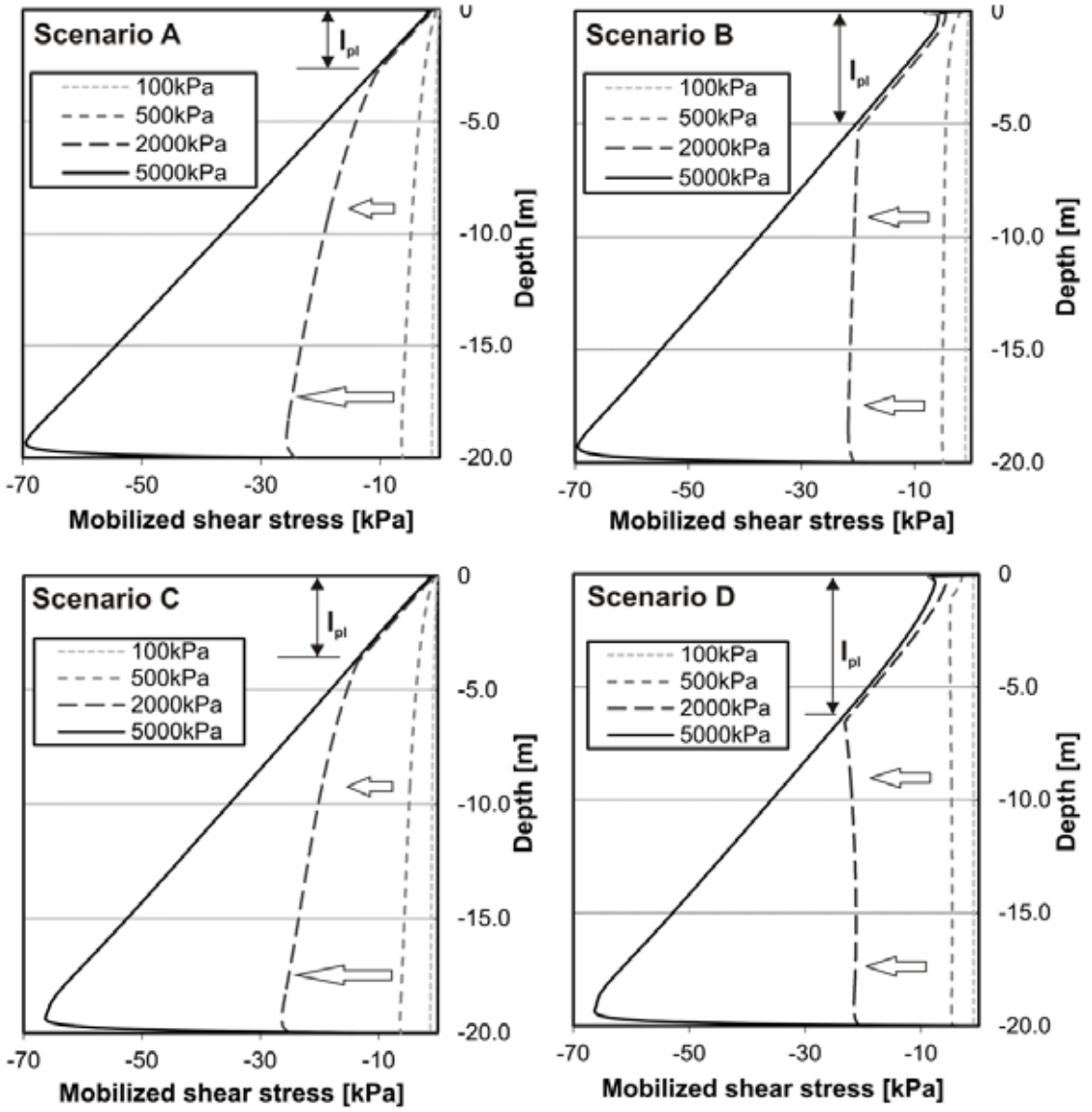

Fig. 57 Shear stress mobilization for different load levels

From this, it can be reasoned that the mobilization of skin friction is mainly related to the stiffness definition of the interface and not to the stiffness definition of the adjacent soil. However, the mesh coarseness also has an influence on the shear stress mobilization.

Further calculations were conducted using different soil types, a loose sand and a soft clay. The obtained results show the same behaviour as the dense sand; furthermore, the influence of the stiffness ratio $\overline{E}$ and calculations with a very soft pile (E_p = 1e5 kPa) were studied. As expected, the influence of the stress dependent interface stiffness is not very pronounced once the pile behaviour is governed by the elastic deformation of the pile.

These studies show that embedded piles, used in combination with stress dependent soil stiffness, have to take the stress dependent interface stiffness into account.

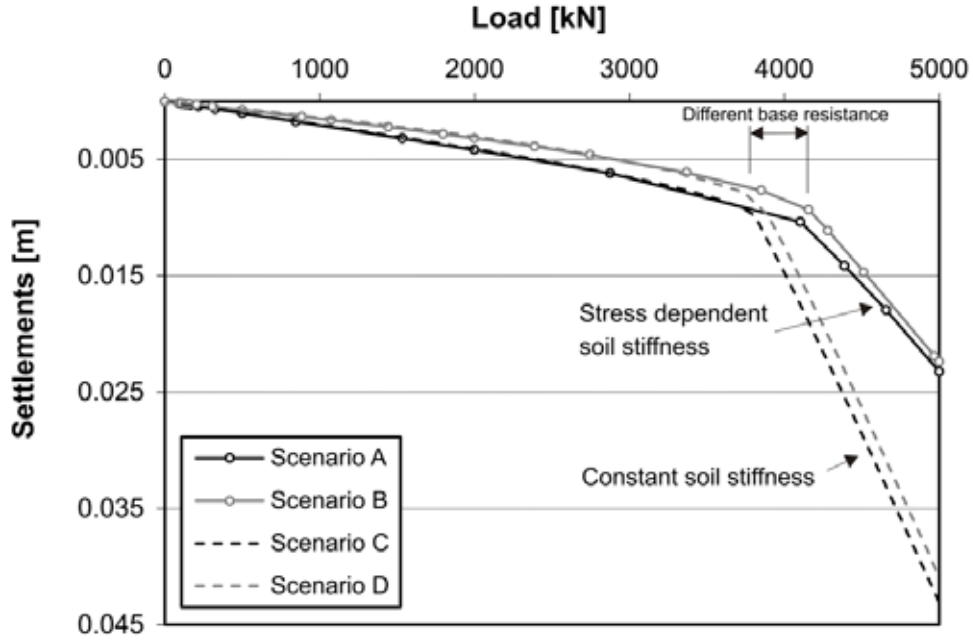

Fig. 58 Load-settlement curves for all four scenarios

To find a suitable value for the skin interface stiffness of an embedded pile and to evaluate the impact of K_s on the load-settlement behaviour, a number of calculations using the MC and the HS model were performed. The finite element model utilized is shown in Fig. 44, and the rather soft Rotterdam clay (Tab. 6 and Tab. 8) and a dense sand (Tab. 5 and Tab. 7) were used again. For these studies, both the skin and the base resistance of the EP were taken into account. The maximum foot resistance F_{max} is defined with 500 kN for the Rotterdam clay and 2300 kN for the dense sand. The foot interface stiffness is increased by a factor Γ_{foot} of 10. The maximum skin resistances are estimated according to DGGT AK 2.1 (2007). A constant ultimate shear stress distribution of 50 kPa for the Rotterdam clay and 100 kPa for the dense sand was defined. Because of the results presented in Fig. 57, the interface stiffness was modified with an Γ_s value and Δ_s set to zero. The normal and tangential interface stiffnesses were not changed ($\Gamma_n = 1$, $\Delta_n = 0$).

Fig. 59 illustrates the results obtained with the Rotterdam clay using the MC model. The normal stress distribution is plotted for 50%, 75% and 100% of the theoretical failure load. Additionally, the mobilized base resistance for 75% of the bearing capacity of the pile is outlined. A modification of the skin interface stiffness does not have an effect on the normal force distribution along the pile, and thus has no influence on the skin friction mobilization. In Fig. 59 only the results for Γ_s of 1 and 10 are plotted. The influence on the mobilization of the

base resistance is very small and the load-settlement curves for different skin friction stiffnesses are more or less identical, but the studies showed that with increasing K_s values, numerical problems (premature failure) arise. With the dense sand the findings are similar, but due to the higher soil stiffness, which affects the embedded interface stiffness, pronounced numerical problems appeared.

Fig. 60 shows the normal force distribution and mobilized base resistance at a load level of 75% for the Rotterdam clay when using the Hardening Soil model. The results confirm that a modification of the skin interface stiffness does not influence the behaviour of an embedded pile.

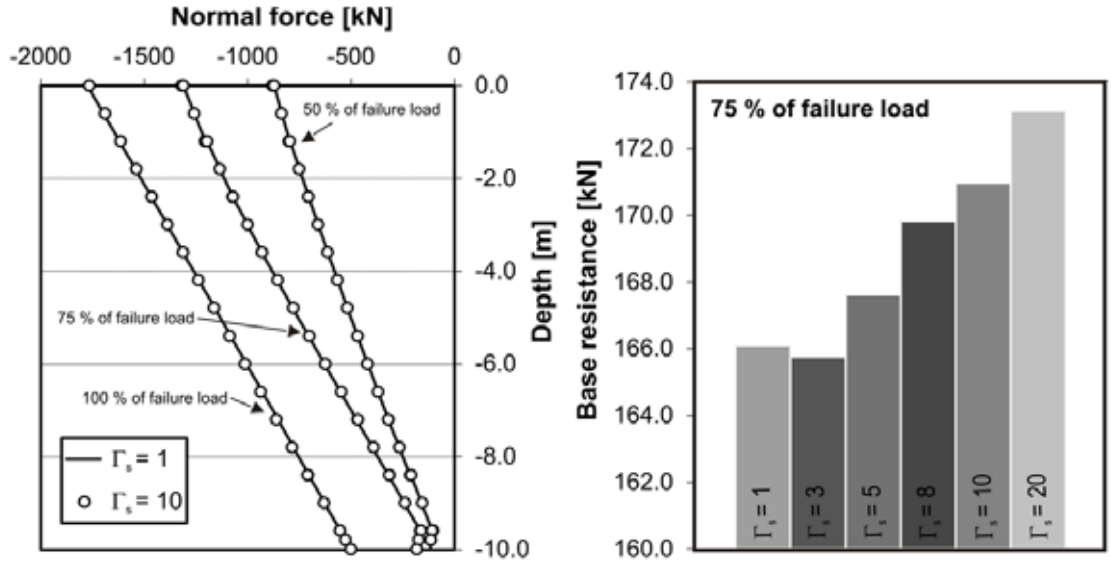

Fig. 59 Normal force distribution (left) and mobilized base resistance (right)- Rotterdam clay (MC model)

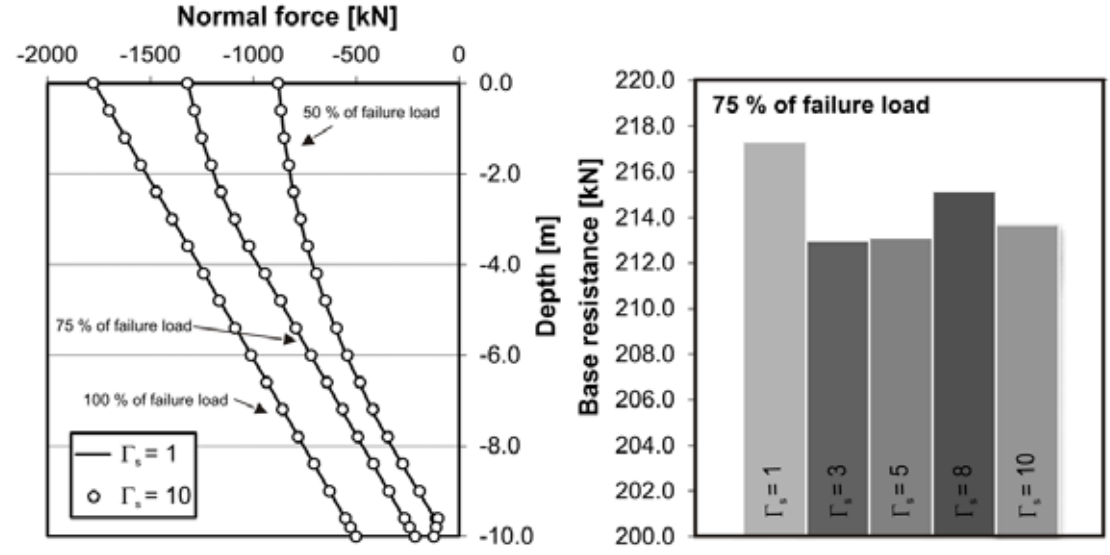

Fig. 60 Normal force distribution (left) and mobilized base resistance (right)- Rotterdam clay (HS model)

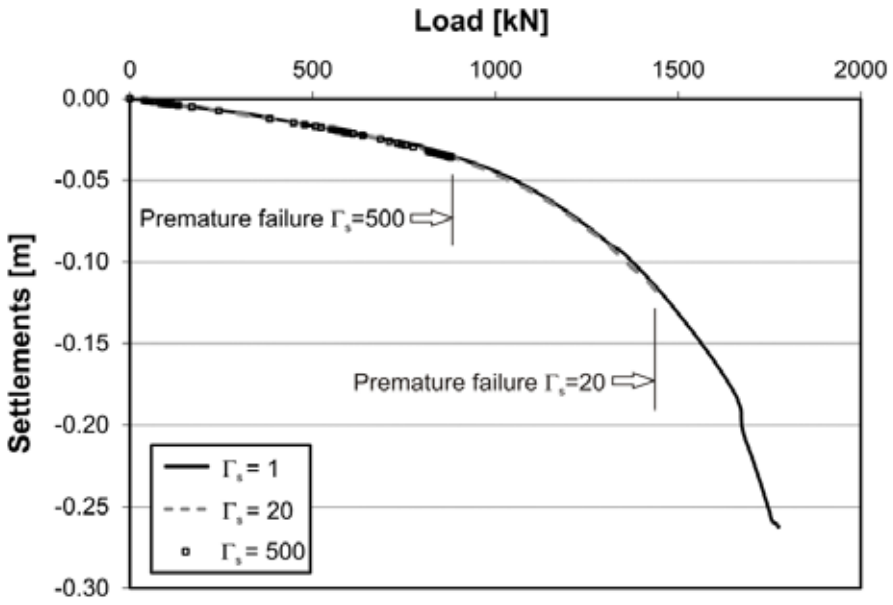

Fig. 61 Load-settlement curves for different interface stiffnesses-Rotterdam clay (HS model)

The global load-settlement behaviour of an axially-loaded pile is not affected by the Γ_s value, but like in the calculations with the MC model, premature failure arises if the skin interface stiffness is increased (Fig. 61). This problem will be discussed in detail in chapter 5.5 of this thesis.

The results of the studies presented, show that the embedded pile interface stiffness should take a stress dependent stiffness into account, but a modification of the default settings ($\Gamma_s = 1$) is not necessary. It is important to remember that it is not possible to model the effect of dilatancy, as explained in chapter 3.5.3, with the embedded pile approach. The influence of ψ has to be considered when defining the ultimate bearing capacity of the embedded pile.

5.4 Influence of vertical mesh coarseness

The normal force distributions illustrated in Fig. 59 and Fig. 60 show an increase close to the pile base, which indicates that (also with an existing foot force) some problems related to the skin friction close to the pile tip occur; in other words, relative displacement u_{rel}. Fig. 62 shows a close-up of the normal force and the mobilized skin friction distribution close to the pile tip. To find the reason for this behaviour and to see the influence of the position of the tip FE node of an embedded pile, a detailed study was performed on the distribution of displacements in the soil and the pile (relative displacements). Due to the fact that the position of the end node of the EP is varied, information regarding the vertical mesh dependency was also obtained. The finite element model has the dimensions $B_m/L_m/D_m$ of 30/30/30 m and consists of roughly 4000 15 noded

wedge elements. The parameters of the embedded pile with an effective length of 10.0 m are given in Tab. 11. This results in a bearing capacity of nearly 3411 KN. The foot interface stiffness is defined with the improved stiffness (I_{foot} = 10). The soil properties are given in Tab. 12.

To realise that the tip node of the embedded pile ends at different positions inside the finite element, the mesh is modified in all calculations (Fig. 63). As a consequence, the pile length remains the same and the different calculations are comparable. The influence of the mesh coarseness, due to the modification of the vertical mesh, can be considered very small. Seven different embedded pile tip node positions were studied (Fig. 63).

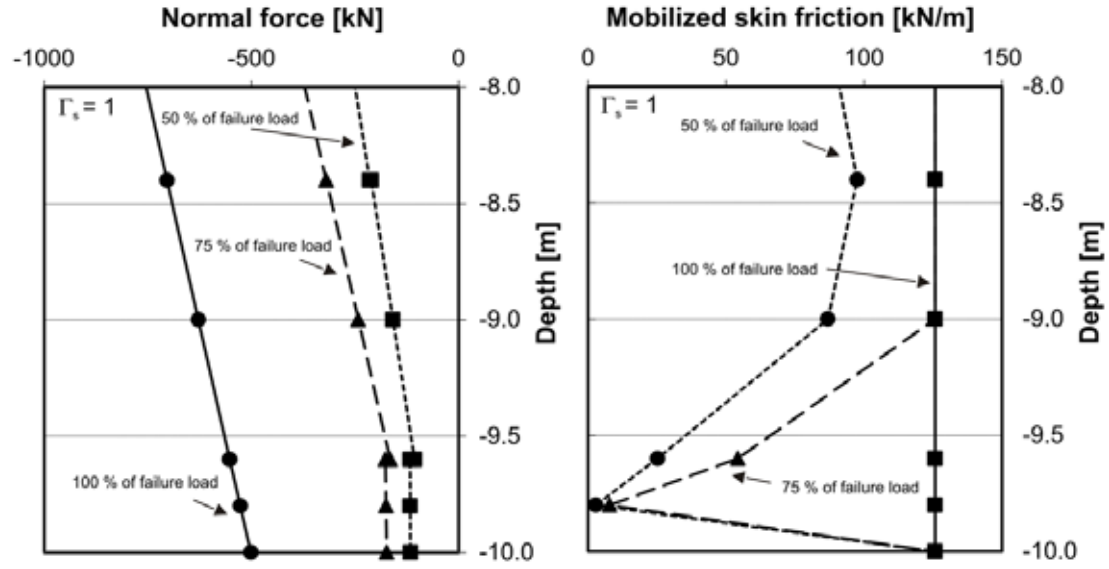

Fig. 62 Normal force distribution (left) and mobilized base resistance (right) close to the pile tip - Rotterdam clay (MC model)

Tab. 11: Input parameters for embedded pile

parameter		**value**	**unit**
Young's modulus	E	3e7	kPa
bulk unit weight	γ	0.0	kN/m^3
diameter	d	0.8	m
skin resistance at pile top	$T_{top,max}$	201.06	kN/m
skin resistance at pile bottom	$T_{bot,max}$	201.06	kN/m
base resistance	F_{foot}	1400	kN

Tab. 12: Mohr-Coulomb model properties of loose sand

parameter		**value**	**unit**
unit weight above groundwater table	γ_{unsat}	18.0	kN/m^3
unit weight below groundwater table	γ_{sat}	20.0	kN/m^3
Young's modulus	E	11 890	kPa
Poisson's ratio	ν'	0.30	--
effective friction angle	φ'	34.0	°
effective cohesion	c'	0.1	kPa
dilatancy angle	ψ	0	°
lateral earth pressure coefficient at rest	K_0	0.441	--

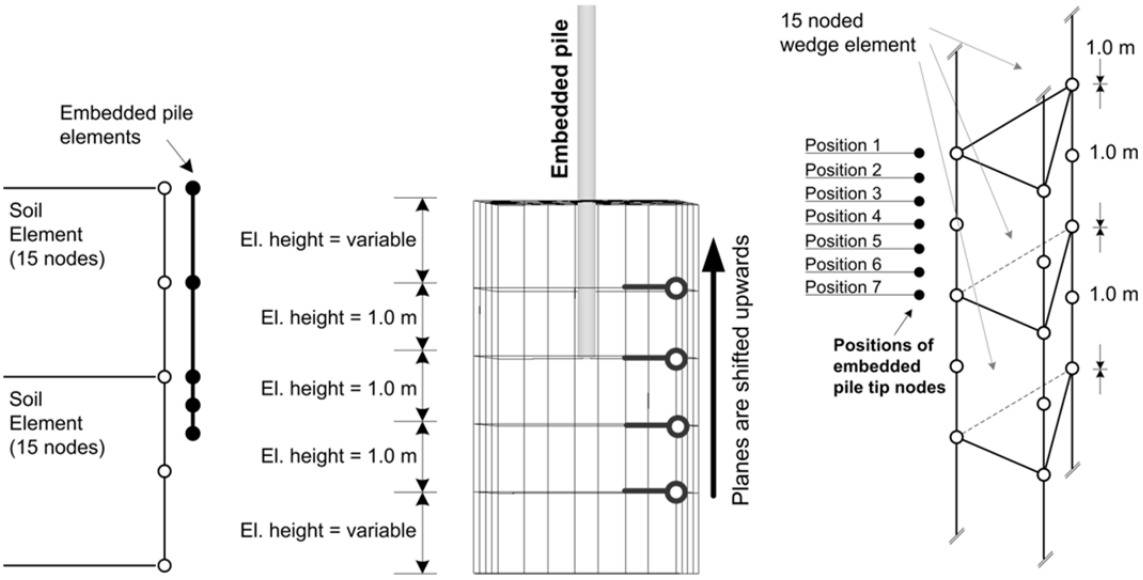

Fig. 63 Schematic representation of EP discretization (left); modelling procedure (middle) and analysed tip node positions (right)

Fig. 64 shows the shear stress and normal force distribution of tip node position 1 for two load levels. Both the normal force and the shear stress distribution do not show any jumps close to the pile base. Also, the computed soil deformations, pile settlements and resulting relative displacements are consistent (Fig. 65).

A jump in the skin friction profile occurs close to the pile tip if pile tip node position 4 is considered (Fig. 66), but the displacements of the soil nodes are smaller than the vertical displacements of the embedded pile.

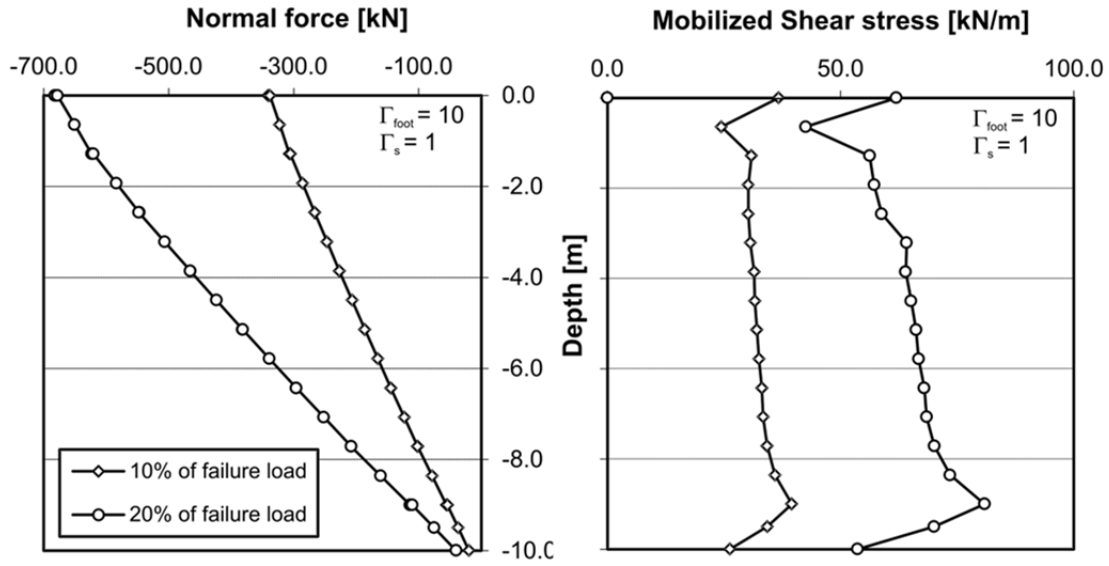

Fig. 64 Normal force and mobilized shear stress for tip node position 1

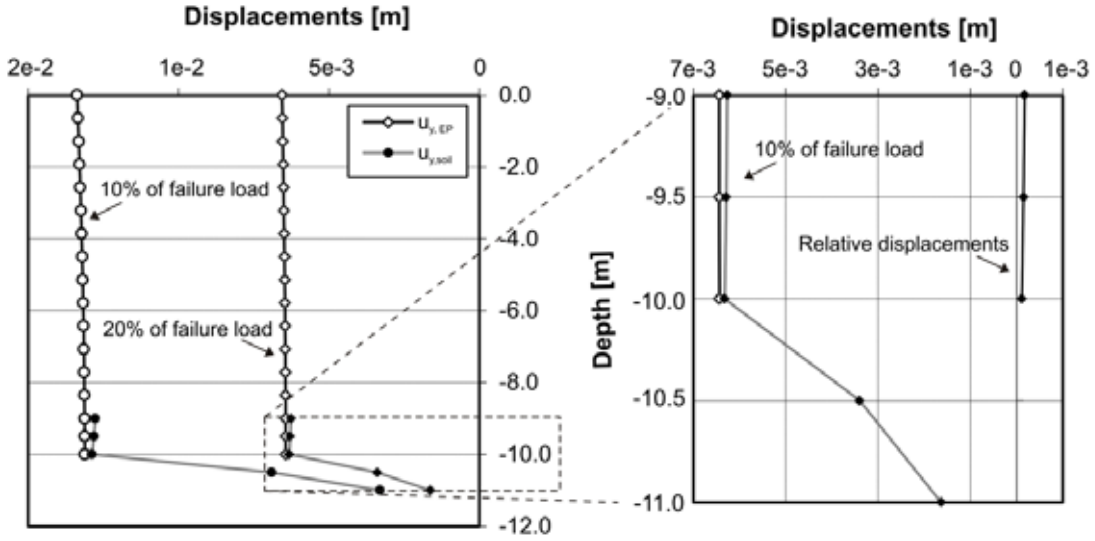

Fig. 65 Soil and pile displacements (left); soil, pile and relative displacements close to the pile tip (right)

The reason for the negative skin friction and negative relative displacements is the evaluation of the displacement field inside the 15 noded wedge elements. The relative displacements $\mathbf{u}_{rel}$ are calculated at the position of the embedded pile nodes, and the displacements of the dedicated virtual soil nodes $\mathbf{u}_s$ are worked out using the nodal displacement values $\mathbf{u}_s^n$ and the matrix $\mathbf{N}_s$, including the shape functions of the solid soil elements (Equation 44). The interpolation functions of a 15 noded wedge element are given in Appendix C. When calculating the virtual soil node displacements for different positions of the embedded pile tip node with a simple *Maple* program, it results in negative relative displacements in some cases.

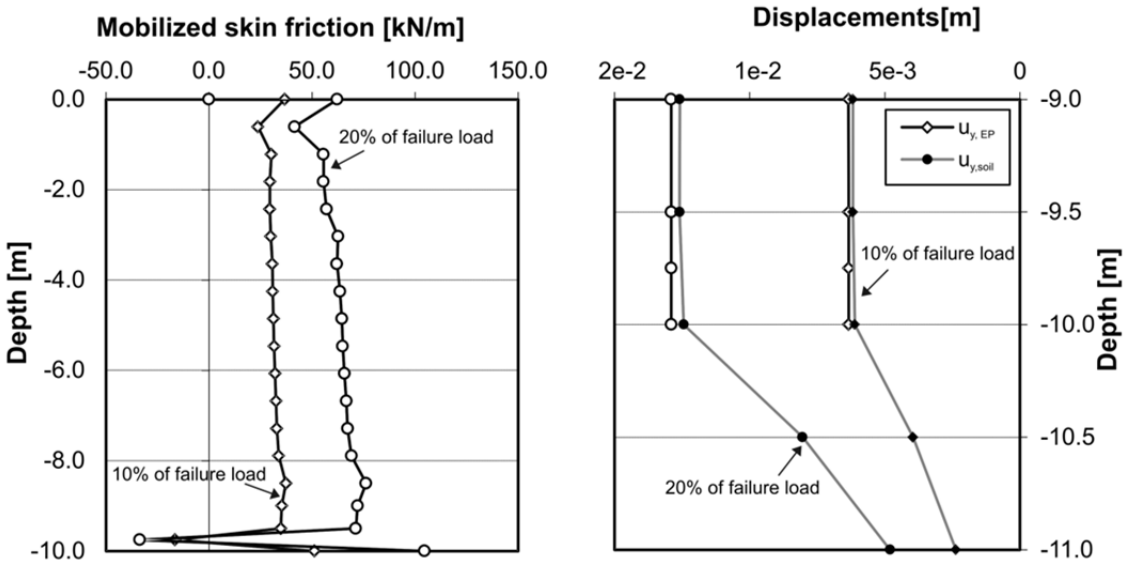

Fig. 66 Normal force and mobilized shear stress for tip node position 4

Fig. 67 shows the relative displacements u_{rel} close to the pile tip for 20% of the failure load. Different distributions of relative displacements are calculated depending on the position of the tip node. Apparently, the behaviour is appropriate only if the embedded pile tip node and a corner node of a 15 noded wedge element correspond. The studies also showed that the minimum relative displacements at the pile tip are obtained once the tip node of the EP coincides with a corner node of the solid soil element.

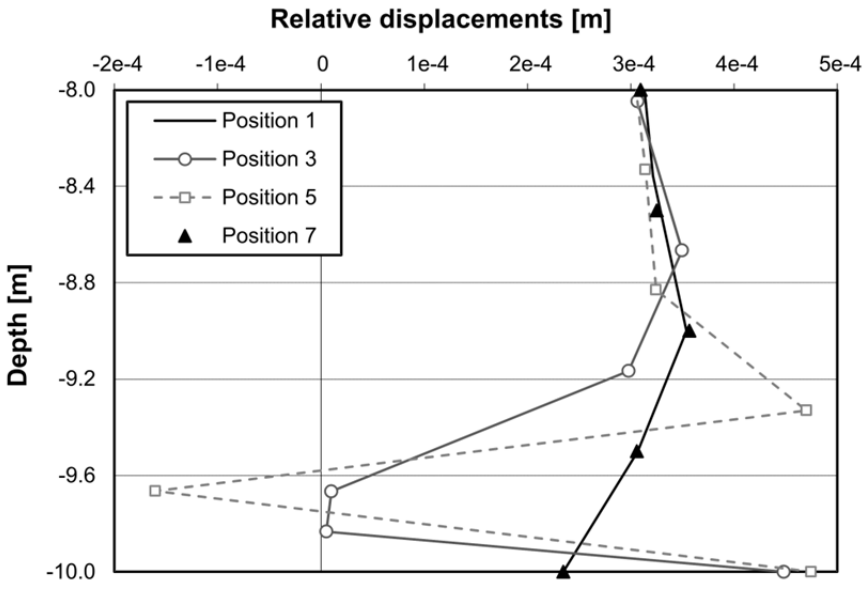

Fig. 67 Relative displacements u_{rel} close to the pile tip

The influence of the foot interface stiffness on embedded pile and soil displacements close to the pile base is shown in Fig. 68. The load level is 20% of the theoretical failure load and the EP tip node position 4 is chosen. The behaviour is similar with a Γ_{foot} factor of 1, but due to the fact that the relative displacements necessary to mobilize the foot resistance are bigger, the EP settlements increase and no negative values of u_{rel} are obtained. Nevertheless, the mobilization of skin friction shows a non-physical jump close to the end of the pile.

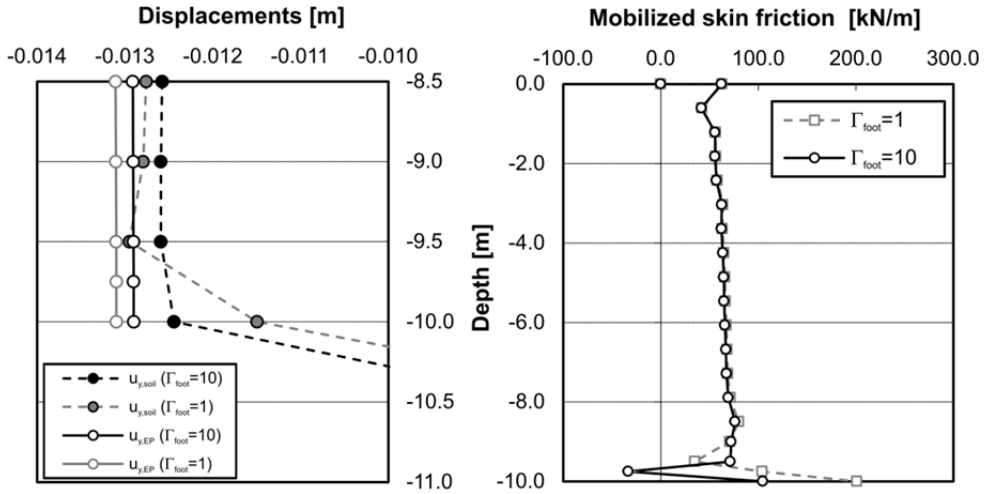

Fig. 68 Influence of Γ_{foot} on displacements close to the pile tip (left) and on the mobilized skin friction (right)

The influence of the EP tip node position on the global load-settlement behaviour is illustrated in Fig. 69. Position 3 yields maximum pile settlements, while position 4 results in minimum pile settlements. A difference of roughly 30% is achieved at a load level of nearly 3400 kN.

The presented results show clearly that both the global behaviour and the mobilization of pile resistance of an embedded pile are different for different positions of the final EP node within a 15 noded wedge element. Hence, it is necessary that the EP tip node corresponds with a corner node of a 15 noded finite element. In PLAXIS 3DF, this is possible by defining a horizontal workplane at the end of the embedded pile. In PLAXIS 3D the mesh generation automatically arranges a corner node of a 10 noded tetrahedral element at the end of the EP.

If a large pile group is considered (with PLAXIS 3DF) and if the difference of pile lengths is small, it is perhaps necessary to model an average pile length in order to avoid very thin finite elements.

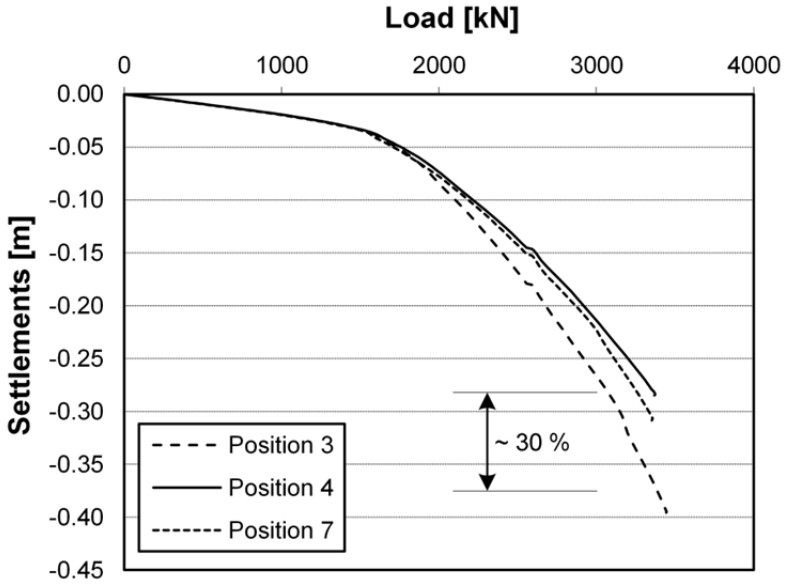

Fig. 69 Global load-settlement behaviour for different EP tip node positions

5.5 Influence of elastic region approach

As shown in chapter 5.2, the mesh coarseness has a significant effect on the load-settlement behaviour of an embedded pile. The influence of the vertical mesh coarseness is related to the position of the EP tip node within the finite element (see chapter 5.4), but additionally, the horizontal mesh coarseness also has a noteworthy impact on the displacements of a single pile. Fig. 70 shows a detail of vertical soil displacements next to the embedded pile. The FE model and the pile and soil parameters are the same as in the last chapter. The EP tip node position 1 is considered.

In reality, the distribution of vertical displacements inside the cross section of a concrete pile is almost constant, and the pile displacements u_p are mainly related to the stiffness and strength of the surrounding soil. Additional displacements inside the elastic region take place when modelling piles with the embedded pile concept, because inside the real pile dimensions only plasticity of the soil is excluded but the stiffness remains unchanged. The amount of vertical displacements obtained inside the elastic region depends on the horizontal mesh coarseness next to the EP, thus finer discretizations yield more deformations.

To get rid of the mesh dependency, the settlements inside the elastic region must be reduced. This can be done with the factors $\Gamma_{G,S}$ and $\Gamma_{G,B}$, which increase the stiffness inside the elastic zone. Hence, the stiffness can be modified in addition to a switch to elastic soil behaviour in all Gauss points.

Fig. 71 shows the effect for a pure friction pile ($\Gamma_{foot} = 0$). The FE model used is illustrated in Fig. 44 and the Hardening Soil input parameters of Rotterdam clay are given in Tab. 6. Because of the relatively fine mesh next to the pile, in combination with an EP pile diameter of 0.8 m, all Gauss points of the allocated finite element are multiplied by $\Gamma_{G,S}$, and as a consequence the skin interface stiffness K_s is also increased by the same factor.

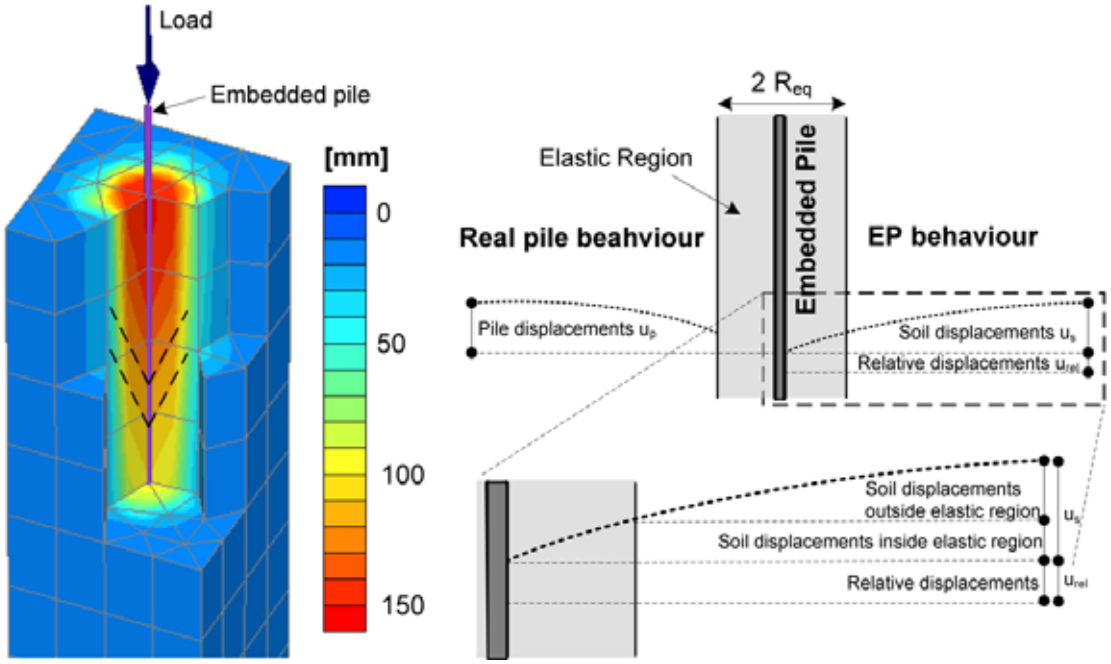

Fig. 70 Detail of vertical soil displacements next to the embedded pile (left) and schematic representation of displacements

The normal force distribution along the embedded pile is more or less independent of the stiffness inside the elastic region, which also points out that the effect on the mobilized shear stresses is relatively small. Nevertheless, the analyses show that with higher interface stiffnesses the skin friction profile is more inclined, which indicates as well that the quantity of K_s has a slight influence on the skin friction mobilization. An increased stiffness inside the elastic region shows a significant effect on the load-settlement behaviour of an axially-loaded pile. Due to the fact that the program deals with a "virtual" volume (see chapter 4.5), a factor $\Gamma_{G,S}$ of 3 already yields an excessive reduction of vertical displacements. But the size and the shape of the modified volume of course depends on the mesh coarseness and the equivalent pile radius R_{eq} of the embedded pile.

When modelling a floating pile where both tip and shaft resistance are present (Fig. 72), the behaviour is very similar. Since the foot interface stiffness has a relevant impact on the vertical displacements of an EP (see chapter 5.3.1), two effects change the load-settlement behaviour, namely the increase of the foot interface stiffness and the modification of the soil stiffness inside the elastic

region. But as shown in Fig. 48, a further increase of Γ_{foot} from 10 to 500 leads to no noteworthy reduction of settlements. Thus the difference in the load-settlement curves can be traced to the increase of stiffness within the elastic region.

One problem recognized during the studies presented in this chapter is that in some circumstances, stresses inside the elastic region decrease. Therefore, the stress flow inside the elastic region and the consequent difficulties are discussed in the following chapter.

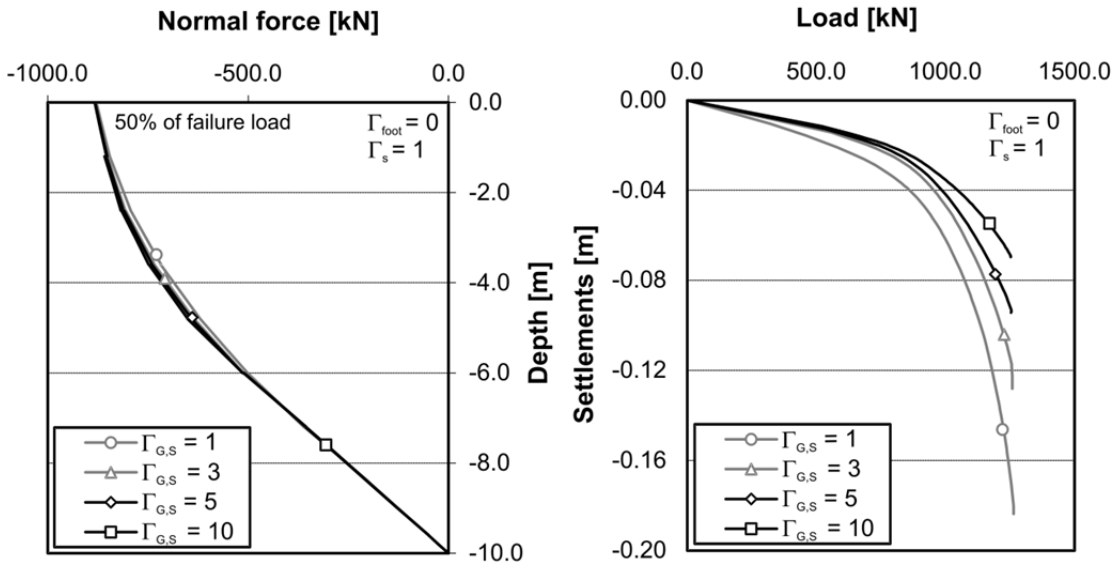

Fig. 71 Normal force distribution (left) and load-settlement curves (right) for different $\Gamma_{G,S}$ factors

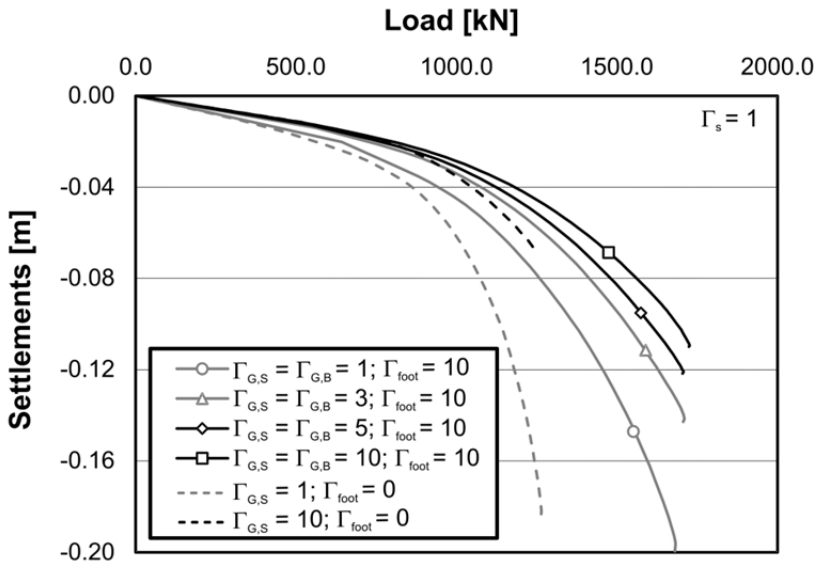

Fig. 72 Load-settlement curves for different $\Gamma_{G,S}$ factors

5.5.1 Stress flow inside the elastic region

To study the stress flow inside the elastic region of the embedded pile concept, a very simple two-dimensional axisymmetric model was used. The model dimensions B_m/D_m are 50/55 m. The pile has a length L of 20.0 m and a "real" radius of 0.4 m. The elastic region and the embedded pile are modelled explicitly. The elastic region has the dimensions of the "real" pile (R_{eq} = 0.4 m), and the EP is defined as a very slender pile in the centre of the elastic region, with a radius of 3.0 cm. The load is applied as a constant distributed load at the top of the small cluster representing the embedded pile. Fig. 73 shows the axisymmetric finite element model.

The soil is described with the Mohr-Coulomb model (Tab. 13) and the stiffness of the elastic region is the same as for the soil. To ensure that no embedded pile deflections occur, the inner cluster (with the radius of 3.0 cm) is defined with a very high Young's modulus of 3e15 kPa. The initial stresses are calculated with the K_0 procedure using a lateral earth pressure coefficient at rest K_0 of 1-sin φ' (Jaky 1944).

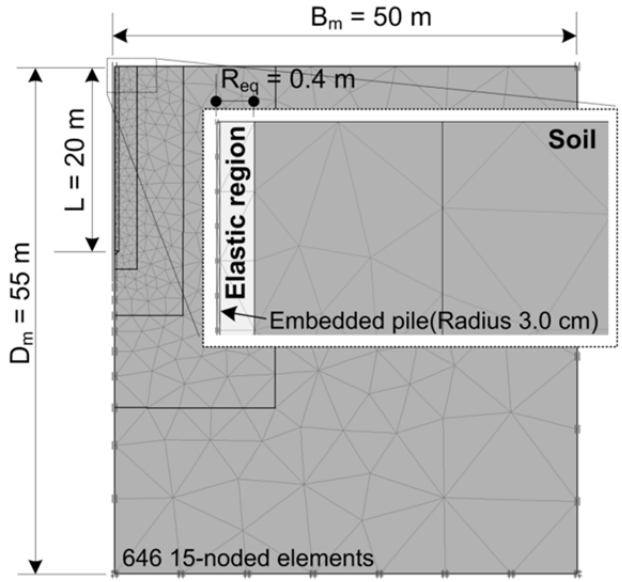

Fig. 73 2D axisymmetric finite element model

Fig. 74 represents the deformed mesh and the rotation of principle stresses (stress flow) inside the elastic region for a pile head load of 500 kN. Due to this rotation, the stresses inside the elastic region vary. Fig. 75 illustrates the stresses next to the embedded pile after the generation of the initial stress filed, with a loading of 500 kN, 1000 kN and 2000 kN. The Cartesian and principle effective stresses are worked out at Gauss points close to the embedded pile shaft.

Tab. 13: Mohr-Coulomb input parameters for medium dense sand

parameter		**value**	**unit**
Young's modulus	E	4e4	kPa
Poisson's ratio	ν'	0.30	--
effective friction angle	φ'	34.0	°
effective cohesion	c'	0.1	kPa
dilatancy angle	ψ	0	°
bulk unit weight of soil	γ	18.0	kN/m^3
lateral earth pressure coefficient at rest	K_0	1-sin φ'	--

At initial conditions, the vertical effective stresses σ'_{yy} and the major principle stresses σ'_1 are equal. The same is true for σ'_{xx} and the minor principle stress σ'_3. Additionally, the vertical and horizontal effective stresses at the pile base are calculated analytically. During loading, the Cartesian effective stresses stay more or less the same but the principle stresses change significantly, with σ'_1 increasing and σ'_3 decreasing. At the load level 2000 kN, the minor principle stress σ'_3 is positive along the entire pile shaft. Of course, if the distance between the embedded pile and the stress points is larger, the minor principle stress is affected at higher loads.

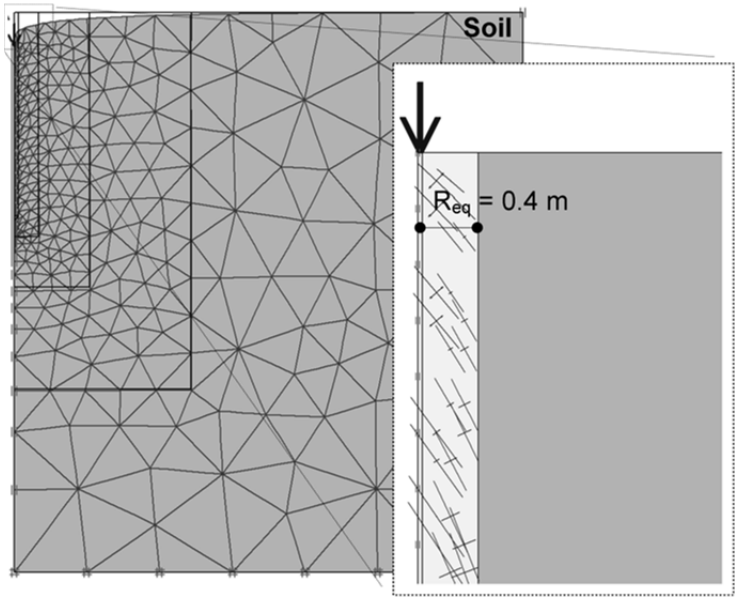

Fig. 74 Deformed mesh and rotation of principle stresses

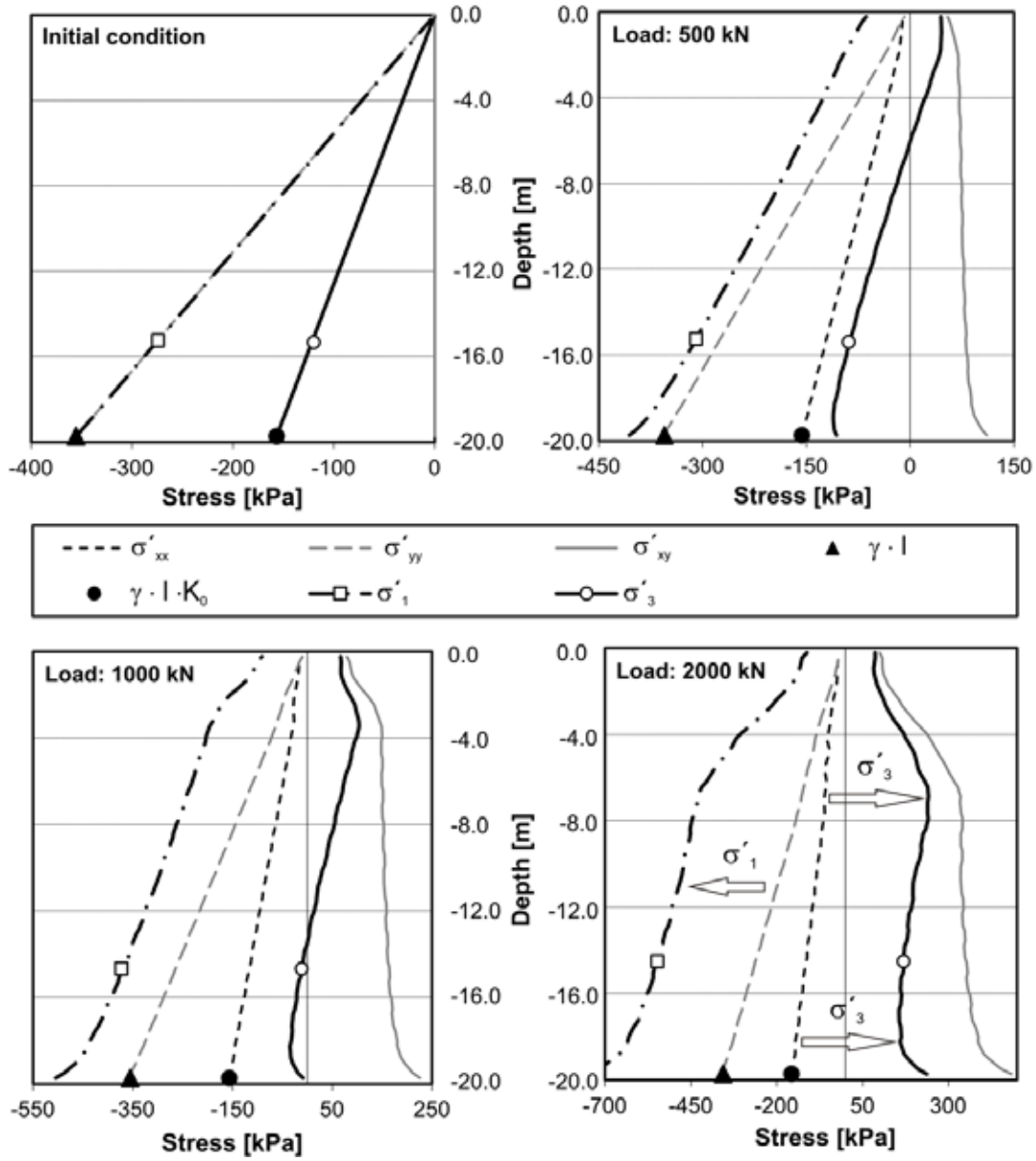

Fig. 75 Variation of stresses inside the elastic region during axial loading

The stress flow within the elastic region seems to be the problem when using embedded piles in combination with high order constitutive models, which take a stress-dependent stiffness into account. Due to the fact that σ'_3 decreases and the stiffness inside the elastic region is related to the minor principle stress (Equation 78), the stiffness within the elastic region is getting very small. The threshold value of E_{ur} is worked out with σ'_3 of 0.

But Fig. 76 indicates that the isotropic effective stress p' does not change much, while the deviatoric stress component q reduces significantly during loading.

$$p' = \frac{\sigma'_{xx} + \sigma'_{yy} + \sigma'_{zz}}{3} \tag{83}$$

$$q = \sqrt{\frac{((\sigma'_{xx}-\sigma'_{yy})^2+(\sigma'_{yy}-\sigma'_{zz})^2+(\sigma'_{zz}-\sigma'_{xx})^2}{2}} \ldots\ldots \sqrt{\frac{6\cdot(\sigma'_{xy}{}^2+\sigma'_{yz}{}^2+\sigma'_{zx}{}^2))}{2}} \quad (84)$$

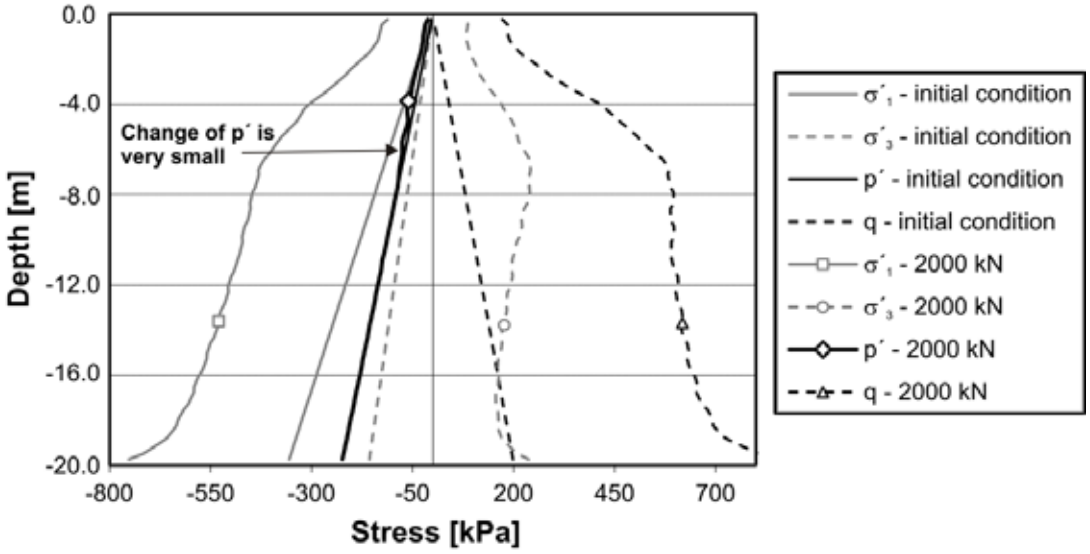

Fig. 76 Variation of effective principle stresses, mean effective stress and deviatoric stress inside the elastic region

5.5.2 Stiffness definition inside the elastic region

The tests presented in the previous chapter showed that the principle stresses inside the elastic region change significantly during axial-loading of a pile. Due to the reduction of σ'_3, the stiffness of the soil reduces if, for example, the HS model is used, and displacements inside the elastic region also occur. At higher load levels numerical problems, like premature failure, arise as well.

Because of the averaging procedure for the definition of the embedded pile interface stiffnesses (see chapter 4.4), K_s, K_n, K_t, and K_{foot} are also affected. But numerical tests with the HS model using different m values and different embedded interface stiffnesses indicated that the problem is rather related to the stress dependency of stiffness inside the elastic region (solid elements) instead of to a reduction of the embedded pile interface stiffnesses. With low m values, the reduction of σ'_3 is much smaller, because the term of Equation 78 (which takes the stress dependency of stiffness into account) does not have a big influence.

However, without stress-dependent stiffness of both the soil inside the elastic region and the embedded interface stiffness, the mobilization of skin friction is not realistic (chapter 5.3.2).

But Fig. 76 demonstrates that the mean effective stress p' does not change significantly. Thus, the use of p' for the definition of the stiffness inside the elastic region ($E_{el.R}$) could improve the behaviour of embedded piles. The problem with this approach is that if the $E_{el.R}$ is related to p', different stiffnesses are present inside the elastic region and in the surrounding soil after the generation of the initial stress field, which is not sustainable. Hence, a correction factor $\Gamma_{el.R}$ must be introduced which compensates the difference. If the stiffness E_{ur} outside the elastic region is equated with $E_{el.R}$, which must be true for the initial conditions, $\Gamma_{el.R}$ can be worked out easily. The $\Gamma_{el.R}$ factor is in the range of 0.5 to 0.75 for normally consolidated and slightly overconsolidated soils with K_0 values between 0.25 and 2.0.

$$E_{el.R} = E_{ur,ref} \cdot \left(\frac{c' \cdot \cos\varphi' + p' \cdot \sin\varphi' \cdot \Gamma_{el.R}}{c' \cdot \cos\varphi' + p^{ref} \cdot \sin\varphi'} \right)^m \tag{85}$$

$$E_{ur} = E_{el.R} \rightarrow \Gamma_{el.R} = \frac{\sigma'_3}{p'} \tag{86}$$

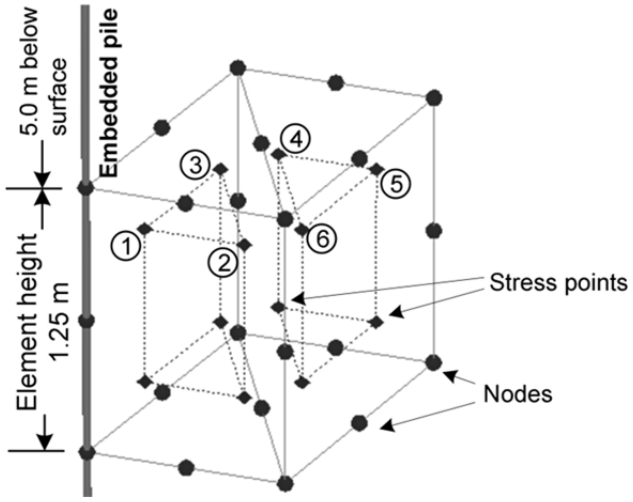

Fig. 77 Finite elements next to the embedded pile

Fig. 77 shows two 15 noded finite elements next to an embedded pile and Tab. 14 and Tab. 15 display the stiffnesses of the six highlighted stress points for different vertical loads. The finite element model used is illustrated in Fig. 36 and

consists of 4556 elements. The groundwater level is 3.5 m below the surface. The Hardening Soil parameters for the soil are given in Tab. 16.

When using the standard definition of stiffness inside the elastic region, $E_{el.R}$ reduces with increasing load level. The closest Gauss point degrades at a load level of 500 kN to a threshold value of 2931 kPa. When using p' in combination with $\Gamma_{el.R}$ as reference stress, the stiffness increases slightly during loading. At a vertical load of 1500 kN, the stiffness inside the elastic region is about 25% higher compared to the initial stiffness. But in the author's opinion, this change of stiffness can be classified as insignificant. Furthermore the distance of the Gauss point to the EP is of minor importance.

Tab. 14: Stiffness for different load levels – reference stress σ'_3

stress point	**distance from EP [m]**	**stiffness $E_{el.R}$ [kPa]**		
		100 kN	**500 kN**	**1500 kN**
1	0.16	25 831	2 931	2 931
2	0.44	27 634	26 127	21 987
3	0.42	27 633	26 218	23 473
4	0.59	27 618	26 353	21 790
5	0.82	27 669	27 508	25 555
6	0.58	27 615	26 303	20 736

Tab. 15: Stiffness for different load levels – reference stress p'

stress point	**distance from EP [m]**	**stiffness $E_{el.R}$ [kPa]**		
		100 kN	**500 kN**	**1500 kN**
1	0.16	27 728	28 609	34 357
2	0.44	27 761	28 745	34 854
3	0.42	27 729	28 627	34 304
4	0.59	27 706	28 502	34 536
5	0.82	27 707	28 508	34 523
6	0.58	27 669	27 695	22 682

Tab. 16: Properties of loose sand (HS)

parameter		**value**	**unit**
unit weight above groundwater table	γ_{unsat}	18.0	kN/m^3
unit weight below groundwater table	γ_{sat}	20.0	kN/m^3
reference secant stiffness in drained triaxial test	$E_{50,ref}$	12 000	kPa
reference oedometric stiffness	$E_{oed,ref}$	16 000	kPa
reference unloading/reloading stiffness	$E_{ur,ref}$	60 000	kPa
isotropic Poisson's ratio	ν'_{ur}	0.2	--
reference pressure	p_{ref}	100	kPa
power index for stress dependency of stiffness	m	0.75	--
effective friction angle	φ'	34	°
effective cohesion	c'	0.1	kPa
dilatancy angle	ψ	0	°
K_0 value for normal consolidated conditions	K_0^{nc}	1-sinφ'	--

Fig. 78 illustrates the contour lines of the current stiffness E_{ur} for the standard definition of the elastic region and for the case where $E_{el.R}$ is related to p'. Fig. 79 shows the distribution of $E_{el.R}$ close to the EP along the entire pile length. The considered load level is 500 kN. When using σ'_3 as reference stress at a load level of 500 kN, the stiffness next to the EP is reduced along the entire pile to the threshold value. If p' is used instead of the minor effective principle stress, no relevant change of stiffness inside the elastic region occurs (at a load of 500 kN). A notable increase of $E_{el.R}$ takes place solely at very high loads. However, this does not change the global behaviour of an axially-loaded pile. The effect on horizontally-loaded piles is shown in chapter 6.2.

The analyses showed that the stress flow inside the elastic region (the previous chapter) is more or less independent of the reference stress used for the stiffness definition inside the elastic region.

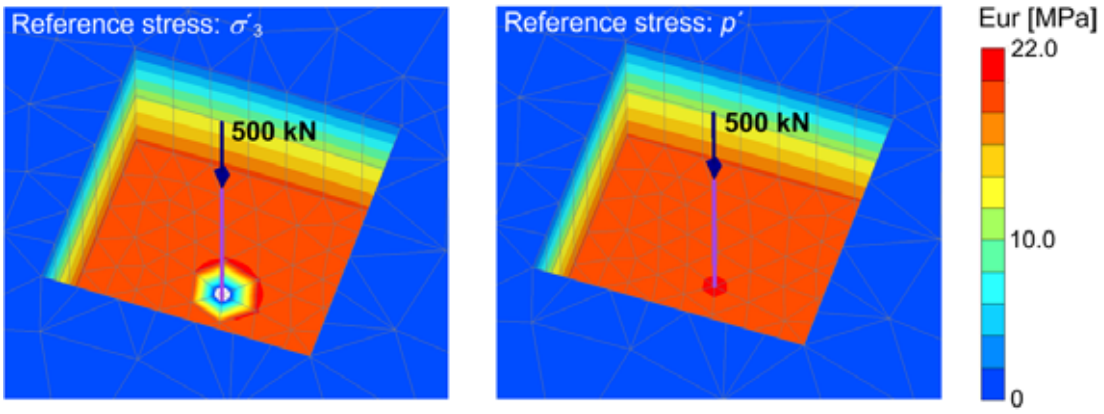

Fig. 78 Influence of reference stress on the stiffness inside the elastic region

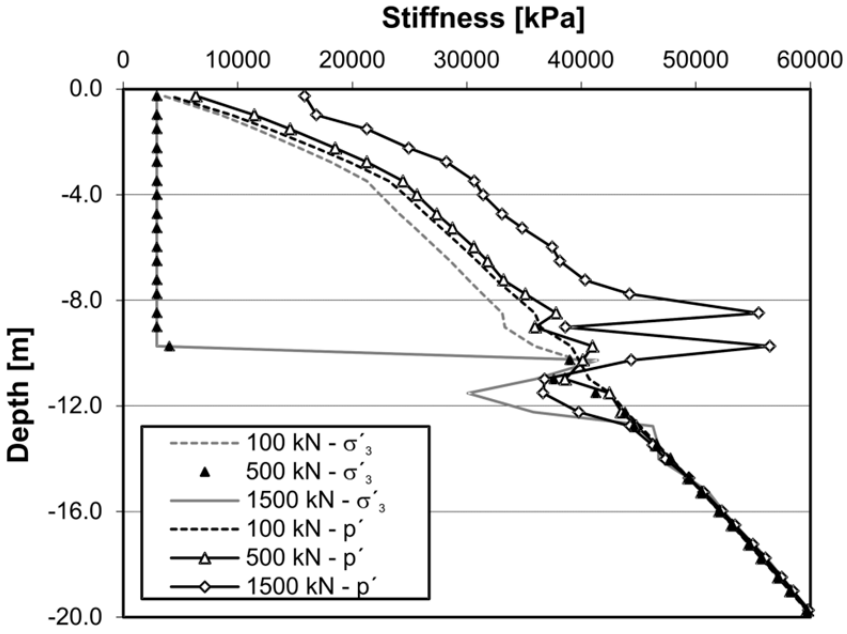

Fig. 79 Stiffness next to an EP

The effect of the mesh coarseness on the shape of the virtual volume (elastic region) is studied in the following. Two additional mesh discretizations (coarse and fine mesh) are investigated (Fig. 80). Fig. 81 shows the stiffnesses present at the Gauss points next to the EP. With the coarse discretization, the standard and new approach uses the same stiffnesses. This is because no stress points are inside the elastic region of the embedded pile, thus no stiffnesses are modified. Also interesting is that the stiffnesses change less when increasing the load. This indicates that the distance of the Gauss points to the embedded pile has a significant effect on the stiffness decrease. When using a very fine mesh in combination with the reference stress σ'_3, the stiffness decreases already at very low load levels to a threshold value. Fig. 82 illustrates the contour lines of current stiffness for the fine mesh and a load level of 500 kN. The horizontal

cross section is 3,2 m below the ground surface and the dimension of the real pile is highlighted. With the improved approach, an approximately constant and unchanged stiffness is acting inside the virtual volume. Hence the numerical displacements inside the elastic region (see Fig. 70) are much smaller and a more realistic load-settlement behaviour can be obtained.

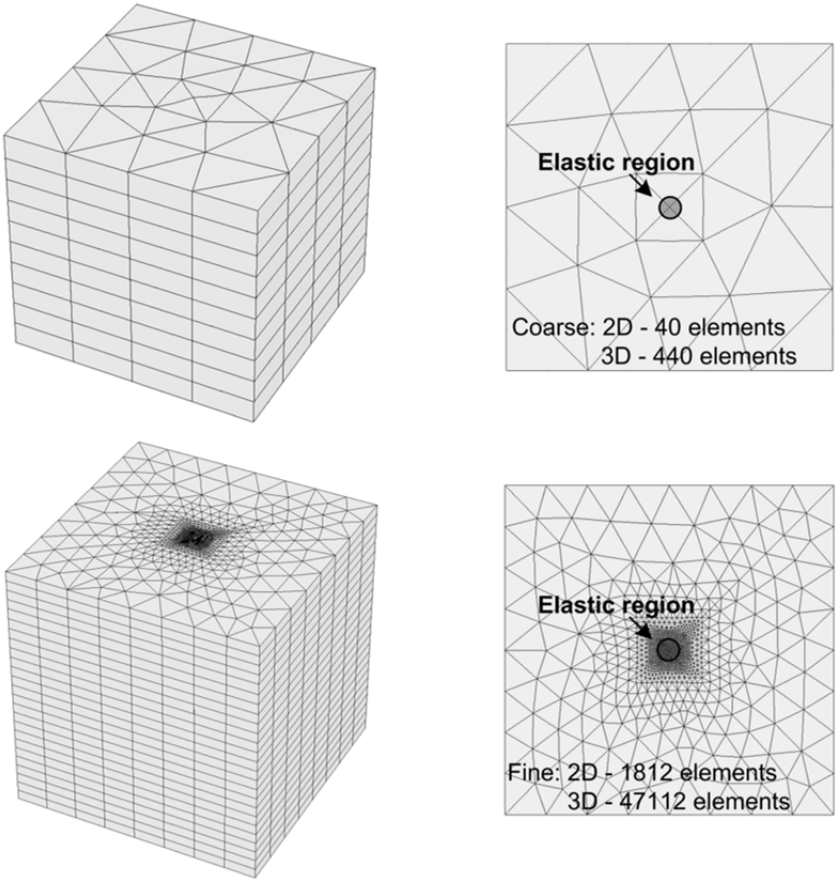

Fig. 80 Coarse and fine mesh discretization

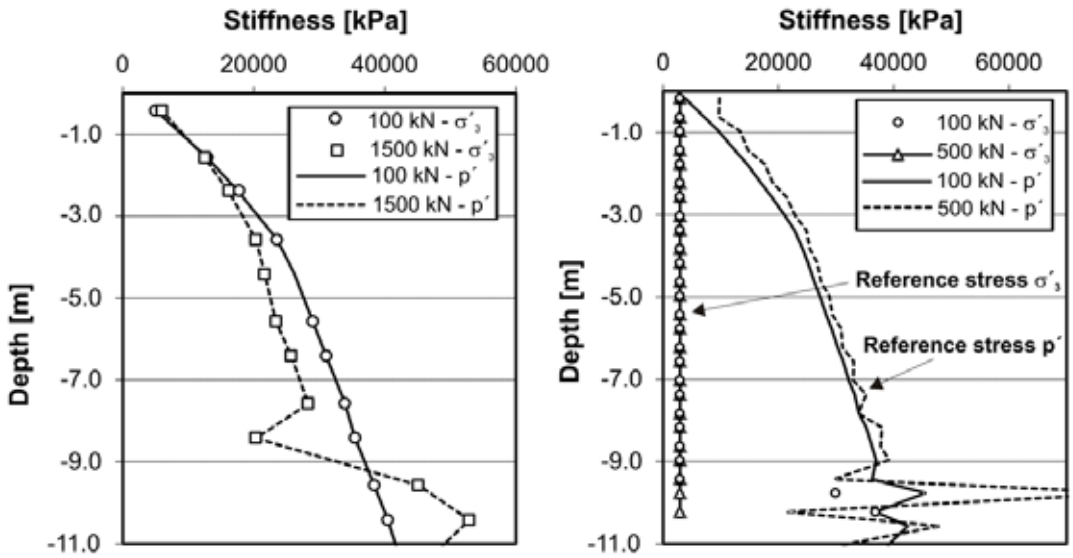

Fig. 81 Stiffness next to an EP for a coarse (left) and a fine mesh (right)

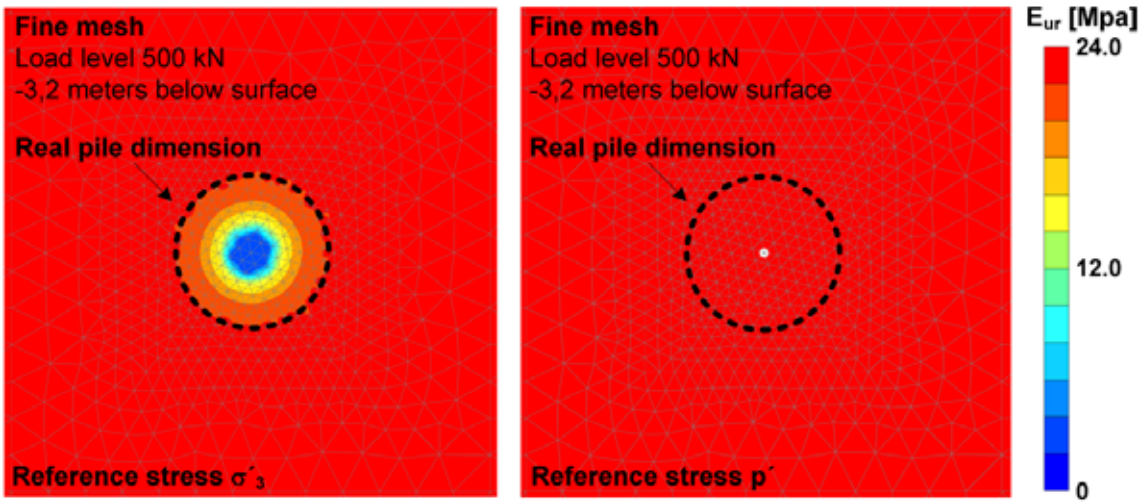

Fig. 82 Contour lines of current stiffness at 500 kN

5.5.3 Influence on load-settlement behaviour

To demonstrate the influence of the stiffness definition of the elastic region on the load-settlement behaviour, the FE models presented in Fig. 36 and Fig. 80 are slightly modified so that the tip node of the embedded pile is located at a corner node of a 15 noded wedge element (see chapter 5.4). The base resistance is neglected to simplify the behaviour of the pile ($\Gamma_{foot} = 0$).

Fig. 83 shows the load-settlement curve for the medium and fine mesh discretization and the two different reference stress approaches. The calculations, where p' is used as reference stiffness inside the elastic region, show a much stiffer global response, and the calculation with a medium mesh naturally behaves a bit stiffer compared to the calculation with a fine mesh discretization. The calculations with σ'_3 as reference stress show kinks in the load-settlement curves. The analysis with the fine mesh shows the kink at about 100 kN and the calculation with the medium mesh at 500 kN vertical load.

For friction piles, a kink in a load-settlement curve generally indicates the load level where the shaft resistance is fully mobilized, but the shaft resistance of the pile is defined with 1913 kN in the calculations presented, thus the kink is not related to R_{su}. With the medium mesh, the vertical displacements - at a load level of 1000 kN - are more than 100% higher compared to the calculation with p' as reference stress. With the fine mesh the difference is even bigger. If the corresponding profile of the current stiffness next to the EP is worked out (Fig. 84), one can see that when using the fine mesh, the stiffness is reduced to a threshold value at a load of 100 kN, and when using the medium mesh, the minimum stiffness is reached at a vertical load of 500 kN, the load level where the kinks occur. Thus, the reduction of stiffness inside the elastic region due to

the reduction of reference stress σ'_3 is the reason for the kink in the load-settlement curves presented in Fig. 83. The load levels where these kinks take place are related to the distance of the Gauss point to the embedded pile, or in other words, to the mesh coarseness of the problem.

Of course, a kink also occurs once the ultimate skin friction is reached. But these kinks are rather related to the embedded interface definition (chapter 5.3.2) and the shape of the ultimate skin friction distribution (chapter 5.6), instead of to the elastic region approach.

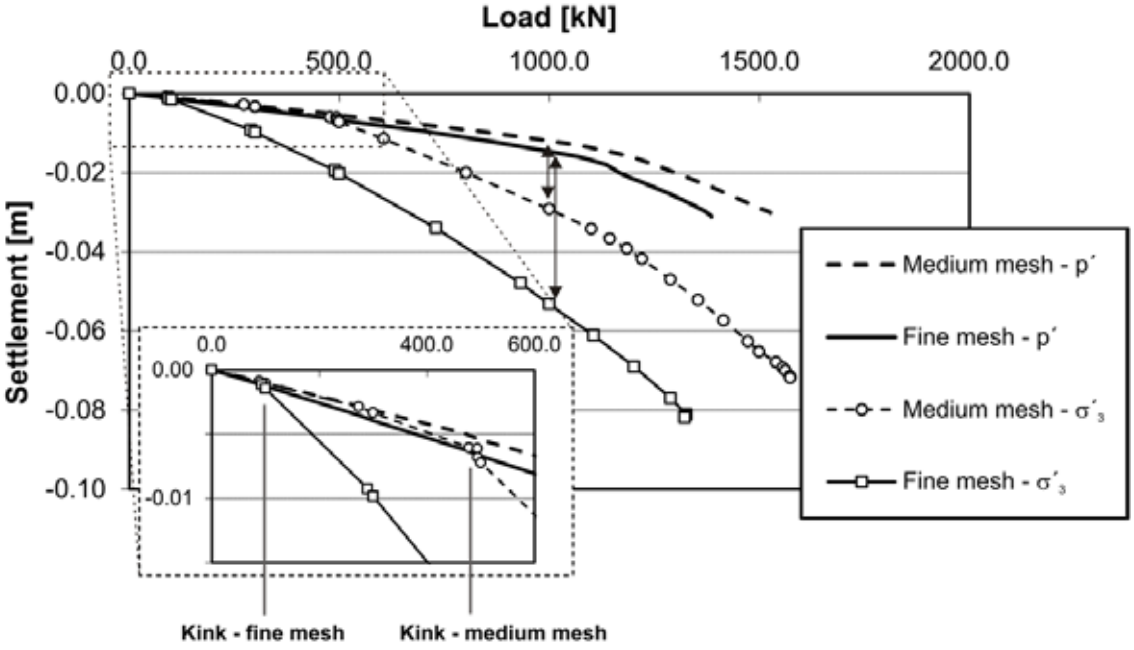

Fig. 83 Load-settlement curves for different mesh coarsenesses and reference stress definitions

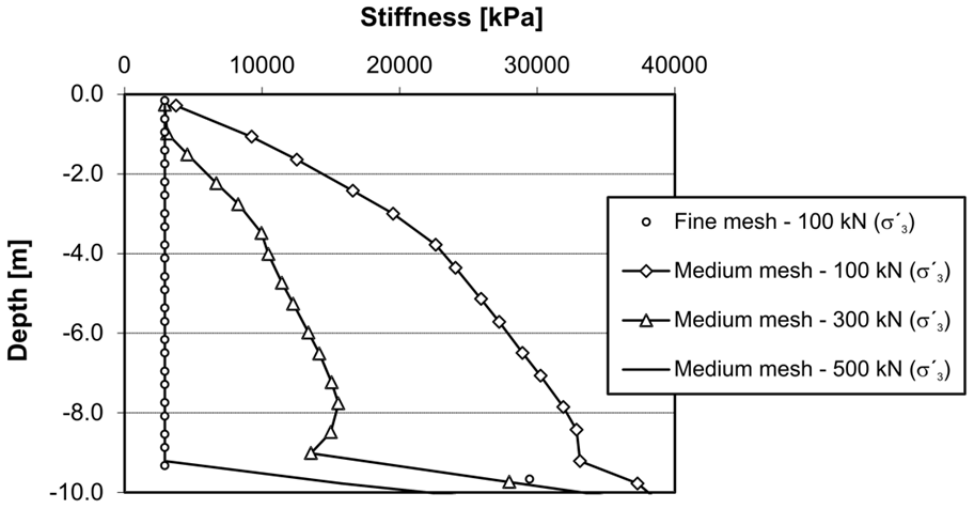

Fig. 84 Current stiffness next to the EP for different mesh coarsenesses and reference stress definitions

Fig. 85 shows load-settlement curves for vertically-loaded embedded piles, including a maximum foot resistance F_{max} of 1320 kN. As explained in chapter 5.3.1, Γ_{foot} has a notable influence on the load-settlement curves when using σ'_3 as reference stress. Once p' is used, an increase from Γ_{foot} of 1 to 5 does not significantly change the load-settlement behaviour. This is because the stiffness inside the elastic region does not reduce; hence the foot interface stiffness also remains almost constant during the calculation. Fig. 86 illustrates the distribution of relative displacements along the EP and the actual foot interface stiffness K_{foot} at a vertical load of 1000 kN.

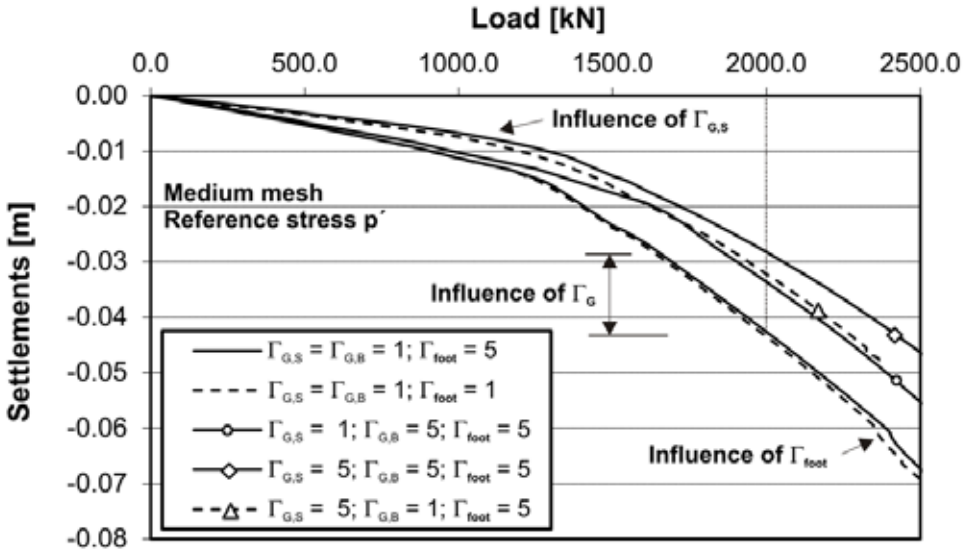

Fig. 85 Load-settlement curves for different Γ_{foot} and Γ_G factors

The averaging procedure (Equation 62) was used to work out the interface stiffness. With the improved definition of the elastic region, the foot interface stiffness is nearly independent of the mesh coarseness. That is also true for the skin interface stiffnesses K_n, K_s and K_t. Also, the distributions of relative displacements are almost the same for different mesh discretizations; a mentionable difference occurs only at the pile tip. Thus, higher base resistances are obtained with coarser meshes. But this deficiency is also present in the standard finite element approach, where coarser meshes yield higher base resistances.

The studies also showed that an increased value of K_{foot} to 5 in combination with p' as reference stress prevents the premature failure and therefore improves the numerical robustness of the model.

The influence of an increased stiffness inside the elastic region is illustrated in Fig. 85. An increase of both the stiffness along the pile shaft ($\Gamma_{G,S}$) and the stiffness below the pile base ($\Gamma_{G,B}$) by a factor of 5 reduces the displacements inside the elastic region and yields, in this particular example with 2000 kN, to a

reduction of vertical displacements of roughly 30%. Of course, the modification of stiffness inside the elastic region also increases the interface stiffnesses of the EP and reduces the settlements of the first part of the load-settlement curve significantly (mainly governed by friction). Such a modification of stiffness inside the real pile dimension is potentially required for large diameter piles or piles with very high skin resistance, where otherwise significant numerical displacements inside R_{eq} are computed. The effect of $\Gamma_{G,B}$ on the settlement behaviour is rather small.

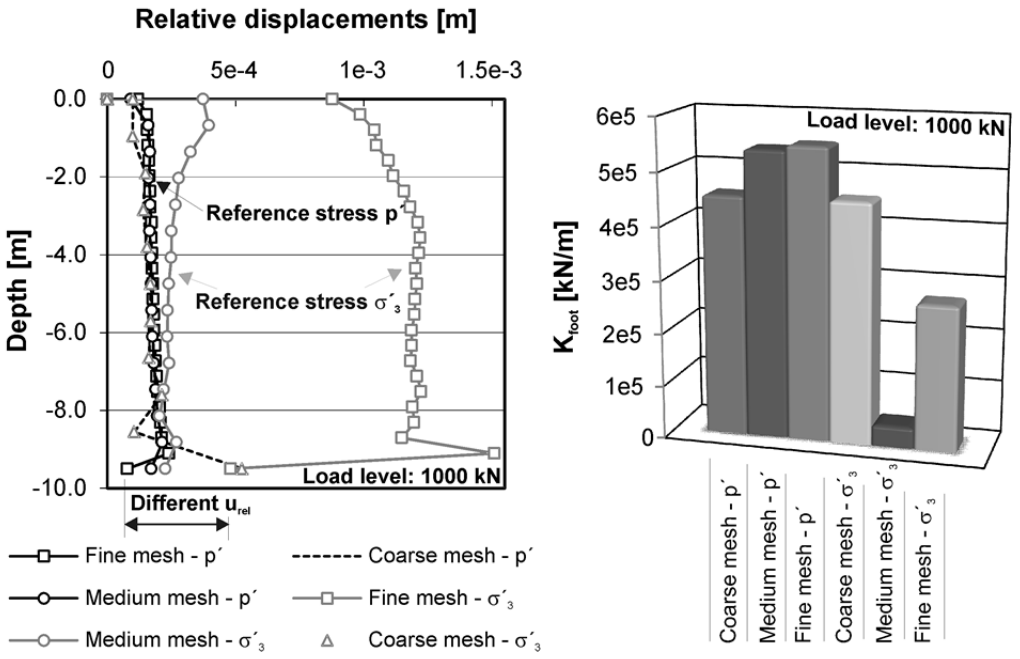

Fig. 86 Load-settlement curves for different foot interface stiffnesses (load level 1000 kN)

5.6 Effect of ultimate skin friction distribution on the behaviour of EPs

In chapter 5.3.2 of this thesis, the influence of stress-dependent interface stiffness on both the skin friction mobilization and the global load-settlement behaviour of a pile is investigated. In this chapter, the effect of the ultimate skin friction ($t_{s,max}$) distribution is studied, which is an input to the analysis. The FE model used is shown in Fig. 44 and the soil parameters of Rotterdam clay are given in Tab. 6 and Tab. 8. Both the Mohr-Coulomb and the Hardening Soil model were used. The foot interface stiffness is increased with a factor Γ_{foot} of 10 and the skin interface stiffness is defined with Γ_s of 1. The properties of the embedded pile are similar to those used in chapter 5.3. The ultimate skin resistance is the same in all calculations, but in one calculation a constant ($T_{top,max} = T_{bot,max}$) is defined, and in the other, a linear ultimate distribution is defined. Fig. 87 shows the normal force

distributions and the corresponding ultimate skin friction profiles for both calculations when using the MC model. A constant ultimate skin friction distribution yields a linear decrease of normal force over the pile length, while a linear ultimate skin friction profile gives a non-linear decrease of normal force.

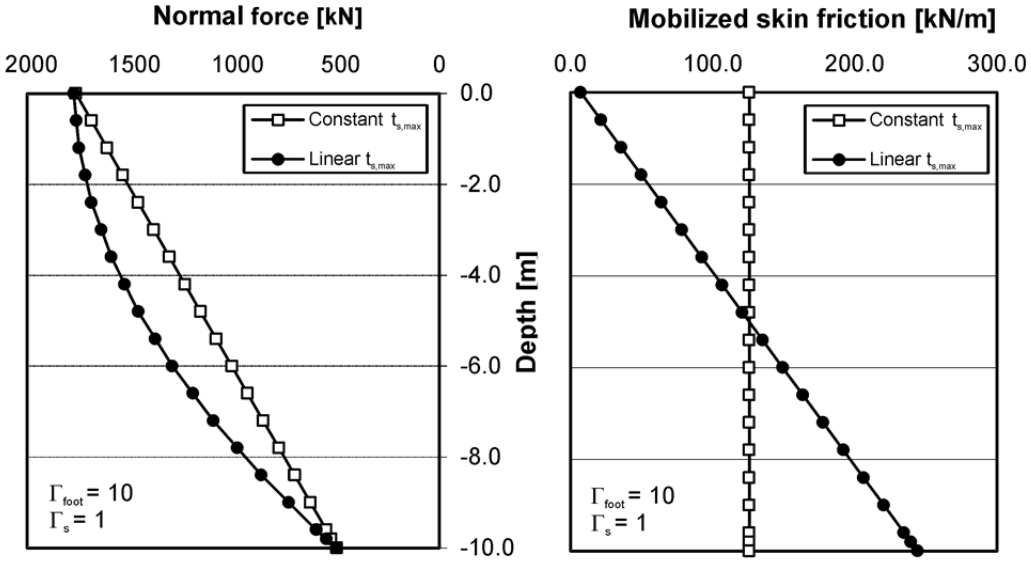

Fig. 87 Normal force distribution at failure (left) and ultimate skin friction distribution (right) – MC model

The global load-settlement behaviour is also influenced by the shear stress distribution at failure. Due to the fact that the pile is very stiff and the Mohr-Coulomb model does not take a stress dependent stiffness into account, the mobilization of skin friction is almost constant (see chapter 5.3.2). As a consequence, the ultimate shaft resistance at the upper parts of the EP is immediately reached when using a linear ultimate skin friction profile, and this yields automatically to a less stiff global behaviour of the pile. Fig. 88 compares the load-settlement curves for both definitions of the ultimate skin friction.

When using the HS model, the skin friction mobilization is not constant due to the stress-dependent stiffness of the soil and the embedded interface stiffness (see e.g. Fig. 52). Thus the calculation with a constant ultimate skin friction reaches the ultimate skin resistance first at the lower part of the pile. With a linear distribution of skin friction at failure, less plasticity at the pile shaft is present before the ultimate shaft resistance R_{su} is reached. Hence the calculation with linear $t_{s,max}$ distribution shows a clear kink in the load-settlement curve, where the maximum shaft capacity is reached. No kink is obtained with a constant $t_{s,max}$ profile, because plasticity at the pile shaft occurs gradually. Fig. 89 illustrates the normal force along the pile and the load-settlement curves for the calculations with constant and linear $t_{s,max}$ profiles.

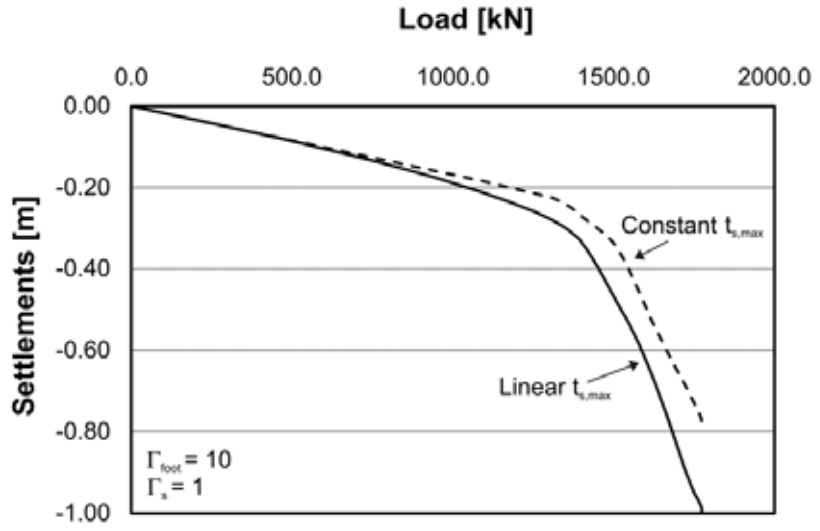

Fig. 88 Comparison of load-settlement behaviour – MC model

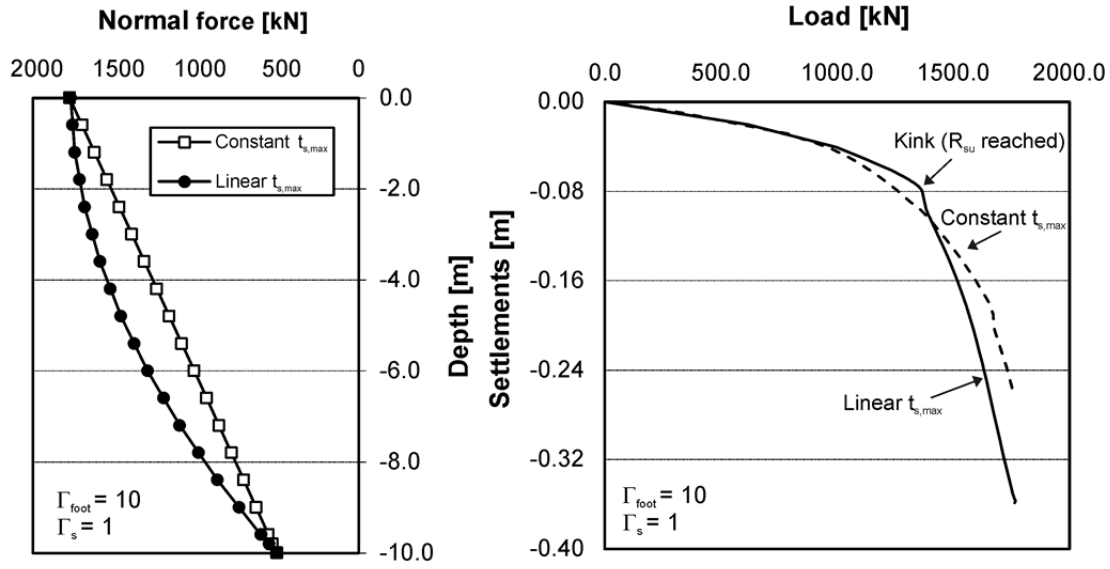

Fig. 89 Normal force distribution at failure (left) and load-settlement curves (right) – HS model

5.7 Improved embedded pile definition

The studies presented in chapters 5.3 to 5.6 demonstrate that the four criteria listed at the beginning of this chapter are influenced by a number of factors. The results indicate that the foot interface stiffness K_{foot} is not high enough. When using high order constitutive models, the influence of Γ_{foot} is smaller, but nevertheless the stiffness should be increased by a factor of 5 to 10.

The skin interface stiffness studies show that the embedded pile skin interface stiffnesses must take a stress dependent stiffness into account to model the correct skin friction mobilization along an embedded pile. A modification of the size of K_s, K_n, and K_t is not necessary.

The problems related to the vertical mesh dependency and the unrealistic distribution of skin friction close to the pile tip is associated with the position of the embedded pile tip node inside the solid finite element. This can be fixed with an embedded pile tip node, which corresponds with a corner node of a solid finite element.

The stress flow within the elastic region yields problems when using embedded piles in combination with constitutive models that take a stress dependent stiffness into account. As σ'_3 decreases, and the stiffness inside and the elastic region is related to the minor principle stress, the stiffness within the elastic region is also reduced. If the mean effective stress is used as reference stress for a stress-dependent stiffness inside the elastic zone, no relevant change of stiffness next to the embedded pile occurs. With this modification, the influence of the mesh coarseness on the load-settlement behaviour is also reduced to an acceptable value.

The utilization of p' as reference stress in combination with an increased foot interface stiffness also prevents premature failure, meaning it improves the numerical robustness of the model. A global increase of the stiffness inside the elastic region reduces the numerical displacements resulting from the fact that an EP is a line element and does not occupy any volume.

It is important to use realistic skin friction distributions at failure. The numerical studies demonstrate that the normal force, the skin traction and the load-settlement behaviour are influenced by the choice of the input for the ultimate shaft resistance. Realistic results for single vertically-loaded piles using constitutive models, which take the stress dependency of stiffness into account, were obtained with a linear increased skin friction profile at failure. Of course, this is only true for drained, frictional material. For other applications it may be that another input of ultimate skin friction is appropriate.

Tab. 17 indicates qualitatively the impact of particular modifications of the embedded pile concept on individual deficiencies of the EP concept. A value of zero stands for no effect, and a value of five for a large effect.

Tab. 17: Additional parameters for the Hardening Soil Small model

criteria	Γ_{foot}	Γ_{s}	$\Gamma_{G,S}$	$\Gamma_{G,B}$	$E_{el.R}$
load-settlement behaviour	4	2	3	5	5
distribution and mobilization of t_s	1	1	2	1	5
mobilization of F_{foot}	5	1	1	3	2
avoid numerical problems	3	3	1	1	5

6 Validation of embedded pile approach

In the literature, a number of papers can be found on the validation of the standard embedded pile concept as implemented in PLAXIS 3DF. Septanika et al. (2007) and Engin et al. (2007) presented back-analyses of pile load tests. Septanika et al. (2008) showed that embedded piles could be applied for modelling soil reinforcements. Engin et al. (2008), Engin & Brinkgreve (2009) and Engin et al. (2009) investigated the pile group behaviour using EP. Regarding piled raft foundations, Lee et al. (2010) presented comparisons with other models. All these validation examples showed a reasonable agreement with other calculation approaches and/or measurements. But for most of the time, only load-settlement behaviour was considered, mainly governed by the stiffness of the surrounding soil. On the other hand, the aim of the following validations is to show that the improved EP concept is able to satisfy all four criteria mentioned in chapter 5.1 and to overcome the deficiencies discussed in chapter 5.2.

In the following, the behaviour of the improved embedded pile concept is compared with results presented in the literature. In the calculations presented, the last node of the embedded pile corresponds with a corner node of a 15 noded wedge element, the foot interface stiffness is increased by a factor of 5 ($\Gamma_{foot} = 5$) and, if not explicitly mentioned, the stiffness inside the elastic region remains unchanged ($\Gamma_{G,S} = \Gamma_{G,B} = 1$).

6.1 Performance of axially-loaded single piles

In the first part of this chapter, linear elastic material behaviour is used to validate the general behaviour of the embedded pile concept related to mesh dependency, mobilization of skin friction for different stiffness ratios $\overline{K}$ and the influence of non-homogeneous soil stiffness. In the second part, more advanced validation examples using non-linear soil behaviour are presented.

The first example considered is a linear elastic axially-loaded pile in homogeneous linear elastic soil. This simple example was used by a number of geotechnical engineers to validate different calculation methods concerning the stress distribution along a single pile. Davis & Poulos (1980) used a method based on the theory of elasticity that employs the equations of Mindlin (1936). They studied the distribution of shear stress for piles with length to diameter ratios (L/D) of 25 and two different relative stiffnesses $\overline{K}$ representing a more or less incompressible ($\overline{K}$ = 5000) and a compressible pile ($\overline{K}$ = 50).

$$\overline{K} = \frac{E_P \cdot R_A}{E_{soil}} \tag{87}$$

$$R_A = \frac{A_P}{\frac{\pi \cdot D^2}{4}} \tag{88}$$

R_A is the ratio of pile section A_p divided by the area bounded by the outer circumference of a pile. R_A equals one for solid piles. To enable rapid estimations in praxis, Poulos & Davis (1980) introduced two dimensionless parameters, one for the shear stress along the pile shaft and one for the depth below the ground surface (z/L).

$$Shear\ stress = \frac{\tau \cdot \pi \cdot D \cdot L}{P_0} \tag{89}$$

In the following the results presented by Poulos & Davis (1980) are compared with results obtained with PLAXIS calculations (Fig. 90) using different programs and modelling techniques. The 2D axisymmetric model has the dimensions B_m/D_m of 30/35 consists of nearly 1600 15 noded elements. The pile has a diameter of 0.8 m and a length of 20 m (L/D = 25). To avoid stress concentrations below the pile tip, the interface is extended below the pile tip (see chapter 3.4.2).

Poulos & Davis (1980) showed that the Poisson's ratio of the soil has hardly any effect on the shear stress distribution; hence a ν value of 0.3 was chosen. In PLAXIS 3DF the same model dimensions were used and the pile was modelled with the both the standard finite element approach using volume piles (VP) and the embedded pile concept. The ultimate skin friction of the EPs is defined as layer dependent, thus no maximum skin resistance is defined because the surrounding soil is modelled as linear elastic material.

For incompressible piles, the shear stress along the pile shaft is almost constant, but for compressible piles high skin friction develops near the pile head. For $\overline{K}$ equals 50 the embedded pile concept mobilizes less stress close to the pile head, however for high relative stiffnesses ($\overline{K}$ = 5000) the agreement of the embedded pile concept with the other results is almost perfect.

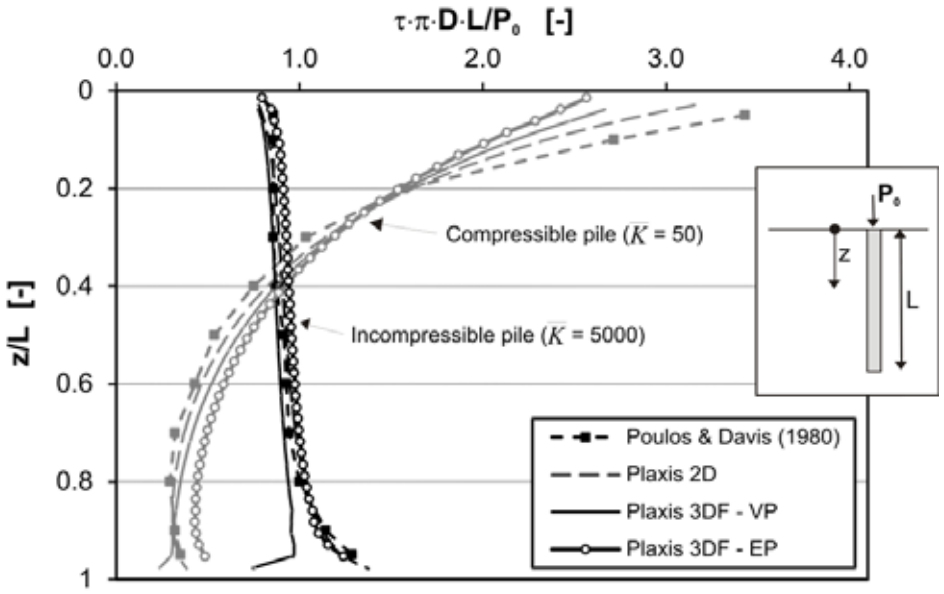

Fig. 90 Poulos & Davis (1980) vs PLAXIS results

Chow & Small (2008) used the same example to validate the computer program APRILS (Analysis of Piled Rafts In Layered Soils). This program uses the finite layer technique developed by Small & Booker (1986) to model the soil layers and employs the finite element method for the piles and the raft. El-Mossallamy (1996) also used the example to examine the shear stresses obtained with his calculation program based on elasticity theory using Mindlin's equations (1936). Finally, the single pile was analysed using the boundary element program BEFE++ (Duenser et al. 2011). Ausweger (2012) showed that when using BEFE++ a reasonable fine discretization close to the pile tip is necessary. Fig. 91 compares the results presented in literature with the EP concept. The EP approach shows a very good agreement with the solutions of other calculation models.

The influence of vertical soil inhomogeneity is considered in the next example. The EP concept is compared with results obtained with the approximated closed form solution presented by Wroth & Randolph (1978). In the closed form solution, it is assumed that the soil stiffness increases linearly with depth, which is commonly referred to as Gibson soil (e.g. Gibson 1967 or Gibson 1974). 2D axisymmetric calculations were performed in the first step. The finite element model used consists of 1633 elements and has a width of 30 m and a depth of 35 m. The pile has a length of 20 m and a diameter of 1.0 m, thus a length to diameter ratio L/D of 20. The soil is modelled as linear elastic material with a linear stiffness increase of 2000 kPa per meter depth (Fig. 92) resulting in a Young's modulus of 40000 kPa and a shear stiffness (G_L) of 14286 kPa ($\nu = 0.4$) at the level of the pile tip. The pile head load is defined according to Equation 90.

$$\frac{P_0}{0.5 \cdot D \cdot G_L} = 0.5 \tag{90}$$

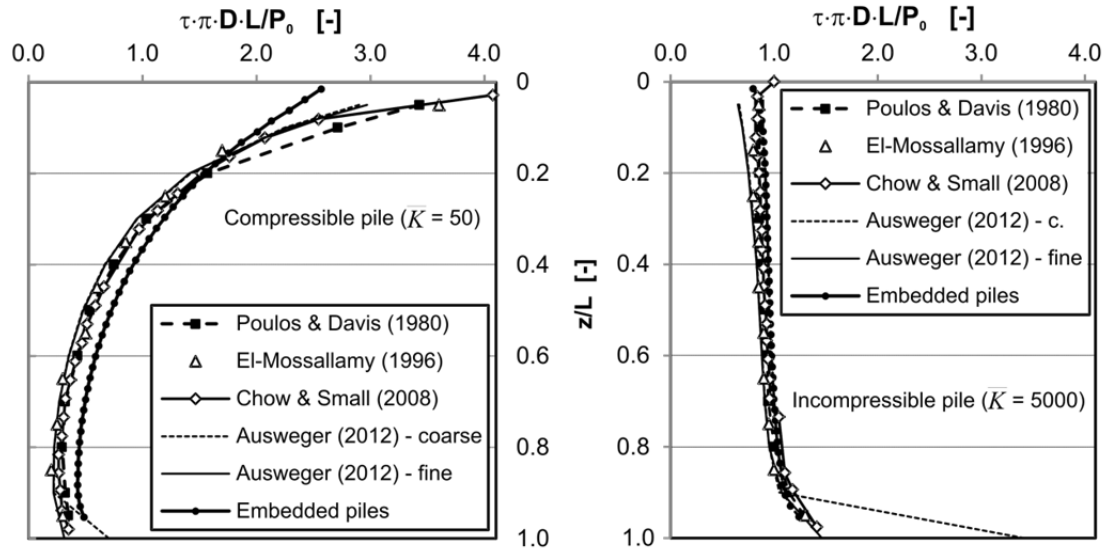

Fig. 91 Normalized skin friction distribution along a pile

In the following step, the example was analysed with the standard finite element and the EP approach using the layer dependent ultimate skin friction definition. Fig. 92 shows the shear stress along the pile obtained with the different analyses. Additionally, results presented by El-Mossallamy (1996) are shown. The pile length is normalized (z/L) and the shear stress is shown in a dimensionless form of τ/G_L.

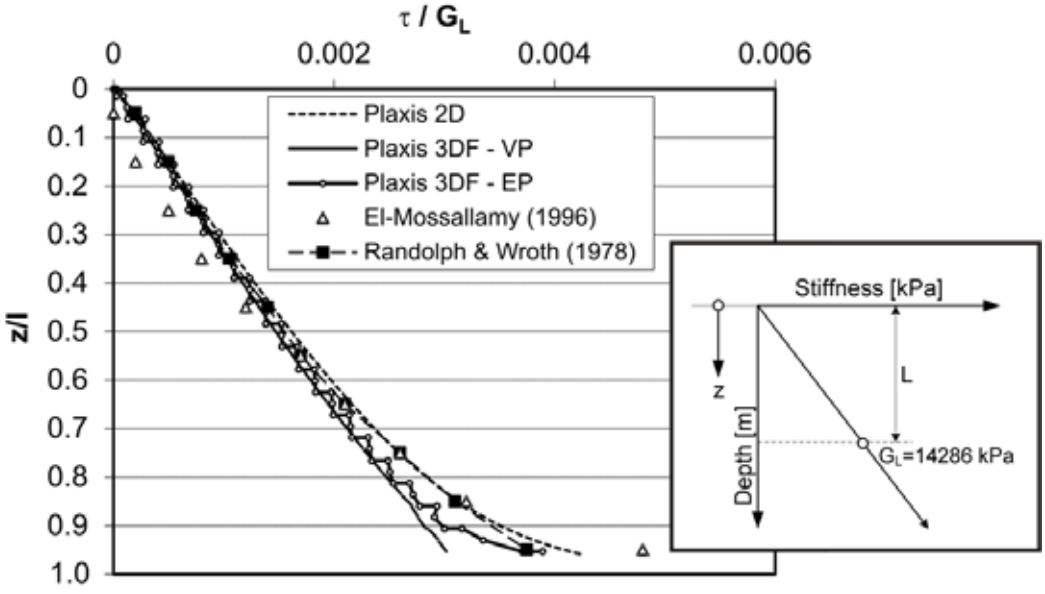

Fig. 92 Normalized skin friction distribution along a pile in "Gibson" soil

The embedded pile approach of course yields to a step shaped skin friction profile, due to the constitutive model of the embedded interface stiffness. The calculations with volume piles mobilize less shear resistance close to the pile tip, but all in all, the agreement is very good.

In the following, analyses presented by Rajapakse (1990) are compared with the embedded pile behaviour. Rajapakse (1990) used a variational formulation coupled with a boundary-integral representation of the soil to study the response of axially-loaded piles in linearly non-homogeneous soil ("Gibson" soil). In addition to the factors given in Equation 79 to 82, he introduced a normalized resultant axial force $\overline{P}_{(z)}$.

$$\overline{P}(z) = \frac{P(z)}{P_0} \tag{91}$$

In the first analyses the slenderness ration $\overline{h}$ is defined with 40 and the degree of non-homogeneity ρ with 0.2. The stiffness ratio $\overline{E}$ is varied and the influence on the axial load-transfer curves is studied (Fig. 93). The distribution of normal force in the pile computed with the embedded pile concept fits well with the results presented in the literature.

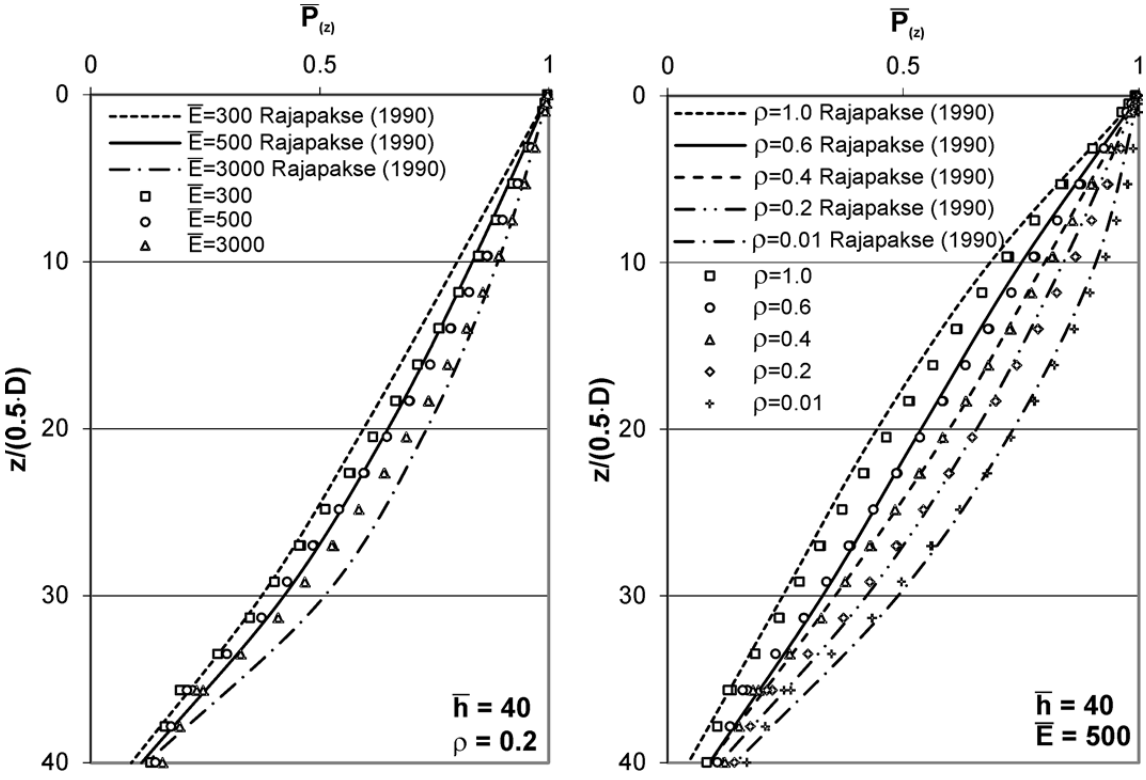

Fig. 93 Embedded pile concept vs Rajapakse (1990)

Only for very high and very low relative stiffnesses do the load distributions show noteworthy differences. Also, the calculations with varying degrees of soil non-homogeneities (Fig. 93) are in accordance with Rajapakse (1990). These results show clearly that the soil non-homogeneity and stiffness ratios have a considerable effect on the contact traction along the pile shaft; however the embedded pile approach is fully capable of modelling the correct mobilization of skin friction for piles with different relative stiffnesses in non-homogeneous soil conditions.

Trochanis et al. (1991) presented studies of 3D FE analysis to examine the non-linear soil behaviour on the response of axially-loaded piles. They modelled the soil either as linear elastic material or as Drucker-Prager elasto-plastic material (Drucker & Prager 1952) and the interface strength is limited in the calculations presented by Trochanis et al. (1991) with a modified Coulomb friction model. The same examples were calculated with PLAXIS 3DF using the embedded pile approach. The model has dimensions $L_m/B_m/D_m$ of 34/34/14 m and consists of 22940 elements. The soil was modelled as MC material (Tab. 18), where the Drucker-Prager failure criterion used by Trochanis et al. (1991) was interpreted as a compression cone. The squared pile with a length L of 10.0 m and a width b of 0.5 m was modelled as linear elastic with a Young's modulus of 2e7 kPa and a Poisson's ratio of 0.3.

Tab. 18: Properties of soil

	$\gamma_{sat} = \gamma_{unsat}$ [kN/m3]	ν [–]	E_{ref} [kPa]	c' [kPa]	φ' [°]
soil	21.8	0.45	20 000	34	16.7

Fig. 94 compares the load-settlement curves obtained with the EP approach with the results presented by Trochanis et al. (1991). The calculations with the default stiffness inside the elastic region ($\Gamma_{G,S} = \Gamma_{G,B} = 1$) result in a too soft response. A closer inspection of the displacement field showed that about 4 mm of vertical displacement are obtained inside the elastic region. If the stiffness inside the elastic region is increased by a factor of 10 ($\Gamma_{G,S} = \Gamma_{G,B}$), the results are in much better agreement.

In the calculation with elasto-plastic material behaviour, the embedded pile was defined with a linearly-increasing ultimate skin friction profile, where $T_{top,max}$ = 4 kN/m and $T_{bot,max}$ = 86 kN/m. The ultimate foot resistance F_{max} = 200 kN and the stiffness inside the elastic region is not modified.

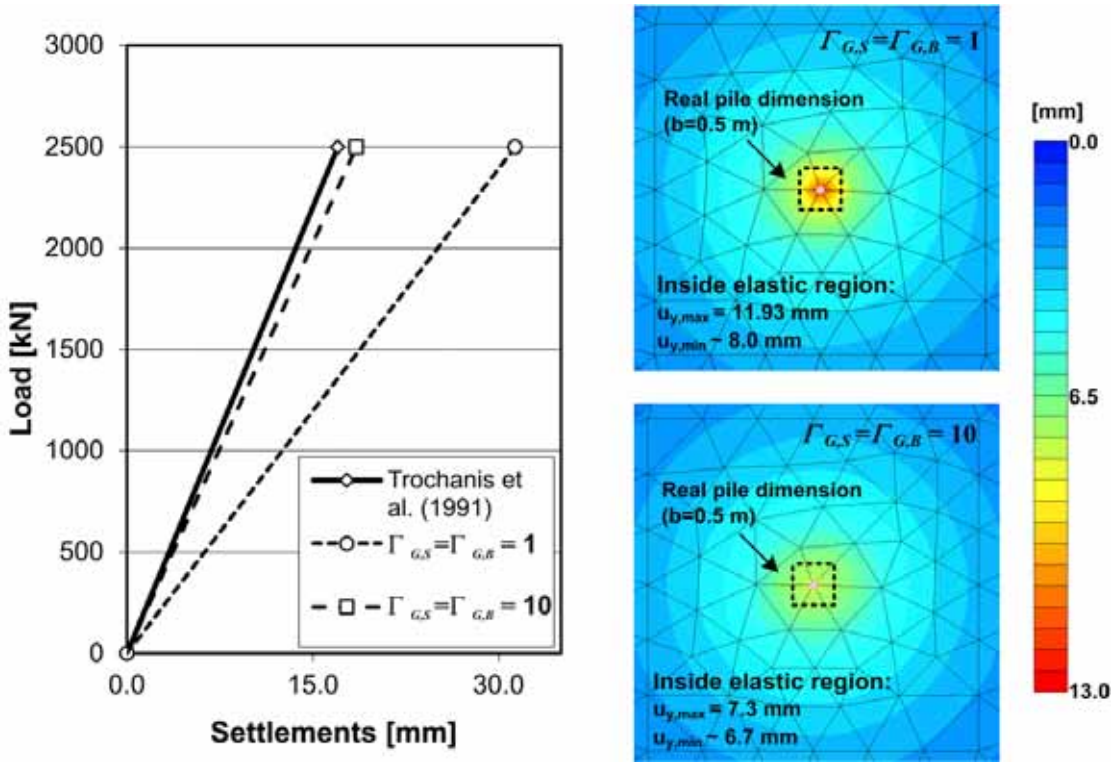

Fig. 94 Load-settlement curve (left); contour lines of vertical displacements for load level 1000 kN (right)

The computed load-settlement curve shows a very good agreement with the result presented in the literature (Fig. 95). The initial stiffness response of the calculation with elasto-plastic behaviour is much smaller compared to the linear elastic calculation, and no increase of stiffness inside the elastic region is necessary to predict the correct initial stiffness. Of course, this could be different when dealing with large diameter piles.

Also Trochanis et al. (1991) stated that the nonlinearity of the soil material and corresponding interface significantly affects the pile response. Fig. 95 also shows the mobilized skin friction profiles for different load levels. The mobilization is very similar in both calculations. In the embedded pile approach, the last embedded pile node mobilizes both skin and foot resistance; therefore the distribution close to the pile toe is a bit different.

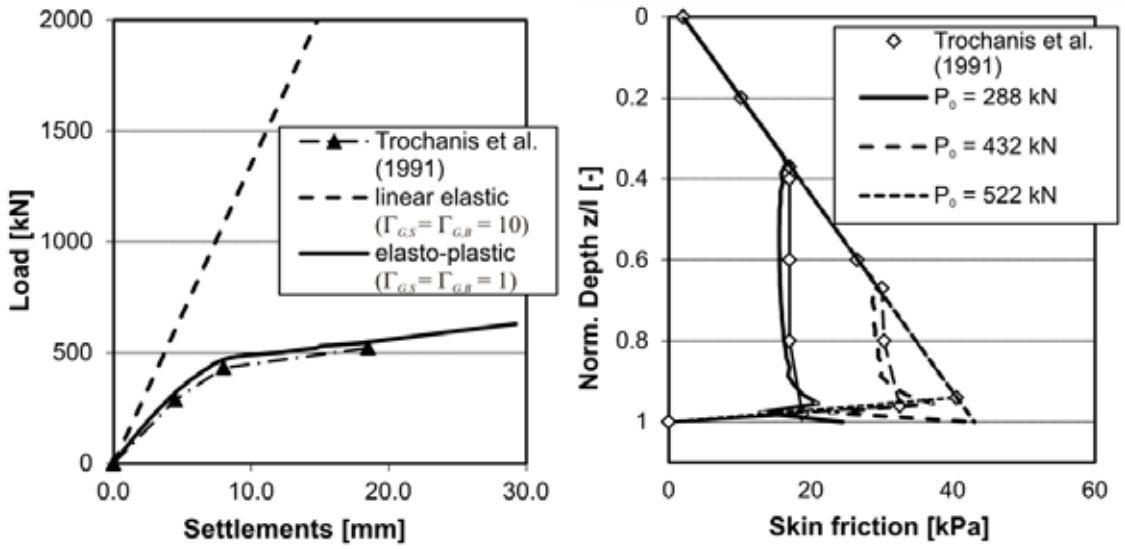

Fig. 95 Load-settlement curves for elasto-plastic soil behaviour (left); contour lines of vertical displacements for load level 1000 kN (right)

In addition, the example presented by Potts & Zdravković (2001) and discussed in chapter 3.5.2 concerning the influence of mesh coarseness was recalculated with the embedded pile option. The embedded pile was defined with a constant ultimate skin friction profile, where $T_{top,max} = T_{bot,max} = 314.2$ kN/m and the ultimate foot resistance $F_{max} = 720$ kN. Three different mesh coarsnesses were considered: coarse, medium and fine.

Fig. 96 demonstrates the influence of mesh discretization. The initial stiffness of the pile is in general underestimated with finer meshes. This effect also comes from the influence of the elastic region approach ($\Gamma_{G,S} = \Gamma_{G,B} = 1$). However, the match of the embedded pile calculations with the reference solution presented by Potts & Zdravković (2001) is satisfying.

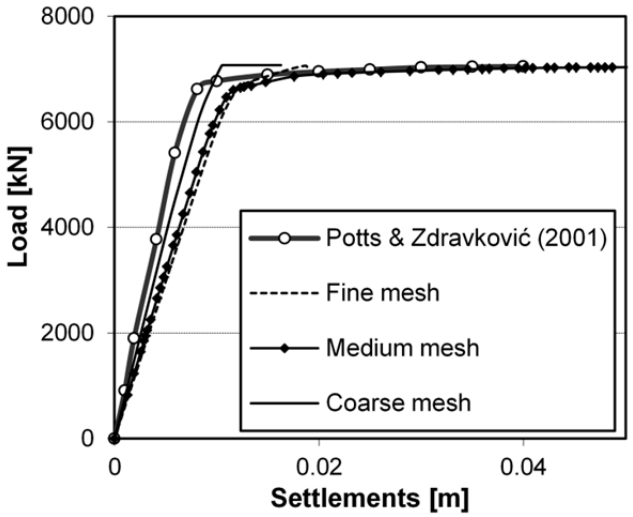

Fig. 96 Load-settlement curve for elasto-plastic soil behaviour

The following validation calculations are based on the analyses discussed in chapter 3.5.3. In this example, the HS model is used for the soil, therefore an $\Gamma_{el,R}$ of 0.72687 is used to ensure that a uniform stiffness is present in the model after the initial stress generation. The embedded pile is defined with an ultimate end-bearing resistance of 3000 kN and a linear distribution for the ultimate skin friction ($T_{top,max}$ = 0; $T_{bot,max}$ = 147 kN/m). Fig. 97 compares the load-settlement curves obtained with different programs and in addition the mobilizations of the base and shaft resistance.

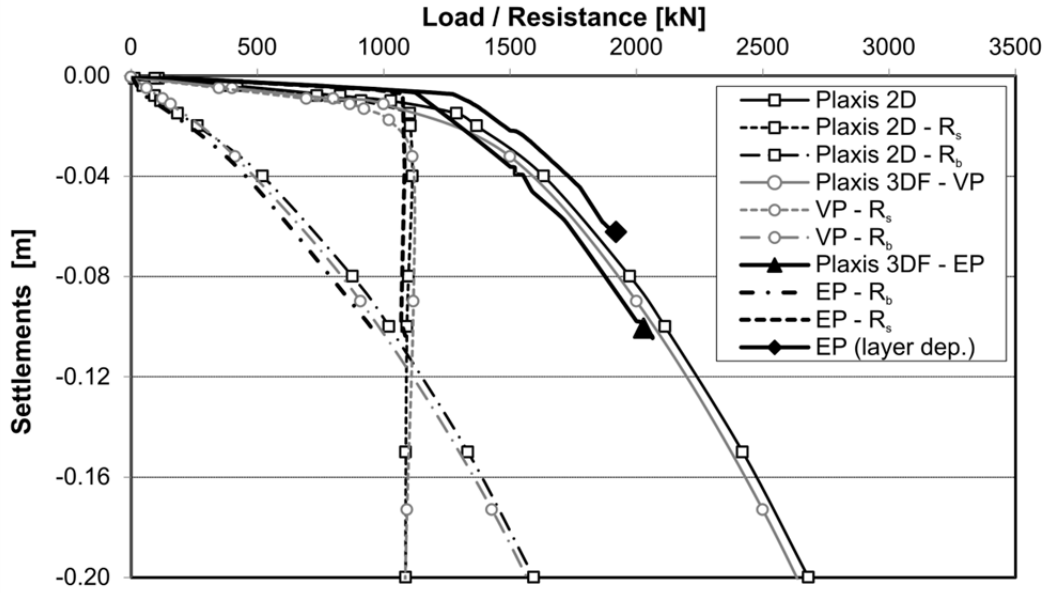

Fig. 97 Load-settlement curve and mobilized shaft / base resistance

In this example, the EP approach yields a stiffer response from the shaft resistance than the standard finite element approach. The reason is a slight underestimation of end-bearing resistance for low load levels. Nevertheless, the agreement is very good, especially for the shaft and base resistance at higher load levels. For this example, an alternative ultimate skin friction definition was also used, the layer dependent option (see chapter 4.3.2) with a R_{inter} value of 0.7. With this calculation a similar load-settlement curve is obtained, however the ultimate skin resistance is slightly overestimated.

The last validation example related to the behaviour of axially-loaded single piles is a back-analysis of a pile load test presented by Sommer & Hambach (1974). The pile has a length of 9.5 m and a diameter of 1.3 m and is embedded in slightly overconsolidated clay. The parameters used for the HS model are given in Tab. 3. Due to the overconsolidation, the K_0 value is increased to 0.8. The groundwater table is located 3.5 m below the surface. The same pile load test was also used for numerical studies presented by Wehnert (2006) and Engin et al. (2007). The pile load test was recalculated with PLAXIS 2D, 3DF and 3D. The

finite element models have the dimensions $L_m/B_m/D_m$ of 20/20/20 m. Due to the fact that PLAXIS 3D does not offer a possibility to read out normal forces inside piles, a workaround with the program SURFER 10 was performed, with the vertical stresses at the pile head being integrated over the cross section (Petternel 2012). Fig. 98 shows load-settlement curves and the mobilized shaft and base resistances obtained with the different programs using the standard finite element approach. One can see that all calculations are in very good agreement.

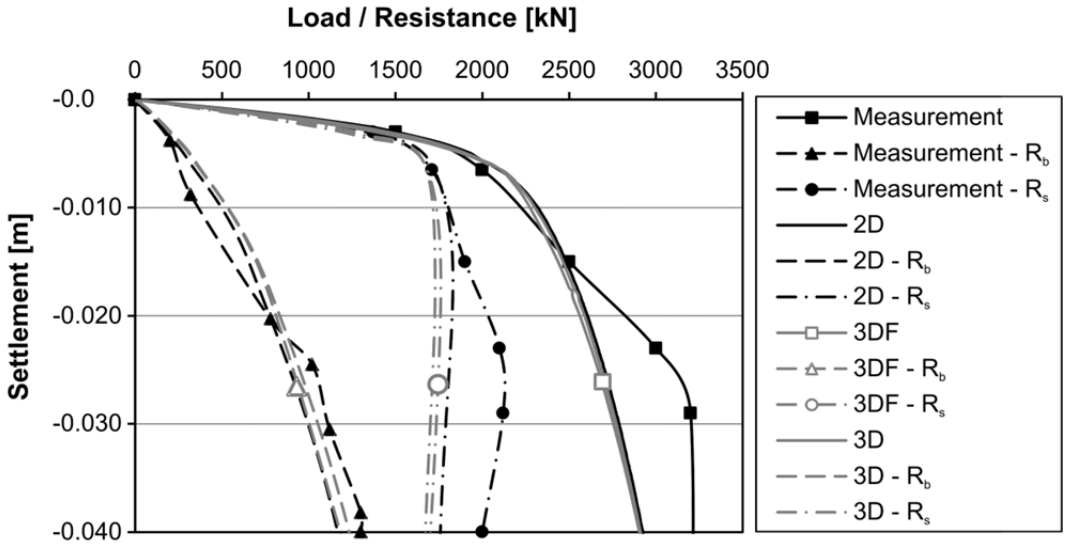

Fig. 98 Load-settlement curve and mobilized shaft/base resistance obtained with different programs

In the following, the pile load test was recalculated with the embedded pile option. The ultimate skin friction profile was defined with a constant value ($T_{top,max} = T_{bot,max}$) of 211 kN/m and the ultimate foot resistance F_{max} = 2005 kN. The stiffness of the elastic region is adjusted with a $\Gamma_{el.R}$ factor of 0.9231. Fig. 99 illustrates the load-settlement curves calculated with the EP approach. The overall agreement with the measurements and the standard FE approach is reasonable. However, if one looks at the displacements that are necessary to mobilize the skin friction (or in other words, at the initial stiffness of the load-settlement curve), one can see that the displacements obtained with the embedded pile models are higher.

Fig. 100 illustrates contour lines of vertical displacements obtained with the EP and the standard FE approach at a load level of 1000 kN. When modelling the pile by means of volume elements, the vertical displacements within the pile cross section are more or less uniform. When using EPs, one can see that the vertical displacements computed are similar at the circumference of the pile, but significantly higher at the centre of the pile. The reason is the elastic region

approach, because the stiffness inside the elastic region is (in general) not increased. The displacements outside the pile cross section are also almost identical for both approaches. In the following, the stiffness inside the elastic region was modified with a $\Gamma_{G,S}$ factor of 5 but the stiffness below the pile remains unchanged ($\Gamma_{G,B}$ = 1). Fig. 99 demonstrates that initial stiffness of the load-settlement curve is in much better agreement with the other solutions when using an increased stiffness inside the elastic region, because with $\Gamma_{G,S}$ = 5 the displacements inside the elastic region are almost uniform. This effect is not that pronounced in other examples studied, because the pile studied in this chapter is relatively thick but short (L/D = 7.3), a rather untypical dimension for a bored pile. Finally, some tests with PLAXIS 3D were performed, which also showed a good agreement.

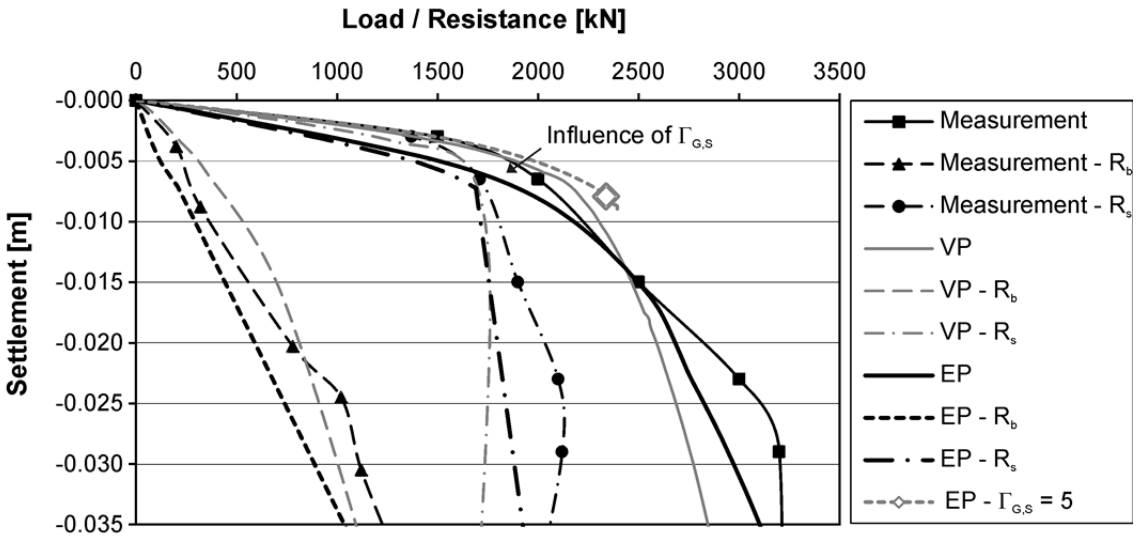

Fig. 99 Load-settlement curves of Alzey pile load test

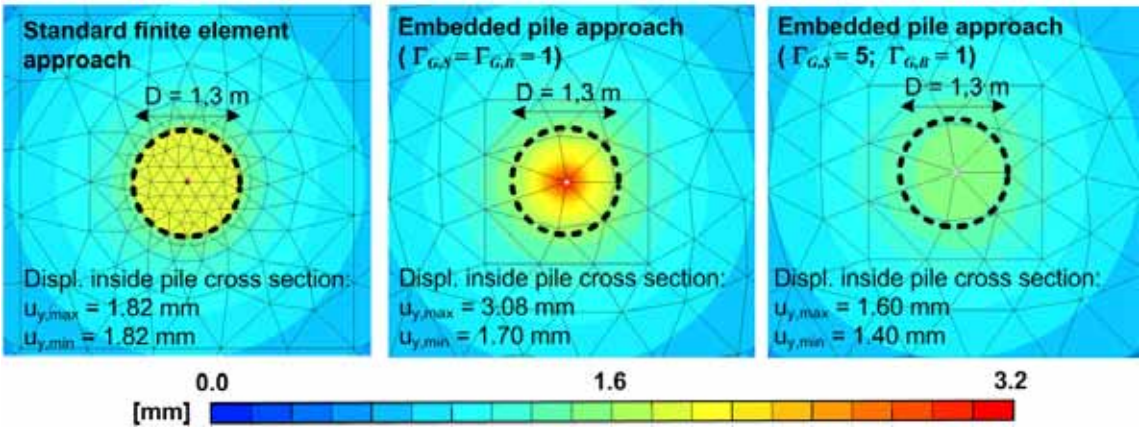

Fig. 100 Contour lines of vertical displacements obtained with VPs and EPs

6.2 Performance of horizontally-loaded single piles

The main focus of this Ph.D. is related to vertically-loaded single piles and pile groups, nevertheless some validation examples for horizontally-loaded single piles are presented in this chapter. The geometry and the soil parameters of the first example are based on studies presented by Potts & Zdravković (2001). The same example is also discussed in chapter 3.5.2. Two different mesh coarsenesses, with and without interfaces, are modelled in the first calculations with the standard finite element approach. The interfaces are defined with a R_{inter} value of 1.0 but no tension stresses are allowed; tensile stresses are tolerated in the soil.

Fig. 101 shows the computed load-deflection curves. The overall behaviour is similar to the results presented in the literature, however volume piles yield a stiffer pile response compared to Potts & Zdravković (2001). The influence of the mesh coarseness is very small but the calculations with and without interface show a different behaviour. The reason for the big influence of the interface is related to tensile stresses in the soil. Fig. 101 shows the horizontal stress distribution "behind" the pile at a load level 2000 kN, as presented by Potts & Zdravković (2001). Of course, such a load transfer affects the global load-settlement behaviour and results in an underestimation of settlements. If an interface is defined between the pile and the soil it is possible to model a gap between soil and pile; hence no tensile stresses can be transferred from the horizontally-loaded pile to soil.

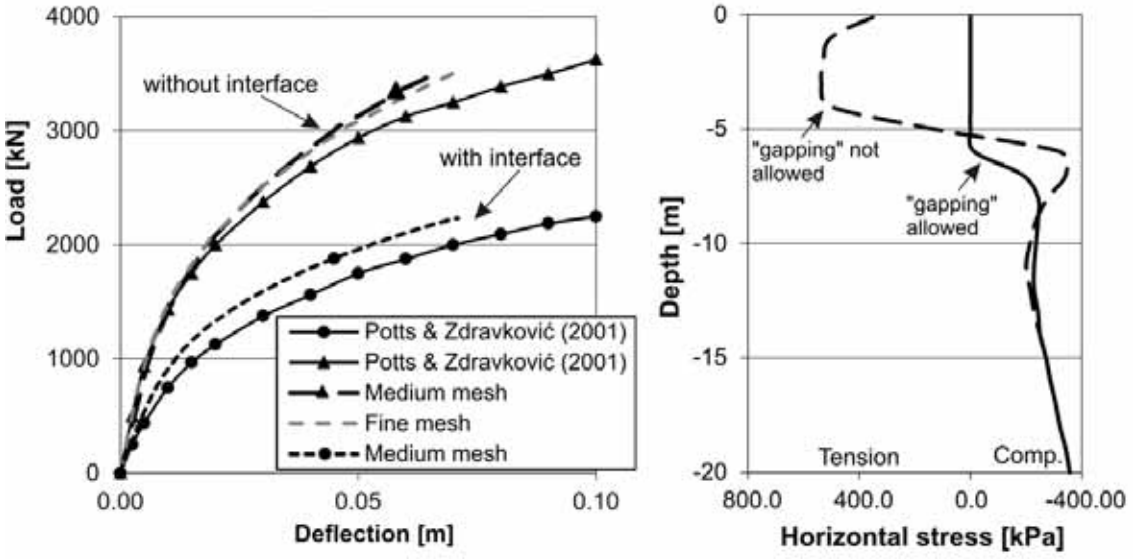

Fig. 101 Load-deflection curves (left) and effect of interface gapping (right) (after Potts & Zdravković 2001)

In the next step, the pile was modelled with the embedded pile concept. Due to the fact that the EP interfaces can only model plastic behaviour in an axial direction, gapping, as a consequence of horizontal loading, is not possible. Hence, it is necessary to ensure that the surrounding soil cannot sustain any tensile stresses.

The study was performed once with the standard parameters given in chapter 3.5.2 and once with the HS model using the parameters given in Tab. 16. To demonstrate the influence of tensile stress transfer in the soil, the calculation with the MC model was conducted once with and once without a tension cut-off. Fig. 102 compares the horizontal deflection along the pile obtained with both constitutive models. The standard finite element approach and the embedded pile concept compute similar pile deformations. Fig. 103 shows that the calculated moments and shear forces along the pile are very similar in both calculation approaches, which indicates that the embedded pile concept is also very capable for horizontally-loaded piles.

Another example investigated is a 15 m long drilled shaft with a diameter of 0.6 m embedded in a linear elastic four layer soil deposit. The same example was also studied by Basu et al. (2009). The results with both the standard finite element approach and the embedded pile option show a reasonable agreement with Basu et al. (2009). However, when using EPs, the stiffness response is a bit underestimated.

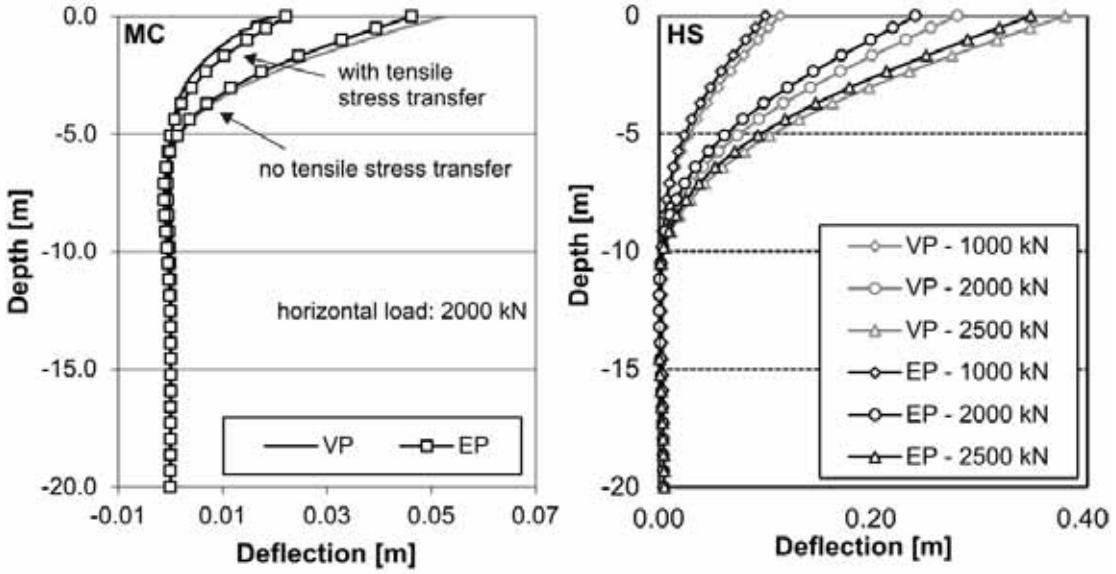

Fig. 102 Load-deflection curves with MC model (left) and HS model (right)

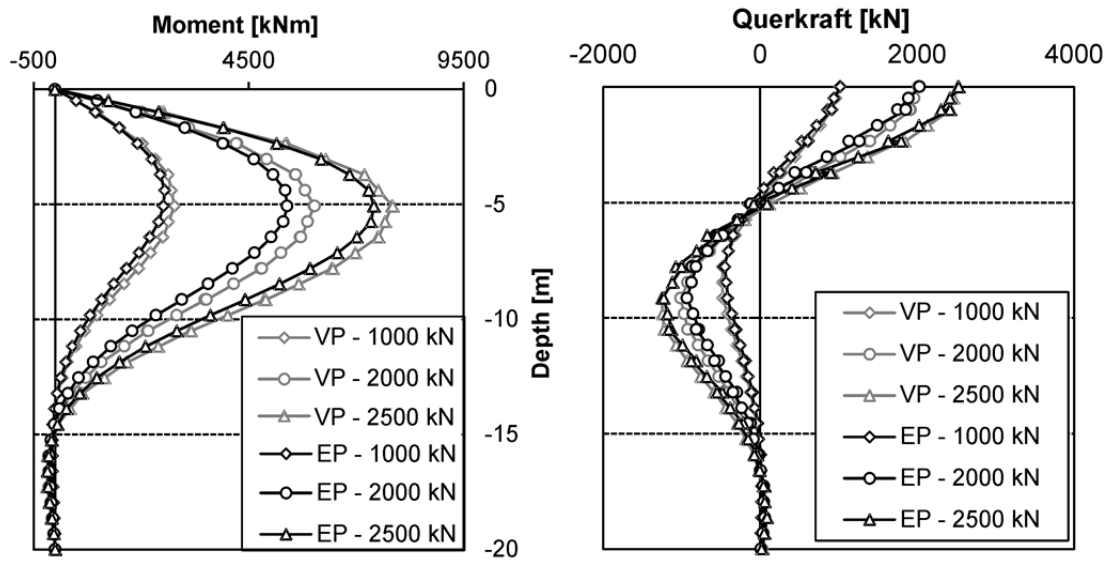

Fig. 103 Moments (left) and shear forces (right) – HS model

6.3 Performance of vertically-loaded pile groups and PRFs

In this chapter the pile group behaviour when using embedded piles is investigated. The first validation examples deal with linear elastic soil conditions to validate the general behaviour of pile groups modelled with EPs, e.g. group size, pile spacing, pile compressibility and the distribution of the load between individual piles. In the second part, more advanced validation examples using non-linear soil behaviour are presented.

Butterfield & Banerjee (1971) presented numerical studies on a pile group consisting of 4 piles with a spacing e_p of 2.5 times the pile diameter D. They used an integral equation developed from Mindlin's analysis to investigate the influence of pile length and relative stiffness on the response of the pile group embedded in linear elastic soil. Liang et al. (2009) used the same example to validate their calculation model, also based on the integral equation method.

A 3D model was set up using geometry similar to that used by the other authors. The model has the dimensions $L_m/B_m/D_m$ of 60/60/80 m and consists of 23200 elements. The EP diameter is defined as 0.8 m, and therefore a raft width of 4.0 m is modelled ($5 \cdot D$). The diameter ratios L/D 0, 5, 10, 20, 30, 40 and 50 were studied. The pile compressibility is modelled with a relative stiffness $\overline{E}$ of 6000. The pile and raft stiffness E is 3e7 kPa and the Poisson's ratio ν is 0.2. As a consequence of $\overline{E}$, the shear modulus of the soil is defined with G = 5000 kPa. The Poisson's ratio of the soil is defined with 0.49, due to the fact that a value of 0.5, as used by Butterfield & Banerjee (1971) would yield an infinite elastic

constitutive matrix **D**. Fig. 104 compares the results presented by Butterfield & Banerjee (1971), Liang et al. (2009) and Ausweger (2012) with the results obtained when using the embedded pile approach, where the vertical pile head displacements u_p are expressed dimensionless according to Equation 92. Both the settlement behaviour and the percentage of load taken by the cap (or the load shared by the subsoil) are almost in perfect agreement with the results presented in the literature.

$$\text{normalized settlements} = \frac{P_0}{D \cdot G_L \cdot u_p} \tag{92}$$

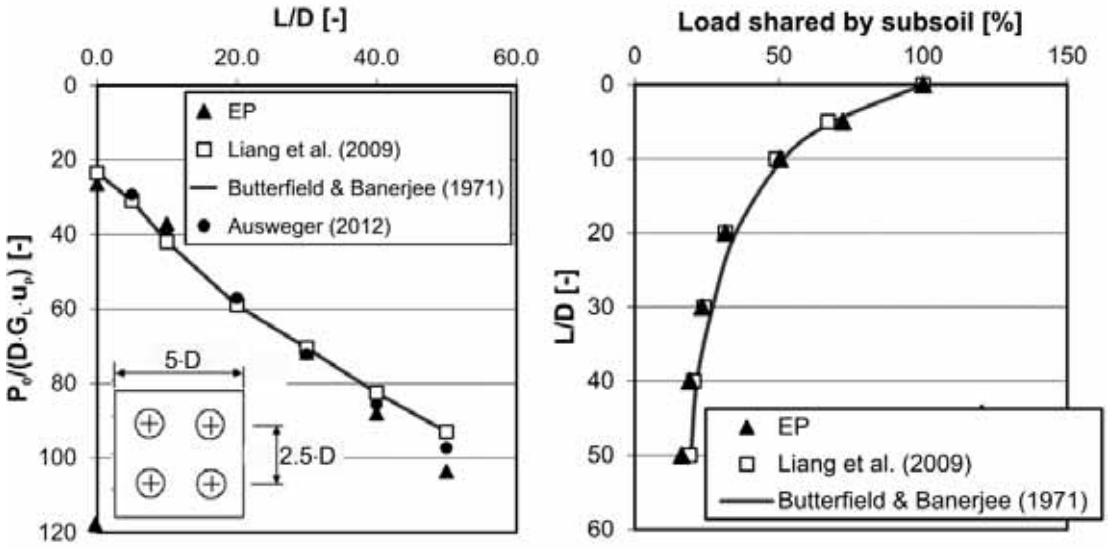

Fig. 104 Settlement behaviour (left) and load carried by the cap (right) for different L/D ratios

In the following, an example presented by Poulos et al. (1997) is used to investigate the behaviour of a 9- and a 15-pile group. Poulos et at. (1997) compared simplified calculation methods, as presented by Poulos & Davis (1980) and Randolph (1983), to approximate computer-based analyses like the strips on springs approach (Poulos 1991) or plate on spring approach (Poulos 1994), and finally with numerical methods. The hypothetical example is shown in Fig. 105. Three different cases are considered: Case A with 15 piles and 12 MN load, Case B with 15 piles and 15 MN load and Case C with 9 piles and 12 MN load (Tab. 19). Fig. 106, Fig. 107 and Fig. 108 show the average pile settlements and the proportion of load carried by piles for the different calculation methods. As reported by Poulos (1997), noteworthy differences appear between the results. The EP approach yields similar results to the standard finite element approach, however the EP concept tends to result in higher average pile settlements and smaller pile loads compared to volume piles.

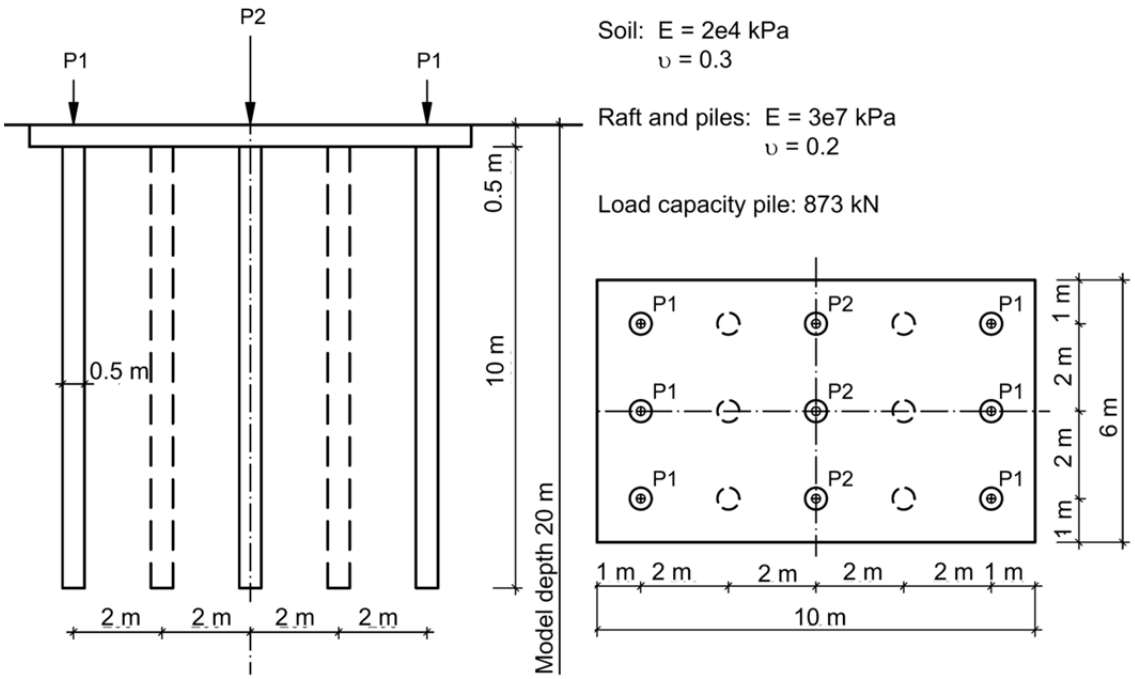

Fig. 105 Geometry of hypothetical example (after Poulos 1997)

Tab. 19: Cases analysed

	No. of piles	total load [MN]	P1 [MN]	P2 [MN]
case A	15	12.0	1.00	2.00
case B	15	15.0	1.25	2.50
case C	12	12.0	1.00	2.00

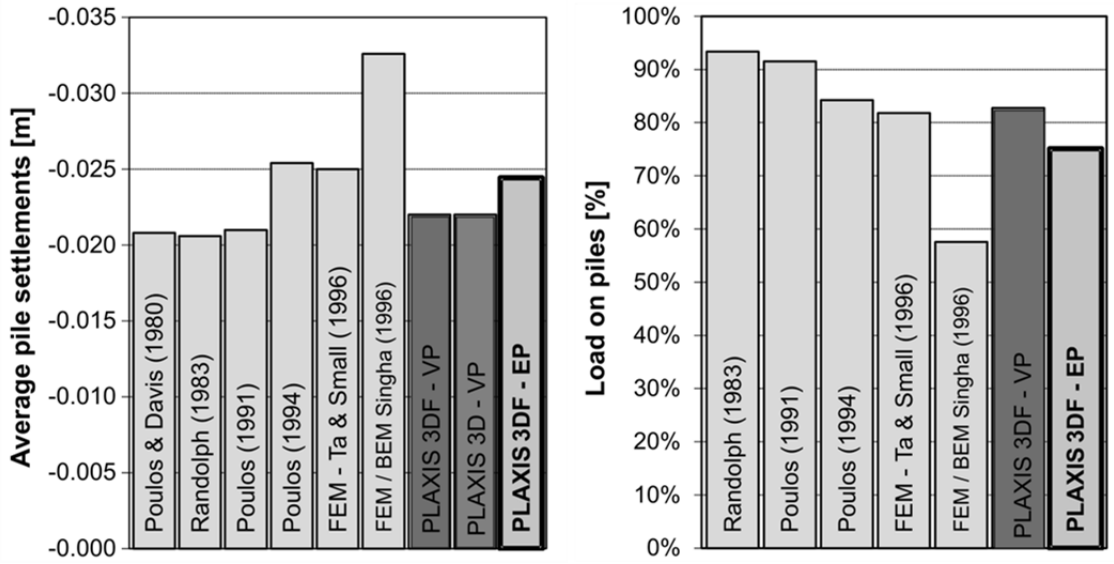

Fig. 106 Average pile settlements (left) and proportion of load carried by piles (right) - Case A

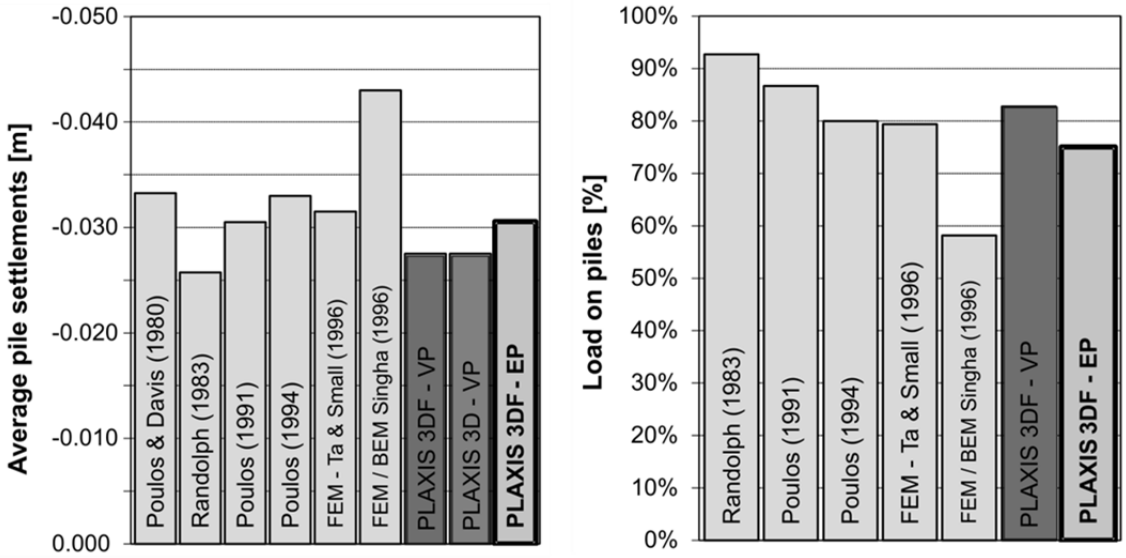

Fig. 107 Average pile settlements (left) and proportion of load carried by piles (right) - Case B

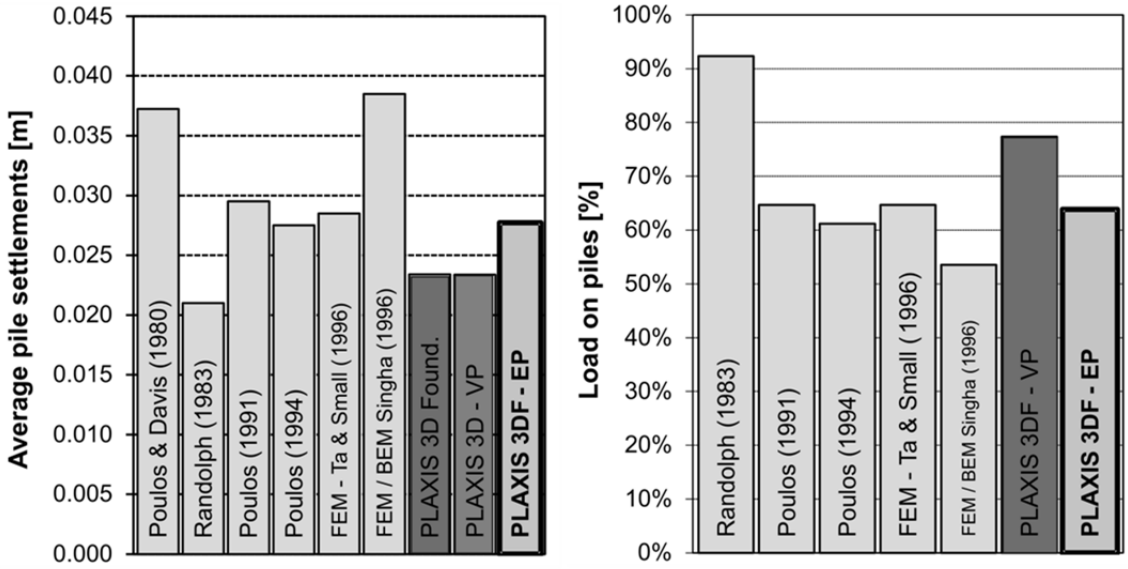

Fig. 108 Average pile settlements (left) and proportion of load carried by piles (right) - Case C

Poulos (2001c) used the same hypothetic example to study the influence of the number of piles on maximum settlements and the proportion of load carried by the piles. He also showed that very similar results are computed if a uniformly-distributed load is applied instead of concentrated loads (Tab. 19). Fig. 109 demonstrates that the same characteristics of the pile group are obtained employing the EPs. Of course the maximum settlement decreases with an increasing number of piles, but reaches an almost constant value for 20 or more piles. This comes from the fact that the load carried by piles increases

significantly for a limited number of piles, however for more than 20 piles, the rate of increase is rather small.

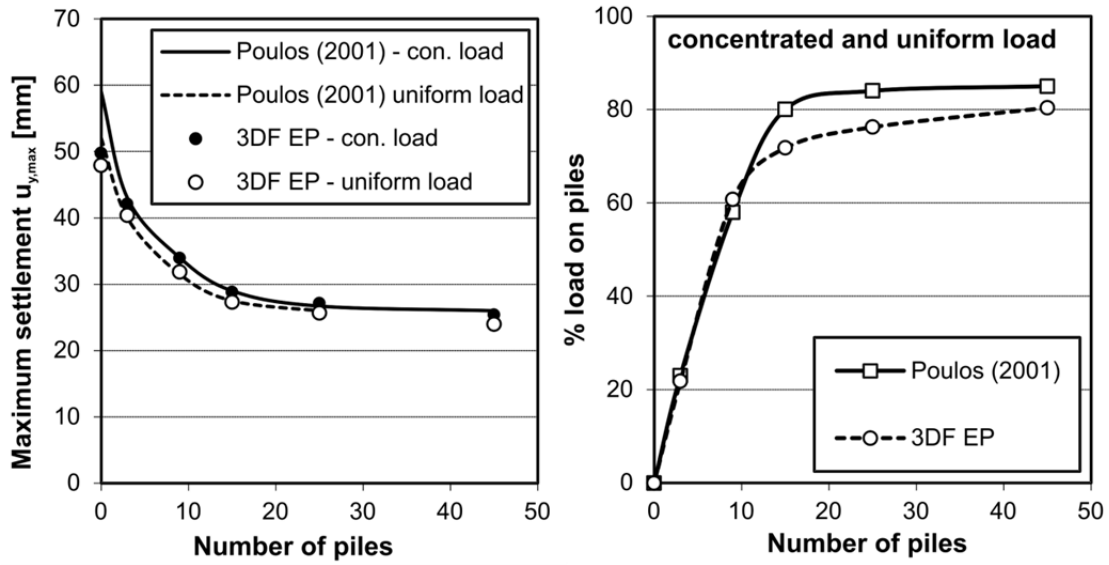

Fig. 109 Effect of number of piles on maximum settlements (left) and load carried by piles (right)

The next example was published by Hain & Lee (1978) and deals with an 8 x 8 pile group. Hain & Lee (1978) represented the raft as thin "plate" finite elements with variable stiffness and the pile response is computed from boundary element analyses (linear elastic). The same pile group was also used by Kitiyodom et al. (2011) to validate their approximate numerical analysis, where the piles and the soil are treated as interactive springs. To consider different relative stiffnesses, Hain & Lee (1978) introduced a relative stiffness K_r in additional to $\overline{K}$, which represents a relative stiffness between raft (E_r) and soil (E_{soil}).

$$\mathrm{K_r} = \frac{4 \cdot E_r \cdot t_r \cdot B_r (1-\nu^2)}{3 \cdot \pi \cdot E_{soil} \cdot L_r^4} \tag{93}$$

t_r, B_r and L_r are the raft thickness, width and length respectively and ν is the Poisson' ration of the soil. The first validation was related to the behaviour of an unsupported squared raft loaded with a uniform load. Fig. 110 compares the obtained settlement troughs and bending moments (M) obtained with PLAXIS 3DF with Hain & Lee (1978), Kitiyodom et al. (2011) and Poulos (1994). K_r values of 0.01 and 10 are considered, where 0.01 represents a relatively flexible raft and 10 a relatively stiff foundation. The vertical raft displacements u_y are presented in normalized form, where q_r is the applied constant distributed load. Both charts show a very good agreement between the different calculation methods.

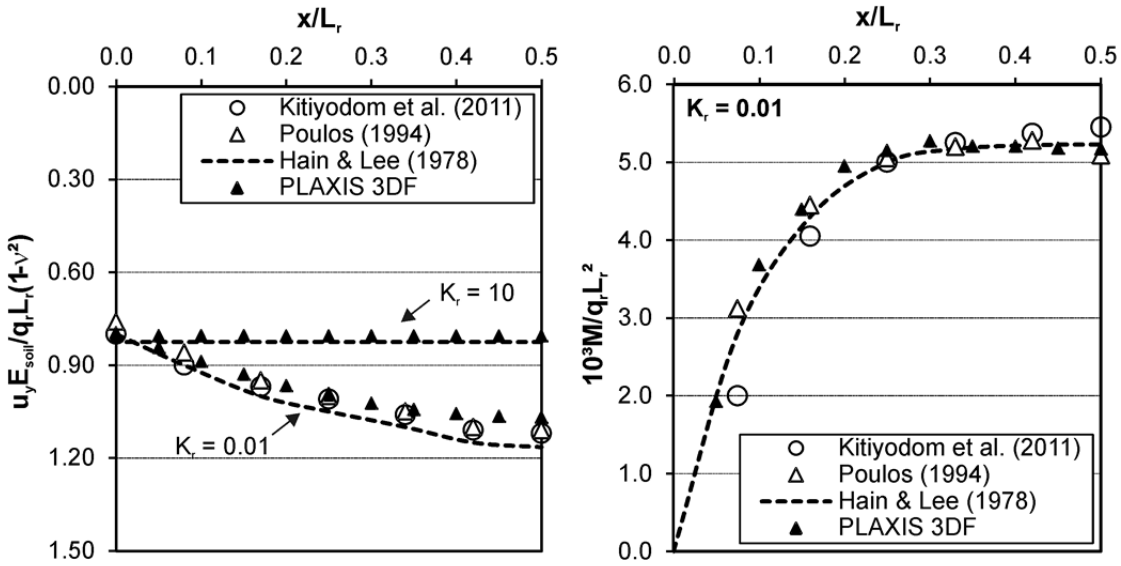

Fig. 110 Comparisons between solutions for uniformly loaded raft

In the next step, the different approaches for modelling piles are compared with the embedded pile option. A squared foundation is analysed, with $L_r = B_r = 50 \cdot D$ supported by 64 piles with a regular spacing e_P of $6.25 \cdot D$. For the finite element model, two axis of symmetry are taken into account; as a consequence, only 16 piles are modelled. The soil is modelled as linear elastic material and the relative stiffness $\overline{K}$ = 1000. Different pile slenderness ratios *L/D* and relative stiffnesses K_r are studied.

Fig. 111 compares the maximum settlements for different K_r values and different pile slenderness ratios. Once the bending stiffness of the raft increases, the maximum vertical displacements decrease due to the fact that less differential displacements take place within the raft. One can see that the results of Poulos (1994) and Hain & Lee (1978) fit very well. The results of Kitiyodom et al. (2011) show less maximum displacements. Also, when using the embedded pile concept, the computed displacements are underestimated compared to Poulos (1994) and Hain & Lee (1978). One reason is probably because a limited depth is used for the finite element analyses, while the approach presented by Hain & Lee (1978) assumes a deep homogenous layer. In the author's opinion, another reason is that the settlements presented by Poulos (1994) and Hain & Lee (1978) are overestimated for *L/D* ratios larger than 50. The tendencies are nevertheless identical, and compared with Kitiyodom et al. (2011), the agreement is reasonable. Fig. 111 also shows the evaluation of maximum differential displacements ($\Delta u_{y,max}$) of the raft for different relative stiffnesses. The agreement between Hain & Lee (1978) and the embedded pile approach is almost perfect. Also, the other models show similar results of raft deflections. It is important to keep in mind that differential displacements are in the majority of cases the key point of interest.

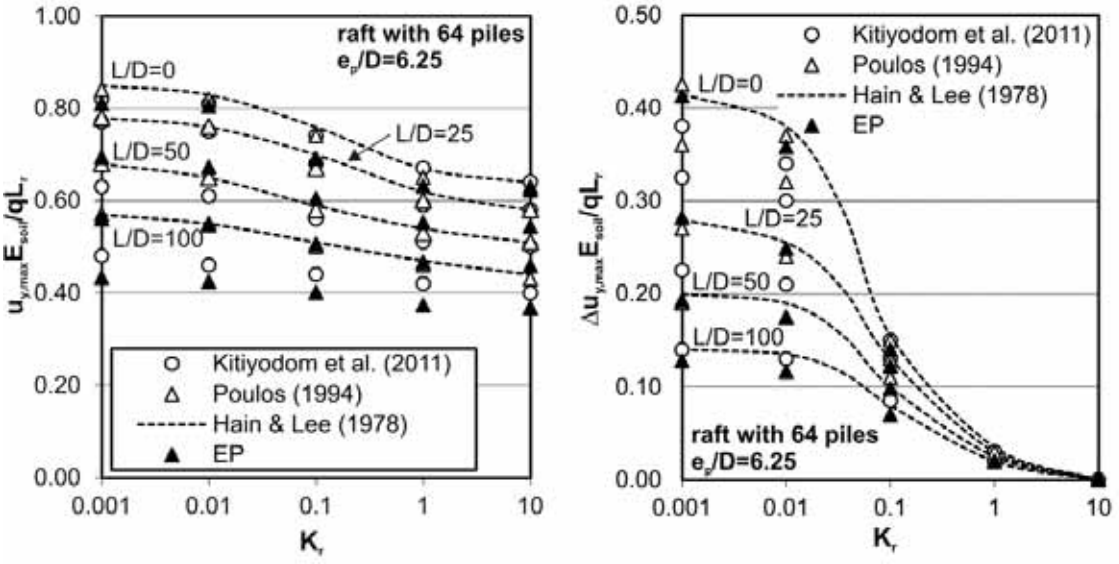

Fig. 111 Maximum settlements (left) and maximum differential displacements (right) obtained with different calculation models

The next piled raft foundation investigated was presented by Chow & Small (2008). The geometrical conditions are shown in Fig. 112. They studied two soil profiles, one with four different layers (where the stiffness of the layers increases with depth) and another simplified profile with one homogenized soil layer. The example was recalculated with both conditions, but in the following, only results related to one homogeneous soil layer are presented. The soil stiffness is 62.5 MPa and the Poisson's ratio is 0.175. The raft and the pile also behave linear elastic, with E = 2e4 MPa and ν = 0.2. The piled raft is subjected to a constant distributed load of 50 kPa. A relatively fine mesh with about 54000 elements was defined, because in addition to the settlement troughs, the normal force in the pile and the skin friction distribution along individual piles are also compared.

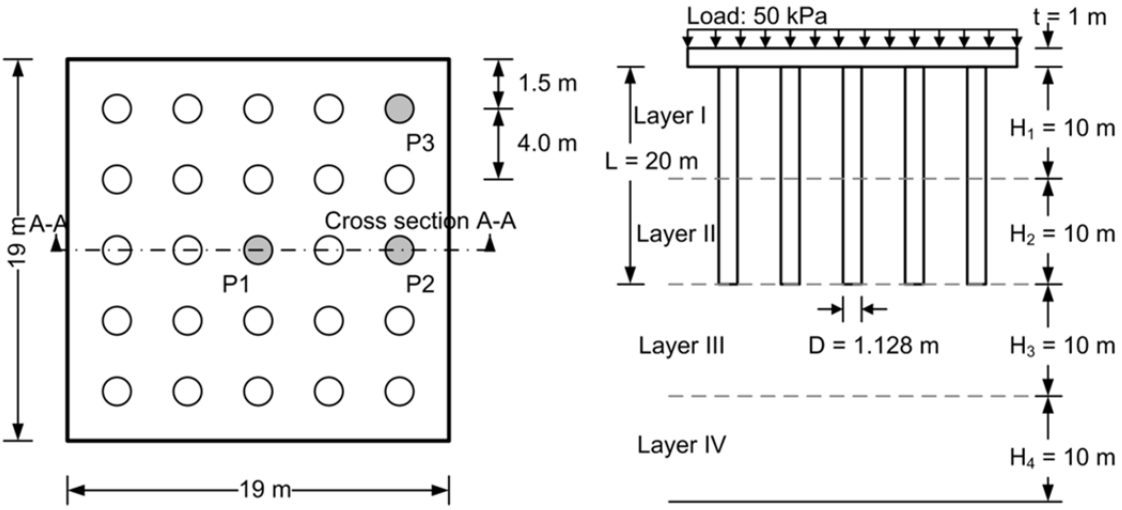

Fig. 112 Layout of piled raft foundation studied by Chow & Small (2008)

Fig. 113 illustrates the settlement troughs obtained with the standard finite element approach and with embedded piles. Both the maximum vertical displacements and the differential settlements (settlement troughs) are in very good agreement with the APRILS analysis presented by Chow & Small (2008). The difference between this analysis and the FEM calculation presented by Chow & Small (2008) is not discussed by the authors. Fig. 113 and Fig. 114 show the normal force and skin friction distributions of pile 1 and pile 2. For both piles, the normal force distribution shows reasonable agreement with the published data, and the skin friction distribution, computed with the EP concept, is very similar to the one presented by Chow & Small (2008).

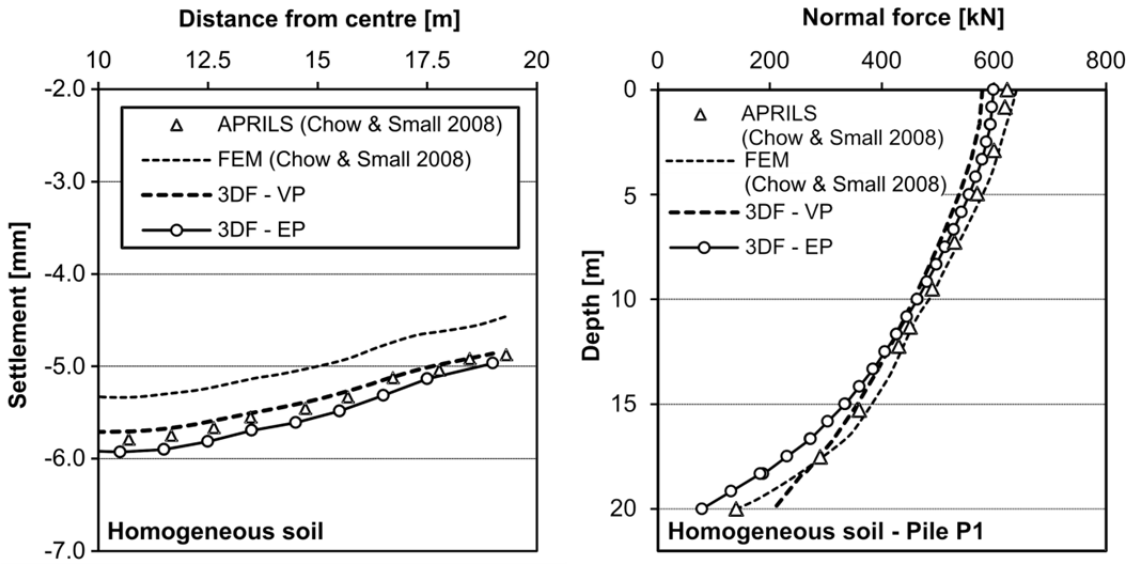

Fig. 113 Differential settlements (left) and normal force in pile P1 (right)

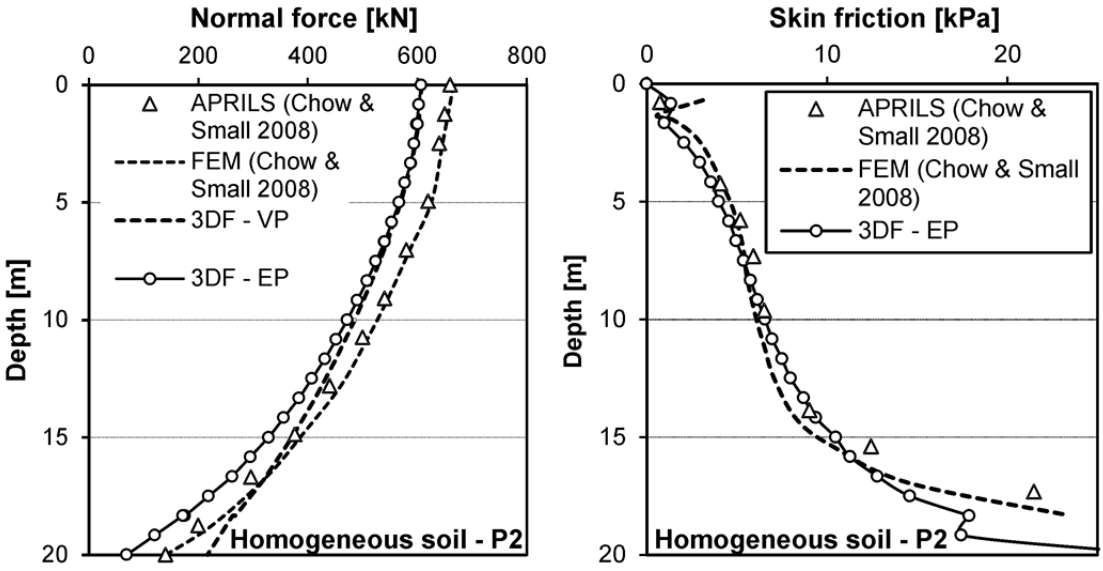

Fig. 114 Normal force in pile P2 (left) and skin friction along pile P2 (right)

Finally, a numerical study of simplified piled raft foundations was performed. The key questions inspected and presented in the following is the relative proportion of load carried by the raft and piles and the mobilization of the skin friction with respect to different piled raft geometries. A simplified model based on a "unit cell approach" is chosen in order to compare 2D axisymmetric analyses with 3D analyses employing volume discretisation for the piles and the embedded pile concept. Two aspects are investigated, the influence of pile spacing and the influence of how the pile is modelled (volume element vs embedded pile).

Fig. 115 illustrates the general layout of the model and the dimensions of the different models. Two geometric conditions are considered: piled raft I and piled raft II, which differ in the spacing of the piles, i.e. the dimension of the unit cell. The most important geometrical relation is the ratio between raft width divided by the diameter of the pile. For all studies presented, the same soil - a dense sand - is used, and no ground water is taken into account. The input parameters for the HS model are given in Tab. 20. The axisymmetric model for geometry piled raft I consists of 460 15 noded elements, and the model for geometry piled raft II has 750 elements. The pile soil interaction is modelled by means of interface elements and a constant distributed load is defined at the top of the raft. The 3D model, using the standard finite element approach, consists of 12600 elements for piled raft I and 22230 elements for piled raft geometry II.

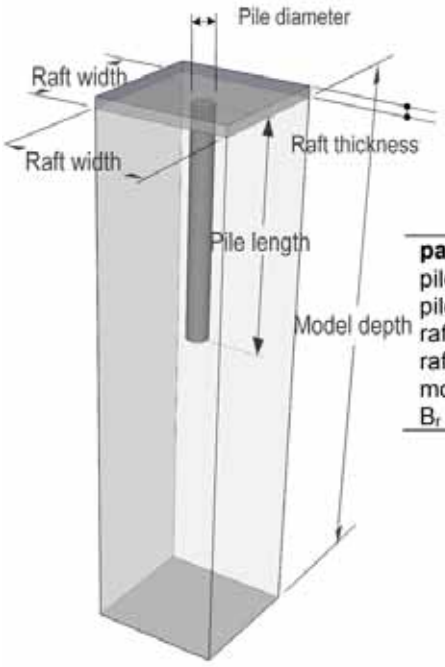

parameter	symbol	piled raft I	piled raft II
pile diameter	D	0.8 m	0.8 m
pile length	L	15.0 m	15.0 m
raft width	B_r	2.0 m	5.0 m
raft thickness	t_r	0.5 m	0.5 m
model depth	D_m	40.0 m	40.0 m
B_r / D	-	2.5	6.25

Fig. 115 Geometry of simplified piled raft foundation

Tab. 20: Hardening Soil properties of dense sand

γ_{unsat} [kN/m^3]	$E_{50,ref}$ [kPa]	$E_{oed,ref}$ [kPa]	$E_{ur,ref}$ [kPa]	ν'_{ur} [-]	p_{ref} [kPa]	m [-]	φ' [°]	c' [kPa]	ψ [°]	K_0^{nc} [-]
19.0	6e4	6e4	1.8e5	0.2	100	0.55	38	0	8	0.38

Fig. 116 shows the mobilized skin friction of piled raft I obtained in the 2D analysis and the distribution of shear stresses for a single pile subjected to a point load of 2000 kN. The distribution of the skin friction increases with depth for a single pile due to the stress-dependent stiffness and the fact that the shear stress is related to the effective normal stress σ'_n along a pile. Additionally, the skin friction distributions (obtained with 2D and 3D analyses) of piled raft geometry II for different load levels are compared. The obtained results from the 3D calculations are generally in very good agreement with the axisymmetric calculations. However, at the end of the pile one can see a difference between the 2D and 3D results. This is because in the 2D axisymmetric calculations the interfaces are slightly longer than the pile to prevent stress oscillations (see chapter 3.4.2.1). This can also be done in the 3D calculations to improve the stress distribution at the end of the pile for high loads, but has not been done here.

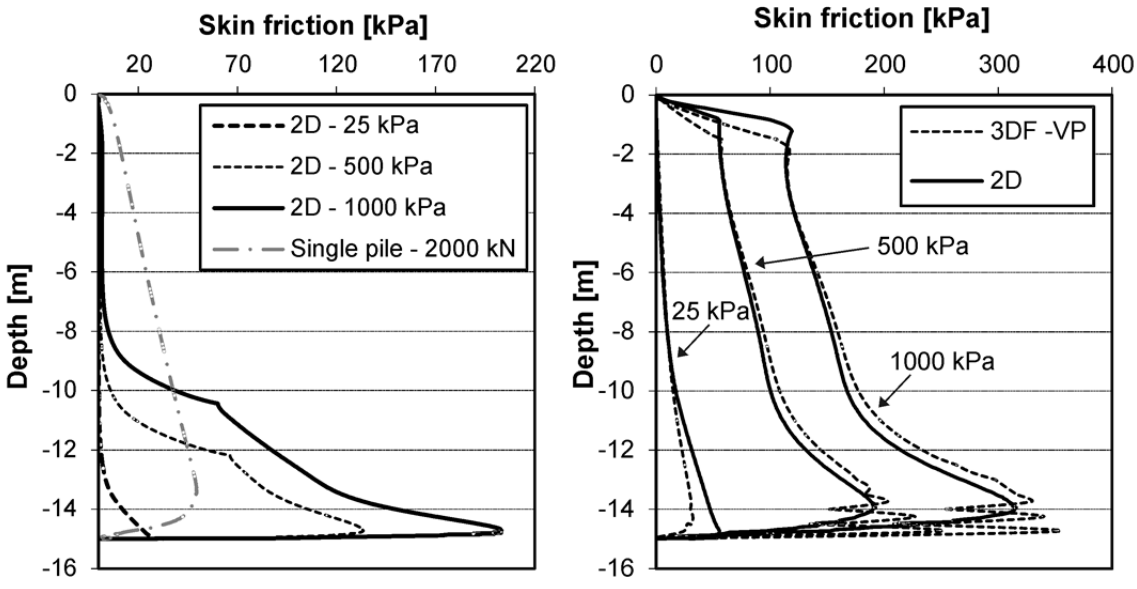

Fig. 116 Skin friction: piled raft I vs single pile (left); 2D vs 3D for piled raft geometry II (right)

For geometry piled raft I, where the spacing between the piles is relatively small, almost no skin friction is mobilized at the top of the pile. For piled raft geometry II the mobilization of shaft resistance is strongly influenced by the pile-raft interaction. As a consequence of the load transfer from the raft to the soil the

stress state in the soil increases, and as a result the maximum skin friction increases (see also Katzenbach et al. 2007). In the following, the raft-soil and raft-pile interactions are studied in detail. Therefore the α_{PR} factor is determined. Fig. 117 represents the evolution of the α_{PR} factor as well as the factor (1 - α_{PR}) that describes the amount of the load, which is transferred by the raft to the soil. The α_{PR} factor is not a constant value, but depends strongly on the load level. Fig. 117 also indicates the significant influence of the interaction between the soil and the pile (R_{inter}). In contrast to single piles, where the R_{inter} value has a big influence on the load-settlement behaviour, the effect of the strength reduction factor on computed displacements is not significant when dealing with piled raft foundations. However, the pile-soil interaction is essential for the load distribution of piled raft foundations and thus important for the design of such foundations. Fig. 117 also illustrates the mobilized resistances of a pile within the piled raft foundation. From that follows, for load levels where α_{PR} is high, that the shaft of the pile (R_s) takes most of the load. Once the load increases, more load is transferred from the raft to soil, which means the (1 - α_{PR}) value increases and more load is transferred from the pile base to the soil (R_b).

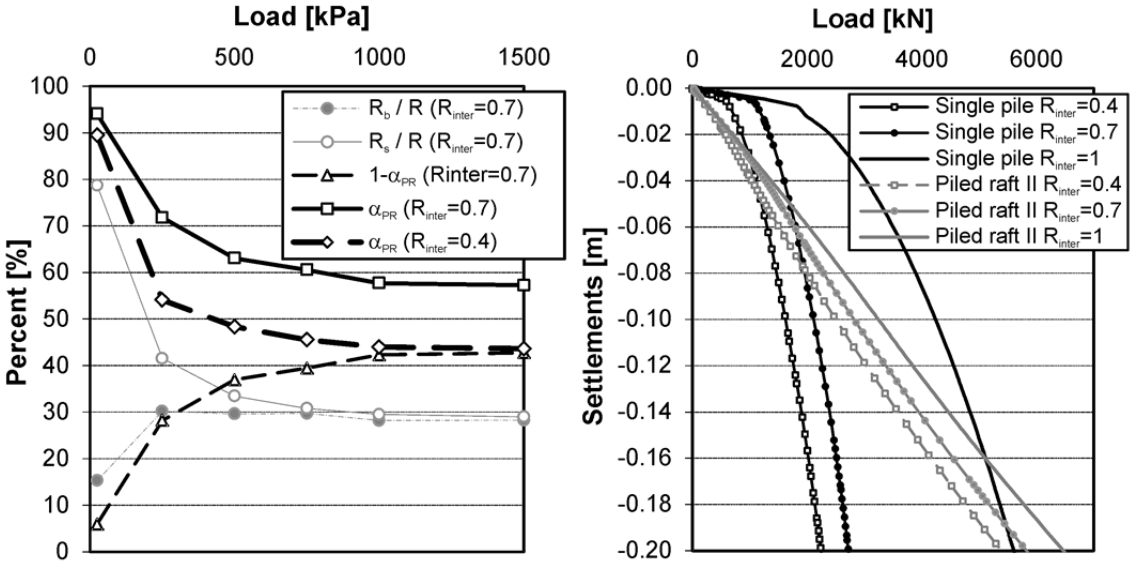

Fig. 117 Behaviour of piled raft geometry II (left); piled raft geometry II vs single pile (right)

In the following, piled raft geometry II was recalculated using the EP concept. The ultimate shaft resistance was definition with different profiles. The first distribution (constant) is defined with a constant value for the skin friction profile, and in the second calculation (multilinear), the skin friction profile at failure is defined with the values for the mobilized skin friction obtained in the appropriate axisymmetric model (Fig. 116). Results showed that the mobilized skin friction at working loads is influenced by the distribution of the ultimate skin friction profile. Of course, the change in the stress state at the top of the pile is not taken into account when using a predefined ultimate skin resistance, hence

the automatic increase of maximum skin friction due to the raft-soil interaction cannot be modelled with the linear or multilinear formulation. Therefore, another calculation with the "layer-dependent" skin friction definition and a strength reduction factor R_{inter} of 0.7 was performed. In contrast to the calculations with linear or multilinear definitions of the maximum skin friction distribution, the calculations with layer-dependent behaviour of the embedded piles (where the shaft resistance is related to the normal stress on the pile) are qualitatively in much better agreement with the 2D solution. Regarding the load-settlement behaviour, all calculation models yield very similar load-settlement curves. The maximum difference is less than 5% between the 2D and 3D results at a load level of 500 kPa.

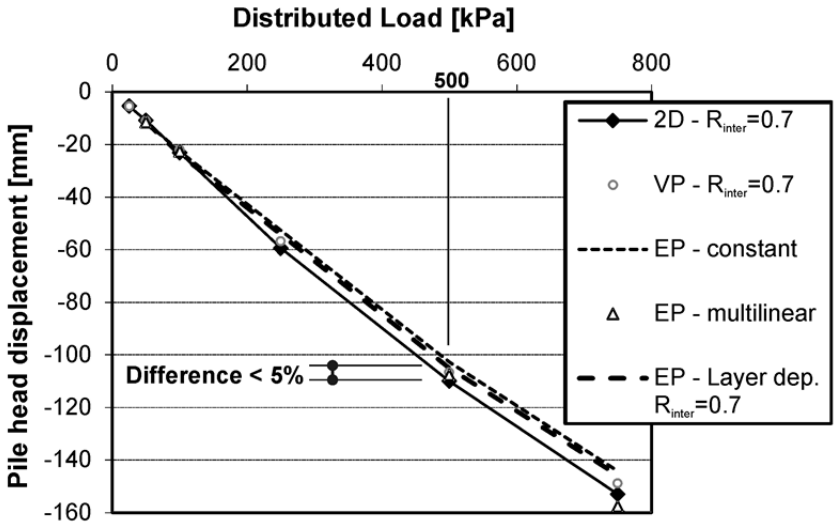

Fig. 118 Load-settlement curves of piled raft geometry II

In the author's opinion, the linear and multilinear definition of the ultimate skin resistance is a very functional tool. Of course, when dealing with pile groups or piled raft foundations, the distribution of $t_{s,max}$ depends, besides the soil properties, on the load level and the foundation geometry. In addition, the distribution is different for different piles (corner pile, edge pile etc.). To define reasonable profiles of $t_{s,max}$, simplified 2D studies - as presented in this chapter - are very convenient. Of course the layer-dependent option is an alternative, but due to the fact that the ultimate skin resistance is related to the stress state of the surrounding "soil" integration points, the mesh coarseness may have an influence on the pile capacity. Additionally, the EP concept cannot deal with a critical state of density; therefore in dilatant soils this option may lead to an overestimation of skin resistance. However, for settlement predictions in working load conditions, the different models yield very similar results.

6.4 Performance of horizontally-loaded pile groups and PRFs

Chow & Small (2008) presented results of a horizontally-loaded pile group of 25 piles. The same example was already used for the validation of a vertically-loaded pile group (Fig. 112). Again, only one homogenized soil layer is considered and a constant distributed load of 50 kPa is applied on top of the raft. Due to the fact that a bending stiff connection between the piles and raft should be modelled, the raft is defined as plate elements. Thus it is possible to couple the rotational degrees of freedom of the raft with those of the piles. Fig. 119 shows the horizontal deflection and the consequential bending moments of the centre pile P1, and Fig. 120 shows the same for the corner pile P3. The computed horizontal deflections and resulting moments of the embedded piles are very similar to those obtained with the standard finite element approach and the results presented by Chow & Small (2008). Tests with finer discretizations were conducted as well, but the results showed that in this example the mesh coarseness does not have a noteworthy influence.

The same example was recalculated with the Hardening Soil model and the parameters of loose sand given in Tab. 16. Fig. 121 illustrates the bending moments in pile P1, P2 and P3 and demonstrates that both calculation models yield very similar results.

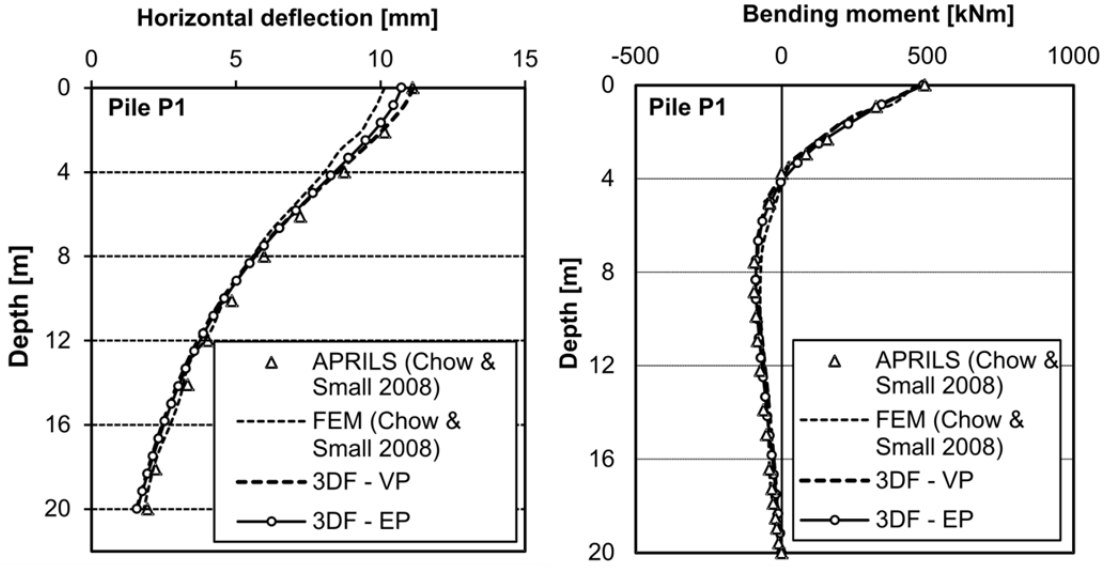

Fig. 119 Horizontal deflection (left) and bending moments of pile P1 (right) for homogeneous soil conditions

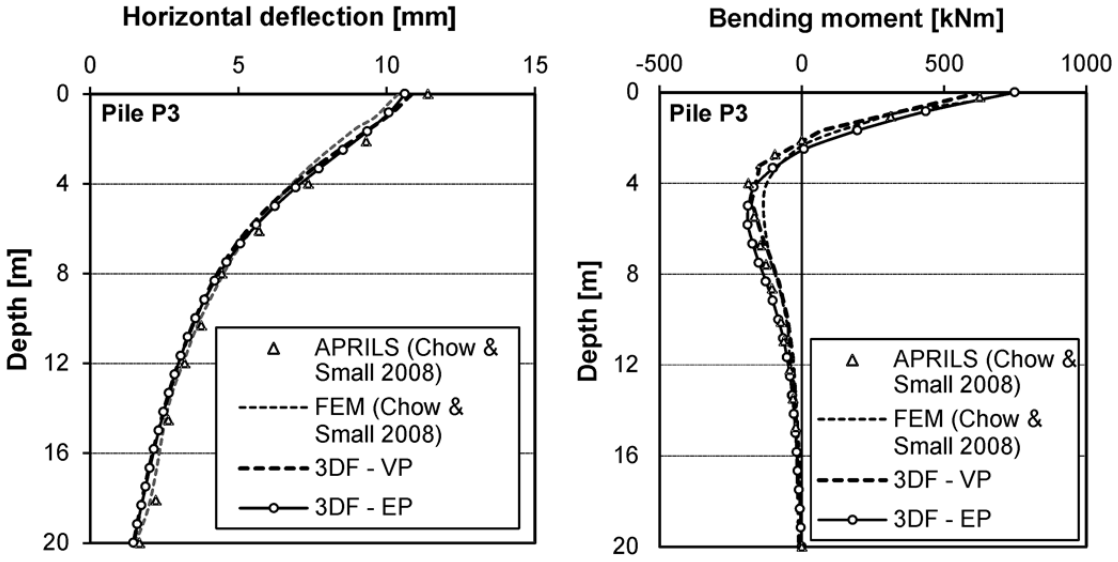

Fig. 120 Horizontal deflection (left) and bending moments of pile P3 (right) for homogeneous soil conditions

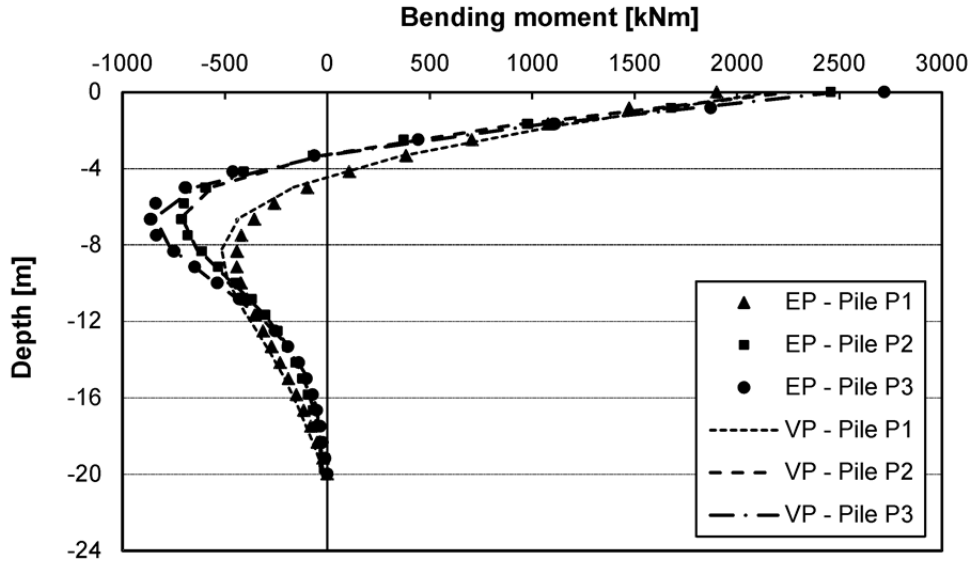

Fig. 121 Bending moments of pile P1, P2 and P3for homogeneous loose sand (HS model)

The final example considered was presented by Small & Zhang (2002). They used the APRAF program (Analysis of Piled RAft Foundations) to investigate the behaviour of piled raft foundations under lateral loading. The program uses the finite layer theory (Small & Booker 1986) to analyse the soil and the FE method to analyse the raft and the piles. The geometry of the studied piled raft foundation is given in Fig. 122. The piles have length of 15 m, a diameter D of 0.564 m and spacing e_p of 3D. The soil is defined as linear elastic material with E_{soil} of 10000 kPa and a Poisson's ratio of 0.3. The relative stiffness $\overline{K}$ is defined

with 3000. Small & Zhang (2002) also conducted FE analysis to validate the APRAF program.

The same example was analysed with different approaches in PLAXIS 3DF and 3D. For the standard FE approach, 9 pairs of concentrated point loads of 1 MN are applied at the top of each pile, and 9 point loads of 2 MN are assigned in the calculations with embedded piles. Fig. 123 compares the raft displacements along cross section A-A and the horizontal deflection of the centre pile A.

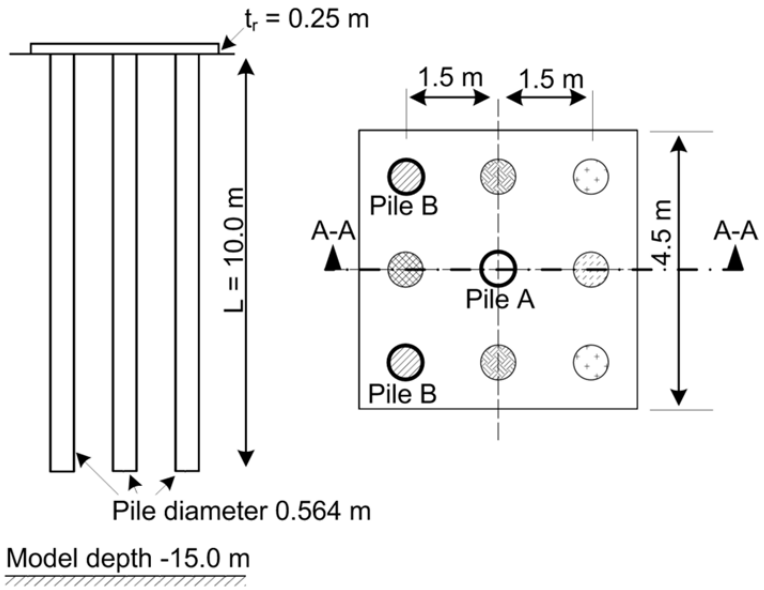

Fig. 122 Geometry of piled raft foundation

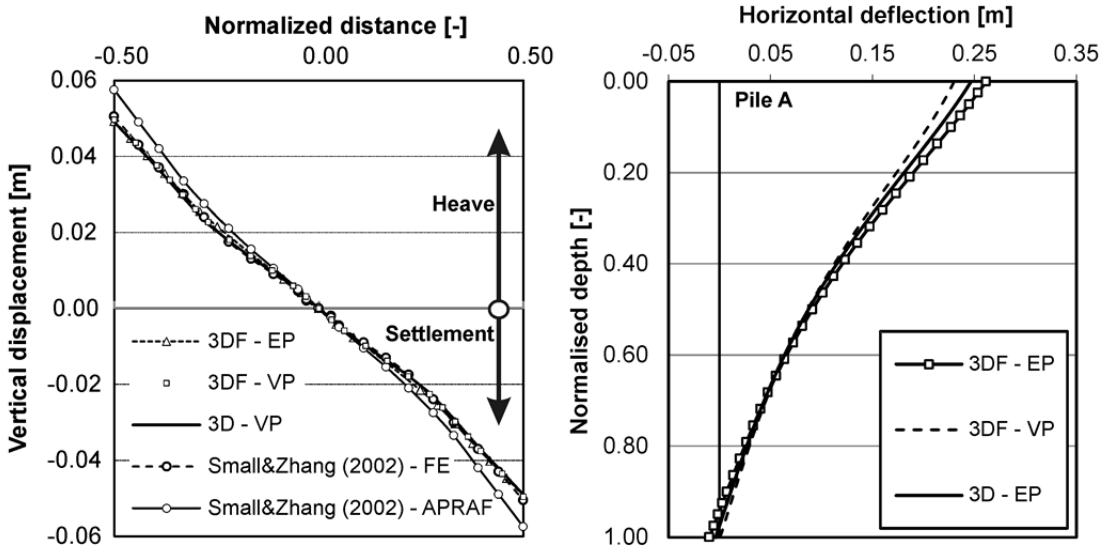

Fig. 123 Vertical displacements along cross section A-A (left) and horizontal deflection of pile A (right)

One can see that the obtained settlements are very similar for the different approaches and programs; only the APRAF calculation results in slightly higher heave and settlements. Also, the horizontal deflections computed with EPs agree very closely with those of the standard FE approach.

The same piled raft foundation was recalculated with the Hardening Soil Small model to verify the improved embedded pile approach. The soil parameters given in Tab. 16 were used, as well as a G_0 of 75000 kPa and a reference shear strain $\gamma_{0.7}$ of 1.5e-4. The interfaces along the volume piles were 0.25 m extended (see chapter 3.4.2.1) and the embedded piles were defined with a constant skin friction distribution $T_{top,max} = T_{bot,max} = 100$ kN/m. The ultimate foot resistance $F_{max} = 500$ kN. Fig. 124 compares the horizontal pile deflection and the resulting bending moments obtained with the volume and the embedded piles.

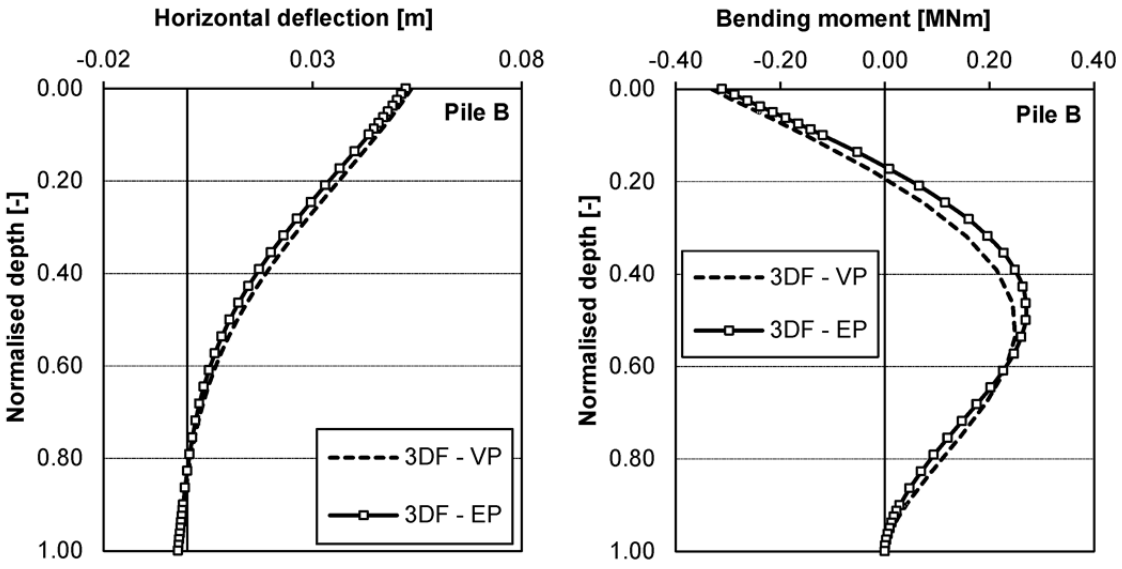

Fig. 124 Horizontal deflection (left) and bending moments of pile B (right) obtained with the HSS model

The agreement between the different approaches is very good, which indicates that the improved EP formulation is well capable for horizontally-loaded pile groups as well.

7 Application to boundary value problems

7.1 DC Towers Vienna

7.1.1 General information

The projects discussed are two very high and slender towers in Vienna. Tower I has a total height of about 220 m and tower II of 165 m. The deep foundation concept for both towers consists of box-shaped barrettes. The general behaviour of this deep foundation system is explained e.g. in Hoffman (2007). It is planned to build the foundations for both towers at the same time but to construct the superstructure of tower I first. Due to the fact that the distance between the two towers is only 24 m it is necessary to take the loads from the later-built tower II into account in the design of the foundation system of tower I. The excavation depth for constructing the base slabs of both towers is about 8.5 m. Fig. 125 illustrates an image of the entire building (©beyer.co.at) and an overview of the designed layout of the diaphragm wall panels. The barrettes have a unit length of 3.6 m and a unit width of 0.6 m. This layout is used for all calculations presented in the following. The circumference of the foundation elements indicates at the same time the dimensions of the two towers. Next to the towers, four stories of underground car parks are planned.

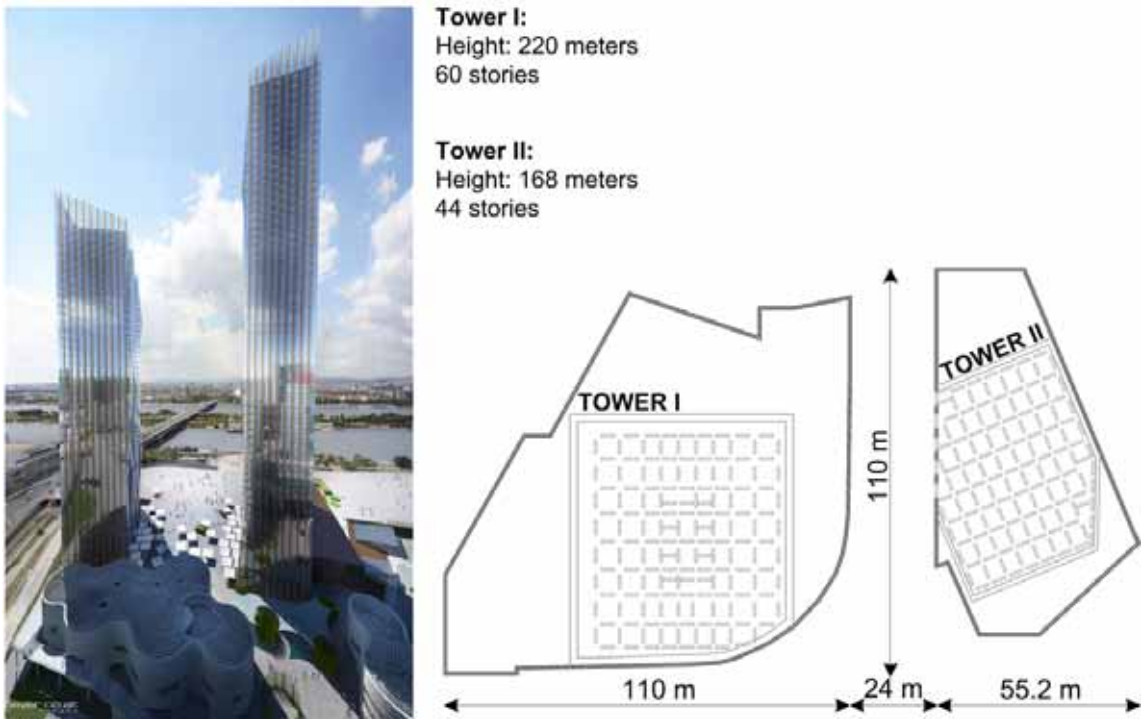

Fig. 125 Project overview (© beyer.co.at) – DC Towers

The soil profile for the finite element simulation is based on core drillings with depths down to -70.0 m from the surface. The first 4 to 5 m consist of deposits, followed by a 6.5 m thick layer of gravel and then alternate layers of either sands or silty clays. A more detailed description of the soil condition is given in Würger (2007) and Martak et al. (2007). Fig. 126 shows the soil profile obtained with the borehole logs together with important levels of the construction and the evaluation of E_{oed} and E_{ur} over depth.

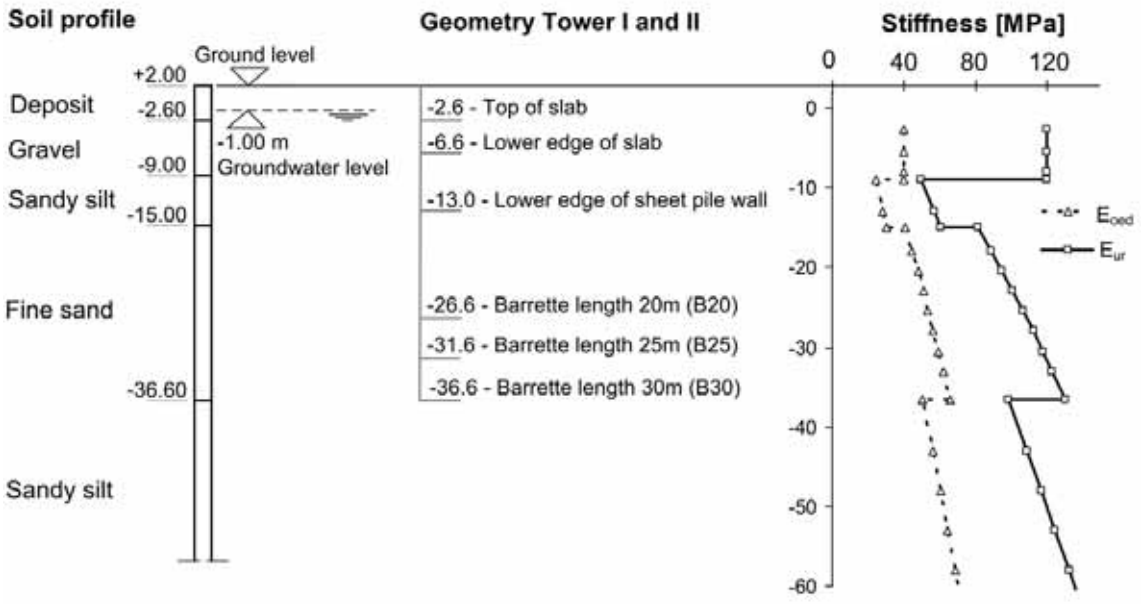

Fig. 126 Soil profile (left), geometry of towers (middle) and evaluations of E_{oed} and E_{ur} (right)

For the calculations presented, either the Hardening Soil or the Hardening Soil Small model was used to model the soil behaviour. The small strain shear modulus G_0 is defined with the help of a correlation between very small strain stiffness and stiffness at larger strains after Alpan (1970). The therefore necessary static Young's modulus is interpreted as unloading/reloading stiffness, which correlates to recent published experimental data (Wichtemann & Triantafyllidis 2009). The value of $\gamma_{0.7}$ is taken from stiffness reduction curves after Vucetic and Dobrey (1991). The input parameters for the Hardening Soil model are given in Tab. 21 and the additional two parameters for the HSS model in Tab. 22.

All slabs behave linear elastic and the diaphragm wall elements are modelled with the Mohr-Coulomb model. In addition, the tensile strength of the barrettes is limited to a value of 3000 kPa.

Tab. 21: Soil properties for the Hardening Soil model

parameter	unit	deposit	gravel	sandy silt	fine sand
γ_{unsat}	kN/m^3	17.5	21.0	20.0	20.0
γ_{sat}	kN/m^3	20.5	22.0	20.0	21.0
$E_{50,ref}$	kPa	2 000	40 000	20 000	25000
$E_{oed,ref}$	kPa	2 000	40 000	20 000	25000
$E_{ur,ref}$	kPa	6 000	120 000	50 000	62 500
ν'_{ur}	-	0.2	0.2	0.2	0.2
p_{ref}	kPa	100	100	100	100
m	-	0.60	0.00	0.80	0.65
φ'	°	27.5	35.0	25.0	32.5
c'	kPa	0.0	0.0	20.0	2.0
ψ	°	0.0	5.0	0.0	2.5
K_0^{nc}	-	0.538	0.426	0.577	0.463

Tab. 22: Additional parameters for the Hardening Soil Small model

parameter	unit	gravel	sandy silt	fine sand
G_0	kPa	150 000	62 500	78125
$\gamma_{0.7}$	-	1e-4	2e-4	2e-4

All calculations are carried out as a drained analysis, thus final settlements are presented. But to obtain realistic final deformations a reliable stress distribution in the soil after the excavation is required. Consequently, it is necessary to model the construction process. This is done in the following phases:

- Generation of initial stresses
- Activation of the sheet pile wall
- Excavation and groundwater lowering
- Activation of barrettes (wished in place)
- Activation of slabs
- Full loads of tower I and loads from basement floors of tower II
- Closing of settlement joint - tower I
- Full loads of tower II
- Closing of settlement joint - tower II
- End of ground water lowering

As reported for example in Fross (1973), the soil layers in the region of Vienna are highly overconsolidated. This was taken into account in the generation of the initial stresses with a pre-overburden value (*POP*) of 600 kPa and an increased earth pressure coefficient K_0 of 0.7. The influence of the overconsolidation on the yield surfaces of the HS respectively HSS model is explained in Appendix A.

7.1.2 Optimisation of deep foundation system

Because of the small distance between the two towers an interaction was expected and thus it was necessary to model both towers. First calculations with connected diaphragm wall panels led to an overestimation of the stiffness of the deep foundation system, hence a non-conservative prediction of differential displacements. But when modelling all barrettes explicitly, the numerical models get very expensive. To reduce the complexity of the 3D model, the barrettes of only one tower are first modelled in full detail and the foundation system of the other tower is modelled as a homogenized block, meaning that the zones of the subsoil in which panels are installed are defined with smeared properties. Fig. 127 shows one finite element model, in which only tower I is modelled in detail. With this approach the global settlement behaviour of the entire structure is calculated because the interaction of the towers is taken into account. All barrettes are modelled by means of volume elements.

However, to validate this modelling assumption an analysis where the foundations of both towers are explicitly modelled is also presented. The detailed model consists of nearly 137000 wedge elements. In these models, 317 barrettes are modelled as volume elements. The results shown in this paragraph are related to the HSS model. In the last section of this chapter the results are compared with the HS model and the benefit of the HSS model will be discussed.

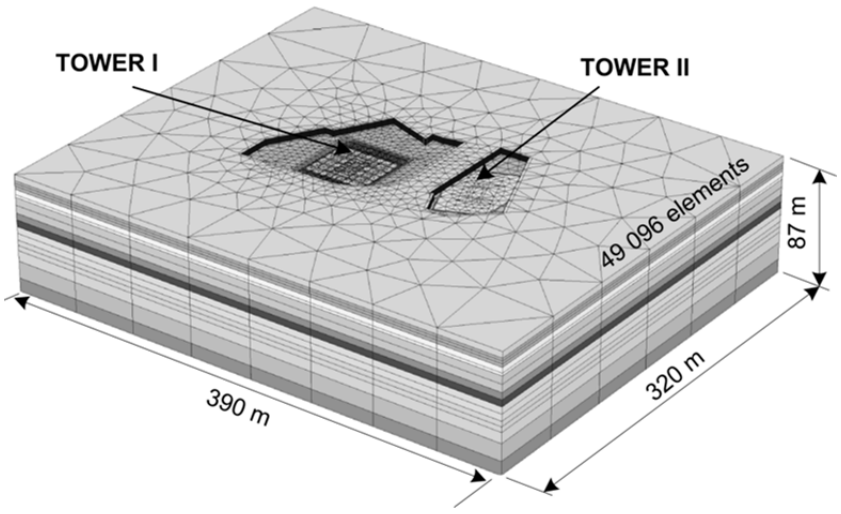

Fig. 127 Simplified finite element model

In the first analysis a constant length of 25.0 m for all barrettes was defined. The calculation was performed once for a detailed geometry of tower I and in a separate calculation for a detailed model of tower II. For both calculations maximum vertical displacements of about 80 mm were calculated, and the assumption that tower II contributes to settlements in the region of tower I was confirmed. Fig. 128 shows the contour lines of vertical displacements for the model where tower II is modelled in detail. Because of the eccentric loading of both towers the maximum settlements are also off-centre and large differential settlements are calculated. Therefore it is necessary to optimise the foundation system in a way that the expected maximum of deformation is in the centre of each tower. In addition, it is required to design the deep foundation elements of tower I with prevision of the settlements coming from the later built tower II. For this optimisation procedure a number of 3D analyses have been performed for both towers.

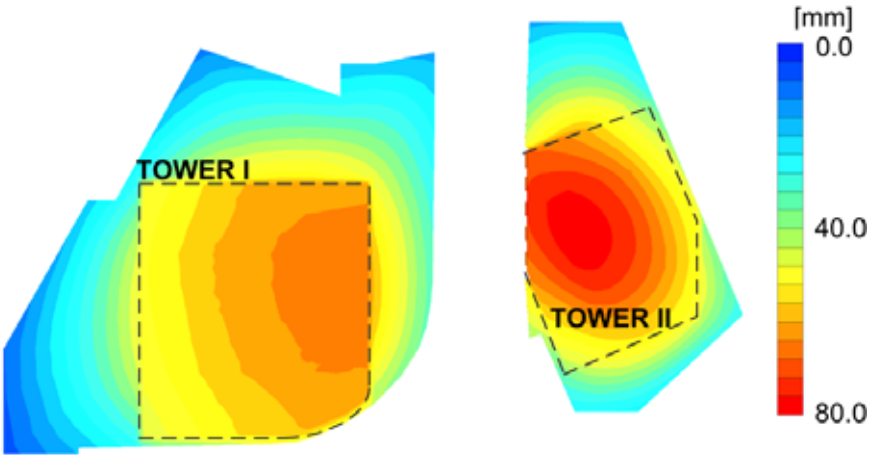

Fig. 128 Contour lines of vertical displacements for detailed model of tower II with 25 m long barrettes

The result of this study is a final layout of the panels with lengths between 20 and 30 m. The maximum settlements calculated are again about 80 mm for both towers, but this foundation set-up does not yield eccentric settlement troughs. Fig. 129 shows the optimised layout for both towers obtained with the simplified models.

Finally, a calculation with the detailed geometry for both towers and a much finer mesh discretisation was performed. Due to the size of the analysis, a 64-bit calculation kernel was used. The maximum vertical displacements are similar to the calculations using the simplified models, but concerning the interaction of both towers and the settlement trough between the buildings a more accurate result is obtained. Fig. 130 illustrates the optimised layout for both towers in a bottom view and the contour lines of vertical displacements of the structural elements when using the detailed FE model.

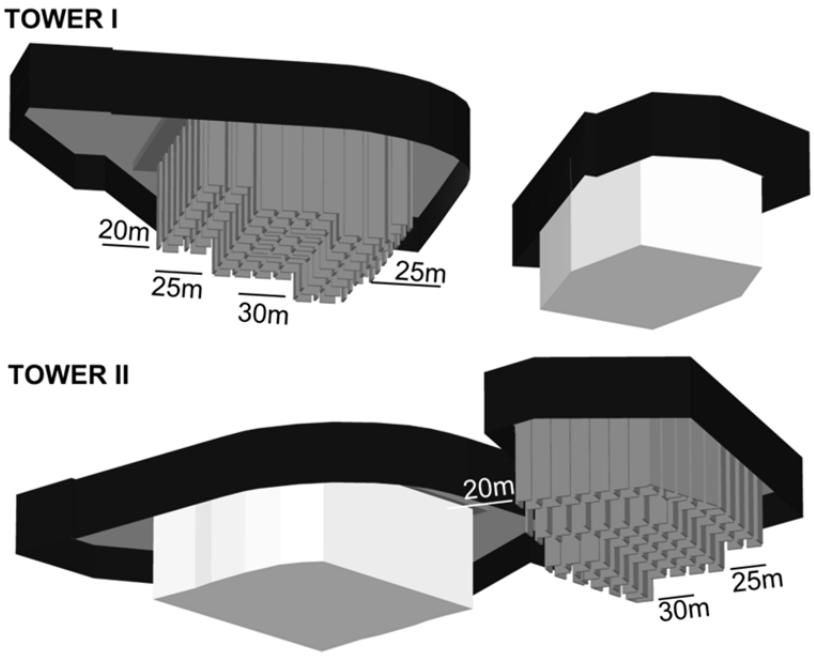

Fig. 129 Optimised barrette layout for tower I and tower II (simplified models)

Due to the fact that the two towers are located in a densely built-up region, settlement troughs are also a key issue of the settlement prediction. Thus, some selected points are presented for which the differential settlements are worked out. Fig. 131 indicates the selected points and presents the vertical displacements u_y and the inclination (tan α) between two neighbouring points. The railway lines are in the most critical area, where a maximum vertical deformation of 18 mm and an inclination of the settlement trough up to 1/600 are calculated. This value is acceptable from a mechanical point of view, after Bjerrum (1973). The settlements are 14 mm in the region of the highways and between the towers, where a road is situated, displacements up to 40 mm are computed.

To demonstrate the effect of small strain stiffness the calculations with the final diaphragm wall layout are considered and the settlement distribution over depth is worked out for a point in the middle of the towers. This is done for the analysis performed with the HS and the HSS model. Fig. 132 shows the comparison of both constitutive models. Because the settlements are almost the same for both towers, only the graph for tower I is shown. Until a depth of 36.6 m below ground level, which is the level of the longest barrettes, the distribution of settlements obtained with the HS model is similar to the one obtained with the HSS model, but the HSS model computes 25% less settlements. Beneath the foundation elements the difference between the HS and HSS model increases and at a depth of -75.0 m below the surface the settlements obtained with the HSS model are 51% smaller than the one calculated with the HS model. This clearly shows the influence of small strain stiffness and indicates that once a model including small strain stiffness is used, the effect of the position of the bottom

boundary condition on the computed displacements is diminished and the right depth of influence is taken into account automatically by the constitutive model. Thus, a more realistic settlement behaviour can be obtained.

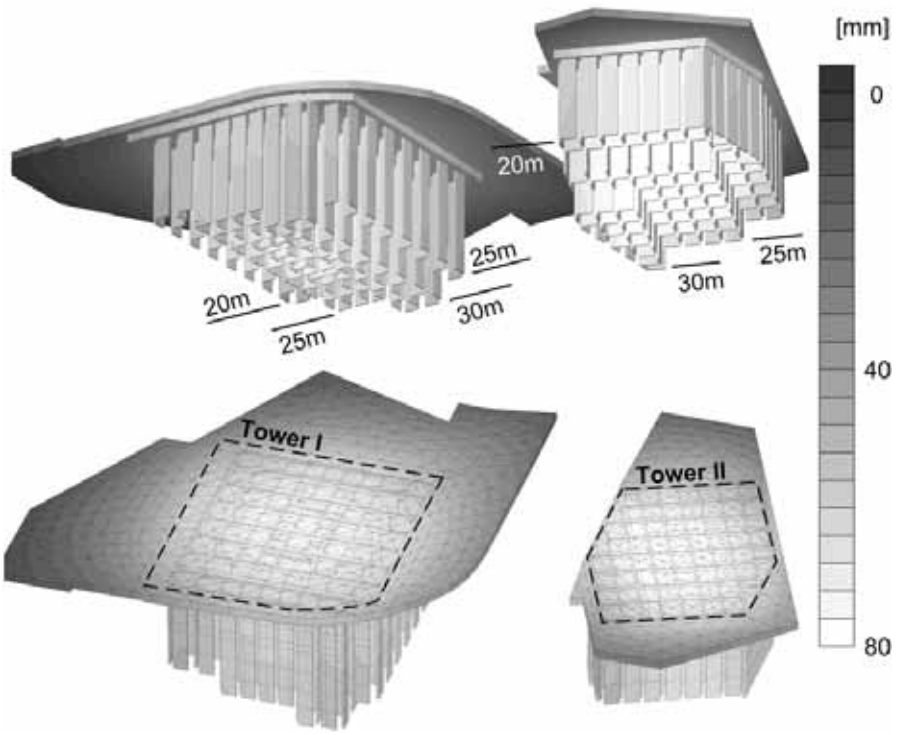

Fig. 130 Optimised barrette layout for tower I and tower II (detailed model)

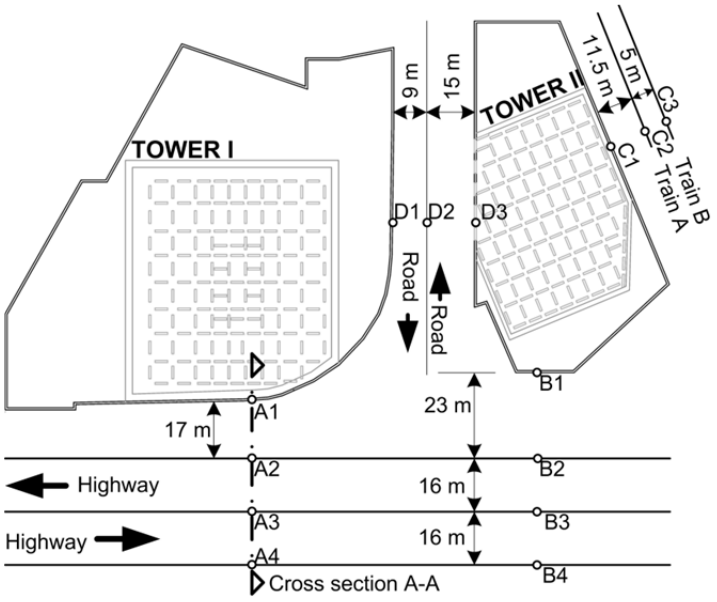

Point	u_y [mm]	tan α [-]
A1	33	
A2	14	1/900
A3	6	1/2000
A4	2	1/4000
B1	19	
B2	5	1/1600
B3	2	1/5300
B4	0	1/8000
C1	36	
C2	18	1/600
C3	13	1/1000
D1	38	
D2	32	1/1500
D3	48	1/900

Fig. 131 Schematic top view including adjacent structures

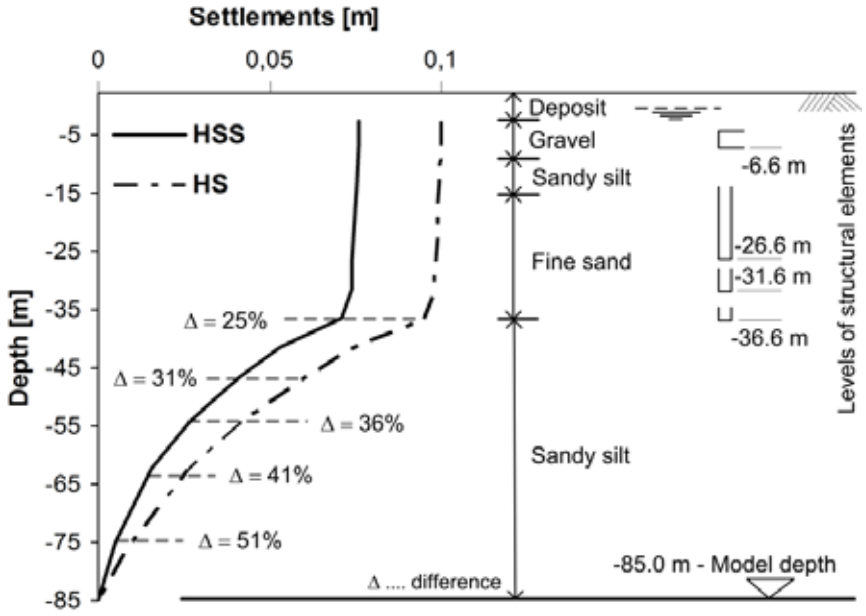

Fig. 132 HS vs HSS – Settlements over depth

Another significant difference is the computed settlement trough. With the HS model, the settlements at the surface are higher and the spread of relevant settlements is wider compared to the HSS model. Fig. 133 shows the settlement trough of cross section A-A (Fig. 131) at the surface for both constitutive models. The Hardening Soil Small model computes differential settlements between point A2 and A3 in the range of 1/2000. When using the HS model, this value decreases significantly to a value of 1/1000. This decrease of tan α is related to the big difference in maximum vertical displacements obtained with the different models. If the settlements are normalized by their maximum values, the behaviour changes and the settlement trough computed with the HSS model is steeper.

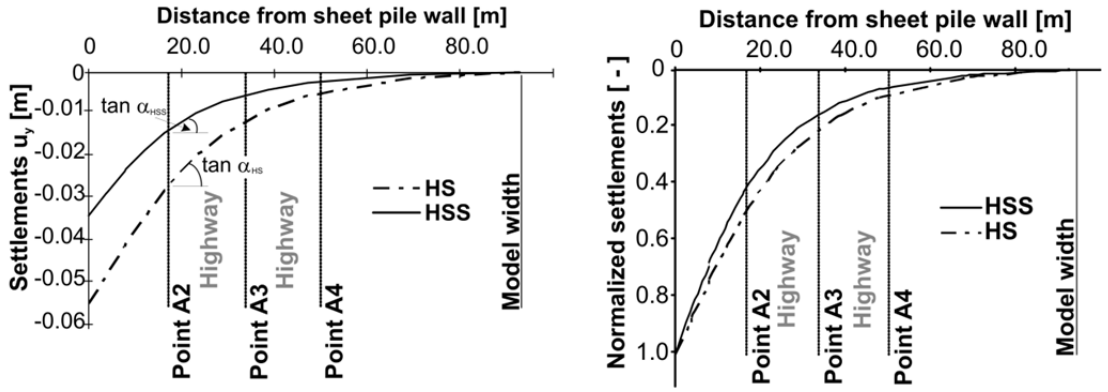

Fig. 133 Settlement troughs (left) and normalized settlement troughs (right)

In this particular project the HS model gives conservative results for both the maximum settlements and the differential settlements, but for other applications it is possible that the HSS model yields steeper settlement troughs, which is the more critical scenario when considering differential displacements.

Finally a numerical study with different input parameters for G_0 and $\gamma_{0.7}$ was performed. Tab. 23 illustrates the input parameters for the sandy silt layer; the other layers are modified with the same ratios. The aim of this study was the evaluation of the impact on the settlement behaviour. Fig. 134 exemplary shows the decay of stiffness for the different calculations and the settlements over depth in the middle of DC tower I. The results indicate that the computed displacement is relatively sensitive on G_0 respectively $\gamma_{0.7}$, however a modification of $\gamma_{0.7}$ shows less influence than a variation of G_0/G_{ur}.

Tab. 23: Variation of HSS parameters

	HSS	**HSS$_2$**	**HSS$_3$**	**HSS$_4$**	**HSS$_5$**
G_0/G_{ur}	3.0	3.0	3.0	6.0	1.5
$\gamma_{0.7}$	2e-4	1e-4	4e-4	2e-4	2e-4

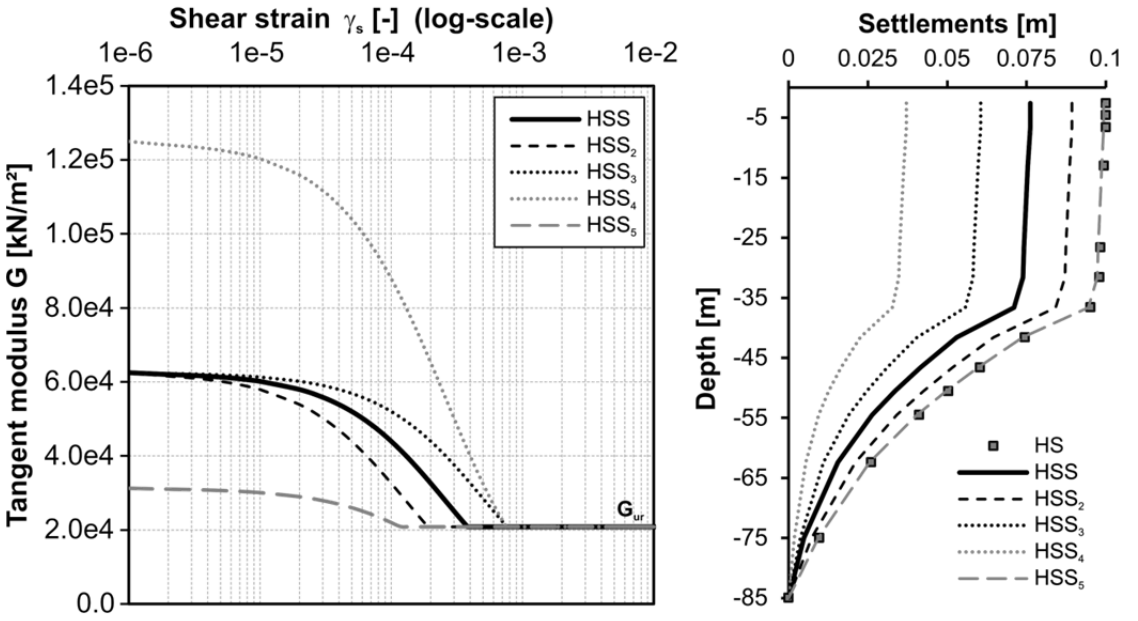

Fig. 134 Variation of stiffness for sandy silt layer (left), settlement profile over depth in the middle of DC tower I (right)

7.1.3 Comparison with alternative foundation concepts

As an alternative deep foundation system pile raft foundations (PRF) are considered. For the PRFs different modelling approaches - namely the standard finite element approach and the embedded pile concept - are used. The first layout (Layout 1) studied consists of piles with a diameter of 1.5 m and a regular spacing of about six times the diameter. Fig. 135 illustrates the finite element model where 75 piles are modelled as volume piles.

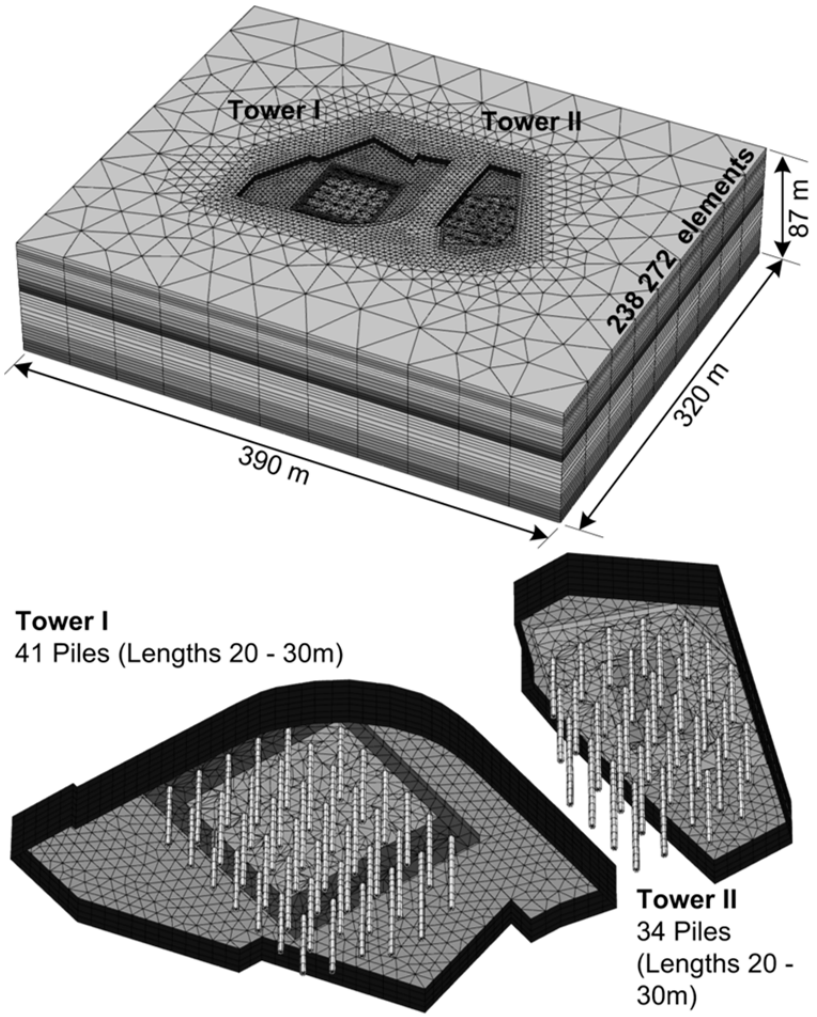

Fig. 135 Piled raft foundation modelled with standard finite element approach

In this calculation, the pile-soil interaction is modelled by means of interface elements with a strength reduction factor R_{inter} of 0.8. The pile length varies between 20-30 m, similar to the final concept with diaphragm wall panels. The number of piles has been chosen by comparing similar projects presented in the literature, and aims first of all to check whether this significant decrease of foundation elements will lead to inacceptable settlements. However, secondly and more importantly, this layout is used for comparison with the embedded pile concept. Fig. 136 demonstrates that the maximum vertical displacements are

almost identical. Both the maximum vertical displacements and the differential settlement increase significantly compared to the deep foundation discussed in the previous section. As a consequence the layout was modified in a way that the spacing of the piles is decreased in the high loaded regions (Layout 2). Again the length of the piles is similar to the barrette foundation. Fig. 137 shows both a bottom view of the foundation system and a top view where the different zones with different pile lengths are also highlighted.

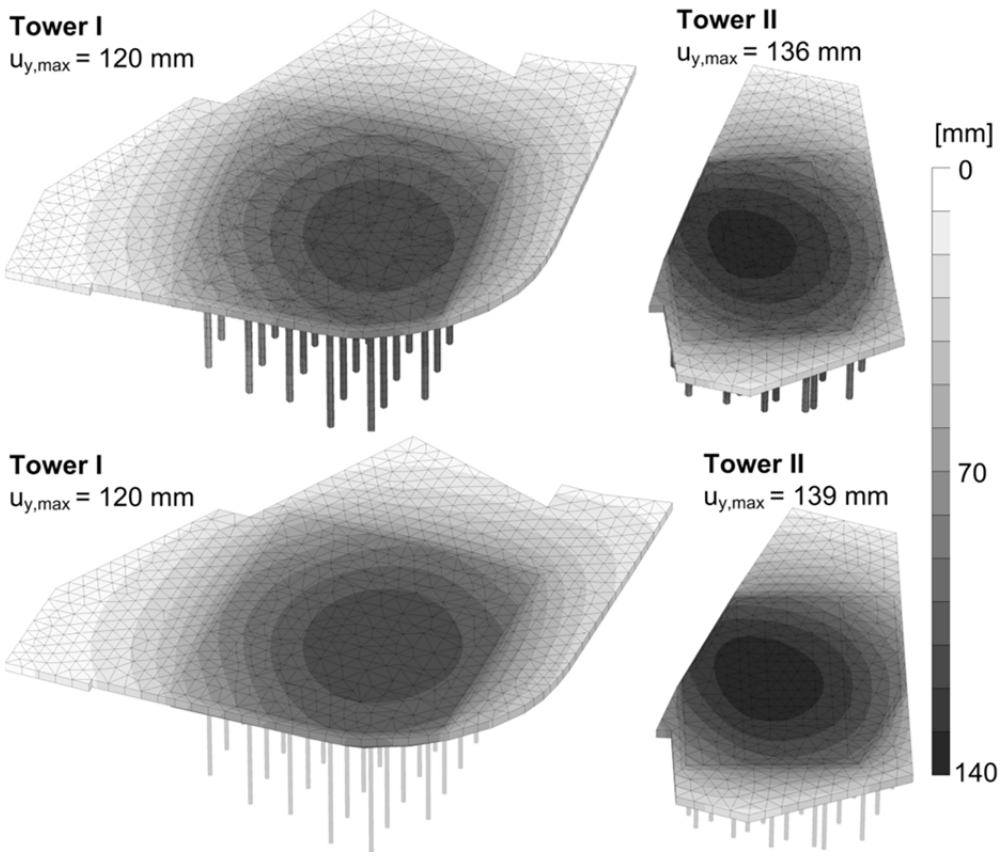

Fig. 136 Settlements of PRF Layout 1 with volume piles (top) and embedded piles (bottom)

This piled raft foundation reduces maximum vertical displacements of tower I from 120 mm to 87 mm and settlements of tower II from 139 mm to 88 mm. Also, the differential settlements are significantly reduced. Fig. 138 shows the differential settlements of tower I for the different foundation systems. The cross-section A-A is shown in Fig. 137. The barrette foundation concept is compared with piled raft foundation Layout 1, Layout 2 and a shallow foundation. Since Layout 1 is analysed with both, the standard finite element approach and the embedded pile option, both curves are presented.

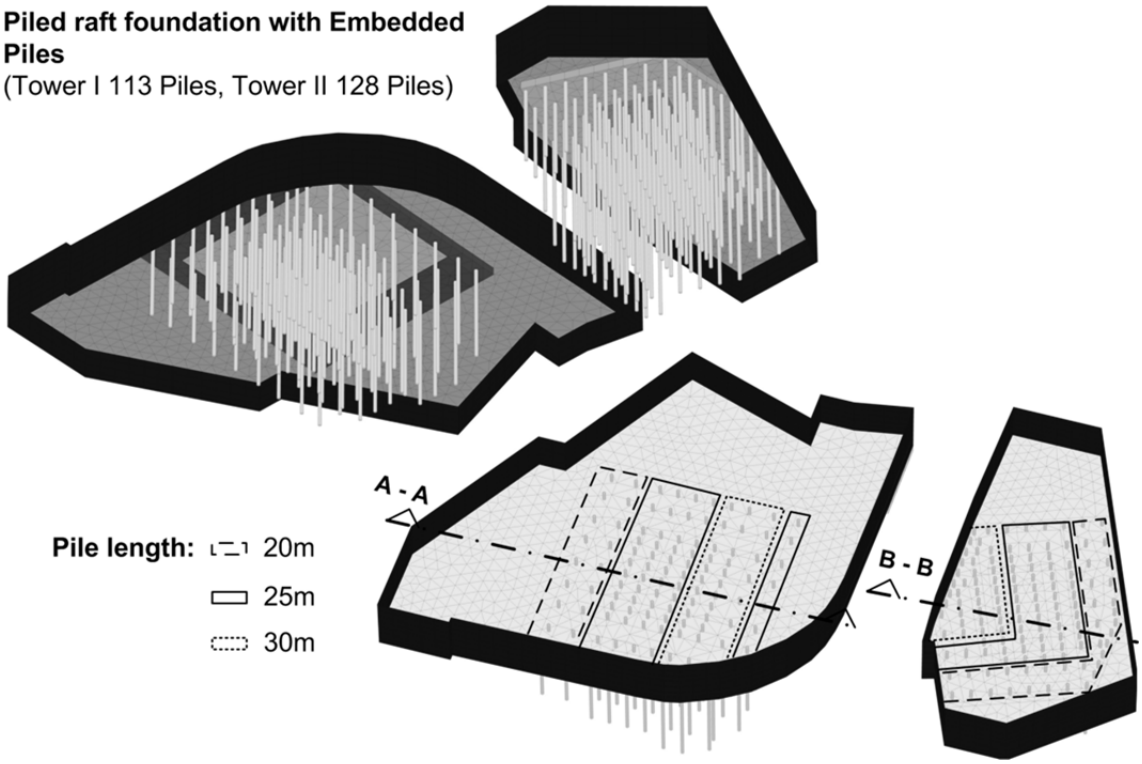

Fig. 137 PRF Layout 2 with embedded piles

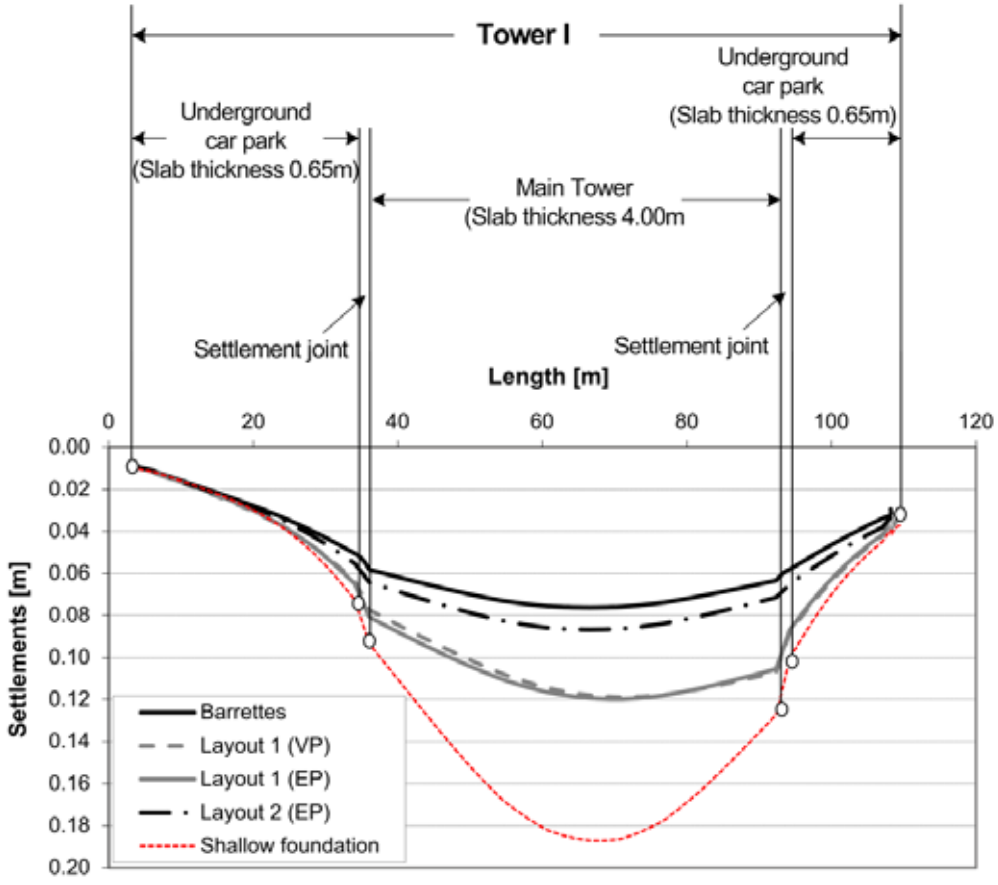

Fig. 138 Comparison of settlements along cross section A-A

The shallow foundation yields, as expected, to large vertical and differential settlements. Additionally, the maximum vertical displacements are off-centre, which would cause a tilting of the tower. The calculations of Layout 1 are performed with the standard finite element approach and the embedded pile option. Both calculation models compute almost the same differential settlements, but unfavourable differential displacements are again obtained. Layout 2 with an increased number of piles reduces both the vertical and differential settlements significantly compared to Layout 1.

Fig. 139 compares the maximum vertical displacements of the different foundation systems investigated. Additionally, the number of deep foundation elements and the total length and total volume of barrettes or piles are shown. For the two piled raft foundations, the α_{PR} factor is also given. In terms of economics piled raft foundation (Layout 2) is a conceivable alternative to the executed foundation system with barrettes, but it has to be pointed out that this is a theoretical study because other considerations than purely technical have influenced the foundation design.

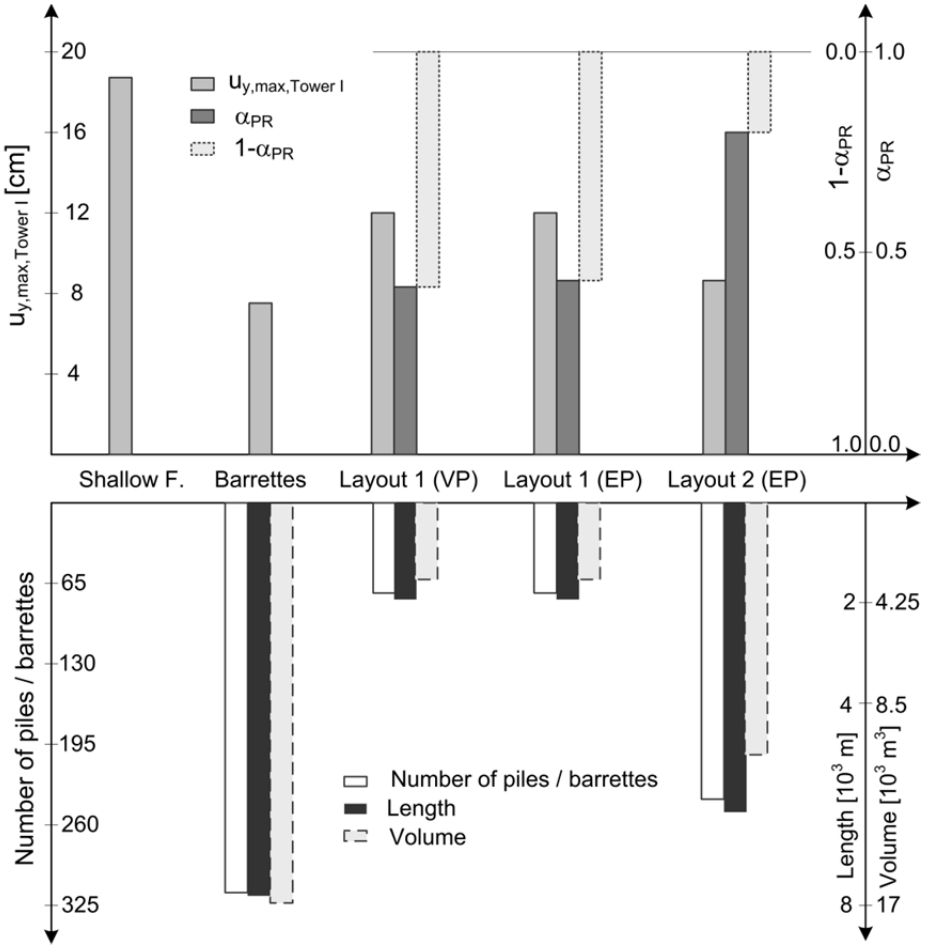

Fig. 139 Comparison of foundation systems

Finally, the influence of the modelling approach and the effect of different definitions of the pile-soil interaction were studied. For the standard finite element approach, one calculation is performed where the strength reduction factor R_{inter} is increased from 0.8 to 1.0, which means the full strength between the piles and the soil is assumed. Also, the analyses with EPs were repeated with different definitions of the ultimate embedded pile resistance. Tab. 24 shows the definition of the pile-soil interaction for all calculations performed. For some calculations, unrealistically high values for the bearing capacity of the pile were chosen intentionally to show the maximum influence on the results.

Tab. 24: Soil properties for the Hardening Soil model

calculation	R_{inter} **[-]**	$T_{top,max} = T_{bot,max}$ **[kN/m]**	F_{max} **[kN]**
Barrettes	No interfaces	-	-
Layout 1 (VP)	0.8	-	-
Layout 1_{Rint} (VP)	1.0	-	-
Layout 1 (EP)	-	471.2 (100 kPa)	10 000
Layout 1_2 (EP)	-	2000	100 000
Layout 2 (EP)	-	471.2 (100 kPa)	10 000
Layout 2_2 (EP)	-	471.2 (100 kPa)	1 500
Layout 2_3 (EP)	-	2000	50 000

The influence on the displacements was studied for tower II along cross-section B-B (Fig. 137). Fig. 140 shows the computed displacements and Tab. 25 the α_{PR} and (1-α_{PR}) factors for the different calculations. The shallow foundation leads to high differential and maximum displacements for tower II. The calculation with increased R_{inter} value shows that the strength reduction factor plays a minor rule in this particular boundary value problem. This finding also confirms the calculation of the foundation concept with barrettes, where no interface elements are modelled around the diaphragm wall panels. Of course, this would not be true for very high loads. The definition of the embedded pile bearing capacity shows a significant influence on Layout 1, because in this foundation system the spacing of the piles is relatively large, thus the individual piles are highly loaded. The obtained results of Layout 2 show that the global behaviour of this layout, with a much smaller spacing of the piles, is not sensitive related to the bearing resistance of the EPs. Layout 2_3 (EP) is not shown because this calculation yields similar differential settlements as Layout 2 (EP).

Tab. 25: Comparisons of raft soil interactions

	L.1 (VP)	**L.1$_{Rint}$ (VP)**	**L.1 (EP)**	**L.1$_2$ (EP)**	**L.2 (EP)**	**L.2$_2$ (EP)**	**L.2$_3$ (EP)**
α_{PR}	0.43	0.47	0.41	0.58	0.82	0.80	0.83
1-α_{PR}	0.57	0.53	0.59	0.42	0.18	0.20	0.17

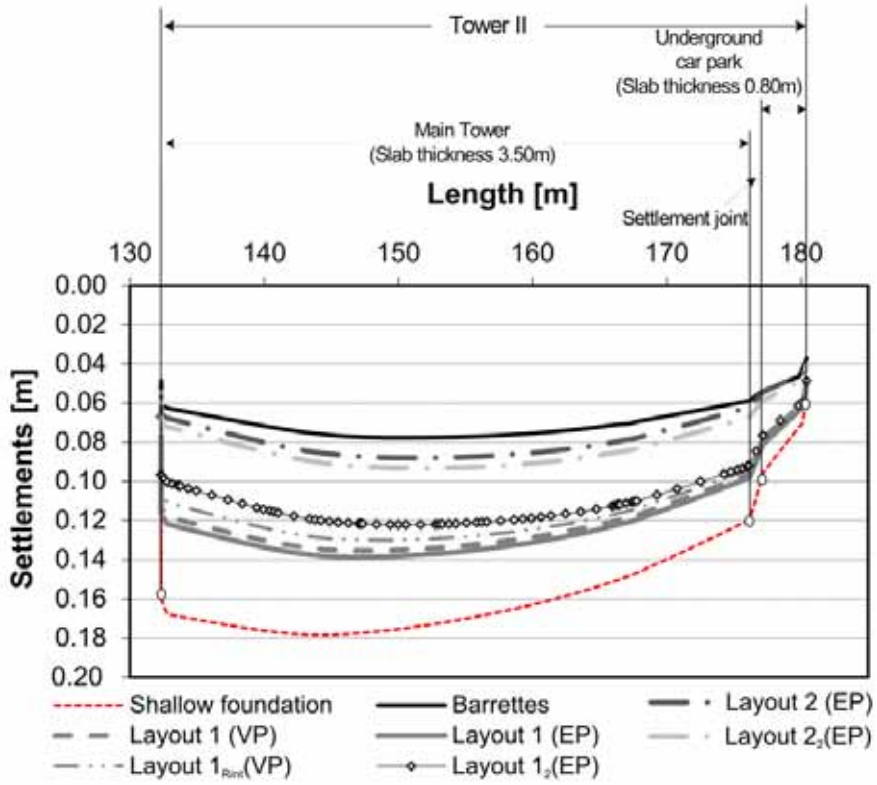

Fig. 140 Comparison of settlements along cross section B-B

7.2 Floreasca City Centre – Sky Tower

7.2.1 Introduction

In this chapter the optimisation of a deep foundation with diaphragm wall panels is presented. The project discussed is the Sky Tower, the most impressive part of the so-called Floreasca City Center in the north-eastern part of Bucharest. The entire site consists of the Promenada mall a shopping and entertainment centre, and two office buildings called the Office Wing and the Sky Tower. The calculations presented in the following focus only on the latter, which will be the highest building in Bucharest with a total height of 137 m.

Fig. 141 illustrates a rendered image of the Floreasca City Center (©beyer.co.at) and the top view of the project layout. The excavation has a maximum length of 93.4 m and a maximum width of 61.7 m. The bottom of the foundation slab is 20.4 m below the ground surface. The two egg-shaped areas represent the regions where high point loads, up to 14900 kN, are acting. The thickness of the foundation slab is 2.5 m in the inner region of the excavation bit and 1.6 m in the outer areas. The diaphragm wall panels have a thickness of 0.8 m beneath the high loaded areas and sensitive zones and 0.6 m in the other regions. The diaphragm wall, which acts as a retaining wall for the excavation and as a foundation element, is 1.0 m thick. It is planned to install the deep foundation elements from the ground surface and to realise the excavation afterwards with the top-down method. As a consequence, the panels are acting as tension elements during excavation and minimise the heave. Detailed information about the construction sequence is given in Zehentner et al. (2011).

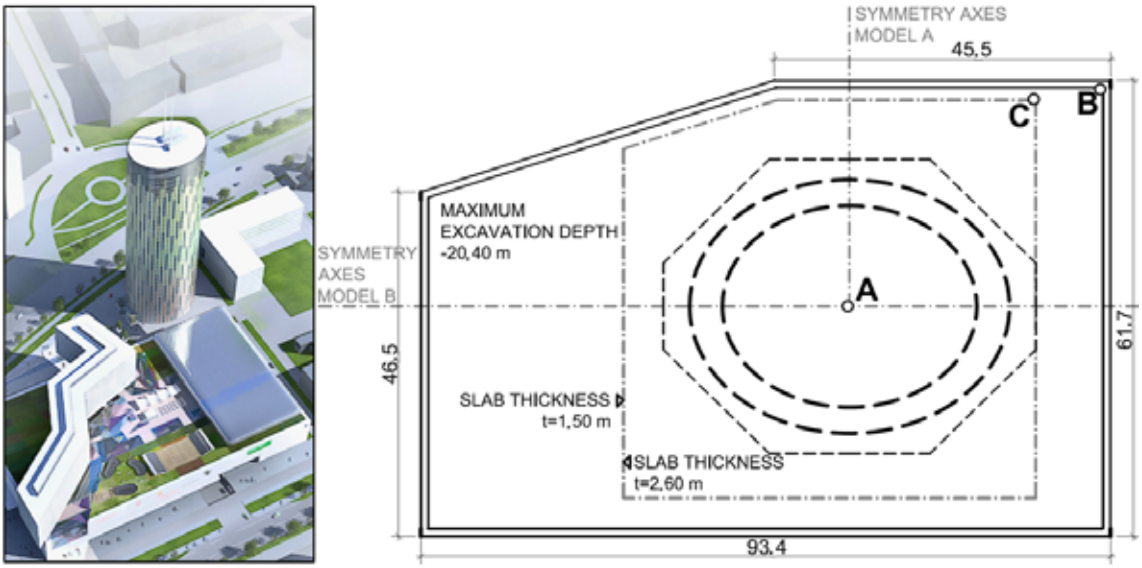

Fig. 141 Project overview (© beyer.co.at) – Sky Tower

Due to the high loads in the core of the construction, large differential settlements of the foundation slab were expected. The aim of the 3D finite element analysis was to minimise both the total deformations of the construction and, even more importantly, the differential displacements of the slab.

The soil profile for the finite element simulation is based on core drillings with depths down to 60.0 m from the surface. All borehole logs showed alternate layers of either sands or silty clays. For the calculations presented, the HS or the HSS model was used (Tab. 27). Fig. 142 shows for both soil types the evaluation of E_{oed}, E_{50} and E_{ur} over depth. All walls and floors in the FE model behave linear elastic with a stiffness of 3e7 kN/m^2 and a Poisson's ration of 0.2. The diaphragm wall elements are modelled with volume elements and described with the Mohr-Coulomb model. The tensile strength of the barrettes is limited to a value of 3000 kPa. The parameters for the deep foundation elements are given in Tab. 26.

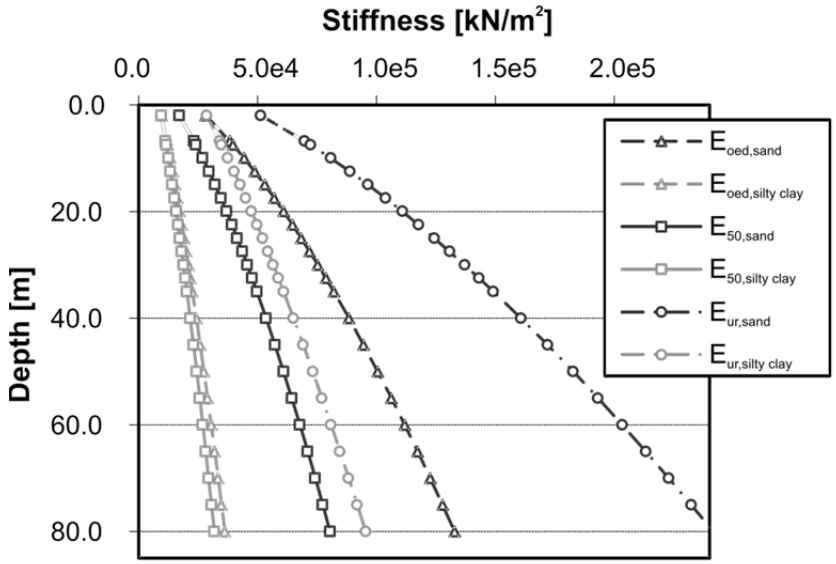

Fig. 142 Evaluations of E_{oed} and E_{ur} (right)

In order to get a first approximation of the behaviour of the structure, a 2D plane strain model consisting of 5500 15 noded elements has been made. In this project the geometry of the high loaded area is almost quadratic and restricts the applicability of 2D models. Therefore, it was expected that the displacements obtained in the 2D cross-sections would overestimate the settlements.

Tab. 26: Properties of diaphragm wall panels

	γ [kN/m3]	ν [–]	E_{ref} [kPa]	c' [kPa]	φ' [°]
diaphragm wall panels	25.0	0.20	2.5e7	5100	45.0

Tab. 27: Soil properties for the HS / HSS model

parameter	unit	silty clay	sand
γ_{unsat}	kN/m^3	20.5	21.0
γ_{sat}	kN/m^3	21.0	21.5
$E_{50,ref}$	kPa	12 000	30 000
$E_{oed,ref}$	kPa	10 000	30 000
$E_{ur,ref}$	kPa	36 000	90 000
ν'_{ur}	-	0.2	0.2
p_{ref}	kPa	100	100
m	-	0.70	0.65
φ'	°	22.5	32.5
c'	kPa	25.0	0.0
ψ	°	0.0	2.5
K_0^{nc}	-	1-sinφ'	1-sinφ'
$G_{0,ref}$	kPa	45 000	112 500
$\gamma_{0.7}$	-	2e-4	2e-4

To reduce the complexity and size of the 3D models, symmetry axes were defined. This is possible because the high loaded area is almost symmetric and the influence of the non-symmetric outer part of the construction is expected to be small. In all 3D calculations, 15 noded wedge elements with quadratic shape functions are used. Fig. 141 shows the symmetry axis for the 3D models where half of the excavation bit is modelled (Model B). As an example, Fig. 143 shows one finite element model of Model B. All models analysed consist of around 52000 finite elements. The model depth of all 3D models is 80.0 m. The deepest borehole reached only a depth of -60.0 m and it is therefore assumed that alternate layers of sands and silty clays continue. Nevertheless, sensibility analyses were performed to assess the influence of the uncertainties in the soil profile. All calculations were performed as drained analysis, which means final settlements are presented. This seems to be justified because of the alternate layers of sands and silty clays, which speeds up the consolidation procedure. To include the high stiffness of the superstructure, which influences both the stress distribution in the foundation slab and the calculated settlements, the core walls of the basement floors are also modelled.

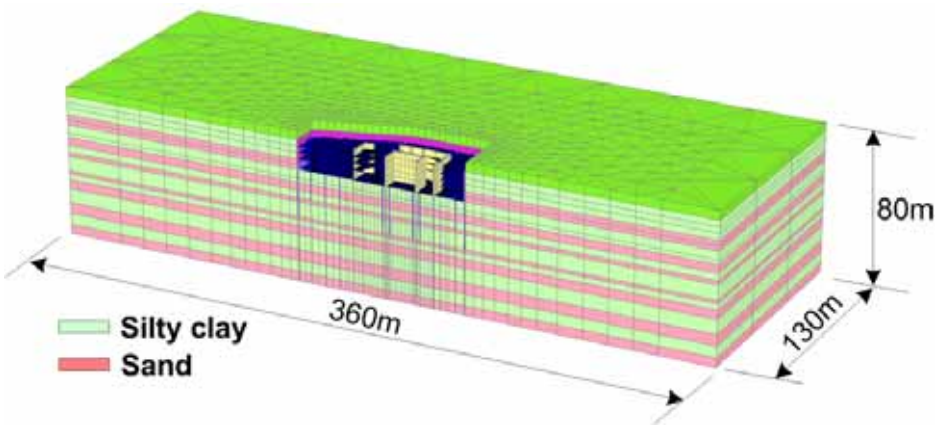

Fig. 143 3D FE model (Model B)

To obtain realistic deformations of the excavation bit and a reliable stress distribution in the soil after the excavation, it is necessary to model the real building process. All displacements presented and discussed in the following are obtained after the final calculation phase. The calculation phases are the following:

- Generation of initial stresses
- Pre-excavation to a level of -4.8 m
- Activation of the diaphragm wall panels (wished in place)
- Groundwater lowering to a level of -8.2 m
- Excavation to a level of -8.2 m
- Activation of the first floor (top-down excavation)
- Groundwater lowering to a level of -15.0 m
- Excavation to a level of -15.0 m
- Activation of the third floor
- Groundwater lowering to a level of -20.4 m
- Excavation to a level of -20.4 m (bottom of foundation slab)
- Activation of the foundation slab
- Activation of the core walls
- End of groundwater lowering
- Activation of loads from superstructure

7.2.2 Optimisation of the diaphragm wall panel layout

All calculations presented in this chapter were performed with the Hardening Soil model. The layout investigated first is shown in Fig. 144 (layout 1). The diaphragm wall panels are arranged radially from the high loaded egg shaped area. All panels beneath the 2.6 m thick slab have a width of 0.8 m and a length of 25.0 m; the 0.6 m thick panels in the outer zones have a length of 15.0 m. This layout was used to work out the difference between a 3D calculation and the 2D plane strain model. The cross section for the 2D model is located in the

symmetry axes used for Model A (see Fig. 141). For this comparison it is assumed that beneath the depth of 60 m only silty clays are present. In the plane strain model, the stiffnesses of the diaphragm walls are reduced to take the spacing into account and assumptions related to the load conditions are chosen accordingly. Nevertheless the results show that in this particular case the obtained maximum and differential settlements in the 2D model are higher almost by a factor of two than the settlements obtained in the related 3D analysis. Fig. 145 illustrates the contour lines of vertical displacements calculated with the plane strain model. The result confirmed that a 2D model is too conservative and does not yield realistic results; as a consequence, 3D models are used for all further studies.

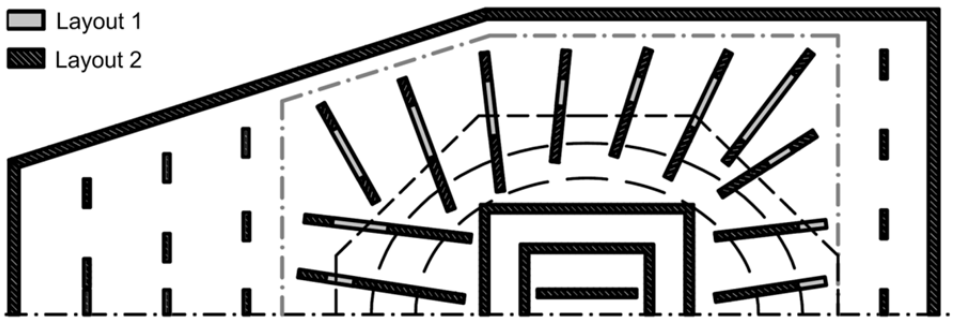

Fig. 144 Top view of layout 1 and 2 for the deep foundation elements

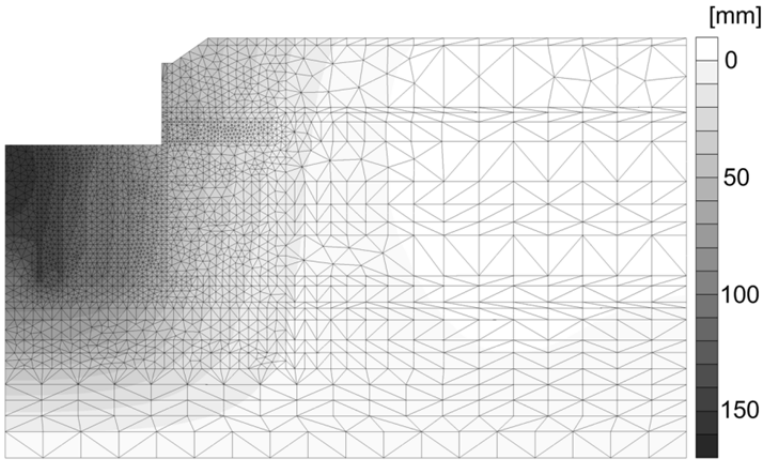

Fig. 145 Contour lines of vertical displacements – 2D plane strain model

Fig. 144 also shows the layout 2 in which the panels are again arranged radially from the high loaded area but are only located beneath the columns of the superstructure. Additionally, the length of the panels outside the high loaded area is reduced to 15.0 m. Both modifications yield to a significant reduction of costs. Fig. 146 illustrates the FE model of the deep foundation elements of layout 2.

With respect to calculated settlements, layout 1 is a better solution and results in 85 mm maximum settlements and about 42 mm differential settlements between point A, in the middle of the construction, and point B, which is located in the upper right corner of the 1.5 m thick foundation slab. From an economical point of view this variation is worthy of an improvement. Layout 2 saves 25% volume of diaphragm wall compared to layout 1, but the maximum vertical displacements increase to 100 mm and, even more critically, the differential settlements to 60 mm.

Layout 3 and 4 are shown in Fig. 147. The barrettes outside the high loaded area again have a reduced length of 15.0 m. In layout 3, the volume of diaphragm walls is about 20% less compared to layout 1. The effect of the stiff connection between the radial arranged barrettes with the inner diaphragm walls yields a reduction of settlements compared to layout 2. The obtained values are 95 mm for the vertical displacements and 52 mm for the differential settlements. But the problem with this concept is that a stiff connection of the panels to the inner walls, as assumed in the finite element calculation, is technically very difficult to accomplish.

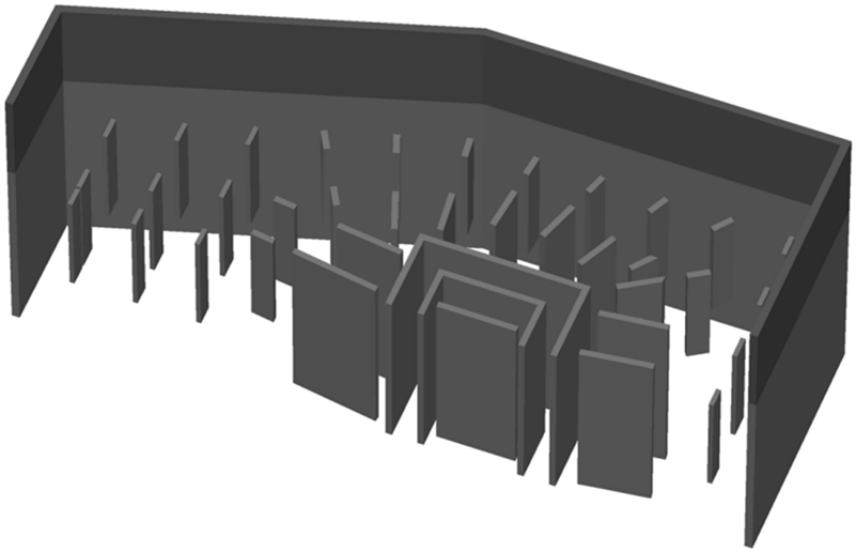

Fig. 146 Diaphragm wall panels of layout 2

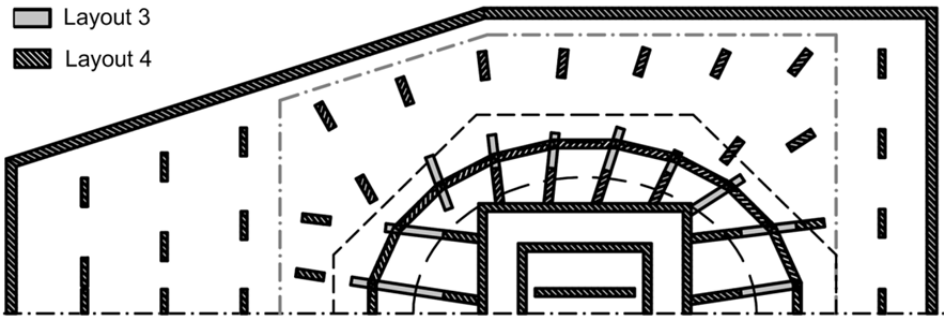

Fig. 147 Top view of layout 3 and 4

Another problem is that the radially-oriented diaphragm wall panels lead to unfavourable stresses in the barrettes. Therefore an alternative geometry is investigated, namely layout 4 with radially and tangentially-arranged panels. This arrangement has the benefit that the high point loads coming from the superstructure are directly transferred to deep foundation panels. With layout 4, the calculated maximum settlements are again about 100 mm and the differential settlements are in the range of 60 mm. Fig. 148 shows the arrangement of the structural elements and the contour lines of vertical displacements in a bottom view. Compared to layout 1, 15% less volume of barrettes is required. But this foundation concept is also problematic from a practical point of view, because a stiff connection between the tangentially-arranged panels is very hard to achieve; as a consequence this foundation system is also not feasible.

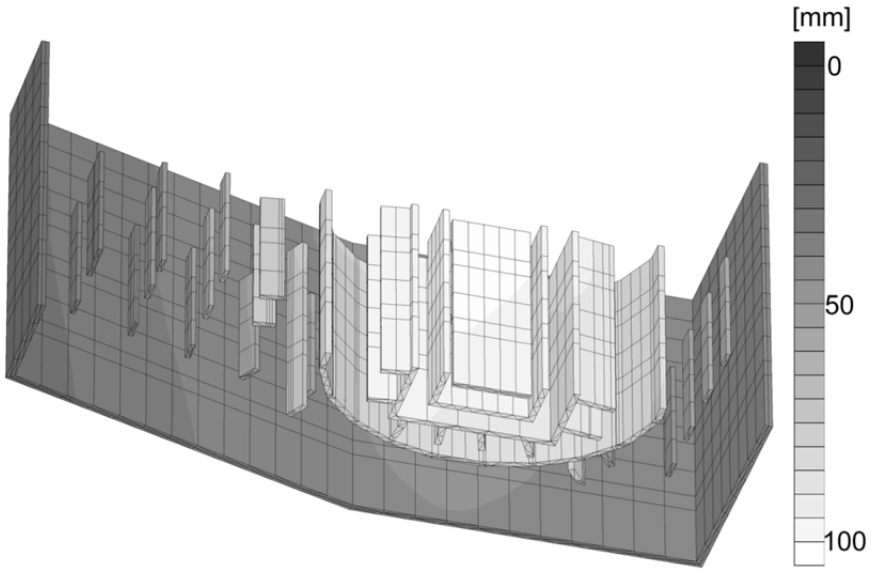

Fig. 148 Contour of vertical displacements – layout 4

Due to these shortcomings of layout 1 to 4, another variation is studied where two discontinuous circles of panels (layout 5) are arranged in the area of concentrated loads (Fig. 149). For these calculations with the final layout of the deep foundation elements, another symmetry axis is defined. Hence, only a quarter of the construction is modelled (Model A), which enables a much finer discretization of the boundary value problem. In layout 5 the inner parts of the diaphragm wall panels are also disconnected with the consequence that the global stiffness of the foundation system is decreased, which automatically yields higher differential settlements. This drawback of the foundation system should be compensated with a second circle of barrettes installed beneath the high loaded region. In terms of economics, this solution needs more panels than the layouts 2 to 4, but compared to the first design (layout 1) it still saves roughly 10% volume of deep foundation elements.

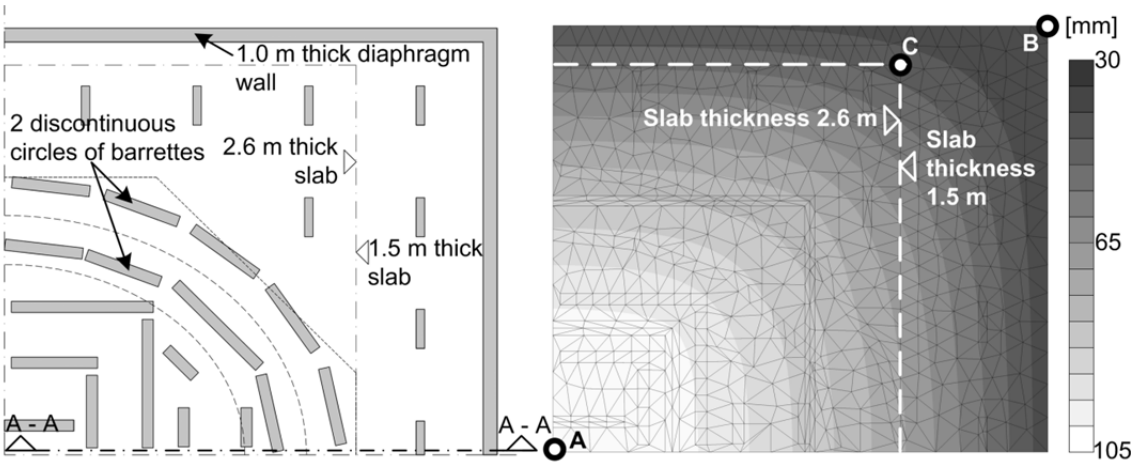

Fig. 149 Top view of layout 5 (final / executed foundation concept)

The vertical settlements calculated are about 100 mm. Fig. 150 shows the contour lines of vertical displacements of the entire 3D model and of the deep foundation elements. The differential settlements of the foundation slab are presented in Fig. 149. Between point A and B, nearly 65 mm of differential settlements and approximately 47 mm within the 2.6 m thick slab (point A to point C) are computed. In order to evaluate the settlement reduction due to the diaphragm wall panels, an analysis without panels was performed. The maximum settlements obtained are in the range of 240 mm.

A further variation involved the replacement of a sand layer by a silty clay layer below -60.0 m in order to take the uncertainty of ground conditions at deeper layers into account. This calculation concludes that settlements increase by 10 mm.

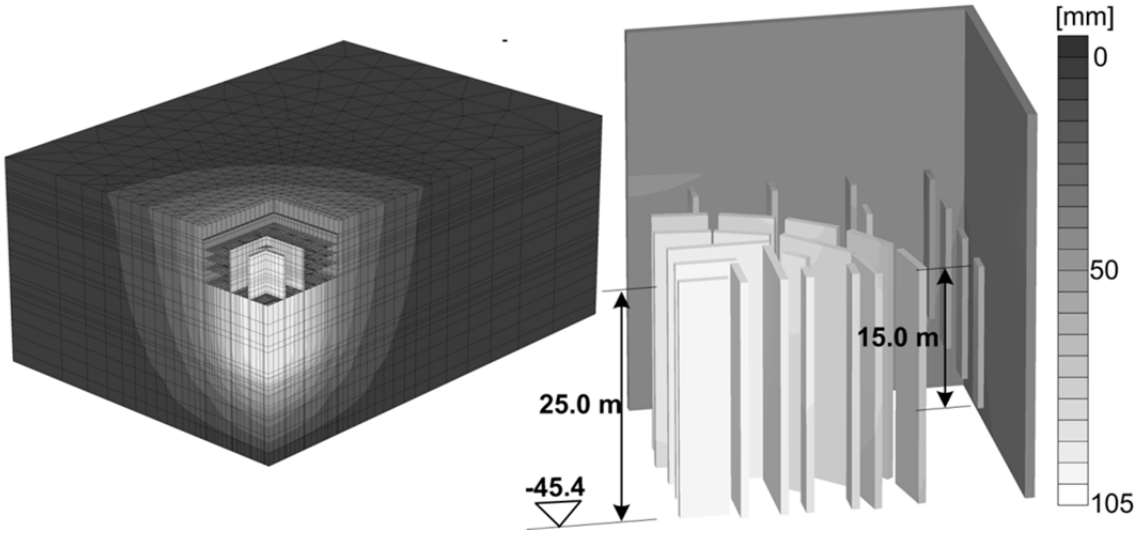

Fig. 150 Contour lines of vertical displacement of entire model (left) and deep foundation elements (right)

7.2.3 Parametric study

The soil parameters used for the settlement predictions discussed above are based on the soil description in the geotechnical reports and laboratory tests. Because high order constitutive models - as used for the numerical analysis - need more input parameters in general than given in standard geotechnical reports, profound knowledge of the used soil models and experience with correlations between certain soil parameters play a significant role. In this section, a parametric study based on recently published soil data not available at the time of analysis is presented. The parameters given by Saidel et al. (2010), are typical for the soil conditions in Bucharest. The published data is based on drained and undrained triaxial tests, oedometer tests, direct shear tests, in-situ tests, cross hole seismic survey, cyclic triaxial tests, observational method and finally experience. In Saidel et al. (2010) a range of most of the input parameters necessary for the HS and HSS Model is given. The aim of this study was firstly to see how the parameters derived from the geotechnical reports and used for the settlement predictions fit to the parameters presented by Saidel et al. (2010), and secondly (and mainly), to work out the influence on the computed settlement troughs. For the comparisons presented in this section, the executed foundation concept was used, where the barrettes beneath the core have a length of 30 m instead of 25 m and the diaphragm wall - which acts as retaining wall and as foundation element - has altering lengths of either 15 or 25 m. This modification of the foundation system yields to a reduction of both maximum and differential settlements of about 6 mm, compared to the layout presented above.

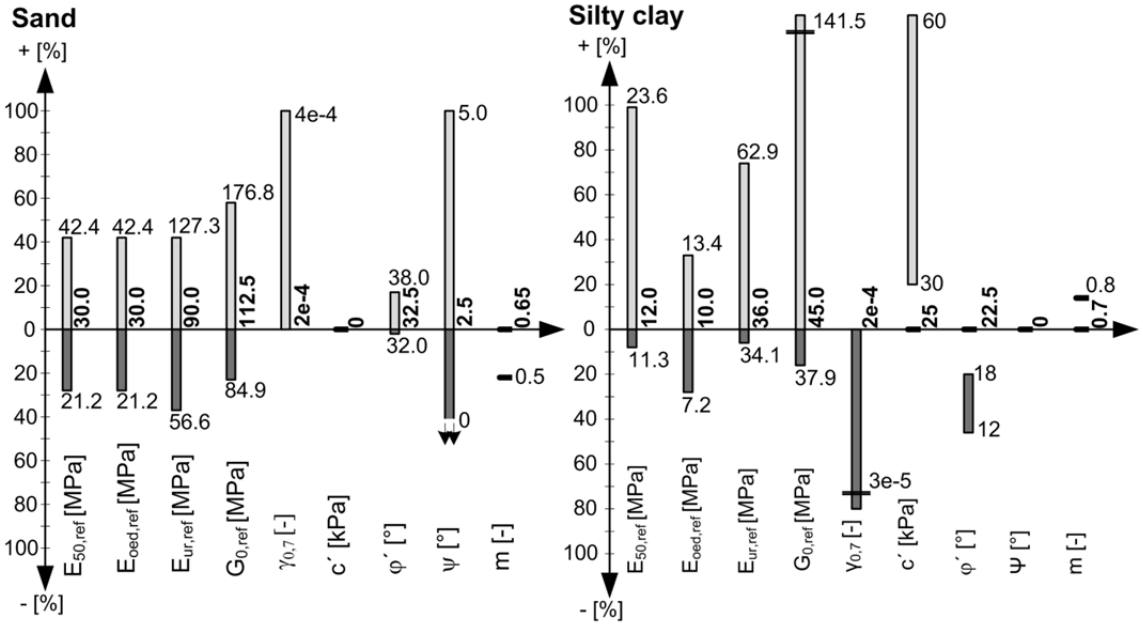

Fig. 151 Overview of soil parameters

Fig. 151 shows the input parameters for the HS and HSS model. The bars represent the range of the soil parameters, whereas the values on the horizontal axes are the used values for the settlement predictions and the light and dark grey bars indicate the deviation of the best and the worst-case scenario according to Saidel et al. (2010). Fig. 152 shows the computed settlement troughs along cross section A-A (Fig. 149). The results of the worst and best-case scenarios are compared with the differential settlements obtained with the parameters used for the settlement predictions presented in the last chapter. The results for both the HS and the HSS model are presented.

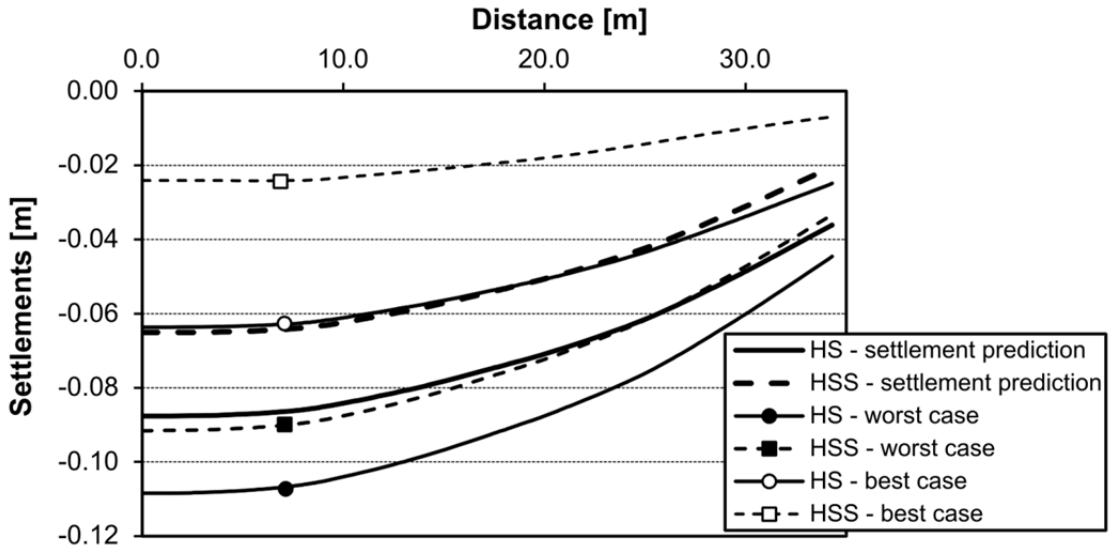

Fig. 152 Settlement troughs along cross section A-A

The difference between the HS and the HSS model clearly shows the influence of the small strain stiffness, where the settlements from deeper depths are automatically reduced. One can also see that the predicted settlement trough computed with the HS model, where the input parameters were derived from the geotechnical report, is more or less exactly between the worst and best-case scenario. The "best-case" calculation with the HSS yields only 25 mm maximum displacements. This comes from the fact that the additional parameters for the HSS model, namely the G_0 and the $\gamma_{0.7}$, are very optimistic in this case.

7.2.4 Validation of numerical model

Although the models presented can be regarded as high level, it has to be made clear that in-situ measurements during construction are essential in order to verify the assumptions made in the calculations. This is especially important in this particular case where no information on ground conditions below -60.0 m from the surface is available. To obtain additional information of the settlement

behaviour of the deep foundation, an in-situ test was conducted on a diaphragm wall element (barrette) using the "Osterberg Method" (Osterberg 1989). In the first part of this chapter some principles of the testing procedure are discussed and in the second part a back-analysis of an O-Cell test is presented.

7.2.4.1 Principles and numerical modelling

A detailed description of the testing procedure is given e.g. in Schmertmann & Hayes (1997). The basic idea of the test is that due to the expansion of the Osterberg cell, the upper part of the pile acts as a reaction for the end-bearing and the end-bearing resistance acts as a reaction system for the shaft resistance. The upward load movement is mainly governed by the strength characteristics of the adjacent soil and the interface properties of the pile soil interaction. The downward load-movement is mostly influenced by the stiffness properties of the soil below the pile tip. The main advantages of the test are:

- Reduction of costs compared to a conventional top load test.
- Shear and end-bearing resistance are measured separately.
- Multilevel testing is possible.
- Improved safety - no overhead dead load.
- Reduced working area - test can be performed in densely built up regions.

Another important benefit is the high test load, which can be applied with the Osterberg method. According to England & Cheesman (2010), reaction systems for traditional top load tests in excess of 40 MN are almost non-existent. The drawbacks of the O-Cell system are a rather complex installation procedure and that the position of the O-Cell has to be "designed" in a way that the base and shaft resistance are almost equal.

With an Osterberg test two primary results are obtained, namely the shaft resistance-deformation curve and the base resistance-deformation curve. But it is important to consider that at the start of the test, the initial load in the pile (at the level of the O-Cell) is carried structurally by the O-Cell, which means that the pressure in the cell is zero. According to Fellenius (2001) and Fellenius (2009), these "locked-in loads" are developed during and after the construction of the pile and are for slender and/or long piles normally larger than the buoyant weight of the pile. For the interpretation of the load test it is important to take these "locked in loads" into account.

To model an O-Cell test with the Finite element technique it is necessary to take some special boundary conditions into account. Fig. 153 shows schematically the different boundary conditions and structural elements in the finite element model.

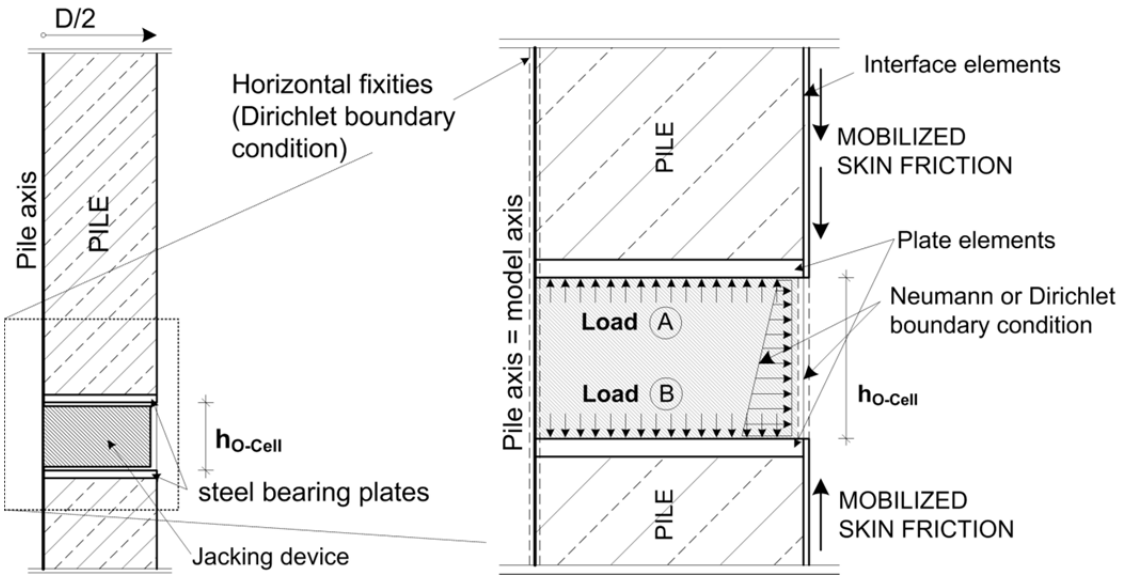

Fig. 153 Schematic representation of boundary condition for a FE model

The calculation procedure for a numerical back-analysis of an O-Cell test must also contain some additional calculation phases. After the generation of the initial stress state, the pile/barrette is activated (wished in place installation); this has to be done with a small interface strength between the deep foundation element and the surrounding soil due to the fact that the concrete is not cured in reality. This ensures that a realistic initial stress state along the pile shaft and below the pile base is present. In the following calculation phase stiff plate elements representing the steel-bearing plates are activated, and next the "locked-in loads" have to be applied in both directions (load A and load B). This calculation phase does not yield to any pile displacements, because in reality, the "break" of the O-Cell devise also cannot occur before the pressure in the O-Cell has become equal to the "locked-in load". In the following phases the O-Cell pressures are applied.

Fig. 154 shows the "primary" results of an O-Cell back-analysis, namely the shaft and end-bearing mobilization. For the shaft resistance-deformation curve a node at the pile toe should be chosen. However, when dealing with drilled shafts the elastic shortening of the pile is relatively small. The shaft resistance shows a much stiffer response compared to the base resistance; only a couple of millimetres heave are enough to mobilize the entire skin friction. If the relative displacements instead of total vertical displacements are plotted, the value would be even smaller. Fig. 154 also illustrates the constructed equivalent top load-settlement curve.

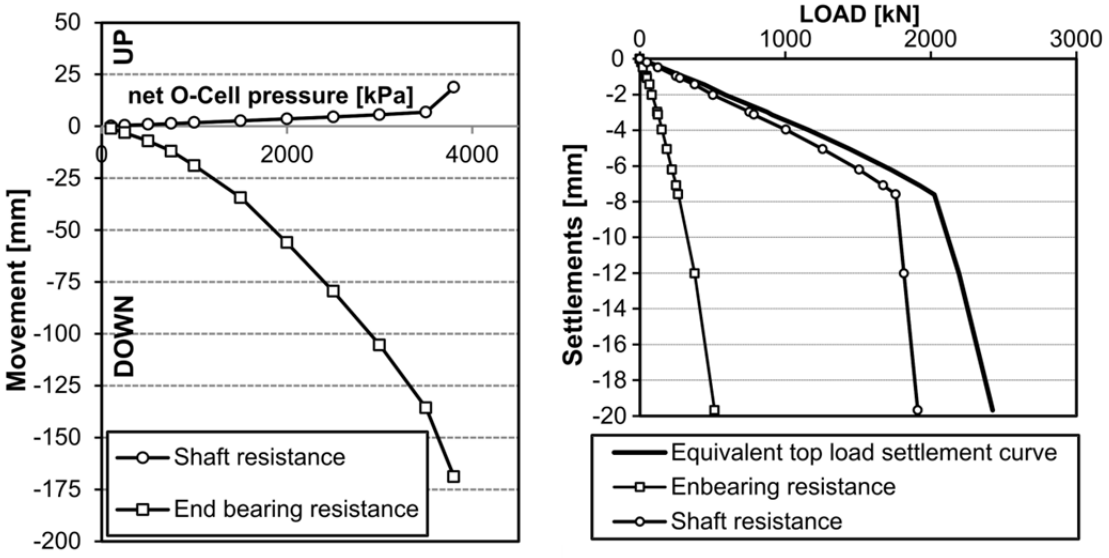

Fig. 154 Results of O-Cell load test (left) and equivalent top load-settlement curve (right)

According to Osterberg (1998), it is assumed that for the construction of the equivalent top load-settlement curve, the side shear load-deflection curve resulting from the upward movement of the tested deep foundation element equals the downward side shear deflection curve in a conventional load test. In addition, it is assumed that the end-bearing load deflection curve resulting from an O-Cell test is the same as the end-bearing-load deflection component in a conventional top down load test. Adding the side shear and end-bearing force at the same deflection gives one point of the equivalent top down curve; by repeating this process for different vertical displacements the entire equivalent top down curve is obtained. Fellenius (2009) stated that it is also important to take the elastic shortening of the pile into account.

A number of numerical studies were performed to confirm the assumptions for the construction of the equivalent top load curve recommended by Osterberg (1998), i.e., the Hardening Soil model without stress dependent stiffness ($m = 0$). In these calculations the upward and downward load of the O-Cell were activated separately to compare the results with a conventional test and a top loaded pile without base resistance. The results showed that the influence of the loading direction on the mobilized skin friction is rather small (Fig. 155). An influence of the O-Cell downward movement is notable only close to the pile toe.

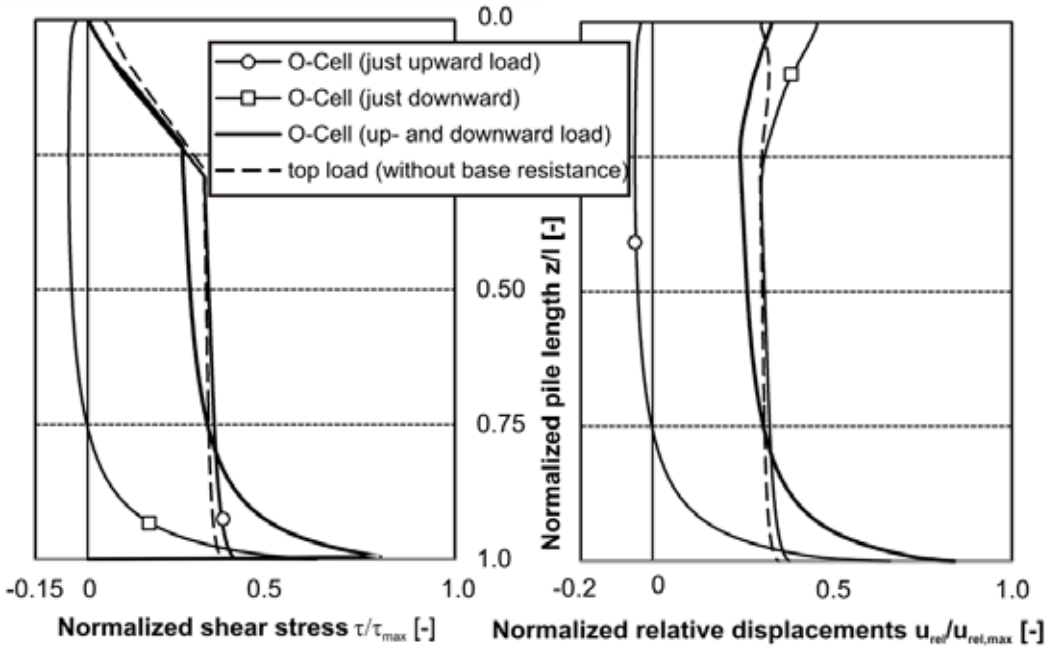

Fig. 155 Normalized shear stress (left) and normalized relative displacements (right) along the pile shaft

Fig. 156 shows contour lines of vertical displacements close to the pile base for a calculation where only the downward load of the O-cell is activated. The obtained vertical displacements of the soil in the lower part of the pile yield to additional mobilization of skin friction, but the influence of gained shear stress mobilization on the global load-settlement behaviour is rather small. However, it was also found that the vertical displacements in the soil yield to a downdrag of the pile and must be considered when constructing the equivalent top down curve based on FE results.

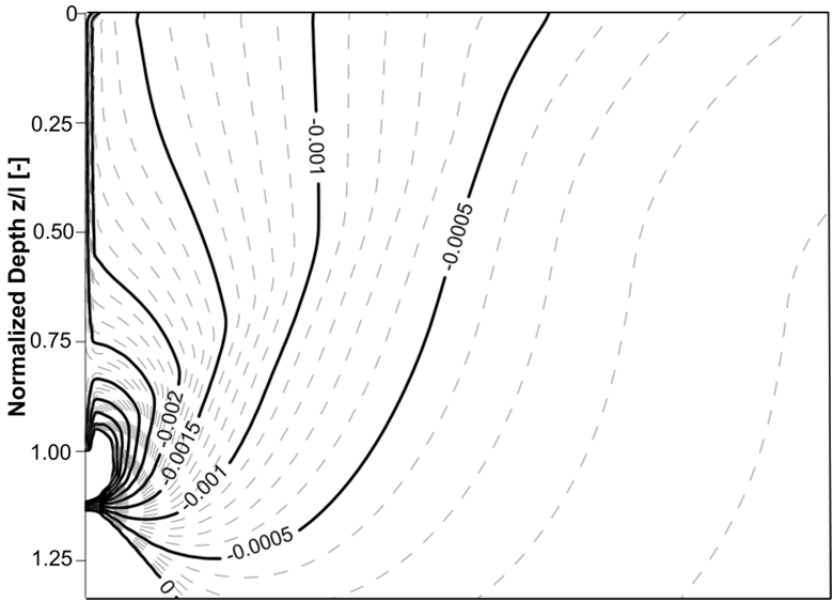

Fig. 156 Contour lines close to the pile base

7.2.4.2 Back-analysis of O-Cell test

The top of the 25.2 m long tested barrette is located 15.3 m beneath the surface and the "Osterberg Cell" is 9.0 m above the bottom of the panel installed. A numerical model was set up in close agreement to the real test. The soil profile and parameters used for the back-analysis are the same as mentioned above. The barrette is discretized by means of volume elements and the soil-structure interaction is defined with a strength reduction factor R_{inter} of 0.8. The finite element model consists of 82500 15 noded wedge elements. Fig. 157 shows the 3D finite element model used and indicates the important levels of the in-situ test.

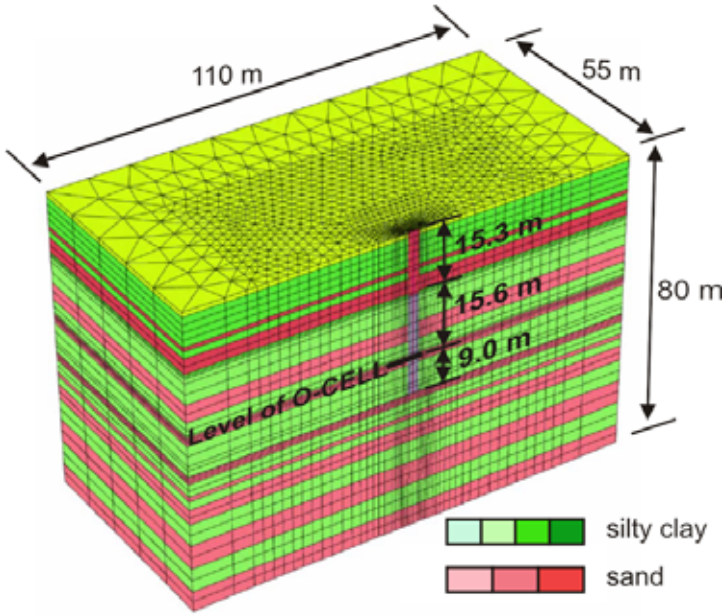

Fig. 157 3D Finite element model of the in-situ test

Fig. 158 shows the displacements of the load test for the upper and lower part of the barrette. As expected, the finite element analysis yields slightly higher displacements because of the cautious estimates of soil parameters used when analysing the entire foundation for the Sky Tower. Also, when using the HSS model, the global stiffness response of the O-Cell test is underestimated. The sudden increase of the upper part of the barrette can be approximately captured with the finite element analysis, but little effort has been put into modelling the sand fill and its very limited friction against the natural soil. For the lower part of the barrette, the agreement can also be considered as reasonable. But the measured kink of the load displacement curve at a load level of about 5 MN was not captured with the FE analysis. Numerical studies with modified soil conditions also did not show this kink. It is found as well that differences between drained and undrained conditions are not significant although the undrained analysis of course results in somewhat smaller settlements.

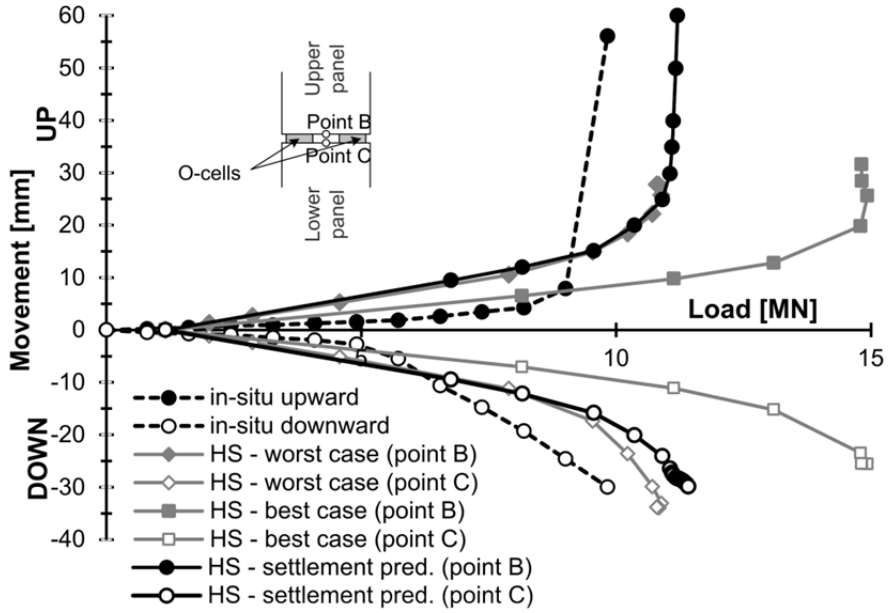

Fig. 158 3D finite element model of the in-situ test

7.3 Ground anchors

7.3.1 Introduction

The ground anchor facility consists of two different parts. The first part represents the free anchor length and the second part the grout body. The free length is modelled as a node-to-node anchor, which defines a connection between the grout body and for example a diaphragm wall. The grout body consists of embedded beam elements. Besides the geometry, six input parameters are required to define a ground anchor. Fig. 159 shows a schematic representation of a ground anchor. The anchor bar is modelled as a spring with a axial stiffness *EA* and, if elasto-plastic material behaviour is chosen, an ultimate force $F_{max,GA}$. The soil-interaction along the grout body is defined with the two separate values for skin resistance ($T_{top,max}$, $T_{bot,max}$), thus a constant and linear ultimate skin friction distribution can be defined (see chapter 4.3.2).

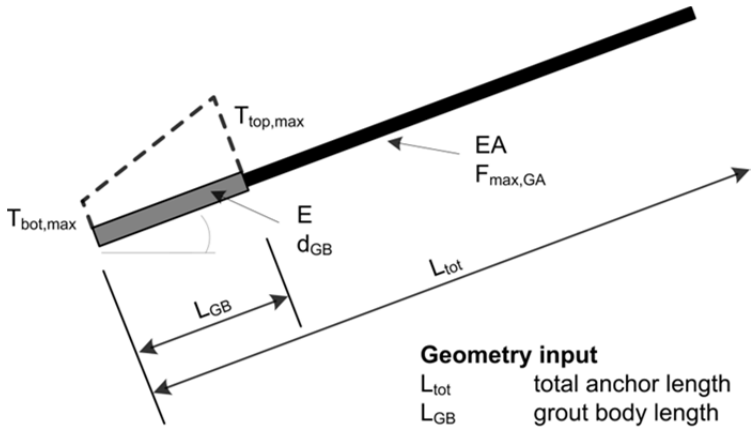

Fig. 159 Schematic representation of a ground anchor

For loads close to the theoretical pull out force, numerical failure may occur due to plasticity in the soil adjacent to the grout body. Although this is of course possible in reality, in the model it may be artificial and caused by the fact that the grout body is a line element. To overcome this problem in ultimate limit state conditions it is necessary to work with an enlarged diameter of the grout body, or in other words, with an increased elastic region (see also chapter 4.5). This virtual diameter d_v of the grout body is defined with an enlargement factor f_{GB}.

$$d_v = f_{GB} \cdot d_{GB} \tag{94}$$

A value of the enlargement factor f_{GB} in the range of 2 to 4 is suggested. This modification of the elastic region does not affect the pull out force (this is an

input due to the input of the limiting skin resistance and the length of the grout body) and has a minor effect on the behaviour under working load conditions.

7.3.2 Application

In order to demonstrate the application of the ground anchors in the PLAXIS 3DF, some results from a practical example are presented, namely a deep excavation in Berlin sand with prestressed anchors. This example was chosen for testing the ground anchor facility under working load conditions because a 2D reference solution was available (Schweiger 2000). The model dimensions and material sets for the soil layers have been taken from the 2D reference solution. Fig. 160 illustrates the deep excavation analysed and Tab. 28 and Tab. 29 give the soil parameters for the three sand layers. A detailed description of the model and further information regarding the soil properties are given in Schweiger (2000).

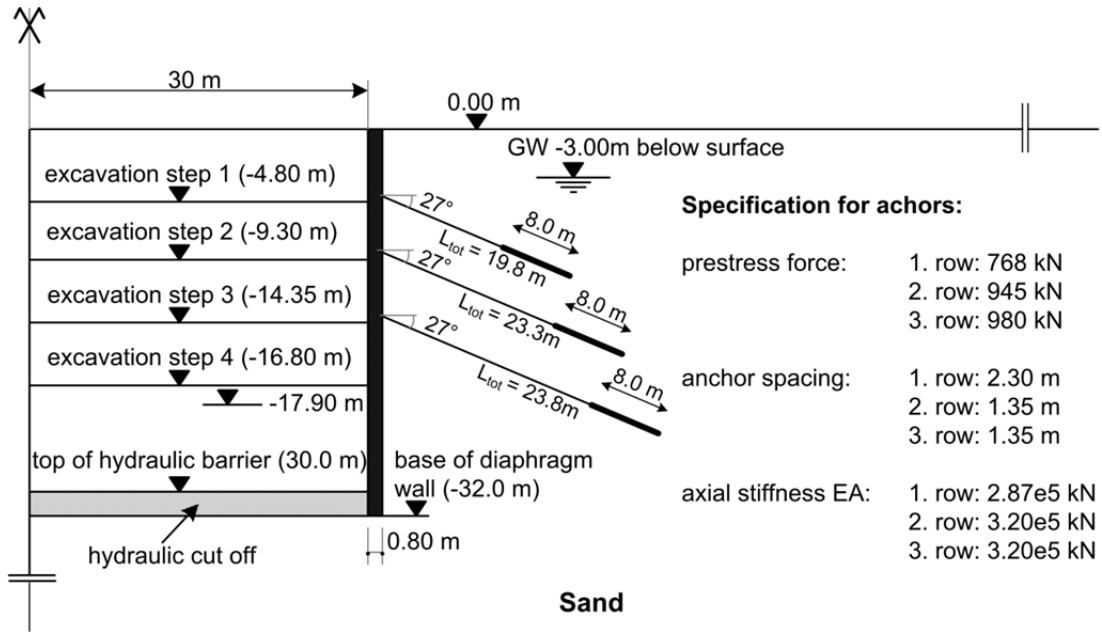

Fig. 160 Geometry of deep excavation

The diaphragm wall was modelled as a continuum element with linear elastic material behaviour and a stiffness of 3.0e7 kN/m^2. The grout body of the ground anchors has a diameter d_{GB} of 0.125 m and a Young's modulus E of 2e7 kPa. The hydraulic cut-off does not act as a structural element, thus the properties are the same as for the soil (Sand 20 - 40 m). Fig. 161 illustrates the 3D finite element model. The aim of the test was to see if the embedded pile model (employed for the grout body) works well in working load conditions, hence the ultimate skin resistance in the grout body has therefore been defined about two times the expected axial load in the node-to-node anchor.

Tab. 28: Input parameters for Mohr-Coulomb model

parameter	unit	Sand 0 - 20 m	Sand 20 - 40 m	Sand > 40 m
γ_{unsat}	kN/m^3	17.0	17.0	17.0
γ_{sat}	kN/m^3	20.0	20.0	20.0
E	kPa	47 000	244 000	373 000
ν'	--	0.30	0.30	0.30
φ'	°	35.0	38.0	38.0
c'	kPa	1.0	1.0	1.0
ψ	°	5.0	6.0	6.0
K_0	--	1-sinφ'	1-sinφ'	1-sinφ'

Tab. 29: Soil properties for the Hardening Soil model

parameter	unit	Sand 0 - 20 m	Sand 20 - 40 m	Sand > 40 m
γ_{unsat}	kN/m^3	17.0	17.0	17.0
γ_{sat}	kN/m^3	20.0	20.0	20.0
$E_{50,ref}$	kPa	45 000	75 000	105 000
$E_{oed,ref}$	kPa	45 000	75 000	105 000
$E_{ur,ref}$	kPa	180 000	300 000	315 000
ν'_{ur}	-	0.2	0.2	0.2
p_{ref}	kPa	100	100	100
m	-	0.55	0.55	0.55
φ'	°	35.0	38.0	38.0
c'	kPa	1.0	1.0	1.0
ψ	°	5.0	6.0	6.0
K_0^{nc}	-	1-sinφ'	1-sinφ'	1-sinφ'

In the different calculations the material model, the shape of the limiting skin resistance and the enlargement of the grout body was varied (Tab. 30). In calculation HS_5 the stiffness of the grout body is modified according to the ratio of the real diameter (0.125 m) to the fictitious enlarged diameter d_v ($0.125 \cdot f_{GB}$ = 0.5m).

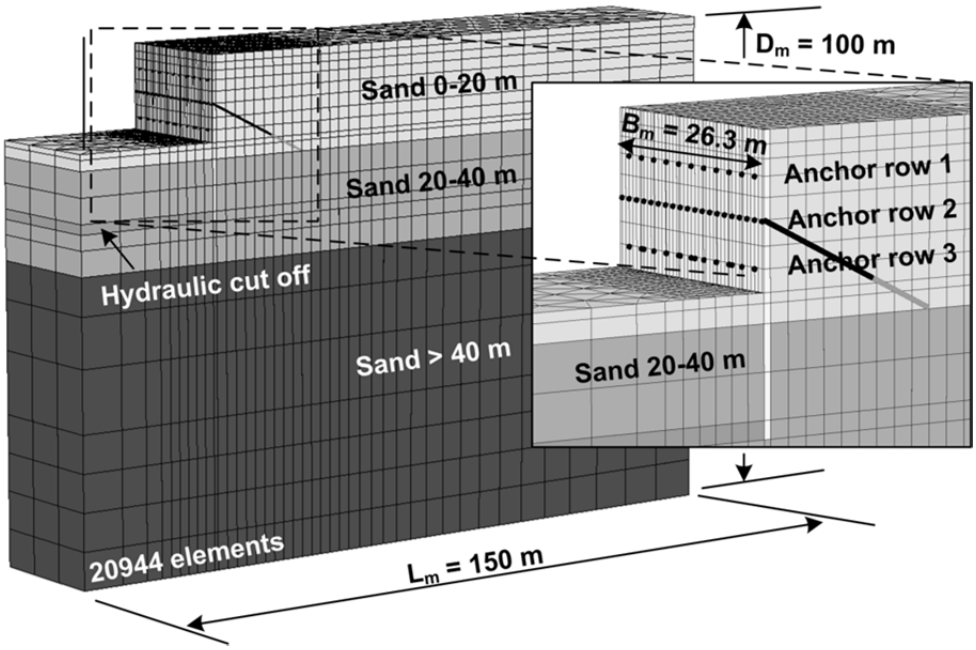

Fig. 161 Finite element model

All analyses were defined with the following calculation phases:

- Initial phase
- Activation of diaphragm wall
- Activation of hydraulic cut-off (reset displacements to zero)
- Groundwater lowering to -4.8 m below ground surface
- First excavation step to -4.8 m
- Activating of first ground anchors row (prestress force 768 kN)
- Groundwater lowering to -9.3 m
- Second excavation step to -9.3 m
- Activating of second ground anchors row (prestress force 945 kN)
- Groundwater lowering to -14.35 m
- Third excavation step to -14.35 m
- Activating of third ground anchors row (prestress force 980 kN)
- Groundwater lowering to -17.90 m
- Fourth excavation step to -16.80 m

It follows from Fig. 162 that neither the variation of the predefined limiting skin resistance of the grout body nor the f_{GB} factor of the enlargement of the grout diameter have a significant influence on the axial forces predicted under working load conditions. If the Mohr-Coulomb model is employed, the results are of course slightly different. It is also notable that by increasing the f_{GB} factor, displacements in the horizontal direction become smaller. The differences are in the order of 10%. With the MC model the highest deformations in horizontal direction are located around the grout body, whereas with the HS model this is not the case (Fig. 163). This effect also occurs with the assignment of a high f_{GB}

factor. The settlements behind the diaphragm wall are in the range of 11 mm with the HS model (almost the same for the different variations), but with the MC model there is a heave of more than 14 mm, an effect which is well known (e.g. Schweiger et al. 2009).

Tab. 30: Performed calculations

calculation	constitutive model	distribution of ultimate skin friction	enlargement factor f_{GB}
HS_1	HS	constant	1.0
HS_2	HS	linear	1.0
HS_3	HS	linear	2.0
HS_4	HS	linear	4.0
HS_5	HS	linear	4.0
MC	MC	linear	1.0

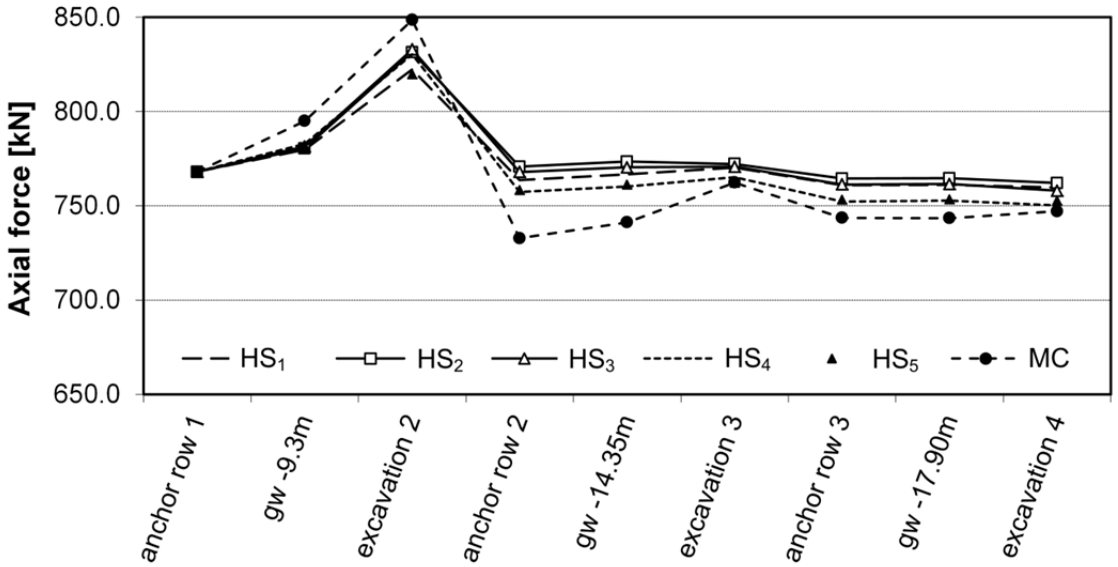

Fig. 162 Axial forces in the first anchor row

In Fig. 164, axial forces in the first anchor row from calculation HS_2 are compared with the axial forces from the 2D reference solution. In the 2D analysis the grout body of the ground anchor is modelled with geogrid elements. These elements have an axial stiffness (*EA*) but no bending stiffness (*EI*). The axial forces from a 2D plane strain calculation have the unit [kN/m]. To compare these results with the 3D analysis, it is necessary to divide the axial forces obtained in the 3D analyses by the anchor spacing.

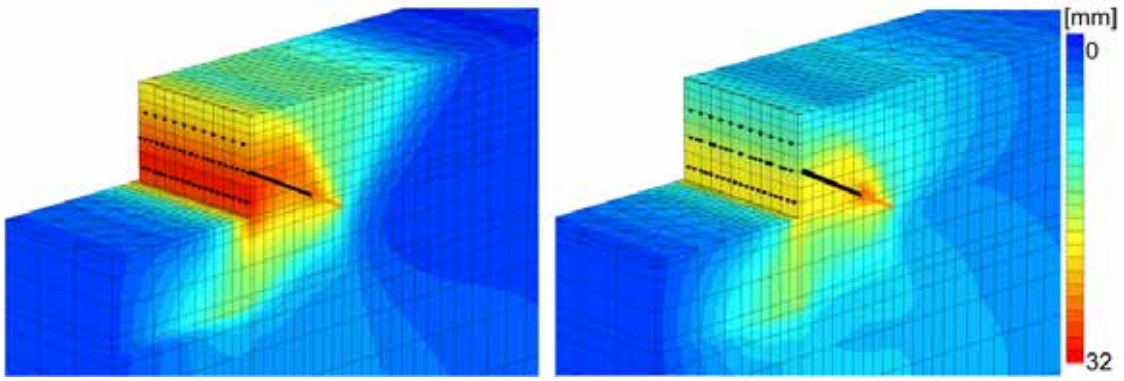

Fig. 163 Contour lines of horizontal displacements of calculation HS_2 (left) and calculation MC (right)

One can see that the axial forces from the 3D calculations are in very good agreement with the reference solution. The deviation of the forces in the node-to-node anchor between both calculations is less than 4%. Also the maximum vertical displacements and the settlement trough behind the diaphragm wall obtained in the 3D calculation are very similar to the ones from the 2D solution.

The results indicate that it is not necessary to artificially increase the diameter of the grout body for working load conditions, but because the limiting skin friction is an input, the grout body length has a minor influence on the result and therefore the length cannot be determined from the analysis. The validation example demonstrates that the embedded pile concept is an efficient tool for modelling the grout body of a ground anchor.

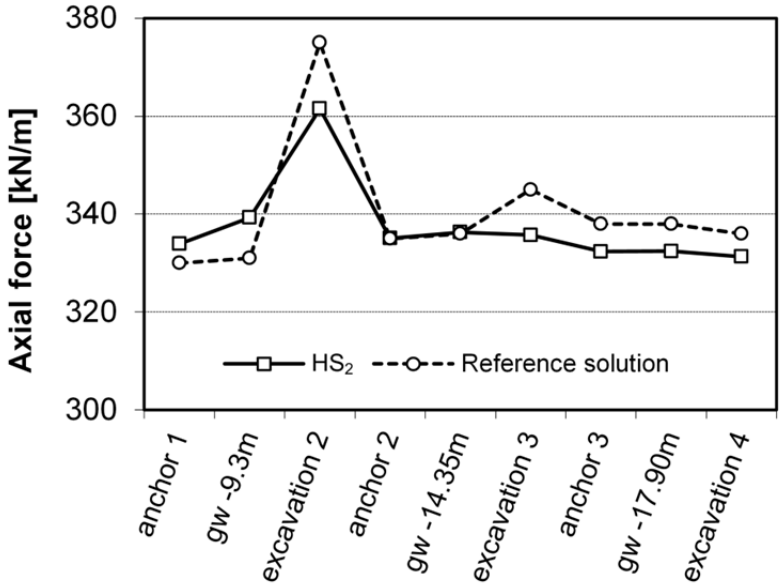

Fig. 164 2D vs 3D analysis

7.4 Project "Wien Mitte"

7.4.1 General information

The railway station "Wien Mitte" is one of the most frequented traffic junctions in Austria. The construction site has a length of about 180 m and a width of nearly 100 m. The planned superstructure, with heights between 35 m and 70 m, consists of 130000 m^2 gross floor-area and is located above the existing railway station. Fig. 165 illustrates an image of the entire building (©beyer.co.at).

Fig. 165 Project overview (© beyer.co.at)

Most parts of the existing superstructure above the station will be removed, however the slab of these buildings, consisting of continuous prestressed concrete beams, will be partly utilized for the new project. Hence, the differential settlements are the key point of interest. Fig. 166 shows the project in the top view including the existing underground structures. In the area of the new superstructure two subway lines, the City Airport Train (CAT) and several ÖBB railway lines operate. In addition, a main sewerage channel crosses the building side and concentrated loads up to 2500 kPa are present.

Due to these complex constructional constrains and the requirement that the serviceability of the railway station has to be ensured during the whole construction period, the use of jet-grouted columns as foundation elements is most likely the only feasible foundation concept. A total length of about 30000 m jet-grouted columns with maximum lengths up to 20.0 m and diameters between 0.8 to 1.0 m were proposed. In distinct zones it was also designed to install inclined columns.

The soil profile for the finite element simulation is based on core drillings with depths down to -45.0 m. Fig. 167 shows the obtained soil profile and the evaluation of E_{oed} and E_{ur} over depth. A more detailed description of the soil condition is given in Würger (2006) and Martak et al. (2007). The Hardening Soil model was used to model the soil behaviour (Tab. 31) and the overconsolidation of the soil (e.g. Fross 1973) is taken into account with a pre-overburden value.

All calculations were carried out as drained analyses and the following phases were defined:

- Generation of initial stresses
- Excavation until lower edge of the slab
- Modelling of the existing subway tunnel U3 (wished in place)
- Installation of deep foundation elements (wished in place)
- Activation of slabs
- Activation of loads from the superstructure

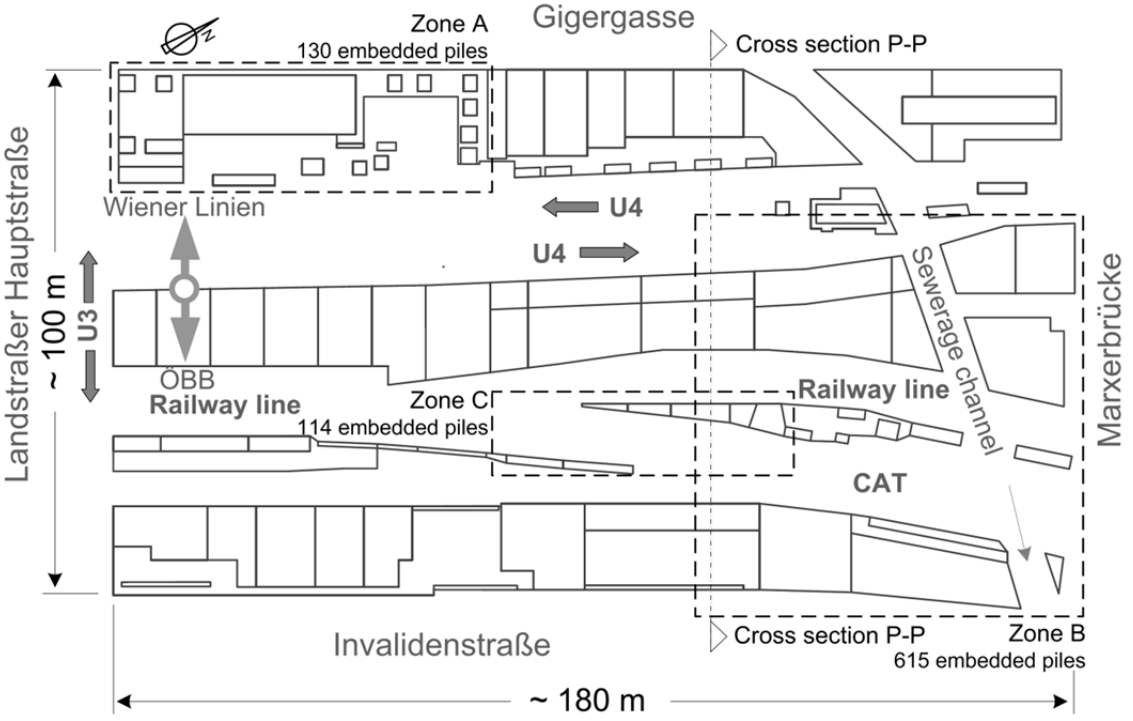

Fig. 166 Top view of the project including existing underground structures

Tab. 31: Soil properties for the Hardening Soil model

parameter	unit	gravel	sandy silt I / II	sand	stiff silt
γ_{unsat}	kN/m^3	21.0	20.0	20.0	20.0
γ_{sat}	kN/m^3	21.5	20.0	21.0	20.0
$E_{50,ref}$	kPa	40 000	20 000	25 000	30 000
$E_{oed,ref}$	kPa	40 000	20 000	25 000	30 000
$E_{ur,ref}$	kPa	120 000	50 000	62 500	90 000
ν'_{ur}	-	0.2	0.2	0.2	0.2
p_{ref}	kPa	100	100	100	100
m	-	0.00	0.80	0.65	0.60
φ'	°	35.0	27.5	32.5	27.5
c'	kPa	0.1	20.0 / 30.0	5.0	30.0
ψ	°	5.0	0.0	2.5	0.0
K_0^{nc}	-	0.426	0.538	0.463	0.538

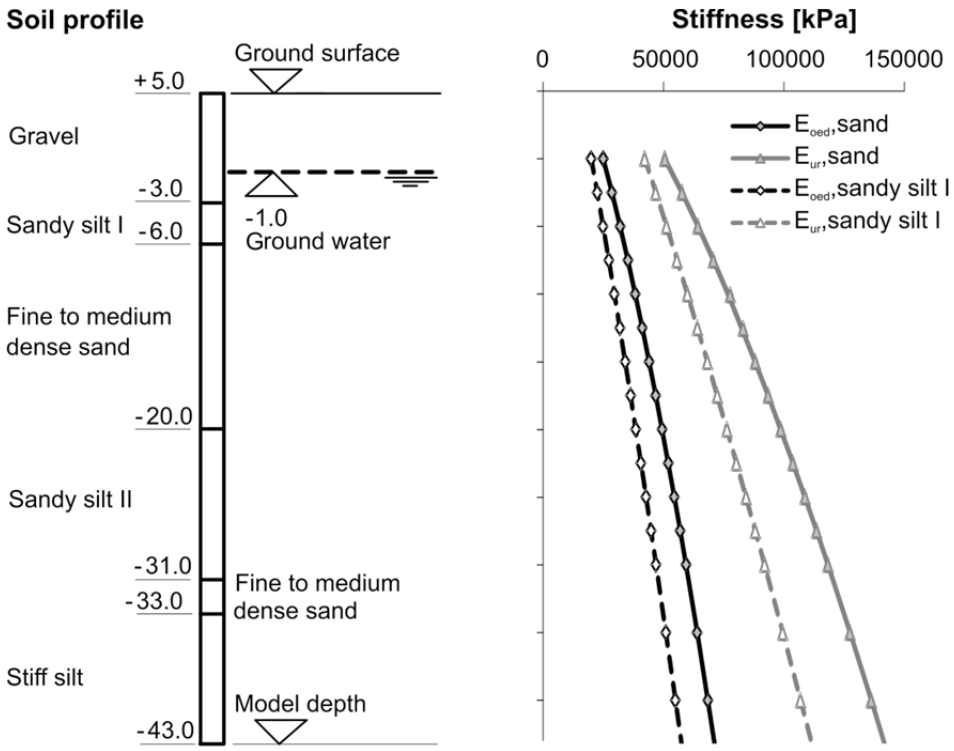

Fig. 167 Soil profile (left) and evaluations of E_{oed} and E_{ur} (right)

7.4.2 Preliminary studies

For the first analysis a 2D plane strain model along cross section P-P (Fig. 166) was defined. This model was convenient for principle studies of variations of inclinations or lengths of the jet-grout columns, but due to the geometrical restrictions in other parts of the construction the calculated settlements are not very reliable, therefore 3D modelling was necessary. However, before the entire structure was modelled, a preliminary study of a raft supported by a limited number of jet-grouted columns was performed with three different models: a 2D plane strain model, a full 3D model with volume discretisation of the columns and one model with the embedded pile formulation. The soil layering is similar to the real project and the overconsolidation is defined with 600 kPa. This value is at the lower limit for the soil conditions in this area of Vienna and has therefore been adopted for this study. The foundation slab is defined as linear elastic material with an elasticity modulus E of 2.8e7 kPa and a Poisson's ratio of 0.15. The jet-grout columns are described with Mohr-Coulomb material behaviour (Tab. 32). Fig. 168 shows the 2D plane strain model for the example. Two different configurations are studied. In the first one, all jet-grout columns are vertical and in the second one the outer piles are inclined.

Tab. 32: Properties of jet-grout columns

	$\gamma_{sat} = \gamma_{unsat}$ [kN/m3]	ν [–]	E_{ref} [kPa]	c' [kPa]	φ' [°]
jet-grout column	21.5	0.15	1E7	2700	32.5

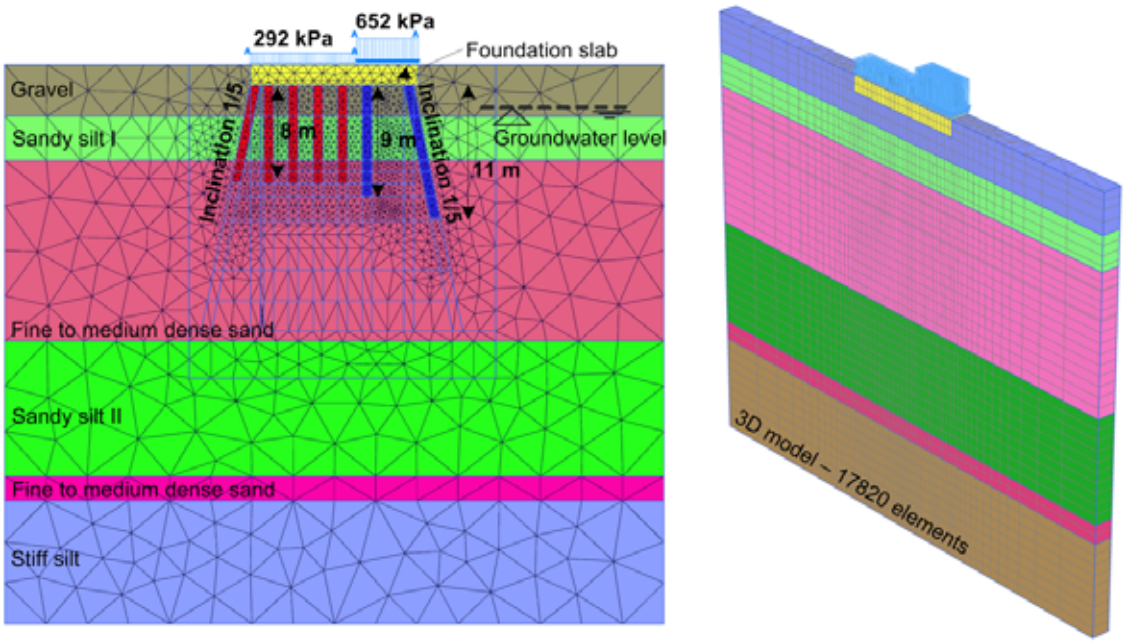

Fig. 168 2D plane strain model (left) and 3D model (right)

In the 2D analyses the stiffness of the jet-grouted columns, with a real diameter of 0.8 m, were converted into equivalent stiffnesses according to their spacing e_P. The interaction between jet-grouted columns and the subsoil can be assumed as very rough, hence no interface elements were defined between columns and soil. For the 3D calculations, the 2D model is extended to a 3D strip (Fig. 168). Due to the fact that it is not possible to define inclined volume piles in PLAXIS 3D Foundation, just one calculation with vertical piles was investigated. However, it is possible to model piles in arbitrary direction in the soil with the embedded pile concept, therefore both configurations as considered for the plane strain case have been compared. The bearing capacity of the embedded pile is defined with a linear distribution of t_s ($T_{top,max}$ = 0; $T_{bot,max}$ = 502 kN/m) and a maximum base resistance F_{max} of 600 kN.

The results show that the inclination of the outer piles leads to a reduction of vertical displacements of roughly 4 mm which corresponds to about 5% of maximum vertical displacements. The maximum difference between the different modelling techniques is roughly 2% (Fig. 169), indicating that the EP formulation is applicable to modelling vertical and inclined jet-grouted columns in layered soil conditions.

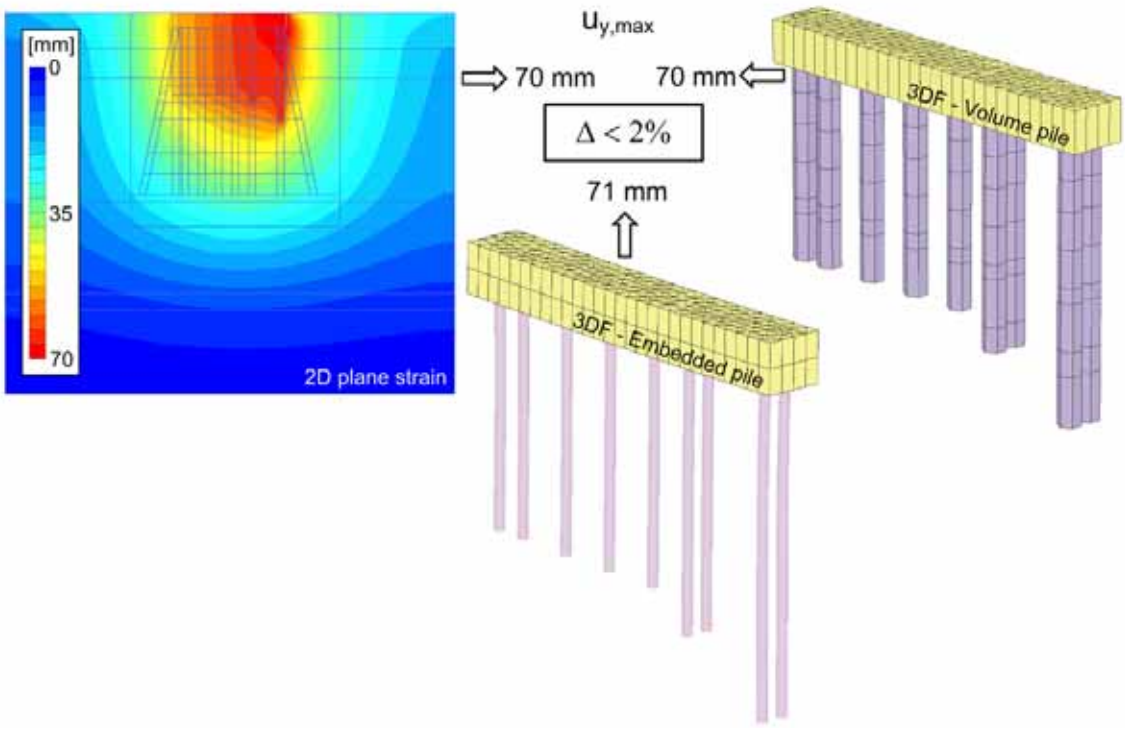

Fig. 169 2D plane strain model (left) and structural elements of 3DF model using embedded piles

7.4.3 Settlement prediction using 3D FE analyses

In this section settlement predictions for the entire project are presented. The soil conditions are similar to those presented in the previous chapter, but the pre-consolidation pressure was increased to 800 kN/m^2. The design of the deep foundation based on the bearing capacity of individual piles required about 3000 jet-grouted columns with diameters between 0.8 m to 1.0 m. The first analyses were performed with a simplified model where the zones improved by jet-grout columns are modelled as blocks, meaning that the zones of the sub-soil in which the columns are installed are defined with smeared properties (Fig. 170). The model with the dimensions $L_m/B_m/D_m$ of 500/400/48 m consists of 46478 elements. The foundation slabs are modelled by means of volume elements and defined as linear elastic material.

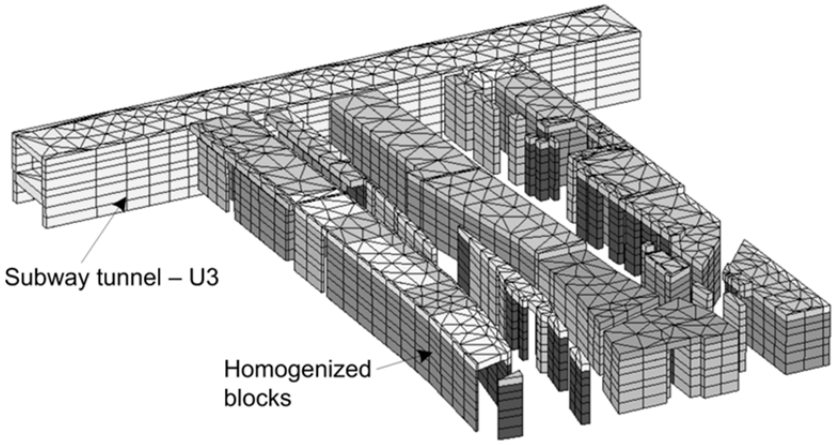

Fig. 170 Structural elements of first 3D model ("Block" model)

This simple model was used to study the effect of different column (resp. block) lengths. But because these calculations can neither consider plastic zones along or beneath jet-grouted columns nor the inclination of foundation elements, they are not applicable for an optimisation of the foundation concept. Additionally, the computed differential settlements are non-conservative due to the fact that blocks generally overestimate the stiffness of a deep foundation. Hence another modelling approach was chosen where two areas are distinguished: Areas that are not sensible for the superstructure and in which the load is not very high, and others where the loads are very high and the superstructure is very sensitive to (differential) settlements. The former are modelled as homogenized blocks, and for the latter, the embedded pile concept is applied. The capacity of the EPs is defined by a constant skin friction distribution ($T_{top,max}$ and $T_{bot,max}$ = 251 kN/m) and a base resistance F_{max} of 600 kN. Fig. 166 shows the three sensitive zones defined. Zone A is a critical zone because of the superstructure, Zone B because of very high concentrated loads and Zone C due to the complex geometrical constraints. Fig. 171 shows the entire 3D model and a zoom of Zone B where

615 jet-grouted columns with different lengths, inclinations and spacings are modelled explicitly. With these models it is possible firstly to predict the global settlement behaviour of the entire construction because the complete structure is modelled, including all areas with significant different load intensities. Secondly, detailed information in the section with embedded piles is obtained, for example relative displacements and mobilization of the skin friction along individual piles.

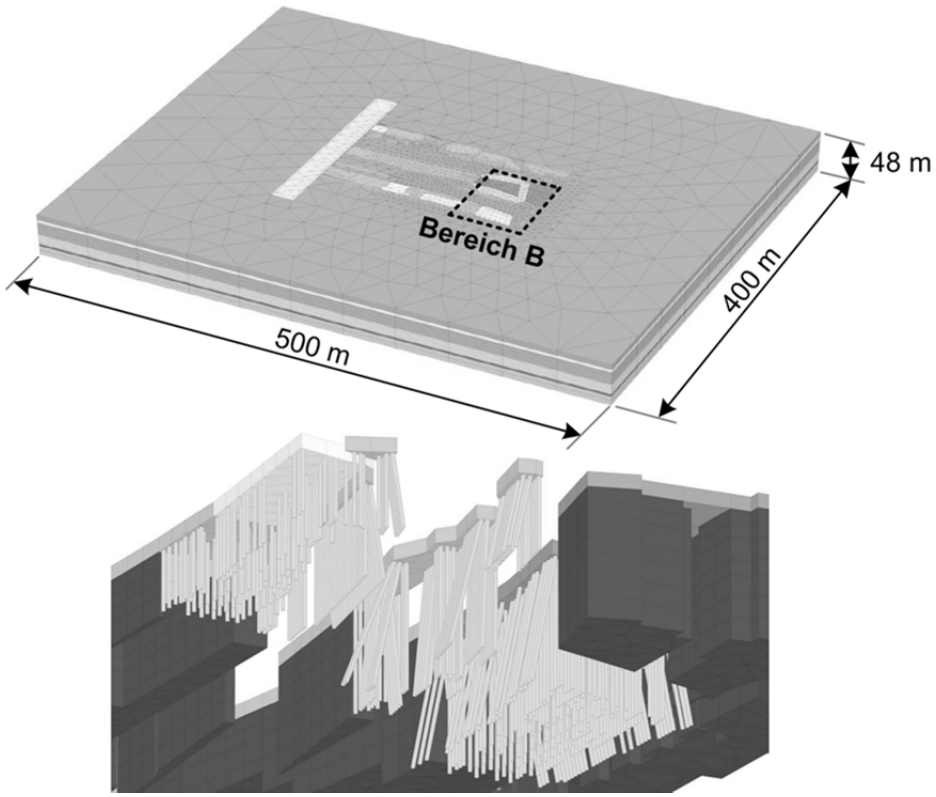

Fig. 171 Entire 3D model (top) and zoom of sensitive zone B (bottom)

In Fig. 172 contour lines of vertical displacements for all three models with sensitive zones, obtained with the HS model, are presented. With the optimised foundation layout, maximum settlements in Zone B of about 61 mm are predicted, and the subway tunnel (in the left part of the model) experiences settlements in the range of 10 mm.

To illustrate the effect of small strain stiffness the model for sensitive zone B was also analysed with the HSS model. The two additional parameters were estimated very conservatively ($G_o = 3 \cdot G_{ur}$; $\gamma_{0.7} = 0.0001$). Fig. 173 shows the comparison of both constitutive models in the region where the maximum vertical displacements are obtained. Even with this conservative estimate of the parameters a difference of nearly 18% was calculated, which clearly shows the necessity to account for small strain stiffness in settlement analyses.

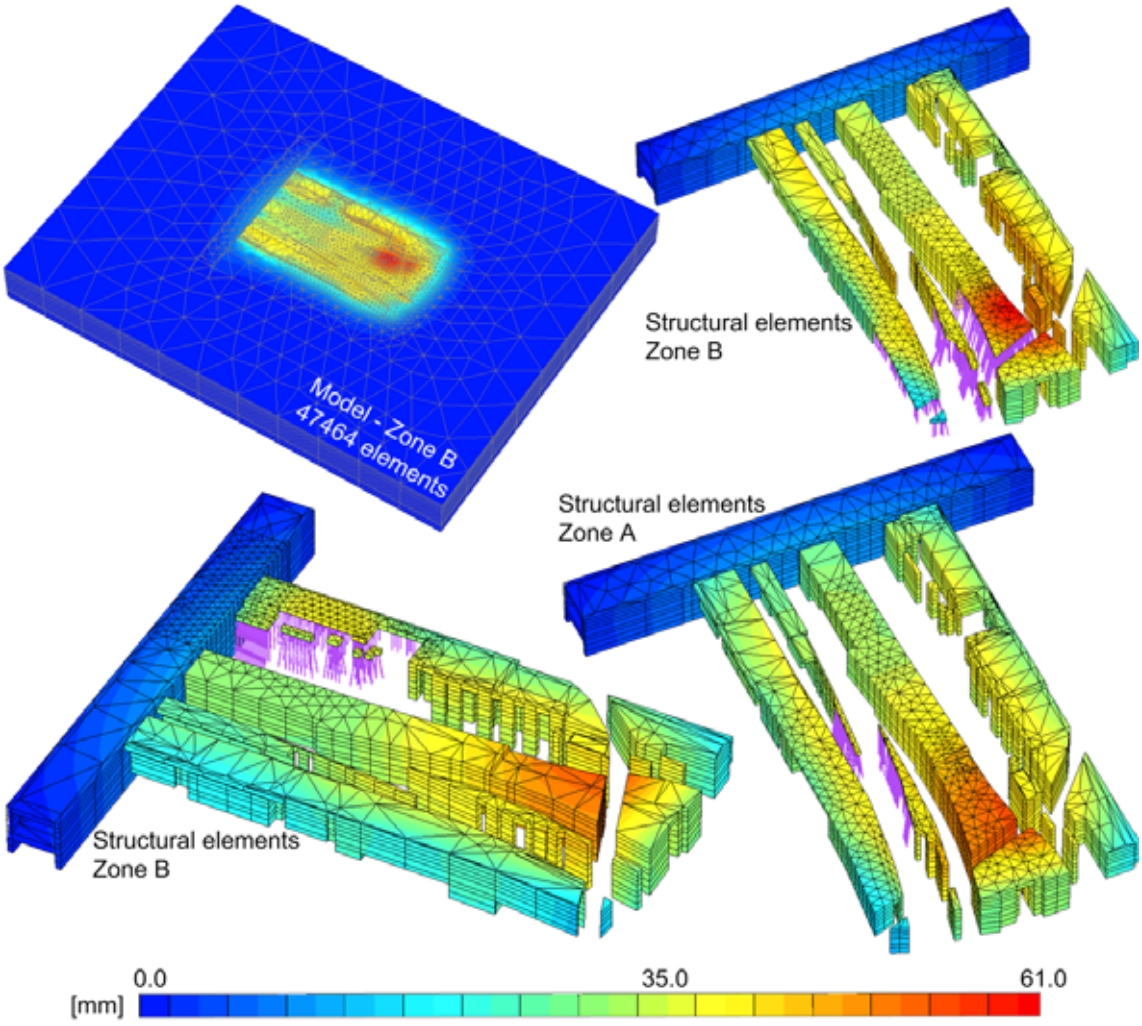

Fig. 172 Contour lines of vertical displacements

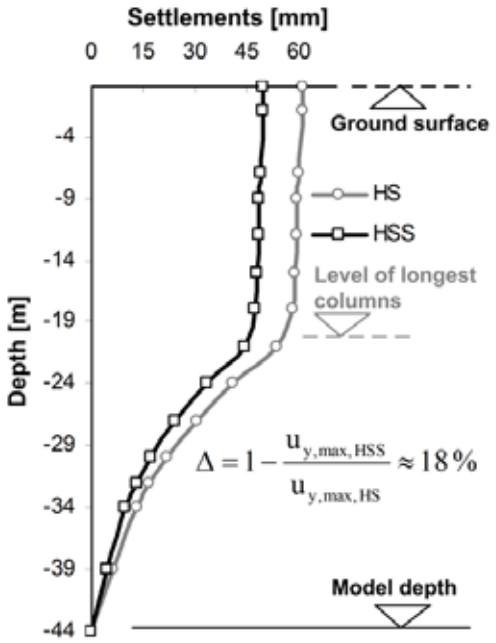

Fig. 173 HS vs HSS model in the high loaded region of sensitive zone B

Finally, a calculation with a 64-bit calculation kernel was performed, where all three sensitive zones were defined in one finite element model. This very complex 3D model includes roughly 1200 embedded piles. The layout and the dimensions of the jet-grout columns for this analysis were adapted according to the detailed design. Fig. 174 shows the structural elements of the model and the contour lines of vertical displacements. The results are more or less identical to the displacements calculated with the simplified models. Only concerning the interaction of sensitive zones B and C a more accurate result is obtained. This confirms clearly that the simplified modelling procedure chosen at the beginning is an efficient tool when analysing complex deep foundation systems.

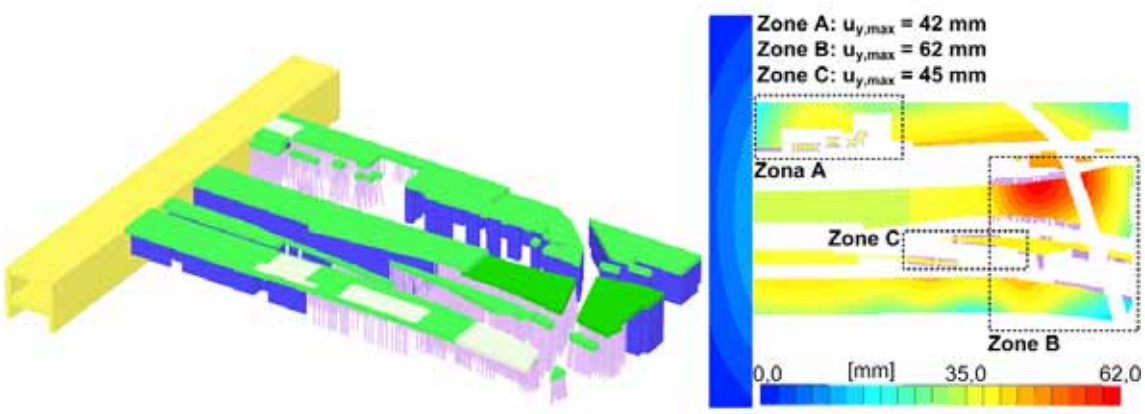

Fig. 174 Structural elements (left) and contour lines of settlements (right) – 64-bit calculation model

8 Conclusions and further research

8.1 Conclusions

If ground conditions are such that shallow foundations cannot support the load from structures such as high-rise buildings, several options exist. Depending on the soil profile and the corresponding soil properties, a pile foundation, a piled raft foundation or a diaphragm wall foundation is the solution for most cases. In this thesis the behaviour of such foundations is studied by means of finite elements. After a general overview of deep foundations, including single piles, pile groups and piled raft foundations, the advantages of numerical modelling of deep foundations are discussed. Due to the fact that a two-dimensional representation of boundary value problems is most of the time not possible, the main focus of this thesis is related to 3D analyses.

The standard finite element approach is studied extensively. In this approach, the piles are discretized by means of volume elements and the pile-soil interaction is describes with interface elements. The behaviour of interfaces and its influence on the mesh discretization was investigated. It is shown that the use of interface elements reduces the mesh dependency significantly. Additionally, the effect of soil dilatancy on the shaft and base resistance is demonstrated. Results indicate that a neglection of dilatancy yields a very conservative design, whereas the consideration of the dilatancy in kinematically constraint problems requires the definition of a critical state of density.

An attractive method to reduce the complexity of numerical models is the use of an embedded pile formulation, where piles are not explicitly modelled with continuum finite elements but replaced by a special “formulation”. The benefit of this concept is that piles are not discretized by means of volume elements and thus do not affect the finite element mesh. The main part of this thesis is related to this rather new and convenient modelling approach. After a short discussion about deficiencies of the current embedded pile version as implemented in PLAXIS 3DF, an improved formulation is presented which fulfils the following four criteria:

- Correct load-settlement curve
- Realistic mobilization and distribution of skin friction
- Realistic mobilization of end-bearing resistance
- Avoid numerical failure

The main changes of the improved embedded pile version are related to different definitions of interface stiffnesses and a modification of the elastic region approach. It is shown that a stress-dependent interface stiffness is necessary to

model a realistic mobilization of skin resistance. Additionally, it was found that the tip node of the embedded pile should correspond with a corner node of a solid soil element. This finding was already utilized for the meshing procedure in PLAXIS 3D, in which the program connects the corner node of the 10 noded tetrahedral elements with the embedded pile tip node. A number of validation examples considering single piles, pile groups and piled raft foundations indicate the capabilities and advantages of this modelling technique.

The application of the embedded piles concept to boundary value problems emphasized the benefit of this approach. Due to the fact that no discretisation of the piles is necessary, this concept allows the modelling of a high number of piles or columns and therefore very large computational models can be avoided. In addition, detailed information is obtained, for example relative displacements and mobilization of the skin friction, and the influence of different spacings, pile lengths and diameters can be evaluated with reasonable effort.

In some projects presented in this thesis, two types of modelling have been combined, where only sensitive parts are modelled in full detail and the rest of the deep foundation system is modelled as homogenized blocks, meaning that the zones of the sub-soil in which panels are installed are defined with smeared properties. Verifications of this assumption using a 64-bit calculation kernel show that the global settlement behaviour can be captured by using simplified models, but of course, concerning interactions of sensitive regions, detailed models are required. For some projects, different arrangements and lengths of deep foundation elements have been investigated to find an economical and technical feasible foundation system. Others were used to compare the behaviour of different foundation concepts. The assumptions made in the calculations are verified with parametric studies, sensitivity analyses and back-calculations of in-situ load tests. Comparisons of the Hardening Soil model with the Hardening Soil Small model show that once the high stiffness at small strains is taken into account, settlements from deeper levels are automatically reduced. Hence the influence of the model boundary conditions on the computed displacement is diminished and a more realistic settlement behaviour can be obtained.

The comparison of the different modelling approaches to define piles within a piled raft foundation shows clearly that the embedded pile option is a convenient alternative to the standard finite element approach. In the author's opinion, serviceability limit state is most of the time the key issue of foundation design, hence considerations regarding settlements play a very dominant role. The embedded pile concept is well capable for these types of analyses and provides a very powerful tool for complex situations with a large number of deep foundation elements.

8.2 Recommendations for further research

In the following, a guideline of useful further research in the field of numerical modelling of deep foundations is given.

- With respect to the standard finite element approach, further research should concentrate on the development of more advanced constitutive models for interface elements.

- Undrained behaviour of deep foundations, especially piled raft foundations should be investigated.

- Numerical modelling of pile installation methods should be part of more extensive research.

- Concerning the embedded pile formulation, further studies of horizontally loaded piles and pile groups are recommended.

- For ultimate limit state considerations, further investigations of the embedded pile interface stiffness are necessary.

- Other types of applications for embedded piles should be tested, e.g. rock bolts, passively loaded piles or large diameter piles etc.

- Multi-processing of software packages in combination with 64-bit calculation kernels, in order to make full 3D analysis suitable for engineering offices.

- Back-analyses of boundary value problems and validation against measured data.

- Development of more advanced constitutive models, which enable modelling of cyclic loading.

9 Bibliography

Alpan, I. (1970)
The geotechnical properties of soils. Earth-Science Reviews 6 (1), 5-49.

Altae, A.; Evgin, E.; Fellenius, B.H. (1993)
Load transfer for piles in sand and the critical depth. Canadian Geotechnical Journal, Vol. 30, No. 3, 455-463.

Arslan, U.; Katzenbach, R.; Quick, H.; Gutwald, J. (1994)
Dreidimensionale Interaktionsberechnung zur Gründung der vier neuen Hochhaustürme in Frankfurt am Main. Proc. Deutsche Baugrundtagung 1994, Köln, Germany, 425-437.

Ausweger, G. (2012)
Berechnung von Pfahlgründungen mit BEFE++. Master-Projekt, Graz University of Technology, Institute of Soil Mechanics and Foundation Engineering.

Baguelin, F.; Frank, R. (1980)
Theoretical studies of piles using the finite element method. Proc. Conference on Numerical methods in offshore piling, London, England, 83–91.

Basu, D.; Salgado, R.; Prezzi, M. (2009)
A continuum-based model for analysis of laterally loaded piles in layered soils. Géotechnique, Vol. 59, No. 2, 127-140.

Basu, D.; Loukidis, D.; Prezzi, M.; Salgado, R. (2011)
Analysis of shaft resistance of jacked piles in sands. Int. Journal for Numerical and Analytical Methods in Geomechanics, Vol. 35, 1605-1635.

Bathe, K.-J. (1986)
Finite-Elemente-Methode. Deutsche Übersetzung von P. Zimmermann. Berlin: Springer.

Beer, G.; Watson, J.O. (1992)
Introduction to finite and boundary element methods for engineers. West Sussex: John Wiley and Sons.

Benz, T. (2007)
Small-strain stiffness of soils and its numerical consequences. Ph.D. Thesis, Mitteilungsheft Nr. 55, Institute for Geotechnical Engineering, University of Stuttgart.

Berezantzev, V.C.; Khristoforov, V.; Golubkov, V. (1961)
Load bearing capacity and deformation of piled foundation. Proc. 5th Int. Conference on Soil Mechanics and Foundation Engineering, Paris, Vol. 2, 11–15.

Bjerrum, L. (1963)
Allowable settlements of structures. Proc. 3rd European Conference on Soil Mechanics and Foundation Engineering, Wiesbaden, Vol. 3, 135-137.

Bolton, M.D. (1986)
The strength and dilatancy of sands. Géotechnique, Vol. 36, No. 1, 65-78.

Brinkgreve, R.B.J. (1994)
Geomaterial models and numerical analysis of softening. Ph.D. Thesis, Technische Universiteit Delft.

Brinkgreve, R.B.J.; Broere, W. (2008)
PLAXIS, Finite element code for soil and rock analyses, Users Manual (Version 9). Plaxis bv, Delft, The Netherlands.

Brinkgreve, R.B.J.; Broere, W.; Waterman, D. (2006)
PLAXIS, Finite element code for soil and rock analyses, Users Manual (Version 8). Plaxis bv, Delft, The Netherlands.

Brinkgreve, R.B.J., Swolfs, W.M. (2007)
PLAXIS 3D Foundation, Finite element code for soil and rock analyses, Users Manual, Plaxis bv, Delft, The Netherlands.

Brinkgreve, R.B.J.; Swolfs, W.M.; Engin, E. (2010)
PLAXIS 2D 2010-Users Manual. Plaxis bv, Delft, The Netherlands.

Brinkgreve, R.B.J.; Swolfs, W.M.; Engin, E. (2011)
PLAXIS 2D 2011-Users Manual. Plaxis bv, Delft, The Netherlands.

Brinkgreve, R.B.J.; Swolfs, W.M.; Engin, E. (2011)
PLAXIS 3D 2011-Users Manual. Plaxis bv, Delft, The Netherlands.

Brown, D. (2002)
Effect of construction on axial capacity of drilled foundations on Piedmont soils. Journal of Geotechnical and Geoenvironmental Engineering, ASCE, Vol. 128, No 12, 967-973.

Burgstaller, M. (2010)
Gegenüberstellung und Vergleich unterschiedlicher Verfahren zur Ermittlung von axialen Pfahlwiderständen. Master-Projekt, Graz University of Technology, Institute of Soil Mechanics and Foundation Engineering.

Burland, J.B. (1973)
Shaft friction of piles in clay - a simple fundamental approach. Ground Engineering, Vol. 6, No. 3, 30-42.

Burland, J.B.; Broms B.B.; De Mello, V.F.B. (1977)
Behaviour of foundations and structures. Proc. 9th Int. Conference on Soil Mechanics and Geotechnical Engineering, Tokyo, Japan, 495-546.

Butterfield, R.; Banerjee, P.K. (1971)
The problem of pile group-pile cap interaction. Géotechnique, Vol. 21, No. 2, 135-142.

Cassan, M. (1966)
Le tassement des pieux: Synthese des recherches recentes et essais comparatifs. Sols-Soils, No. 18,19 43-58.

Cheng, Y.M. (2004)
N_q factors for pile foundations by Berezantzev. Géotechnique, Vol. 54, No. 2 58-67.

Chow, H. (2007)
Analyses of piled-raft foundations with piles of different lengths and diameters. Ph.D. Thesis, University of Sydney.

Chow, H.; Small, J. (2008)
Case histories for piled rafts. Proc. BGA Int. Conf. on Foundations, Dundee, Scotland, 12 pages.

Chow, Y.K.; Teh, C.I. (1991)
Pile-cap-pile-group interaction in nonhomogeneous soil. Journal of Geotechn. Engng, ASCE, Vol. 11, No 11, 1655-1668.

Comodromos, E.M.; Bareka, S.V. (2009)
Response evaluation of axially loaded fixed-head pile groups in clayey soils. Int. Journal for Numerical and Analytical Methods in Geomechanics, Vol. 33, 1839-1865.

Gennaro, V.; Frank, R. (2002)
Elasto-plastic analysis of the interface behaviour between granular media and structure. Computers and Geotechnics, Vol. 29, 547-572.

Desai, C.S. (1974)
Numerical design-analysis for piles in sands. Journal of Geotechn. Engng, ASCE, Vol. 100, GT 6, 613-635.

Desai, C.S.; Johnson L.D.; Hargett C.M. (1974)
Analysis of pile supported gravity lock. Journal of Geotechn. Engng, ASCE, Vol. 100, GT 9, 1009-1029.

DGGT AK 2.1 (2007)
Empfehlungen des Arbeitskreises „Pfähle“ (EA Pfähle). Berlin: Ernst & Sohn.

Dijkstra, J. (2009)
On the modelling of pile installation. Ph.D. Thesis, Delft University of Technology. The Netherlands.

Drucker, D.C.; Prager, W. (1952)
Soil mechanics and plastic analysis in limit design. Quart. Appl. Mech., Vol. 10, 157-165.

Duenser, C.; Thoeni, K.; Riederer, K.; Lindner, B.; Beer, G. (2011)
New developments of the boundary element method for underground constructions. International Journal of Geomechanics, ASCE, In print.

Ellison, R.D.; D'Appolonia, E.; Thiers, G.R. (1971)
Load-deformation mechanism for bored piles. Journal of the soil mechanics and foundations division, ASCE, Vol. 97, SM 4, 661-678.

El-Mossallamy, Y. (1996)
Ein Berechnungsmodell zum Tragverhalten der Kombinierten Pfahl-Plattengründung. Ph.D. Thesis, Mitteilungen des Institutes und der Versuchsanstalt für Geotechnik der TU Darmstadt, Heft Nr. 36.

El-Mossallamy, Y. (1999)
Load-settlement behaviour of large diameter bored piles in over-consolidated clay. Proc. 7th International Symposium on Numerical Models in Geomechanics (NUMOG), Pande et al. (eds.), Graz, Austria, 443-450. Rotterdam: Balkema.

England, M.; Cheesman P.F. (2010)
Design benefits of bi-directional load testing of barrettes. Proc. Geotechnical Challenges in Urban Regeneration, London, England.

Engin, H.K. (2006)
A report on embedded piles. PLAXIS internal report, 55 pages.

Engin, H.K.; Andresen, L. (2011)
Comparison of zipper type techniques for finite element analysis of pile penetration problem. Proc. 13th International Conference of the International Association of Computer Methods and Advances in Geomechanics (IACMAG), Khalili & Oeser (eds.), Melbourne, Australia.

Engin, H.K.; Brinkgreve R.B.J. (2009)
Investigation of pile behaviour using embedded piles. Proc. 17th Int. Conference on Soil Mechanics and Geotechnical Engineering, Alexandria, Egypt, 1189-1192.

Engin, H.K.; Septanika E.G.; Brinkgreve R.B.J. (2007)
Improved embedded beam elements for the modelling of piles. Proc. 10rd International Symposium on Numerical Models in Geomechanics (NUMOG), Pietruszczak & Pande (eds.), Rhodes, Greece, 475-480. London: Taylor & Francis Group.

Engin, H.K.; Septanika E.G.; Brinkgreve R.B.J. (2008)
Estimation of pile group behavior using embedded piles. Proc. 12th International Conference of the International Association of Computer Methods and Advances in Geomechanics (IACMAG), Singh (ed.), Goa, India. 3231-3238.

Engin, H.K.; Septanika E.G.; Brinkgreve R.B.J.; Bonnier, P.G. (2009)
Modelling piled foundations by means of embedded piles. Proc. 2nd Int. Workshop on Geotechnics of Soft Soils - Focus on Ground Improvement, Karstunen & Leoni (eds.), Glasgow, Scotland, 131-136.

Fellenius, B.H. (2001)
The O-Cell – An innovative engineering tool. Geotechnical News Magazine, Vol 19, No. 2, 32-33.

Fellenius, B.H. (2002)
Determining the true distributions of load in instrumented piles. Proc. Deep Foundations 2002: An International Perspective on Theory, Design, Construction, and Performance, Florida, United States, Vol. 2, 1455-1470.

Fellenius, B.H. (2009)
Basics of foundation design. Revised electronic edition, [www.Fellenius.net], 330 pages.

Fellenius, B.H.; Altae, A.A. (1995)
Critical depth: how it came into being and why it does not exist. Proc. of the ICE - Geotechnical Engineering, Vol. 113, No. 2, 107-111.

Fleming, K.W.G. (1992)
A new method for single pile settlement prediction and analysis. Géotechnique, Vol. 42, No. 3, 411-425.

Fleming K.W.G.; Weltman A.J.; Randolph M.F.; Elson K.W. (2009)
Piling engineering. England: Taylor & Francis.

Fross, M. (1973)
Untersuchung über die Zusammendrückbarkeit vorbelasteter toniger Böden des Wiener Beckens. Mittelungen des Institutes für Grundbau und Bodenmechanik, TU Wien, Heft 12, 10-21.

Giannopoulos, K.L.; Zdravković, L.; Potts, D.M. (2010)
A numerical study on the effects of time on the axial load capacity of piles in soft clays. Proc. Numerical methods in geotechnical engineering NUMGE 2010, Benz & Nordal (eds.), Trondheim, Norway, 595-600. London: Taylor & Francis Group.

Gibson, R.E. (1967)
Some results concerning displacements and stress in a non-homogeneous elastic half-space. Géotechnique, Vol. 17, 58-67.

Gibson, R.E. (1974)
The analytical method in soil mechanics. Rankine lecture, Géotechnique, Vol. 24, No. 2, 115-140.

Goodman, R.E.; Taylor R.L.; Brekke T.L. (1968)
A model for the mechanics of jointed rock. Journal of Geotechn. Engng, ASCE, Vol. 94, SM 3, 637-659.

Hain, S.J.; Lee, I.K. (1978)
The analysis of flexible raft-pile systems. Géotechnique, Vol. 28, No. 1, 65-83.

Hanisch, J.; Katzenbach, R.; König, G. (2002)
Kombinierte Pfahl-Plattengründungen. Berlin: Ernst & Sohn.

Hasen, J.B. (1970)
A revised and extended formula for bearing capacity. Danish Geotechnical Institute Bul., No. 28, Copenhagen.

Henke, S. (2008)
Herstellungseinflüsse aus Pfahlrammung im Kaimauerbau. Ph.D. Thesis, Veröffentlichungen des Instituts for Geotechnik und Baubetrieb, Nr. 18, Technische Universität Hamburg-Harburg.

Hettler, A. (1986)
Setzungen von vertikalen, axial belasteten Pfahlgruppen in Sand. Der Bauingenieur, Vol. 61, 417-421.

Hofmann, R. (2007)
Kastenförmige Tieffundierungen. Proc. 6. Österreichische Geotechniktagung, Vienna, Austria, 99-110.

Hooper, J.A. (1973)
Observations on the behaviour of a piled raft foundation on London clay. Proc. Instn. Civil Engineers, Vol. 55, No 2, 855-877.

Ittershagen, M. (2009)
Optimierte Baugruben- und Gründungskonzepte für Baumaßnahmen in dicht bebauten Innenstadtgebieten. Bauingenieur, Vol. 84, 349-357.

Jaky, J. (1944)
The coefficient of earth pressure at rest. (In Hungarian: A nyugalmi nyomas tenyezoje). Journal of the Society of Hungarian Architects and Engineers, Budapest, Vol. 78 (22), 355-358.

Janbu, N.D. (1976)
Static bearing capacity of friction piles. Proc. 6th European Conference on Soil Mechanics and Foundation Engineering, Vienna, Austria, Vol. 1.2, 479-488.

Jardine, R.J.; Potts, D.M.; Fourie, A.B.; Burland, J.B. (1986)
Studies of the influence of non-linear stress-strain characteristics in soil-structure interaction. Géotechnique, Vol. 36, No. 3, 377-396.

Kaineder, F. (2009)
Einfluss der Interfaceeigenschaften auf das Setzungsverhalten von Pfählen. Master-Thesis, Graz University of Technology, Institute of Soil Mechanics and Foundation Engineering.

Karabatakis, D.A.; Hatzigogos, T.N. (2002)
Analysis of creep behaviour using interface elements. Computers and Geotechnics, Vol. 29, 257-277.

Katzenbach, R.; Arslan, U.; Gutwald, J. (1994)
A numerical study on pile foundation of the 300m high Commerzbank tower in Frankfurt am Main. Proc. Numerical methods in geotechnical engineering NUMGE 1994, Smith (ed.), Manchester, England, 271-277. Rotterdam: Balkema.

Katzenbach, R.; Arslan, U.; Moormann, C.; Reul, O. (1998)
Piled raft foundation - Interaction between piles and raft. Proc. Int. Conf. on Soil-Structure Interaction in Urban Civil Engineering, Katzenbach & Arslan (eds.), Darmstadt, Germany, 279-296.

Katzenbach, R.; Gutberlet, C.; Bachmann, G. (2007)
Soil-structure interaction aspects for ultimate limit state design of complex foundations. Proc. First Int. Symposium on Geotechnical Safety & Risk, Shanghai, China, 585-596.

Kempfert, H.-G.; Eigenbrod, K. D.; Smoltczyk, U. (2003)
Pile foundation. Geotechnical Engineering Handbook, Ernst & Sohn Berlin, Vol. 3, 83-227.

Kitiyodom, P.; Matsumoto, T.; Sonoda, R. (2009)
Approximate numerical analysis of a large piled raft foundation. Soils and Foundations, Vol. 51, No 1, 1-10.

König, F. (2008)
Zur zeitlichen Traglastentwicklung von Pfählen und der nachträglichen Erweiterung bestehender Pfahlgündungen. Ph.D. Thesis, Veröffentlichungen des Instituts for Geotechnik und Baubetrieb, Nr. 17, Technische Universität Hamburg-Harburg.

Körber, G. (2009)
Vorwegnahme von Setzungen bei hochbelasteten Großbohrpfählen durch den Einbau von Hubkissen an der Pfahlsohle. Proc. Pfahl-Symposium 2009, Braunschweig, Germany, 425-436.

Kraft, L.M. (1991)
Performance of axially loaded pipe piles in sand. Journal of Geotechn. Engng, ASCE, Vol. 117, No 2, 272-296.

Krajewski, W.; Reul, O. (2009)
Einfluss der Diskretisierung bei räumlichen Berechnungen von Gründungen. Proc. Workshop on Aktuelle Entwicklungen bei der Anwendung numerischer Verfahren in der Geotechnik, DGGT/AK 1.6, Karlsruhe, Germany, 77-83.

Kulhawy, F.H. (1984)
Limiting tip and side resistance: Fact or fallacy? Proc. Analysis and design of pile foundations, J.R. Meyer (ed.), San Francisco, California, 80-98.

Lashkari, A. (2011)
A plasticity approach to shaft resistance-displacement behaviour of bored piles in sand. Proc. 13th International Conference of the International Association of Computer Methods and Advances in Geomechanics (IACMAG), Khalili & Oeser (eds.), Melbourne, Australia.

Lee, S.W.; Cheang, W.W.L. Swolfs, W.M.; Brinkgreve R.B.J. (2010)
Modelling of piled rafts with different pile models. Proc. Numerical methods in geotechnical engineering NUMGE 2010, Benz & Nordal (eds.), Trondheim, Norway, 637-642. London: Taylor & Francis Group.

Lee, S.; L; Long, J.H. (2008)
Skin friction features of drilled CIP piles in sand from pile segment analysis. Int. Journal for Numerical and Analytical Methods in Geomechanics, Vol. 32, 745-770.

Lee, J.H.; Salgado, R. (1999)
Determination of pile base resistance in sands. Journal of Geotechnical and Geoenvironmental Engineering, ASCE, Vol. 125, No 8, 673-683.

Lehane, B.M.; Jardine, R.J.; Bond, A.J.; Frank, R. (1993)
Mechanisms of shaft friction in sand from instrumented pile tests. Journal of Geotechn. Engng, ASCE, Vol. 119, No 1, 19-35.

Liang, F.; Chen, L.; Han, J. (2009)
Integral equation method for analysis of piled rafts with dissimilar piles under vertical loading. Computers and Geotechnics, Vol. 36, 419-426.

Liu, W.; Novak, M. (1991)
Soil-pile-cap static interaction analysis by finite and infinite elements. Canadian Geotechnical Journal, Vol. 28, No. 6, 771-783.

Lokadis, D.; Salgado, R. (2008)
Analysis of the shaft resistance on non-displacement piles in sand. Géotechnique, Vol. 58, No. 4, 283-296.

Marcher, T. (2003)
Nichtlokale Modellierung der Entfestigung dichter Sande und steifer Tone. Ph.D. Thesis, Mitteilungsheft Nr. 50, Institute for Geotechnical Engineering, University of Stuttgart.

Martak, L., Mayerhofer, A.F., Tschuchnigg, F., Vorwagner, A. (2007)
Bahnhof Wien Mitte – Ein zentrales Infrastrukturprojekt im Herzen Wiens. Proc. 23th Christian Veder Kolloquium, M. Dietzel et al. (eds.), Graz, Austria, 79-96.

Meissner, H. (1983)
Tragverhalten von axial oder horizontal belasteter Borhpfähle in körnigen Böden. Ph.D. Thesis, Veröffentlichungen des Instituts für Bodenmechanik und Felsmechanik der Universität Fridericiana in Karlsruhe, Nr. 93.

Memon, B.A.; Su, X.Z. (2004)
Arc-length technique for nonlinear finite element analysis. Journal of Zhejiang University SCIENCE, Vol. 5 (5), 618-628.

Meyerhof, G.G. (1976)
Bearing capacity and settlement of pile foundations. Journal of Geotechn. Engng, ASCE, Vol. 102, GT 3, 197-228.

Mindlin, R.D. (1936)
Force at a point in the Interior of a Semi-Infinite Solid. Physics, Vol. 7, 195-202.

Mroueh, H.; Shahrour, I. (2009)
Numerical analysis of the response of battered piles to inclined pullout loads. Int. Journal for Numerical and Analytical Methods in Geomechanics, Vol. 33, 1277-1288.

Osterberg, J.O. (1989)
New device for load testing driven piles and drilled shafts separates friction and end bearing. Proc. Int. Conf. On Piling and Deep Foundations, London, England, 421-431.

Osterberg, J.O. (1998)
The Osterberg load test method for bored and driven piles - The first ten years. Proc. 7th Int. Conf. On Piling and Deep Foundations, Vienna, Austria, 1-17.

Ottaviani, M. (1975)
Three-dimensional finite element analysis of vertically loaded pile groups. Géotechnique, Vol. 25, No. 2, 159-174.

Petternel, P. (2012)
Numerische Studien zum Tragverhalten von Pfählen und Pfahlgruppen in PLAXIS 3D. Master-Thesis, Graz University of Technology, Institute of Soil Mechanics and Foundation Engineering.

Potts, D. (2003)
Numerical analysis: a virtual dream practical reality. Rankine lecture, Géotechnique, Vol. 53, No. 6, 535-573.

Potts, D.M.; Zdravković, L. (1999)
Finite element analysis in geotechnical engineering, Theory. London: Telford.

Potts, D.M.; Zdravković, L. (2001)
Finite element analysis in geotechnical engineering, Application. London: Telford.

Potyondy, J.G. (1961)
Skin friction between various soils and construction materials. Géotechnique, Vol. 11, No. 4, 339-353.

Poulos, H.G. (1989)
Pile behaviour – theory and application. Rankine lecture, Géotechnique, Vol. 39, No. 3, 365-415.

Poulos, H.G. (1991)
Analysis of piled strip foundations. Proc. 7th International Conference of the International Association of Computer Methods and Advances in Geomechanics (IACMAG), Beer et al. (eds.), Cairns, Australia, 183-191.

Poulos, H.G. (1994)
An approximate numerical analysis of pile-raft interaction. Int. Journal for Numerical and Analytical Methods in Geomechanics, Vol. 18, 73-92.

Poulos, H.G. (2001a)
Spannungen und Setzungen im Boden. Grundbautaschenbuch, 6. Auflage, Band 1, Smoltczyk (ed.), 255-305. Berlin: Ernst & Sohn.

Poulos, H.G. (2001b)
Methods of analysis of piled raft foundations. Report Technical Committee TC18 on Piled Foundations, ISSMGE.

Poulos, H.G. (2001c)
Piled raft foundations: design and applications. Géotechnique, Vol. 51, No. 2, 95-113.

Poulos, H.G. (2006)
Pile group settlement estimation – Research to practice. Proc. GeoShanghai International Conference 2006, Foundation Analysis and Design: Innovative Methods, Shanghai, China, 1-22.

Poulos, H.G.; Davis, E.H. (1980)
Pile Foundation Analysis and Design. New York: John Wiley and Sons

Poulos, H.G.; Small, J.C.; Ta, L.D.; Singha, J.; Chen, L. (1997)
Comparison of some methods for analysis of piled rafts. Proc. 14th Int. Conference on Soil Mechanics and Foundation Engineering, Hamburg, Germany, Vol. 2, 1119-1124.

Prakoso, W.A.; Kulhawy, F.H. (2001)
Contribution to piled raft design. Journal of Geotechnical and Geoenvironmental Engineering, ASCE, Vol. 127 (1), 17-24.

Prandtl, L. (1920)
Über die Härte plastischer Körper. Nachrichten von der Königlichen Gesellschaft der Wissenschaften zu Göttingen, Göttingen, 74-85.

Pressley, J.S.; Poulos, H.G. (1986)
Finite element analysis of mechanisms of pile group behaviour. Int. Journal for Numerical and Analytical Methods in Geomechanics, Vol. 10, 213-221.

Rajapakse, R.K.N.D. (1990)
Response of an axially loaded elastic pile in a Gibson soil. Géotechnique, Vol. 40, No. 2, 237-249.

Randolph, M.F. (1983)
Design of piled raft foundations. Cambridge University Engineering Department, CUED/D Soils TR. 143.

Randolph, M.F. (1994)
Design methods for pile groups and piled rafts. Proc. 13th Int. Conference on Soil Mechanics and Geotechnical Engineering, New Delhi, India, 61-82.

Randolph, M.F. (2003)
Science and empiricism in pile foundation design. Rankine lecture, Géotechnique, Vol. 53, No. 10, 847-875.

Randolph, M.F.; Wroth, C.P. (1978)
Analysis of deformation of vertically loaded piles. Journal of Geotechn. Engng Div., ASCE, Vol. 104, GT 12, 1465-1488.

Randolph, M.F.; Wroth, C.P. (1979)
An analysis of the vertical deformation of pile groups. Géotechnique, Vol. 29, No. 4, 423-439.

Reul, O. (2000)
In-situ-Messungen und numerische Studien zum Tragverhalten der Kombinierten Pfahl-Plattengründung. Ph.D. Thesis, Mitteilungen des Institutes und der Versuchsanstalt für Geotechnik der TU Darmstadt, Heft Nr. 53.

Reul, O. (2004)
Numerical study of the bearing behavior of piled rafts. International Journal of Geomechanics, ASCE, Vol. 4, No.2, 59-68.

Reul, O. (2010)
Entwurfsoptimierung von Hochhausgründungen. Der Bauingenieur, Vol. 85, 177-187.

Reul, O.; Randolph, M.F. (2003)
Piled rafts in overconsolidated clay: comparison of in situ measurements and numerical analyses. Géotechnique, Vol. 53, No. 3, 301-249.

Reul, O.; Randolph, M.F. (2004)
Design strategies for piled rafts subjected to nonuniform vertical loading. Journal of Geotechnical and Geoenvironmental Engineering, ASCE, Vol. 130, No 1, 1-13.

Rollberg, D. (1978)
Die Kraft-Setzungslinie von Pfählen. Bauingenieur, Vol. 53, 309-313.

Rudolf, M. (2005)
Beanspruchung und Verformung von Gründungskonstruktionen auf Pfahlrosten und Pfahlgruppen unter Berücksichtigung des Teilsicherheitskonzeptes. Ph.D. Thesis, Schriftreihe Geotechnik Universität Kassel, Heft Nr. 17, Universität Kassel.

Sadek, M.; Shahrour, I. (2004)
A three dimensional embedded beam element for reinforced geomaterials. International Journal for Numerical and Analytical Methods in Geomechanics, Vol. 28, No.9, 931-946.

Said, I.; De Gennaro, V.; Frank, R. (2009)
Axisymmetric finite element analysis of pile loading tests. Computers and Geotechnics, Vol. 36, 6-19.

Saidel, T.; Căpraru, C.; Marcu, A. (2010)
Influence of constitutive laws and geotechnical parameters on deep excavations design, and evaluation of their influence on neighbouring buildings: examples from recent projects in Bucharest. Proc. 14th Danube-European Conference on Geotechnical Engineering, J. Frankovská et al. (eds.), Bratislava, Slovakia.

Schanz, T. (1998).
Zur Modellierung des mechanischen Verhaltens von Reibungsmaterialien. Habilitation, Universität Stuttgart, Mitteilungen des Instituts für Geotechnik, Heft 45, Germany.

Schanz, T., Vermeer, P.A., Bonnier, P.G. (1999).
The Hardening-Soil model: Formulation and verification. Beyond 2000 in Computational Geotechnics, R.B.J. Brinkgreve (ed), 281-290. Rotterdam: Balkema.

Schmertmann, J.H.; Hayes, J.A. (1997)
The Osterberg cell and bored pile testing - A symbiosis. Proc. 3rd Int. Geotechnical Engineering Conference, Cairo University, Cairo, Egypt, 139-166.

Schreib, G.; Vujcic, I.; Moormann, C. (2010)
Optimierung von Gründung und Baugrube für den Block 8 des Rheinhafen-Dampfkraftwerkes in Karlsruhe. Proc. 7. Kolloquium, Bauen in Boden und Fels, Ostfildern, Germany, 45-59.

Schweiger, H.F. (1995)
Ein Beitrag zur Anwendung der Finite-Elemente-Methode in der Geotechnik. Habilitation, Graz University of Technology, Austria.

Schweiger, H.F. (2000)
Berechnungsbeispiel Nr. 3: 3-fach verankerte Baugrube. Proc. Workshop on Verformungsprognose for tiefe Baugruben, DGGT/AK 1.6 (ed.), Stuttgart, Germany, 1-6.

Schweiger, H.F.; Vermeer P.A.; Wehnert, M. (2009)
On the design of deep excavations based on finite element analysis. Geomechanics and Tunnelling, Vol. 2, No.4, 333-344.

Septanika, E.G.; Bonnier, P.G.; Brinkgreve, R.B.J.; Bakker, K.J. (2007)
An efficient 3D modeling of (multi) pile-soil interaction. Proc. 3rd Int. Geomechanics Conf., Nessebar, Bulgaria.

Septanika, E.G.; Bonnier, P.G.; Bakker, K.J.; Brinkgreve, R.B.J. (2008)
3D soil reinforcement modeling by means of embedded pile. Proc. 3rd Int. Conf. of IS-Kyushu, Fukuoka, Japan, 473-478.

Sinha, J. (1996)
Analysis of piles and piled rafts in swelling and shrinking soils. Ph.D. Thesis, University of Sydney, Australia.

Skempton, A.W. (1953)
Discussion contribution: Piles and pile foundations, settlements of pile foundations. Proc. 3rd Int. Conference on Soil Mechanics and Geotechnical Engineering, Zurich, Switzerland, 172.

Sladen, J.A. (1992)
The adhesion factor: applications and limitations. Canadian Geotechnical Journal, Vol. 29, No. 2, 322-326.

Small, J.C.; Booker, J.R. (1986)
Finite layer analysis of layered elastic materials using a flexibility approach. Part 2-Circular and rectangular loadings. Int. Journal for Numerical and Analytical Methods in Geomechanics, Vol. 23, No.5, 959-978.

Small, J.C.; Zhang, H.H. (2002)
Behaviour of pile raft foundations under lateral and vertical loading. International Journal of Geomechanics, ASCE, Vol. 2, No.1, 29-45.

Sommer, H.; Hambach, P. (1974)
Großpfahlversuche im Ton für die Gründung der Talbrücke Alzey. Der Bauingenieur, Vol. 49, 310-317.

Stewart, J.F.; Kulhawy, F.H. (1981)
Interpretation of uplift load distribution data. Proc. 10th Int. Conference on Soil Mechanics and Foundation Engineering, Stockholm, Vol. 2, 277-280.

Ta, L.D.; Small, J.C. (1996)
Analysis of piled raft systems in layered soils. Journal for Numerical and Analytical Methods in Geomechanics, Vol. 20, No.1, 52-72.

Therzaghi, K. (1943)
Theoretical soil mechanics. New York: Wiley.

Tomlinson, M.J. (1957)
The adhesion of piles driven in clay soils. Proc. 4th Int. Conference on Soil Mechanics and Foundation Engineering, London Vol. 2, 66-71.

Trochanis, A.M.; Bielak, B.; Christiano, P. (1991)
Three-dimensional nonlinear study of piles. Journal of Geotechn. Engng, ASCE, Vol. 117, GT 3, 429-447.

Van Langen, H. (1991)
Numerical analysis of soil structure interaction. Ph.D. Thesis, Delft University of Technology. The Netherlands.

Van Langen, H.; Vermeer, P.A. (1991)
Interface elements for singular plasticity points. International Journal for Numerical and Analytical Methods in Geomechanics, Vol. 15, No. 5, 301-315.

Vermeer, P.A.; de Borst R. (1970)
Non-associated plasticity for soils, concrete and rock. Heron, Vol. 29, No.3.

Vesic, A.S. (1972)
Expansion of cavities in infinite soil mass. Journal of Geotechn. Engng, ASCE, Vol. 98, SM 3, 265-290.

Vesic, A.S. (1975)
Principles of pile foundation design. Soil mechanics series No. 38, School of engineering Duke University, Durham, North Carolina.

Vesic, A.S. (1977)
Design of pile foundation. Nat. Cooperative Hwy. Res. Program Synthesis of Pract. No. 42, Transportation Research Board, Washington, D.C.

Vijayvergiya, V. N.; Focht, J. A. (1972)
A new way to predict the capacity of piles in clay. Proc. 4th Annual Offshore Technology Conf., Houston, United States, Vol. 2, 865-874.

Vucetic, M., Dobry, R. (1991)
Effect of soil plasticity on cyclic response. Journal of Geotechnical Engineering 117 (1), 89-107.

Wehnert, M. (2006)
Ein Beitrag zur drainierten und undrainierten Analyse in der Geotechnik. Ph.D. Thesis, Mitteilungsheft Nr. 53, Institute for Geotechnical Engineering, University of Stuttgart.

Wehnert, M.; Benz, T.; Gollub, B.; Cubaleski, T. (2010)
Settlement analysis of a large piled raft foundation. Proc. Numerical methods in geotechnical engineering NUMGE 2010, Benz & Nordal (eds.), Trondheim, Norway, 673-678. London: Taylor & Francis Group.

Wichtemann, T., Triantafyllidis, T. (2009)
On the correlation of "static" and "dynamic" stiffness moduli of non-cohesive soils. Bautechnik Special Issue 2009 – Geotechnical Engineering 86 (S1), 28-39.

Wittke, W.; Spang, J.; Rodatz, W.; Semprich, S. (1974)
Bemessung von horizontal belasteten Großbohrpfählen nach der Methode Finiter Elemente. Bauingenieur, Vol. 49, 219-226.

Würger, E. (2006)
Geotechnisches Gutachten betreffend die Untergrundverhältnisse und Projekt "Wien Mitte". Geotechnical report, 26 pages.

Würger, E. (2007)
Geotechnisches Gutachten betreffend die Untergrundverhältnisse und Gründungsmöglichkeiten für den Neubau der Tower 1und 2 der Donau City Wien. Geotechnical report, 32 pages.

Yang, Y. (2006)
Influence zone for end bearing of piles in sand. Journal of Geotechnical and Geoenvironmental Engineering, ASCE, Vol. 132, No 9, 1229-1237.

Zehentner, H.; Tschuchnigg, F.; Schweiger, H.F. (2011)
Die Baugrube des Sky Tower in Bukarest. Proc. 26th Christian Veder Kolloquium, M. Dietzel et al. (eds.), Graz, Austria, 147-162.

Zienkiewicz, O.C.; Taylor, R.L. (1991)
The finite element method (4 edition). London: McGraw Hill.

Appendix A

A.1 Linear elastic perfectly plastic model - Mohr-Coulomb model

The linear elastic-perfectly plastic Mohr Coulomb (MC) constitutive model is, due to its simplicity, probably still the most frequently used constitutive model in geotechnics. An substantial advantage of the model is that the used parameters are well established. The model represents only a first order approximation of the real soil behaviour, hence, for most practical applications and scientific research, it is not appropriate. But due to its popularity and the fact that linear elastic-perfectly plastic models represent the simplest case of plasticity, the MC model was used for numerical studies and validation examples.

The Mohr-Coulomb yield condition is an extension of the basic Coulomb friction law, where τ_f is the shear stress at failure, σ'_n the normal stress on the failure plane and φ' and c' are the effective strength parameters of the soil.

$$\left|\tau_f\right| = \sigma'_n \cdot \tan\varphi' + c' \tag{A1}$$

In terms of principle stresses (σ'_1, σ'_2, σ'_3) the full Mohr-Coulomb yield condition is defined with six yield functions (f).

$$f_{1a} = \frac{1}{2}(\sigma'_2 - \sigma'_3) + \frac{1}{2}(\sigma'_2 + \sigma'_3) \cdot \sin\varphi' - c' \cdot \cos\varphi' \leq 0 \tag{A2}$$

$$f_{1b} = \frac{1}{2}(\sigma'_3 - \sigma'_2) + \frac{1}{2}(\sigma'_3 + \sigma'_2) \cdot \sin\varphi' - c' \cdot \cos\varphi' \leq 0 \tag{A3}$$

$$f_{2a} = \frac{1}{2}(\sigma'_3 - \sigma'_1) + \frac{1}{2}(\sigma'_3 + \sigma'_1) \cdot \sin\varphi' - c' \cdot \cos\varphi' \leq 0 \tag{A4}$$

$$f_{2b} = \frac{1}{2}(\sigma'_1 - \sigma'_3) + \frac{1}{2}(\sigma'_1 + \sigma'_3) \cdot \sin\varphi' - c' \cdot \cos\varphi' \leq 0 \tag{A5}$$

$$f_{3a} = \frac{1}{2}(\sigma'_1 - \sigma'_2) + \frac{1}{2}(\sigma'_1 + \sigma'_2) \cdot \sin\varphi' - c' \cdot \cos\varphi' \leq 0 \tag{A6}$$

$$f_{3b} = \frac{1}{2}(\sigma'_2 - \sigma'_1) + \frac{1}{2}(\sigma'_2 + \sigma'_1) \cdot \sin\varphi' - c' \cdot \cos\varphi' \leq 0 \qquad \text{(A7)}$$

Due to the fact that associated plasticity would yield to an overestimation of the dilatant behaviour of soil, the dilatancy angle ψ is used to define the plastic potential. Fig. A1 shows the yield surface of the Mohr-Coulomb model in the principle stress space.

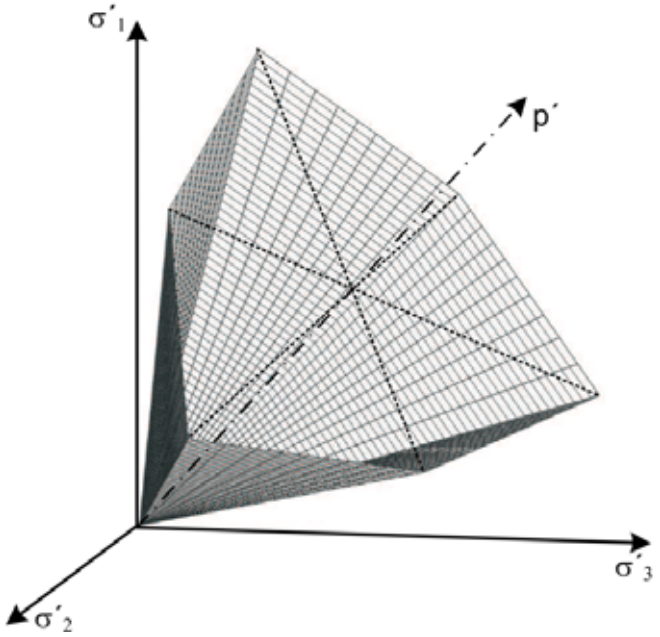

Fig. A1 Mohr-Coulomb yield surface in principle stress space (c´=0) (after Brinkgreve et al. 2010)

The MC model requires the following five input parameters:

E	elasticity modulus [kN/m^2]
υ	Poisson's ratio [-]
c	cohesion [kN/m^2]
φ	friction angle [°]
ψ	dilatancy angle [°]

The major deficiencies of the Mohr-Coulomb model are:

a) No plastic straining for stress paths which do not reach the Mohr-Coulomb yield surface.
b) No plastic straining for isotropic stress paths.
c) Same stiffness is used for primary loading and un-/ reloading.
d) No stress dependency of stiffness.
e) Constant dilatancy angle.
f) No small strain stiffness.

A.2 Hardening Soil Model

The Hardening Soil model (HS) is an elasto-plastic constitutive model that enables modelling of both deviatoric and volumetric hardening (double hardening model). The model was developed by Schanz (1998) and Schanz et al. (1999) on the basis of Vermeer (1978).

The basic features of the Hardening Soil model are:

1. Stress dependent stiffness according to a power law.
2. Hyperbolic relation between strains and deviatoric stress for drained triaxial stress paths (based on Duncan & Chang 1970).
3. Distinction between deviatoric primary loading and unloading/reloading.
4. Mohr-Coulomb failure criterion.

Figure A2 shows a basic idea of the Hardening Soil model, namely the hyperbolic relationship of axial strain ε_1 and the deviatoric stress q in primary loading of a standard drained triaxial test.

$$-\varepsilon_1 = \frac{1}{E_i}\frac{q}{1-\frac{q}{q_a}} \qquad \text{for } q < q_f \tag{A8}$$

with

E_i initial stiffness in a drained triaxial test
q_a asymptotic value of shear strength
q_f ultimate deviatoric stress

Due to the fact that the model distinguishes automatically between primary deviatoric loading, primary compression and unloading/reloading, different stiffness input parameters are required. The stress dependency of soil stiffness is taken into account in the HS model as proposed by Ohde (1938), but slightly modified according to the following equations:

$$E_{50} = E_{50,ref} \cdot \left(\frac{c' \cdot \cos\varphi' + \sigma'_3 \cdot \sin\varphi'}{c' \cdot \cos\varphi' + p_{ref} \cdot \sin\varphi'} \right)^m \tag{A9}$$

$$E_{ur} = E_{ur,ref} \cdot \left(\frac{c' \cdot \cos\varphi' + \sigma'_3 \cdot \sin\varphi'}{c' \cdot \cos\varphi' + p_{ref} \cdot \sin\varphi'} \right)^m \tag{A10}$$

$$E_{oed} = E_{oed,ref} \cdot \left(\frac{c' \cdot \cos\varphi' + \frac{\sigma'_3}{K_0^{nc}} \cdot \sin\varphi'}{c' \cdot \cos\varphi' + p_{ref} \cdot \sin\varphi'} \right)^m \tag{A11}$$

with

$E_{50,ref}$	reference secant stiffness modulus in a drained triaxial test
$E_{ur,ref}$	reference Young's modulus for unloading and reloading
$E_{oed,ref}$	reference oedometric stiffness
p_{ref}	reference pressure
K_o^{nc}	Lateral earth pressure coefficient for normally consolidated conditions
m	parameter which controls the amount of stress dependency

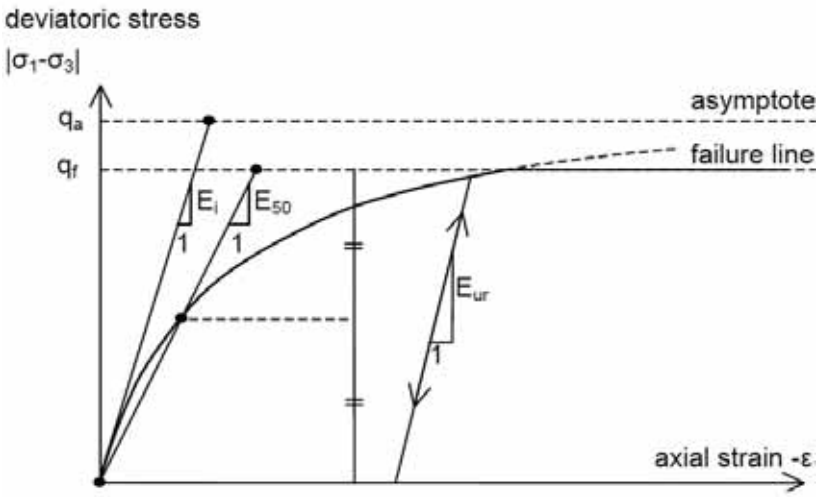

Fig. A2 Hyperbolic stress-strain relation for a drained triaxial test (Brinkgreve et al. 2010)

Figure A3 shows schematically the deviatoric yield surfaces according to the shear hardening law, which is a function of plastic (shear) strains. Additionally illustrated is the total yield contour (deviatoric locus and yield cap) of the HS model in the principle stress space.

The flow rule of the deviatoric yield function is non-associated and based on the "stress dilatancy theory" of Rowe (1962), but slightly modified as explained by Schanz & Vermeer (1996).

$$\dot{\varepsilon}_v^p = \sin\psi_m \cdot \dot{\gamma}^p \tag{A12}$$

$$\sin\psi_m = \frac{\sin\varphi'_m - \sin\varphi'_{cv}}{1 - \sin\varphi'_m \sin\varphi'_{cv}} \tag{A13}$$

with

$\dot{\varepsilon}_v^p$	rate of plastic volumetric strain
$\dot{\gamma}^p$	rate of plastic shear strain
ψ_m	mobilised dilatancy angle
φ'_{cv}	critical state friction angle
φ'_m	mobilised friction angle

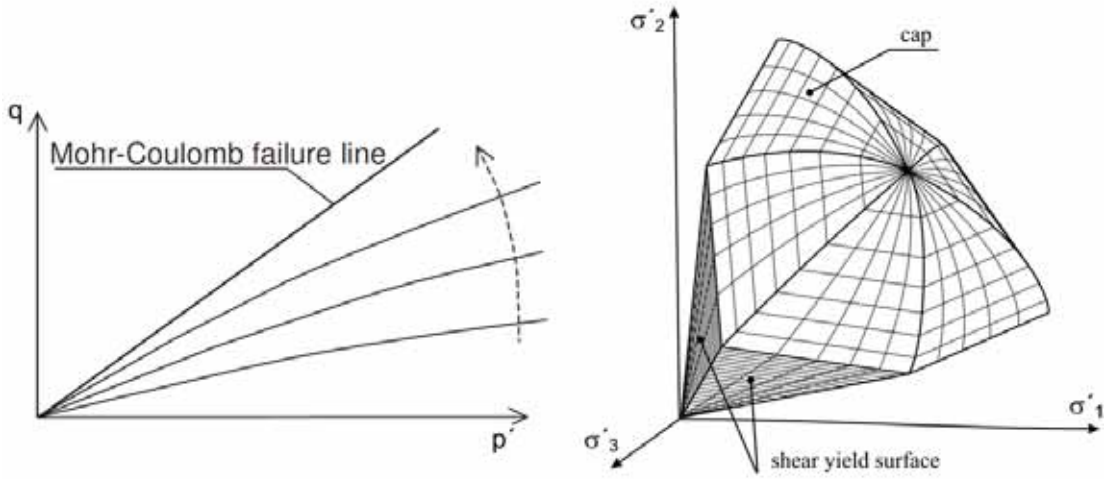

Fig. A3 Deviatoric yield loci (left) and total yield contour in the principle stress space (Brinkgreve et al. 2010)

The Hardening Soil model includes the possibility of limiting the dilatant behaviour of soils using a dilatancy-cut-off. Once the maximum void ratio e_{max} (an input) is reached, ψ_m is set to zero (Figure A4). The change of void ratio e is related to the change of volumetric strain ε_v.

$$-(\varepsilon_v - \varepsilon_v^{init}) = \ln\left(\frac{1+e}{1+e_{init}}\right) \tag{A14}$$

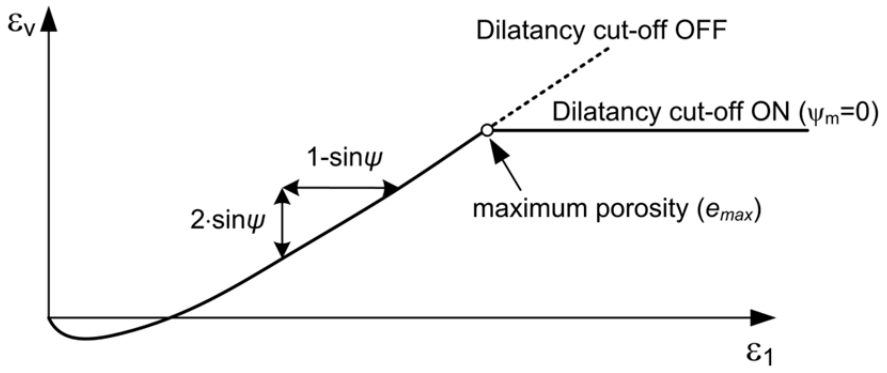

Fig. A4 Schematically representation of dilatancy-cut-off option (after Brinkgreve et al. 2010)

The so-called cap yield surface controls the plastic volumetric strains. The shape of the ellipse is mainly defined by the oedometric stiffness E_{oed} and K_0^{nc}. For the plastic potential the same function as for the yield surface is used. The initial position of the cap yield surface in the p'-q space is computed from the initial stress state in the soil and expands as a function of the pre-consolidation stress p'_p (Figure A5). Because the volumetric and deviatoric yield functions are shifted, the elastic region of the Hardening Soil model is increased. The mathematical definition of the cap yield surface is given in equation A15, where $\tilde{q}$ is special measure for deviatoric stress and α_c a model parameter defining the shape of the cap yield function.

$$f^c = \frac{\tilde{q}^2}{\alpha_c^2} + p'^2 - p'^2_p \tag{A15}$$

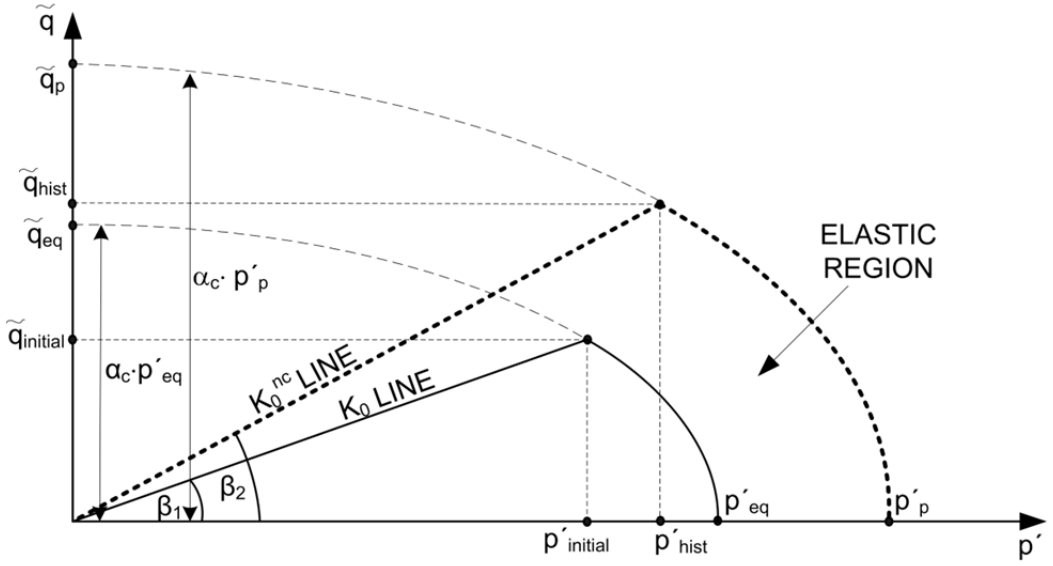

Fig. A5 Schematically representation of cap yield surface

The pre-consolidation stress p'_p depends on the overconsolidation of the soil. If the soil is overconsolidated, one has two different options to model this effect in the initial conditions. The first option is to use an over-consolidation-ratio (*OCR*) value, which is the ratio of the highest vertical stress σ'_p reached in the past divided by the in-situ effective vertical stress $\sigma'_{yy}{}^0$. The second option is to use a so-called pre-overburden pressure (*POP*), which directly determines a geological overburden. Figure A6 compares these two approaches. An *OCR* value increases the effective vertical stress according to equation A16, whereas the *POP* value increases the vertical stresses by a constant value.

$$OCR = \frac{\sigma'_p{}^{OCR}}{\sigma'_{yy}{}^0} \tag{A16}$$

$$POP = \left|\sigma'_p{}^{POP} - \sigma'_{yy}{}^0\right| \tag{A17}$$

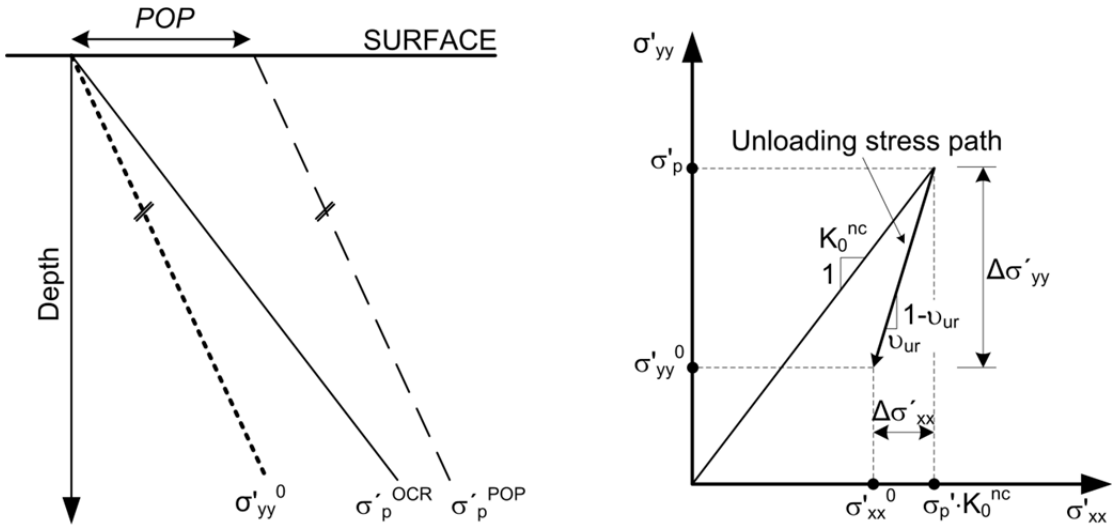

Fig. A6 *OCR* vs *POP* (left) and definition of K_0 (right) (after Brinkgreve et al. 2010)

For normally consolidated conditions *OCR* is 1 while *POP* equals 0. In this case the highest mean effective stress p'_{hist} reached in the past and the initial stress $p'_{initial}$ are the same and as a consequence p'_p and p'_{eq} also coincide (see Figure A5).

In overconsolidated soils the value of K_0 is expected to be larger than the K_0^{nc} value. In the HS model the unloading stress path from σ'_p to $\sigma'_{yy}{}^0$ is defined as shown in Figure A6 and equation A18.

$$\frac{\Delta\sigma'_{xx}}{\Delta\sigma'_{yy}} = \frac{\sigma'_p \cdot K_0^{nc} - \sigma'_{xx}{}^0}{\sigma'_p - \sigma'_{yy}{}^0} \tag{A18}$$

From this, it follows that when using an *OCR* for the definition of the overconsolidation a constant value of K_0 is obtained.

$$\frac{\Delta\sigma'_{xx}}{\Delta\sigma'_{yy}} = \frac{K_0^{nc} * OCR * \sigma'^{\,0}_{yy} - \sigma'^{\,0}_{xx}}{(OCR-1) * \sigma'^{\,0}_{yy}} = \frac{\nu_{ur}}{1-\nu_{ur}} \tag{A19}$$

$$\frac{\sigma'^{\,0}_{xx}}{\sigma'^{\,0}_{yy}} = K_0^{nc} * OCR - \frac{\nu_{ur}}{1-\nu_{ur}} * (OCR-1) = K_0 \tag{A20}$$

When using a pre-overburden-pressure, the internally calculated K_0 value increases with increasing σ'_{yy}, in other words, increases with depth.

$$\frac{\Delta\sigma'_{xx}}{\Delta\sigma'_{yy}} = \frac{K_0^{nc} \cdot (POP + \sigma'^{\,0}_{yy}) - \sigma'^{\,0}_{xx}}{(POP + \sigma'^{\,0}_{yy}) - \sigma'^{\,0}_{yy}} \tag{A21}$$

$$\frac{\sigma'^{\,0}_{xx}}{\sigma'^{\,0}_{yy}} = K_0 = \frac{K_0^{nc} \cdot \left(\sigma'^{\,0}_{yy} + POP\right)}{\sigma'^{\,0}_{yy}} - \frac{POP \cdot \left(\frac{\nu_{ur}}{1-\nu_{ur}}\right)}{\sigma'^{\,0}_{yy}} \tag{A22}$$

However it is also possible to overrule the calculated lateral earth pressure coefficient values with the input of a constant K_0. Relationships between K_0 and OCR values are given e.g. in Mayne et al. (1982).

The Hardening Soil model requires the following input parameters:

c	cohesion [kN/m^2]
φ	friction angle [°]
ψ	dilatancy angle [°]
$E_{50,ref}$	reference secant stiffness modulus in a drained triaxial test [kN/m^2]
$E_{ur,ref}$	reference Young's modulus for unloading and reloading [kN/m^2]
$E_{oed,ref}$	reference oedometric stiffness [kN/m^2]
p_{ref}	reference pressure for stress dependent stiffness [kN/m^2]
m	parameter which controls the amount of stress dependency [-]
υ_{ur}	Poisson's ratio for unloading/reloading [-]
K_o^{nc}	Lateral earth pressure coefficient for normally consolidated conditions

The major deficiencies of the Hardening Soil model are:

a) No softening behaviour.
b) Elastic behaviour in dynamic or cyclic loading.
c) No small strain stiffness.

A.2 Hardening Soil Small Model

The Hardening Soil Small model (HSS) is based on the Hardening Soil model and additionally allows for modelling the high stiffness at very low strains. Compared with the Hardening Soil model, the HSS model needs two additional parameters to describe the stiffness behaviour at small strains. Namely, the initial shear modulus G_0 and the shear strain level $\gamma_{0.7}$, which represents the amount of shear strains (γ_s) where the secant shear modulus is reduced to 70% of its initial value. Figure A7 shows schematically the stiffness-strain behaviour in a logarithmic scale. The tangent shear modulus is defined according to equation A23 and bounded by the unloading/reloading shear stiffness G_{ur}. From that follows the cut-off shear strain $\gamma_{cut\text{-}off}$.

$$G_t = \frac{G_0}{\left(1 + 0.385 \frac{\gamma}{\gamma_{0.7}}\right)^2} \tag{A23}$$

$$\gamma_{cut-off} = \frac{1}{0.385}\left(\sqrt{\frac{G_0}{G_{ur}}} - 1\right) \cdot \gamma_{0.7} \tag{A24}$$

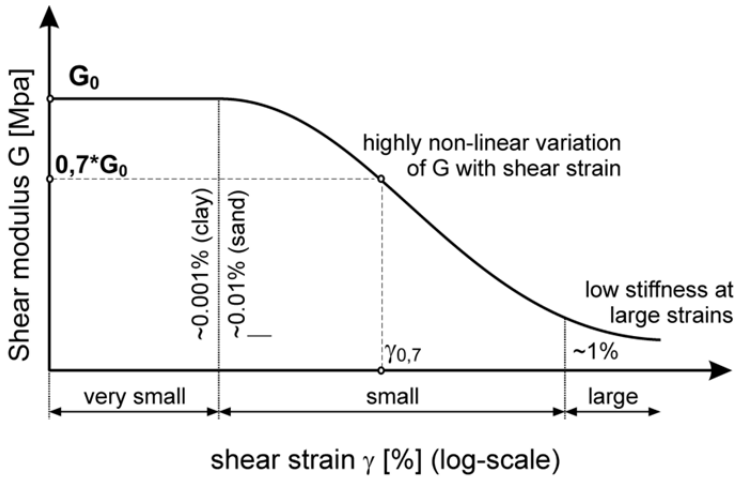

Fig. A7 Variation of stiffness with strain at small strain level (after Scharinger 2007)

In contrast to the HS model, the HSS model shows, due to small strain stiffness, a hysteretic behaviour within unloading-reloading loops (Figure A8). The actual shear stiffness present in the model also takes the stress dependency into account, as in all other stiffness parameters.

$$G_0 = G_{0,ref} \cdot \left(\frac{c' \cdot \cos\varphi' + \sigma'_3 \cdot \sin\varphi'}{c' \cdot \cos\varphi' + p^{ref} \cdot \sin\varphi'} \right)^m \tag{A25}$$

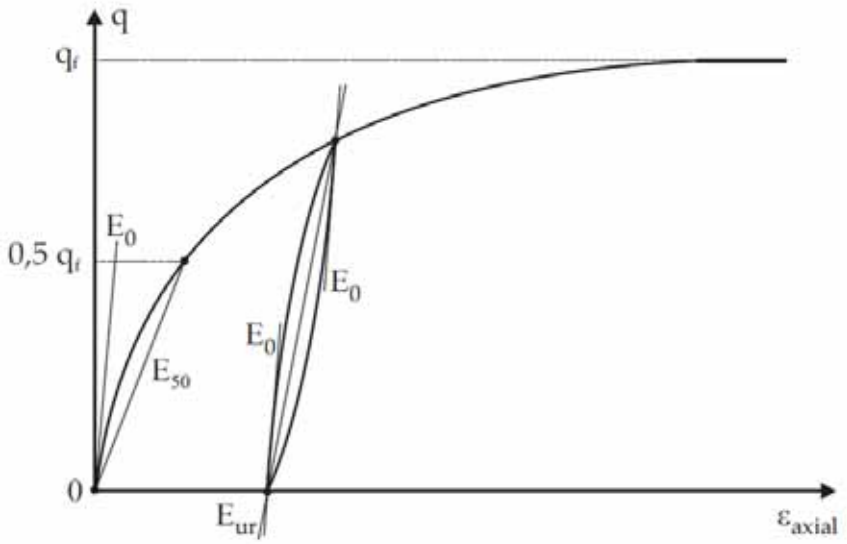

Fig. A8 Stiffness parameters of the HSS model in a standard drained triaxial test (Benz et al. 2009a)

The Hardening Soil Small model requires the following input in addition to the HS parameters:

$G_{0,ref}$	reference shear stiffness at very small strains [kN/m^2]
$\gamma_{0.7}$	shear strain at which $G_s = 0.722 \cdot G_0$ [-]

The major deficiencies of the Hardening Soil Small model are:

a) No softening behaviour.
b) No accumulation of strains in dynamic analyses.
c) No liquefaction behaviour with cyclic loading.

A more detailed description of the model can be found in Benz (2007) and Benz et al. (2009).

References:

Benz, T. (2007)
Small-strain stiffness of soils and its numerical consequences. Ph.D. Thesis, Mitteilungsheft Nr. 55, Institute for Geotechnical Engineering, University of Stuttgart.

Benz, T.; Vermeer, P.; Schwab, R. (2009)
A small-strain overlay model. International Journal for Numerical and Analytical Methods in Geomechanics, Vol. 33, No.1, 25-44.

Benz, T.; Schwab, R.; Vermeer, P. (2009a)
Small strain stiffness in geotechnical analyses. Bautechnik Special Issue 2009 – Geotechnical Engineering 86 (S1), 16-27.

Brinkgreve, R.B.J.; Swolfs, W.M.; Engin, E. (2010)
PLAXIS 2D 2010 - Users Manual. Plaxis bv, Delft, The Netherlands.

Duncan, J.M.; Chang, C.-Y. (1970)
Nonlinear analysis of stress and strain in soil. Journal of Soil Mech. and Found. Div., ASCE, Vol. 96, No. 5, 1629-1653.

Mayne, P.W.; Kulhawy, F.H. (1982)
K_0-OCR relationships in soil. Journal of Soil Mech. and Found. Div., ASCE, Vol. 108, GT 6, 851-872.

Ohde, J. (1939)
Zur Theorie der Druckverteilung im Baugrund. Der Bauingenieur, Vol. 20, 451-459.

Rowe, P.W. (1962)
The stress-dilatancy relation for static equilibrium of an assembly of particles in contact. *Proc. Roy. Soc. A.,* No. 269, pp. 500-527.

Schanz, T; Vermeer, P.A. (1996)
Angles of friction and dilatancy of sand. Géotechnique, Vol. 46, No. 1, 145-151.

Schanz, T. (1998)
Zur Modellierung des mechanischen Verhaltens von Reibungsmaterialien. Habilitation, Universität Stuttgart, Mitteilungen des Instituts für Geotechnik, Heft 45, Germany.

Schanz, T.; Vermeer, P.A.; Bonnier, P.G. (1999).
The Hardening-Soil model: Formulation and verification. Beyond 2000 in Computational Geotechnics, R.B.J. Brinkgreve (ed), 281-290. Rotterdam: Balkema.

Scharinger, F. (2007)
A multilaminate model for soil incorporating small strain stiffness. Ph.D. thesis, Gruppe Geotechnik Graz, Graz University of Technology, Austria, Heft 31.

Vermeer, P.A. (1978)
A double hardening model for sand. Géotechnique, Vol. 28, No. 4, 413-433.

Appendix B

In the following the basic theory of an isoparametric interface element is presented. Figure B1 shows a two-dimensional interface with second order shape function. It consists of 6 nodes, 3 at the top of the element and 3 at the bottom. v_g and u_g represent the global, and v_{loc} and u_{loc} the local coordinates. χ is the rotation angle from the global to the local coordinate system.

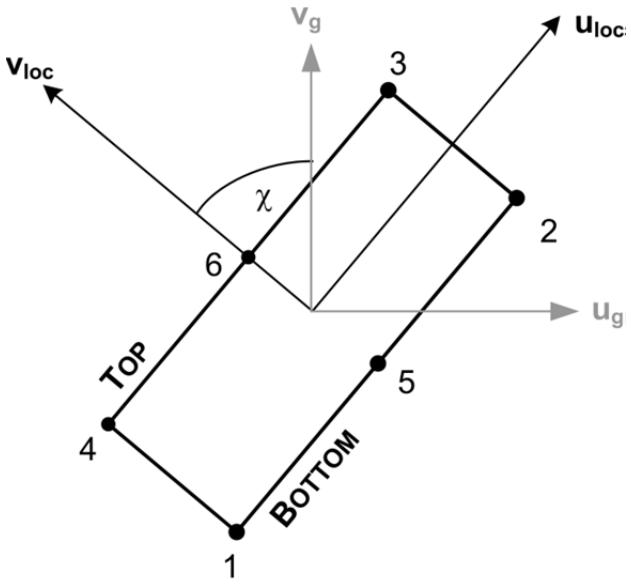

Fig. B1: Two dimensional interface element with quadratic shape function

The interface stress consists of a normal stress component σ_n and the shear stress component τ. These stresses are calculated from the element strains ε and γ. $\mathbf{D}_i$ represents the constitutive matrix of the interface.

$$\begin{Bmatrix} \Delta\tau \\ \Delta\sigma \end{Bmatrix} = \mathbf{D}_i \begin{Bmatrix} \Delta\gamma \\ \Delta\varepsilon \end{Bmatrix} \tag{B26}$$

$$\mathbf{D}_i = \begin{bmatrix} K_s & K_{sn} \\ K_{ns} & K_n \end{bmatrix} \tag{B27}$$

with

K_s	elastic shear stiffness
K_n	elastic normal stiffness
K_{ns} / K_{sn}	mixed terms

For isotropic linear elastic behaviour, $\mathbf{D}_i$ reduces to Equation B3.

$$\mathbf{D}_i = \begin{bmatrix} K_s & 0 \\ 0 & K_n \end{bmatrix} \tag{B28}$$

The strains of an interface are defined as relative displacements between the node pairs. In other words, the strains are the difference between displacements at the "top" and at the "bottom" of an interface (in local coordinates).

$$\gamma = \Delta u_{loc} = u_{loc}^{bot} - u_{loc}^{top} \tag{B29}$$

$$\varepsilon = \Delta v_{loc} = v_{loc}^{bot} - v_{loc}^{top} \tag{B30}$$

$$\gamma = (v_g^{bot} - v_g^{top}) \cdot \sin\chi + (u_g^{bot} - u_g^{top}) \cdot \cos\chi \tag{B31}$$

$$\varepsilon = (v_g^{bot} - v_g^{top}) \cdot \cos\chi + (u_g^{bot} - u_g^{top}) \cdot \sin\chi \tag{B32}$$

$$\begin{Bmatrix} \gamma \\ \varepsilon \end{Bmatrix} = \begin{bmatrix} \cos\chi \cdot (u_g^{bot} - u_g^{top}) & \sin\chi \cdot (v_g^{bot} - v_g^{top}) \\ -\sin\chi \cdot (u_g^{bot} - u_g^{top}) & \cos\chi \cdot (v_g^{bot} - v_g^{top}) \end{bmatrix} \tag{B33}$$

The equations show that strains are defined as relative displacements (unit [m]). The global displacements u_g and v_g are calculated at every point via the shape function. In this example a quadratic shape function is used. ξ represents the intrinsic (local) coordinate axis.

$$N_1 = N_4 = \frac{1}{2}\xi(\xi - 1) \tag{B34}$$

$$N_2 = N_5 = \frac{1}{2}\xi(\xi + 1) \tag{B35}$$

$$N_3 = N_6 = (1 - \xi^2) \tag{B36}$$

Or in short form:

$$\begin{Bmatrix} \gamma \\ \varepsilon \end{Bmatrix} = \mathbf{B} \cdot \boldsymbol{\delta} \tag{B37}$$

Where $\boldsymbol{\delta}$ is a vector with all degrees of freedom within the interface element:

$$\boldsymbol{\delta} = \{u_1 v_1 u_2 v_2 u_3 v_3 u_4 v_4 u_5 v_5 u_6 v_6\}^T \tag{B38}$$

And the **B** matrix is defined as:

$$\mathbf{B} = \begin{bmatrix} \cos\chi & \sin\chi \\ -\sin\chi & \cos\chi \end{bmatrix} \begin{bmatrix} N_1 & 0 & N_2 & 0 & -N_3 & 0 & -N_4 & 0 & N_5 & 0 & -N_6 & 0 \\ 0 & N_1 & 0 & N_2 & 0 & -N_3 & 0 & -N_4 & 0 & N_5 & 0 & -N_6 \end{bmatrix} \tag{B39}$$

And finally the element stiffness matrix is given by:

$$\mathbf{K_e} = \int_{-1}^{1} \mathbf{B}^T \cdot \mathbf{D}_i \cdot \mathbf{B} \cdot |\mathbf{J}| \, d\xi \tag{B40}$$

where $|\mathbf{J}|$ is the determinant of the Jacobean matrix **J**.

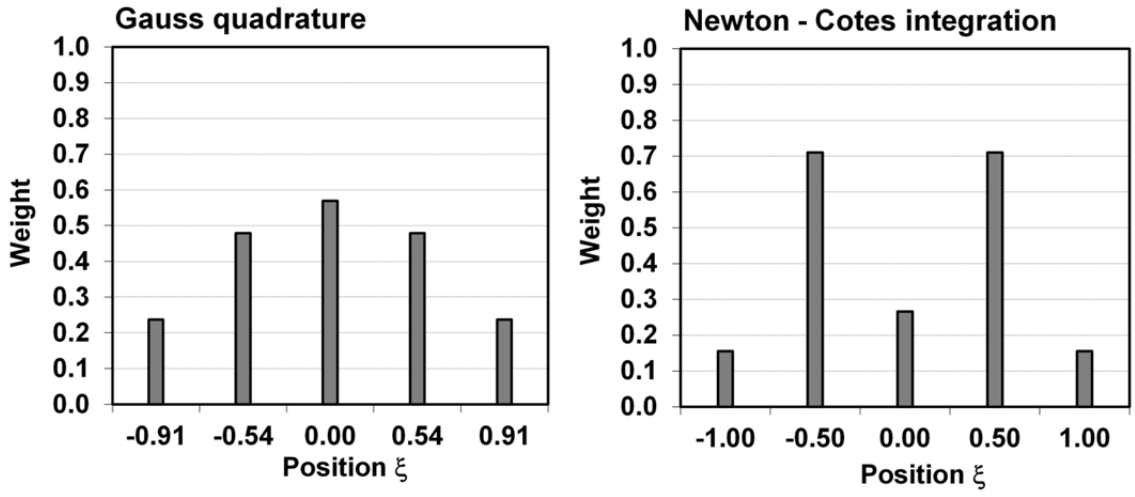

Fig. B2: Gauss (left) vs Newton-Cotes integration (right)

For the evaluation of the element stiffness matrix $\boldsymbol{K}_e$, numerical integration is used. Two methods to do so are frequently applied, namely the Gauss quadrature and the Newton-Cotes integration scheme. For the first method the integration points are defined at certain positions between the finite element nodes; for the latter method, stress integration points and finite element nodes coincide (Figure B2).

Van Langen (1991) studied a simple shallow foundation on homogeneous elastic material and showed that Gauss integration yields more stress oscillations than Newton-Cotes integration at the interface defined underneath the footing (Figure B3).

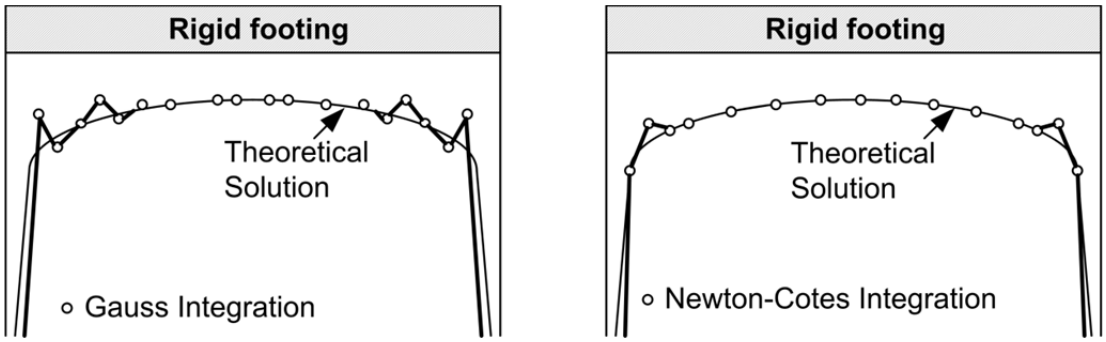

Fig. B3: Normal stress distribution at the interface underneath a rigid footing (after Van Langen 1991)

He introduced a stress transfer matrix $\boldsymbol{T}$, which reduces to a unity matrix in the case where the same numerical integration procedure is used for both the interface and the surrounding soil. But when using Newton-Cotes integration for an interface and Gauss integration for the solid soil elements $\boldsymbol{M_i}$ and $\boldsymbol{M_{soil}}$ are completely different.

$$\mathbf{T} = \mathbf{M}_i^{-1} \cdot \mathbf{M}_{Soil} \tag{B41}$$

$$\mathbf{M} = \int_{Sc} \mathbf{B}^T \cdot \mathbf{B} \cdot dS \tag{B42}$$

where the subscript “i” indicates an interface and “soil” a soil element. Van Langen (1991) concluded that for an interface element, which corresponds to a 15-noded solid element (5 pairs of nodes), the Newton-Cotes integration suppresses two types and amplifies one type of stress oscillation. But, he also states that the suppressed types are likely to be present in stress results.

A detailed description of interface elements is given e.g. in Beer & Watson (1992) or Potts & Zdravković (1999).

References:

Beer, G.; Watson, J.O. (1992)
Introduction to finite and boundary element methods for engineers. West Sussex: John Wiley and Sons.

Potts, D.M.; Zdravković, L. (1999)
Finite element analysis in geotechnical engineering, Theory. London: Telford.

Van Langen, H. (1991)
Numerical analysis of soil structure interaction. Ph.D. Thesis, Delft University of Technology. The Netherlands.

Appendix C

In the finite element method as used in this thesis, the unknowns of each FE node correspond to the displacement components. And within a finite element, the distribution is obtained using the nodal displacement values and the interpolation functions of the element (Brinkgreve & Swolfs 2007).

$$\mathbf{u} = \mathbf{N} \cdot \mathbf{u}^n \tag{C43}$$

with

u	displacement field within a solid soil element
N	matrix with interpolation function of the finite element
$\mathbf{u}^n$	vector of nodal displacements

The shape functions (interpolation functions) are defined using intrinsic coordinates. In the three dimensional case of a 15 noded wedge element the local coordinates ξ, η and ζ are used. Figure C1 shows the local numbering of a standard 15 noded wedge element as used in PLAXIS 3DF. The related interpolation functions are given in equation C2 to C16.

More detailed descriptions of interpolation functions are given e.g. in Beer & Watson (1992).

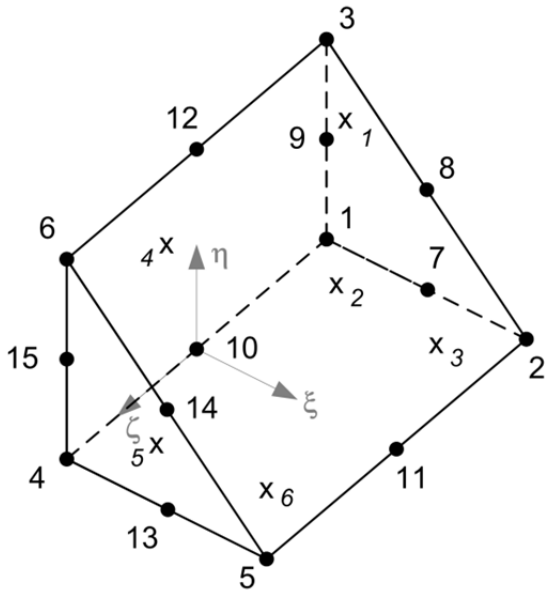

Fig. C1: Local numbering of a 15 noded wedge element (after Brinkgreve & Swolfs 2007)

$$N_1 = -(1-\xi-\eta)(1-\zeta)(2\cdot\xi+2\cdot\eta+\zeta)/2 \tag{C44}$$

$$N_2 = (-\xi)(1-\zeta)(2-2\cdot\xi-\zeta)/2 \tag{C45}$$

$$N_3 = (-\eta)(1-\zeta)(2-2\cdot\eta+\zeta)/2 \tag{C46}$$

$$N_4 = -(1-\xi-\eta)(1+\zeta)(2\cdot\xi+2\cdot\eta-\zeta)/2 \tag{C47}$$

$$N_5 = -(-\xi)(1+\zeta)(2-2\cdot\xi+\zeta)/2 \tag{C48}$$

$$N_6 = -(-\eta)(1+\zeta)(2-2\cdot\eta-\zeta)/2 \tag{C49}$$

$$N_7 = (1-\xi-\eta)\xi(1-\zeta)\cdot 2 \tag{C50}$$

$$N_8 = -\eta\cdot\xi(1-\zeta)\cdot 2 \tag{C51}$$

$$N_9 = (1-\xi-\eta)\eta(1-\zeta)\cdot 2 \tag{C52}$$

$$N_{10} = (1-\xi-\eta)(1-\zeta)(1+\zeta) \tag{C53}$$

$$N_{11} = \xi(1-\zeta)(1+\zeta) \tag{C54}$$

$$N_{12} = \eta(1-\zeta)(1+\zeta) \tag{C55}$$

$$N_{13} = (1-\xi-\eta)\xi(1+\zeta)\cdot 2 \tag{C56}$$

$$N_{14} = \xi\cdot\eta(1+\zeta)\cdot 2 \tag{C57}$$

$$N_{15} = (1-\xi-\eta)\eta(1+\zeta)\cdot 2 \tag{C58}$$

References:

Beer, G.; Watson, J.O. (1992)
Introduction to finite and boundary element methods for engineers. West Sussex: John Wiley and Sons.

Brinkgreve, R.B.J.; Swolfs, W.M. (2007)
Plaxis 3D Foundation, Finite element code for soil and rock analyses, Users Manual, Plaxis bv, Delft, The Netherlands.